

Crystallization kinetics  
in antimony and tellurium alloys  
used for phase change recording

Von der Fakultät für  
Mathematik, Informatik und Naturwissenschaften  
der Rheinisch-Westfälischen Technischen Hochschule Aachen  
zur Erlangung des akademischen Grades eines Doktors  
der Naturwissenschaften genehmigte Dissertation

vorgelegt von  
Diplom-Physiker Johannes Andreas Kalb  
aus Neuss

Berichter: Universitätsprofessor Dr. Matthias Wuttig  
Universitätsprofessor Dr. Frans Spaepen  
Tag der mündlichen Prüfung: 10. Februar 2006

Diese Dissertation ist auf den Internetseiten  
der Hochschulbibliothek online verfügbar.



# Abstract

Modern computers usually employ several types of data storage devices. Most frequently, magnetic and optical storage media are used. The latter have become of great importance throughout the last decade: nowadays a significant amount of data is stored on compact discs (CDs) and digital versatile discs (DVDs). A few years ago, *rewritable* CDs and DVDs have become commercially available and are widely used these days. In these storage media, a thin film of an antimony (Sb) or tellurium (Te) alloy is locally and reversibly switched by laser heating between the amorphous and the crystalline state. These states can be distinguished optically by their difference in reflectivity. Due to the reversibility of the phase transformation, rewritable CDs and DVDs are also called *phase change media*. The corresponding Sb and Te alloys are frequently termed *phase change materials*.

Recently, phase change materials have also shown high potential for the development of non-volatile *electronic phase change random access memories*. In this application, a current pulse provides the heat that is necessary to induce the phase transformation between the amorphous and the crystalline state, which can be distinguished by their difference in electrical conductivity. First prototypes of this memory type are currently developed by the industry and demonstrate fast non-volatile data storage. There are good prospects that these memories finally replace current data storage devices in modern computers. In order to accomplish this, however, it is highly necessary to understand the phase transformation between the amorphous and the crystalline phase for Sb and Te alloys. This thesis makes a contribution to a fundamental understanding of the crystallization kinetics of amorphous and liquid phase change materials. The results should help to optimize both optical and electronic phase change media in terms of data transfer rates and scalability.

In one project of this study, *ex situ* atomic force microscopy (AFM) in combination with a high-precision furnace was identified as a powerful and accurate tool to determine isothermal crystallization parameters in thin films as a function of time and temperature. This method was employed for a systematic study of crystallization kinetics in sputtered amorphous  $\text{Ag}_{0.055}\text{In}_{0.065}\text{Sb}_{0.59}\text{Te}_{0.29}$  (hereafter: AgIn-Sb<sub>2</sub>Te),  $\text{Ge}_4\text{Sb}_1\text{Te}_5$ ,  $\text{Ge}_2\text{Sb}_2\text{Te}_5$ , and  $\text{Ge}_1\text{Sb}_2\text{Te}_4$  thin films used for phase change recording. The temperature dependence of the crystal nucleation rate and the crystal growth velocity, which are the two fundamental quantities involved in crystallization, were determined between around 90 and 190°C by direct observation of crystals. Using these quantities, the critical work for crystalline cluster formation could be calculated. The time dependence of the nucleation rate was also investigated. The knowledge of these crystallization parameters provides the basis to model crystallization and therefore to optimize data transfer rates.

*Ex situ* transmission electron microscopy (TEM) was used to study the crystal morphology in these alloys. Tilting of plan view samples revealed that each crystallized growth formation is a bent single crystal. Cross-sectional TEM showed that only heterogeneous (not homogeneous) crystal nucleation occurs. These findings help to interpret the nucleation parameters obtained from the experiment mentioned above.

In general, all alloys exhibited similar crystal growth characteristics, but the crystal nucleation behavior of AgIn-Sb<sub>2</sub>Te differed remarkably from that of the GeSbTe alloys. These observations provide an explanation for the different re-crystallization mechanisms observed for these materials under operating conditions. They also demonstrate that in particular the crystal nucleation rate is of great importance to control crystallization kinetics and therefore data transfer rates in phase change media.

In a second project, sputtered amorphous films of the compositions mentioned above were studied by differential scanning calorimetry (DSC). Upon continuous heating, a heat release due to structural relaxation of the amorphous phase between 0.5 and 1.0 kJ/mol was observed. This value depends on the thermal history of the sample. Pre-annealing of the amorphous phase revealed the glass transition temperature within 10 K of the crystallization temperature upon continuous heating at 40 K/min. The knowledge of the glass transition temperature is of fundamental importance to understand and interpret crystal nucleation rates and crystal growth velocities.

In a third project, droplets of molten alloys of composition  $\text{Ge}_{12}\text{Sb}_{88}$ ,  $\text{AgIn-Sb}_2\text{Te}$ ,  $\text{Ge}_4\text{Sb}_1\text{Te}_5$  and  $\text{Ge}_2\text{Sb}_2\text{Te}_5$ , surrounded by a molten dehydrated  $\text{B}_2\text{O}_3$  flux, were under-cooled to 40–80 K below their liquidus temperature in a differential thermal analyzer (DTA). The crystal-melt interfacial energy, which is the most important parameter for the calculation of the crystal nucleation rate, was determined from the nucleation temperature using the classical nucleation theory. This gave values of around 0.20 times the heat of fusion per atom in the interface for all alloys. This value should be a lower limit since it was not established that nucleation was homogeneous in the experiments. The steady-state nucleation rate was calculated between the liquidus and glass transition temperature and was higher for the GeSbTe alloys than for the Sb-rich alloys. This explains the different crystallization behavior of these materials under operating conditions. Nevertheless, the nucleation rates appear too high to allow amorphization under operating conditions for the highest achievable cooling rates. Therefore, in conclusion, it is the presence of an incubation time for nucleation that makes amorphization and therefore phase change recording possible in both optical and electronic phase change media.



# Kurzfassung

**Übersetzung des englischen Originaltitels:** Kristallisationskinetik in Antimon- und Tellur-Verbindungen, die zur Datenspeicherung in Phasenwechselmedien eingesetzt werden.

In modernen Computern werden üblicherweise verschiedene Arten von Datenspeichern eingesetzt. Sehr häufig werden magnetische und optische Speichermedien benutzt. Letztere haben innerhalb des vergangenen Jahrzehnts an großer Bedeutung gewonnen: Heute wird ein Großteil der anfallenden Datenmenge auf CDs (englisch: compact disks) und DVDs (englisch: digital versatile disks) gespeichert. Seit einigen Jahren sind auch *wiederbeschreibbare* CDs und DVDs kommerziell erhältlich und sind heutzutage weit verbreitet. In diesen Datenspeichern wird ein dünner Film einer Antimon- oder Tellur-Verbindung (Abk.: Sb- oder Te-Verbindung) durch Laser-Heizen lokal und reversibel zwischen dem amorphen und kristallinen Zustand hin- und zurückgeschaltet. Diese Zustände können aufgrund ihrer verschiedenen Reflektivitätskoeffizienten optisch unterschieden werden. Wegen der Umkehrbarkeit des Phasenübergangs werden wiederbeschreibbare CDs und DVDs auch *Phasenwechselmedien* genannt. Die entsprechenden Sb- und Te-Verbindungen werden häufig als *Phasenwechselmaterialien* bezeichnet.

Kürzlich haben Phasenwechselmaterialien auch hohes Potenzial zur Entwicklung nicht flüchtiger elektronischer Datenspeicher mit wahlfreiem Zugriff (englisch: non-volatile electronic phase change random access memories) gezeigt. In dieser Anwendung wird die Joulsche Wärme, die zur Phasentransformation zwischen dem amorphen und kristallinen Zustand benötigt wird, durch einen Strompuls lokal in das Material eingekoppelt. Die beiden Zustände unterscheiden sich stark durch ihre elektrische Leitfähigkeit und können daher auf diese Art ausgelesen werden. Erste Prototypen dieses

Speichertypen werden derzeit industriell entwickelt und demonstrieren schnelle nicht flüchtige Datenspeicherung. Die Aussichten, dass dieser Speichertyp in der Zukunft gängige Datenspeicher in modernen Computern ersetzt, sind sehr gut. Um diesen Schritt jedoch zu erreichen, ist es zwingend notwendig, die Phasentransformation zwischen amorpher und kristalliner Phase in Sb- und Te-Verbindungen besser zu verstehen. Diese Doktorarbeit trägt zu einem grundlegenden Verständnis der Kristallisationskinetik amorpher und flüssiger Phasenwechselmaterialien bei. Die Ergebnisse sind eine wichtige Hilfe für die Optimierung von Datenspeicherraten und der Skalierbarkeit sowohl in optischen als auch in elektronischen Phasenwechselmedien.

In einem Projekt dieser Arbeit wurde „*Ex situ*“-Rasterkraftmikroskopie in Kombination mit einem Hochpräzisionsofen als eine leistungsfähige und genaue Methode identifiziert, um isotherme Kristallisationsparameter in dünnen Filmen als Funktion von Zeit und Temperatur zu bestimmen. Diese Methode wurde benutzt, um dünne gesputterte amorphe Filme der Zusammensetzungen  $\text{Ag}_{0.055}\text{In}_{0.065}\text{Sb}_{0.59}\text{Te}_{0.29}$  (im Folgenden  $\text{AgIn-Sb}_2\text{Te}$  genannt),  $\text{Ge}_4\text{Sb}_1\text{Te}_5$ ,  $\text{Ge}_2\text{Sb}_2\text{Te}_5$  und  $\text{Ge}_1\text{Sb}_2\text{Te}_4$ , die in Phasenwechselmedien zum Einsatz kommen, systematisch im Hinblick auf ihre Kristallisationskinetik zu untersuchen. Die Temperaturabhängigkeit der Kristall-Keimbildungsrate und der Kristall-Wachstumsgeschwindigkeit, welche die beiden elementaren zur Kristallisation beitragenden Größen sind, wurde in einem Temperaturbereich zwischen 90 und 190°C durch direkte Beobachtung der Kristalle bestimmt. Aus diesen Größen konnte die kritische Arbeit zur Bildung eines kristallinen Clusters berechnet werden. Die Zeitabhängigkeit der Keimbildungsrate wurde ebenfalls untersucht. Die Kenntnis der Kristallisationsparameter eröffnet Möglichkeiten zur Modellierung der Kristallisation und daher zur Erhöhung von Datentransferraten.

Die Form der Kristalle wurde durch „*Ex situ*“-Transmissions-Elektronenmikroskopie bestimmt. Drehexperimente an „Plan-View“-Proben zeigten, dass jedes kristalline Objekt ein gebogener Einkristall ist. Untersuchung von Querschnittsproben machte deutlich, dass nur heterogene (nicht homogene) Kristall-Keimbildung auftritt. Diese Ergebnisse helfen, die Keimbildungsparameter, die mit dem oben genannten Experiment bestimmt wurden, zu interpretieren.

Alle Legierungen zeigten ähnliche Kristallwachstums-Eigenschaften, die Kristall-Keimbildung von  $\text{AgIn-Sb}_2\text{Te}$  verhielt sich jedoch sehr unterschiedlich zu der Keimbil-

derung in den GeSbTe-Legierungen. Diese Beobachtungen erklären die verschiedenen Rekristallisations-Mechanismen dieser Materialien beim Einsatz in Datenspeichern. Sie zeigen auch, dass insbesondere die Kristall-Keimbildungsrate von grundlegender Wichtigkeit ist, um Kristallisationskinetik und daher auch Datentransferraten in Phasenwechselmedien zu regulieren.

In einem zweiten Projekt wurden gesputterte amorphe Filme der oben genannten Verbindungen mit Hilfe von Differenzial-Rasterkalorimetrie untersucht. Beim kontinuierlichen Heizen wurde eine Wärmeabgabe zwischen 0.5 und 1.0 kJ/mol beobachtet, die auf strukturelle Relaxation der amorphen Phase zurückgeführt werden konnte. Dieser Wert hängt von der Dauer und der Temperatur vorangegangener Tempervorgänge ab. Ein vorausgehendes Tempern der amorphen Phase zeigte beim anschließenden kontinuierlichen Heizen mit 40 K/min den Glasübergang in einem Temperaturbereich von 10 K um die Kristallisationstemperatur. Die Kenntnis der Glasübergangs-Temperatur ist von bedeutender Wichtigkeit für das Verständnis und die Interpretation von Kristall-Keimbildungsraten und Kristall-Wachstumsgeschwindigkeiten.

In einem dritten Projekt wurden Tropfen geschmolzener Legierungen der Zusammensetzung  $\text{Ge}_{12}\text{Sb}_{88}$ ,  $\text{AgIn-Sb}_2\text{Te}$ ,  $\text{Ge}_4\text{Sb}_1\text{Te}_5$  und  $\text{Ge}_2\text{Sb}_2\text{Te}_5$ , die von dem entwässerten Flussmittel  $\text{B}_2\text{O}_3$  umgeben waren, zwischen 40 und 80 K unter ihre Liquidustemperatur unterkühlt. Die Kristall-Keimbildungstemperatur wurde durch Differenzial-Thermoanalyse gemessen. Aus den Ergebnissen wurde mit Hilfe der klassischen Kristall-Keimbildungstheorie die kristallin-flüssige Grenzflächenenergie ermittelt, welche der wichtigste Parameter zur Berechnung der Keimbildungsrate ist. Die Grenzflächenenergie betrug ungefähr das 0.20-fache der Schmelzwärme pro Grenzflächenatom für alle Legierungen. Dieser Wert ist eine untere Grenze, denn es wurde nicht gezeigt, dass die auftretende Keimbildung homogen war. Die stationäre Keimbildungsrate wurde zwischen der Liquidus- und der Glasübergangs-Temperatur berechnet und nahm für die GeSbTe-Legierungen höhere Werte an als für die Sb-reichen Legierungen. Dies erklärt das unterschiedliche Kristallisations-Verhalten dieser Materialien beim Einsatz in Datenspeichern. Die Keimbildungsraten erscheinen jedoch zu hoch, um Amorphisierung in Phasenwechselmedien für die höchsten erreichbaren Kühlraten zu erlauben. Von daher kann gefolgert werden, dass eine Inkubationszeit

für Keimbildung die Amorphisierung und daher die Datenspeicherung sowohl in optischen als auch in elektronischen Phasenwechselmedien ermöglicht.

# Contents

Title page . . . . .	i
Abstract . . . . .	iii
Kurzfassung . . . . .	vii
Contents . . . . .	xi
List of Figures . . . . .	xvii
List of Tables . . . . .	xxi
<b>I Background</b>	<b>1</b>
<b>1 Introduction</b>	<b>3</b>
1.1 Phase change recording . . . . .	3
1.2 Structure of this study . . . . .	6
1.2.1 Goal and approach . . . . .	6
1.2.2 Procedure and outline . . . . .	6
<b>2 Theory: Thermodynamics of solidification</b>	<b>9</b>
2.1 Thermodynamics of alloys . . . . .	9
2.1.1 The Gibbs phase rule . . . . .	9
2.1.2 The phase diagram . . . . .	10
2.2 The undercooled liquid and the glass transition . . . . .	13
2.2.1 Configurational freezing of undercooled liquids . . . . .	13
2.2.2 The temperature dependence of the viscosity in the undercooled liquid . . . . .	16
2.3 Thermodynamics of the undercooled liquid . . . . .	18
2.3.1 The Heat Capacity at constant pressure $C_p$ . . . . .	19

2.3.2	Enthalpy $H$ , Entropy $S$ , and Gibbs Free Energy $G$ . . . . .	19
2.3.3	Approximations of the free energy change on crystallization . . . . .	26
2.4	The link between thermodynamics and kinetics . . . . .	27
<b>3</b>	<b>Theory: Kinetics of solidification</b>	<b>31</b>
3.1	Crystal nucleation . . . . .	31
3.1.1	Homogeneous nucleation . . . . .	31
3.1.2	Heterogeneous nucleation . . . . .	42
3.1.3	Transient nucleation . . . . .	48
3.2	Crystal growth . . . . .	50
3.2.1	Interface-controlled growth . . . . .	50
3.2.2	Diffusion-controlled growth . . . . .	54
3.3	Isothermal transformation curves . . . . .	55
3.3.1	Three-dimensional analysis . . . . .	55
3.3.2	Two-dimensional analysis . . . . .	60
<b>4</b>	<b>Scientific instruments</b>	<b>63</b>
4.1	The sputter chamber . . . . .	63
4.2	The differential scanning calorimeter (DSC) . . . . .	65
4.3	The differential thermal analyzer (DTA) . . . . .	67
4.4	The atomic force microscope (AFM) . . . . .	69
4.5	The transmission electron microscope (TEM) . . . . .	70
<b>II</b>	<b>Nucleation and growth parameters in thin films measured around the glass transition temperature</b>	<b>77</b>
<b>5</b>	<b>The crystal growth velocity</b>	<b>79</b>
5.1	Preface . . . . .	79
5.2	Experimental methods . . . . .	80
5.2.1	Sample preparation . . . . .	80
5.2.2	Microscopic methods . . . . .	81
5.2.3	Ex-situ anneal methods (isothermal) . . . . .	82
5.3	Results . . . . .	89

5.4	Discussion . . . . .	99
5.4.1	Type of crystallization kinetics . . . . .	99
5.4.2	Activation energy for diffusion . . . . .	100
5.4.3	Structural relaxation . . . . .	102
5.5	Conclusions . . . . .	105
<b>6</b>	<b>The crystal morphology</b>	<b>107</b>
6.1	Preface . . . . .	107
6.2	Experimental methods . . . . .	108
6.2.1	Sample preparation . . . . .	108
6.2.2	The transmission electron microscope (TEM) . . . . .	110
6.3	Results . . . . .	111
6.3.1	Plan view analysis . . . . .	111
6.3.2	Cross-sectional analysis . . . . .	122
6.4	Discussion . . . . .	126
6.4.1	Heterogeneous nucleation sites . . . . .	126
6.4.2	Density change and bend contours . . . . .	129
6.5	Conclusions . . . . .	129
<b>7</b>	<b>The crystal nucleation rate</b>	<b>131</b>
7.1	Preface . . . . .	131
7.2	Computational methods . . . . .	132
7.2.1	Johnson-Mehl-Avrami analysis . . . . .	132
7.2.2	Back calculation of crystal diameters . . . . .	133
7.3	Results . . . . .	133
7.3.1	Back calculation of crystal diameters: time lag determination . .	133
7.3.2	Johnson-Mehl-Avrami-Analysis . . . . .	136
7.3.3	Back calculation of crystal diameters: nucleation rate determi- nation . . . . .	150
7.4	Discussion . . . . .	156
7.4.1	Activation energy $E_k$ for the Avrami rate constant $k$ . . . . .	156
7.4.2	Avrami exponent $n$ . . . . .	157

7.4.3	Activation energy for the steady state nucleation rate $E_{I_{ss}}$ and critical work for nucleation $\Delta G_c$ . . . . .	159
7.4.4	Amorphous phase and undercooled liquid . . . . .	159
7.4.5	Time dependence of the nucleation rate . . . . .	160
7.4.6	Steady-state nucleation . . . . .	161
7.5	Conclusions . . . . .	165
<b>8</b>	<b>The calorimetric glass transition temperature</b>	<b>167</b>
8.1	Preface . . . . .	167
8.2	Experimental methods . . . . .	168
8.3	Results and discussion . . . . .	169
8.4	Conclusions . . . . .	177
<b>III</b>	<b>Nucleation parameters in undercooled droplets measured close to the melting point of liquidus temperature</b>	<b>179</b>
<b>9</b>	<b>The crystal nucleation rate</b>	<b>181</b>
9.1	Preface . . . . .	181
9.2	Experimental methods . . . . .	183
9.3	Results . . . . .	186
9.4	Analysis . . . . .	190
9.4.1	General method: Determination of the interfacial energy and the steady-state nucleation rate from observations during continuous cooling . . . . .	190
9.4.2	Crystal-melt interfacial energy . . . . .	192
9.4.3	Critical work for cluster formation $\Delta G_c$ and critical radius $r_c$ . .	198
9.4.4	Nucleation rate . . . . .	198
9.5	Discussion . . . . .	205
9.5.1	Entropy of fusion . . . . .	205
9.5.2	Crystal-melt interfacial energy . . . . .	205
9.5.3	Critical work for cluster formation $\Delta G_c$ and critical radius $r_c$ . .	206
9.5.4	Nucleation rate . . . . .	208
9.6	Conclusions . . . . .	210

*CONTENTS*

xv

**Acknowledgements (Danksagungen)**

**213**

**Bibliography**

**217**

**Curriculum Vitae**

**237**



# List of Figures

1.1	Principle of rewritable optical data storage based on phase change materials . . . . .	4
1.2	Mechanisms of re-crystallization . . . . .	6
1.3	Time-temperature-transformation diagram of an undercooled liquid . . . . .	8
2.1	Binary phase diagram showing complete solid solution . . . . .	11
2.2	Degrees of freedom for various locations in the binary phase diagram . . . . .	12
2.3	Determination of the solid and liquid composition in the binary phase diagram . . . . .	12
2.4	Viscosity in various stability regimes . . . . .	15
2.5	Viscosity for strong, intermediate, and fragile liquids . . . . .	18
2.6	Heat Capacity in various stability regimes . . . . .	20
2.7	Difference in enthalpy between liquid and crystal . . . . .	21
2.8	Difference in entropy between liquid and crystal . . . . .	22
2.9	Gibbs free energy in various stability regimes . . . . .	25
2.10	Molar Gibbs free energy for various phases. . . . .	29
3.1	Reversible work for the formation of crystalline clusters . . . . .	33
3.2	Statistical cluster distribution function for two models . . . . .	36
3.3	Volmer's spherical cap model for heterogeneous cluster formation . . . . .	43
3.4	Heterogeneous cluster formation: mathematical functions . . . . .	43
3.5	Reversible work for heterogeneous cluster formation . . . . .	46
3.6	Ratio of heterogeneous to homogenous nucleation rate . . . . .	47
3.7	Statistical cluster distribution function for transient nucleation . . . . .	48
3.8	Time dependence of the nucleation rate . . . . .	49

3.9	Free energy per atom versus position across the liquid-crystalline interface	52
4.1	Schematic view of a magnetron sputter chamber	64
4.2	Schematic view of the two furnaces in a power-compensated differential scanning calorimeter (DSC)	67
4.3	Measurement principle of an atomic force microscope (AFM)	69
4.4	Schematic drawing of the two basic operation modes of the transmission electron microscope (TEM)	72
4.5	Schematic diagram showing how the objective aperture in a TEM forms a bright field, dark field, and centered dark field image	73
4.6	Atomic energy levels for x-ray transitions	75
5.1	Schematic top view of a commercial (100) Silicon wafer	80
5.2	Schematic view of a substrate in the DSC furnace	83
5.3	Experimental setup of the immersion experiment	86
5.4	Sample holder for the immersion experiment	88
5.5	AFM scans on AgIn-Sb <sub>2</sub> Te at 160 °C	90
5.6	AFM scans on AgIn-Sb <sub>2</sub> Te at 185 °C	90
5.7	AFM scans on Ge <sub>4</sub> Sb <sub>1</sub> Te <sub>5</sub> at 140 °C	91
5.8	AFM scans on Ge <sub>4</sub> Sb <sub>1</sub> Te <sub>5</sub> at 180 °C	92
5.9	AFM scans on Ge <sub>2</sub> Sb <sub>2</sub> Te <sub>5</sub> at 115 °C	93
5.10	AFM scans on Ge <sub>2</sub> Sb <sub>2</sub> Te <sub>5</sub> at 145 °C	94
5.11	AFM scans on Ge <sub>1</sub> Sb <sub>2</sub> Te <sub>4</sub> at 95 °C	95
5.12	AFM scans on Ge <sub>1</sub> Sb <sub>2</sub> Te <sub>4</sub> at 125 °C	95
5.13	Height scale for the AFM scans	96
5.14	Crystal growth velocity as a function of temperature	97
5.15	Schematic drawing of diffusivity and crystal growth velocity around the glass transition temperature	103
5.16	Schematic drawing of the diffusivity evolution upon annealing	104
6.1	Comparison of crystal size and crystal density observed by AFM and TEM for Ge <sub>4</sub> Sb <sub>1</sub> Te <sub>5</sub>	112
6.2	High resolution TEM images on a Ge <sub>4</sub> Sb <sub>1</sub> Te <sub>5</sub> crystal	113
6.3	Ge <sub>4</sub> Sb <sub>1</sub> Te <sub>5</sub> crystal for three tilting angles	115

6.4	Ge <sub>2</sub> Sb <sub>2</sub> Te <sub>5</sub> crystal for three tilting angles . . . . .	116
6.5	AgIn-Sb <sub>2</sub> Te crystal for three tilting angles . . . . .	117
6.6	Schematic illustration of heterogeneous crystal nucleation at the film surface . . . . .	118
6.7	Schematic illustration of diffraction from grains in the TEM . . . . .	119
6.8	Schematic illustration of stacking faults . . . . .	119
6.9	Schematic illustration of a bent TEM specimen . . . . .	121
6.10	EDS line scan across a Ge <sub>4</sub> Sb <sub>1</sub> Te <sub>5</sub> crystal . . . . .	123
6.11	EDS line scan across a Ge <sub>2</sub> Sb <sub>2</sub> Te <sub>5</sub> crystal . . . . .	124
6.12	EDS line scan across a AgIn-Sb <sub>2</sub> Te crystal . . . . .	125
6.13	Cross-sectional TEM micrographs in comparison with a plan view AFM image for Ge <sub>4</sub> Sb <sub>1</sub> Te <sub>5</sub> . . . . .	127
6.14	Cross-sectional HRTEM micrograph of the crystallized film surface for Ge <sub>4</sub> Sb <sub>1</sub> Te <sub>5</sub> . . . . .	128
6.15	Cross-sectional TEM micrograph of the film-substrate interface for Ge <sub>4</sub> Sb <sub>1</sub> Te <sub>5</sub> . . . . .	128
7.1	Time lag for nucleation . . . . .	135
7.2	Johnson Mehl Avrami plot for Ge <sub>4</sub> Sb <sub>1</sub> Te <sub>5</sub> (DSC furnace anneals) . . . .	137
7.3	Johnson Mehl Avrami plot for Ge <sub>4</sub> Sb <sub>1</sub> Te <sub>5</sub> (Immersion anneals) . . . .	138
7.4	Johnson Mehl Avrami plot for Ge <sub>2</sub> Sb <sub>2</sub> Te <sub>5</sub> (DSC furnace anneals) . . . .	139
7.5	Avrami exponent $n$ as a function of temperature for Ge <sub>4</sub> Sb <sub>1</sub> Te <sub>5</sub> . . . .	140
7.6	Avrami exponent $n$ as a function of temperature for Ge <sub>2</sub> Sb <sub>2</sub> Te <sub>5</sub> . . . .	141
7.7	Avrami rate constant $k$ . . . . .	142
7.8	Nucleation rate prefactor $I_0$ . . . . .	144
7.9	Number of crystals per unit area after complete crystallization . . . . .	147
7.10	Average grain radius after complete crystallization . . . . .	149
7.11	Crystallization of Ge <sub>4</sub> Sb <sub>1</sub> Te <sub>5</sub> at 140°C . . . . .	152
7.12	Crystallization of Ge <sub>2</sub> Sb <sub>2</sub> Te <sub>5</sub> at 115°C . . . . .	153
7.13	Steady state nucleation rate . . . . .	155
7.14	Nucleation probability in a thin slice (schematic sketch) . . . . .	163
8.1	DSC curves for amorphous samples that were not pre-annealed . . . . .	170

8.2	Schematic evolution of the enthalpy and its temperature derivative as a function of temperature . . . . .	173
8.3	DSC curves for amorphous samples that were pre-annealed . . . . .	176
9.1	Gibbs free energy of formation for various oxides . . . . .	184
9.2	Heat flow as a function of temperature for Sb and Te alloys measured by differential thermal analysis (DTA) . . . . .	187
9.3	Difference in free energy between undercooled liquid and crystal for AgIn-Sb <sub>2</sub> Te . . . . .	193
9.4	Crystal-melt interfacial energy versus molar heat of fusion . . . . .	197
9.5	Lower limit for the critical work for homogeneous cluster formation $\Delta G_c$	199
9.6	Lower limit for the critical radius $r_c$ . . . . .	200
9.7	Upper limit for the homogeneous steady state crystal nucleation rate $I^{ss}$ for a fragility index of $m = 45$ . . . . .	201
9.8	Upper limit for the homogeneous steady state crystal nucleation rate $I^{ss}$ for a fragility index of $m = 60$ . . . . .	202

# List of Tables

1.1	Thesis outline . . . . .	8
3.1	Values of the Avrami exponent for different conditions . . . . .	59
5.1	Thermal constants of silicon . . . . .	84
5.2	Smoke points of various oils . . . . .	87
5.3	Arrhenius fit parameters for the crystal growth velocity . . . . .	98
7.1	Fit parameters for the time lag for nucleation . . . . .	134
7.2	Arrhenius fit parameters for the Avrami rate constant and the nucleation rate prefactor . . . . .	136
7.3	Arrhenius fit parameters for the number of crystals and average grain size	148
7.4	Steady state nucleation rate and critical work for heterogeneous cluster formation . . . . .	154
8.1	Thermal parameters measured by DSC . . . . .	171
9.1	Thermal data obtained from DTA and DSC measurements . . . . .	189
9.2	Crystal-melt interfacial energy, entropy of fusion, and reduced glass transition temperature . . . . .	195
9.3	Undercooling data for liquid metallic and semi-metallic elements . . . . .	196



# Part I

## Background



# Chapter 1

## Introduction

### 1.1 Phase change recording

Sb- and Te-based alloys<sup>1</sup> have been used for optical data storage in commercial rewritable compact disks (CDs) and digital versatile disks (DVDs) over the last years [1, 2, 3]. In those so-called *phase change media*, a laser pulse is focussed on an initially crystalline film of an Sb or Te alloy. If the laser power is large enough, the film is heated locally above the melting temperature  $T_m$ . Subsequently, the heated volume element cools rapidly so that crystallization cannot occur. When the temperature has cooled significantly below the glass transition temperature  $T_g$ , the mobility of the atoms is too low to allow a significant structural change. Hence, crystallization practically does not occur significantly below  $T_g$ . The ‘frozen’ film volume element then exhibits the atomic structure of a liquid at a fixed time, i. e., it lacks long-range translational order. This structure is called ‘amorphous’ (Fig. 1.1). The local amorphization of the film corresponds to the writing of a binary digit (bit), which is the usual term for the most basic information unit used in data storage. As the optical properties of the amorphous and crystalline states are remarkably different for many Sb and Te alloys, this bit can be distinguished from the crystalline matrix by measuring its reflectivity using low laser power (reading, Fig. 1.1). Intermediate laser power heats the bit above the glass<sup>2</sup> transition temperature  $T_g$  into the regime of the undercooled liquid ( $T_g < T < T_m$ ),

---

<sup>1</sup>Sb: Antimony; Te: Tellurium.

<sup>2</sup>An amorphous solid formed by continuous cooling from the liquid state is also called a glass.

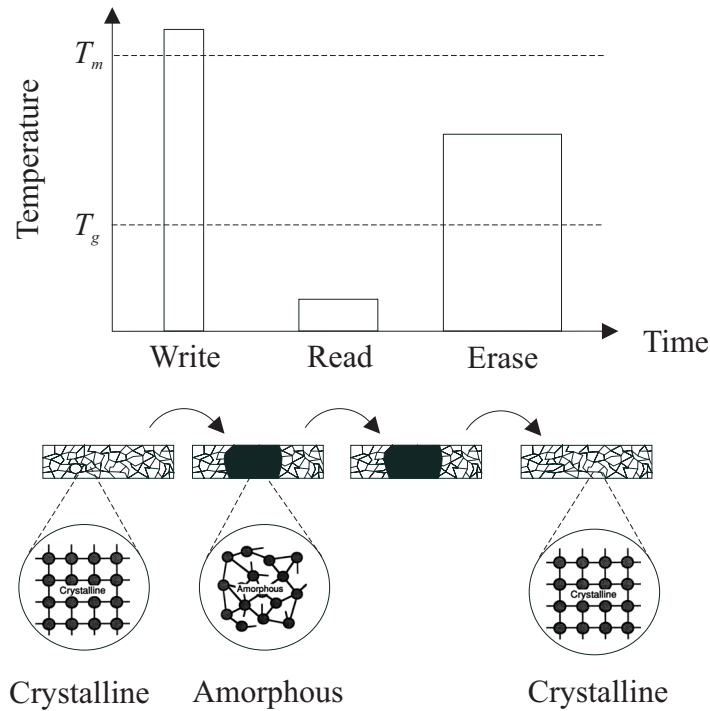


**Figure 1.1:** Principle of rewritable optical data storage based on phase change materials. The phase transformation is induced by high laser power for the case of amorphization (writing) and intermediate laser power for the case of re-crystallization (erasure). Reading is accomplished by low laser power. The width of the erasure pulse indicates that re-crystallization is the slowest process and therefore the time-limiting factor to achieve high data transfer rates.

where atomic mobility is high. This induces a phase transition back to the energetically more favorable crystalline phase (bit erasure, Fig. 1.1). Due to the reversibility of the transition, the tellurium alloys used for optical data storage are also called *phase change materials*.

Recently, phase change materials have also shown high potential for future electronic non-volatile<sup>3</sup> data storage [4, 5, 6]. In these so-called phase change random access memories (PC-RAMs), *electrical* power rather than laser power provides the heat that is necessary for transformations between the amorphous and crystalline states, which can be distinguished subsequently by their pronounced difference in electrical conductivity

<sup>3</sup>The term *non-volatile* denotes that no power is consumed to maintain the stored information permanently. This is in contrast to dynamic random access memories (DRAMs) currently used as working memories in commercial computers.

[4, 7, 8, 9, 10, 11]. There are good prospects that PC-RAMs finally replace current commercial data storage devices in the future due to their high data transfer rate, good scalability, and non-volatility.

In order to compete with other existing and emerging data storage technologies, a higher data transfer rate is required for both optical and electronic phase change media. This can only be achieved by accelerating the re-crystallization, which is the slowest process and therefore the time-limiting step in both optical and electronic media (Fig. 1.1). Hence, it is highly necessary to understand the crystallization kinetics of phase change materials better.

For optical phase change media, depending on the composition of the material, two mechanisms of re-crystallization have been observed in laser experiments that correlate the bit diameter with the re-crystallization time. For instance, for AgIn-doped  $\text{Sb}_2\text{Te}$  (the material of choice in DVD-RW and DVD+RW) and  $\text{Ge}_{12}\text{Sb}_{88}$ , the re-crystallization time of an amorphous bit upon laser heating is observed to *increase* with increasing bit diameter. Therefore, the bits in these alloys have been assumed to re-crystallize by the growth of the crystalline phase from the *rim* of the amorphous mark [3, 12, 13] [Fig. 1.2(a)]. In contrast, for  $\text{Ge}_4\text{Sb}_1\text{Te}_5$ ,  $\text{Ge}_1\text{Sb}_2\text{Te}_4$ , and  $\text{Ge}_2\text{Sb}_2\text{Te}_5$  (the latter is the material of choice in DVD-RAM), the re-crystallization time is observed to be *independent* of bit diameter. Therefore, the bits in these alloys have been assumed to re-crystallize by nucleation and subsequent growth of crystals *inside* the amorphous mark [14] [Fig. 1.2(b)]. The atomistic basis for this difference is still not clearly understood. Even though several research groups have assumed that these alloys differ in their crystal nucleation rate and crystal growth velocity (which are the two fundamental steps involved in crystallization), systematic measurements of these two quantities as a function of temperature for both re-crystallization mechanisms have not been performed. Therefore, in many modeling studies of re-crystallization the fitting parameters have no direct experimental justification [15, 16, 17].

(a) AgIn-doped  $\text{Sb}_2\text{Te}$  and  $\text{Ge}_{12}\text{Sb}_{88}$ (b)  $\text{Ge}_4\text{Sb}_1\text{Te}_5$ ,  $\text{Ge}_1\text{Sb}_2\text{Te}_4$ , and  $\text{Ge}_2\text{Sb}_2\text{Te}_5$ 

**Figure 1.2:** Schematic top view of an amorphous mark showing the two fundamentally different mechanisms of re-crystallization (bit erasure). Dark: crystalline phase. Bright: amorphous phase. (a) Growth of the crystalline phase from the *rim* of the amorphous mark (growth-dominated re-crystallization). (b) Crystal nucleation and subsequent growth *inside* the amorphous mark (nucleation-dominated re-crystallization).

## 1.2 Structure of this study

### 1.2.1 Goal and approach

The goal of this work is to make a contribution to a *fundamental understanding* of the crystallization kinetics of amorphous and liquid phase change materials. This should provide a deeper insight into the factors that determine the speed of crystallization and therefore help to increase data transfer rates in both optical and electronic phase change media.

The approach to attain this goal is to perform *systematic* measurements of crystal nucleation rates and crystal growth velocities as a function of temperature and re-crystallization mechanism for the five alloys mentioned above.

### 1.2.2 Procedure and outline

The ‘speed’ of crystallization, which is determined by the magnitude of nucleation rate and growth velocity, strongly depends on the temperature (Fig. 1.3). [This will be explained in more detail in the theory chapters of this work (Chaps. 2 and 3)]. Crystallization is thermodynamically forbidden above the melting temperature  $T_m$  (for a

multi-component system: above the melting point of liquidus temperature  $T_l$ ).<sup>4</sup> For temperatures slightly below  $T_l$ , crystallization occurs only slowly because the Gibbs free energy difference between undercooled liquid and crystalline state, which is the driving force for crystallization, is low. Far below the glass transition temperature  $T_g$ ,<sup>5</sup> crystallization is not observed within experimental timescales due to the low atomic mobility associated with a solid-like shear viscosity. However, the mobility increases with increasing temperatures and allows atomic rearrangements within experimental timescales around  $T_g$ , where crystallization can slowly occur. At intermediate temperatures between  $T_g$  and  $T_l$ , both mobility and driving force are large enough to allow rapid crystallization.

For the phase change alloys, crystallization rates are so high that most of the temperature range between  $T_g$  and  $T_l$  is not available for a *systematic* experimental study of nucleation and growth parameters. Such a study relies on crystallization time scales between a few seconds and a few hours. Hence, crystallization parameters can only be measured around  $T_g$  and close to  $T_l$  for the phase change alloys. For this reason, the data in this thesis are presented in two major parts, which focus on the determination of crystallization parameters from measurements around  $T_g$  (Part II) and close to  $T_l$  (Part III). The study around  $T_g$  is performed in *thin films*, whereas the study close to  $T_l$  is performed in the *bulk* (undercooled droplets). Table 1.1 displays the thesis outline for Parts II and III in a clearly arranged form. Chapters 6 and 8 are not listed but provide further information on the crystallization kinetics in thin films around  $T_g$ : In Chap. 6, a study of the crystal morphology is provided, which is important for a correct determination of the crystal nucleation rate in the subsequent Chap. 7. Chapter 8 presents precise measurements of  $T_g$ , which help to interpret and understand the crystallization data presented in the other chapters.

Part I reviews the basic background required to understand Parts II and III. The *theoretical* background is provided in Chaps. 2 and 3 and *experimental* background in Chap. 4.

---

<sup>4</sup>According to estimates based on phase diagrams,  $T_l$  is around 500–700°C for materials usually used in phase change recording.

<sup>5</sup> $T_g$  is expected to be around 100–250°C for materials usually used in phase change recording. Exact values have not been determined in previous studies.

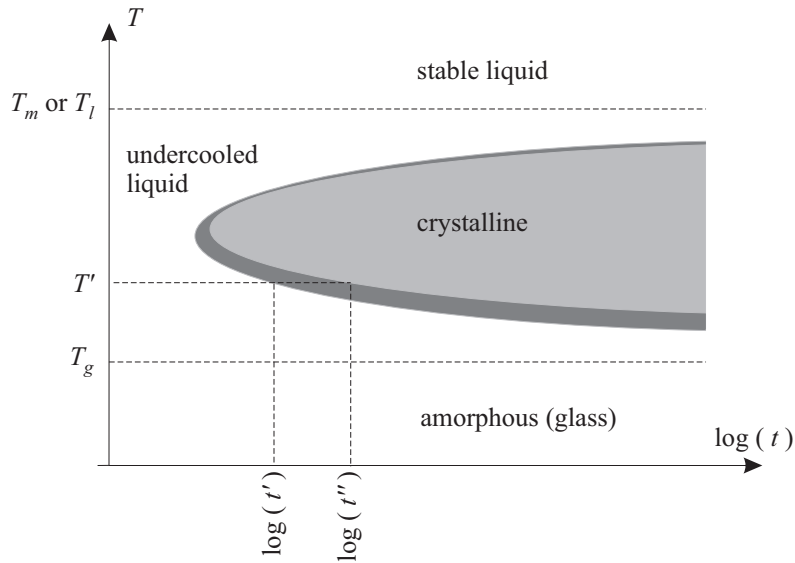


**Figure 1.3:** Time-temperature-transformation diagram of an undercooled liquid.  $t$ : time;  $T$ : temperature;  $T_g$ : glass transition temperature;  $T_m$ : melting temperature (for a single-component system);  $T_l$ : melting point of liquidus temperature (for a multi-component system). The width of the dark curve to the left of the grey area *qualitatively* denotes the time interval during which crystallization occurs: At a constant temperature  $T'$ , crystallization is initiated at time  $t'$  and completed at time  $t''$  (counted from that point of time at which the undercooled liquid state was established). The strong curvature of the dark curve is a consequence of the fact that the crystal nucleation rate is a strong function of temperature (this will be discussed in detail in Chap. 3).

**Table 1.1:** Outline for Parts II and III of this thesis in table form. A table entry states the chapter in which the results of a particular measurement (top) at a specific condition (left) are presented and discussed.

	Measurements of <i>growth</i> parameters	Measurements of <i>nucleation</i> parameters
Measurements in <i>thin films</i> around $T_g$	Part II: Chap. 5	Part II: Chap. 7
Measurements in the <i>bulk</i> close to $T_l$	–	Part III: Chap. 9

# Chapter 2

## Theory: Thermodynamics of solidification

### 2.1 Thermodynamics of alloys

#### 2.1.1 The Gibbs phase rule

Equilibrium thermodynamics can describe the macroscopic state of a system uniquely in terms of a set of thermodynamic state variables. In particular, the state of a multi-component system of  $C$  components is described by a set of  $C + 2$  independent state variables, which can be either *extensive* or *intensive*. Extensive variables scale with the size of the system (like the volume  $V$  and the particle number  $N$ ), whereas intensive variables are independent of the system size (like the pressure  $p$ , the temperature  $T$  or the chemical potential  $\mu$ ). It is always possible to choose a set of  $C + 2$  state variables that are all extensive. Through state variable transformations, the system can be described by a set of  $C + 2$  other variables, of which some may be intensive. The maximum number  $F$  of intensive state variables in equilibrium is given by the *Gibbs phase rule* [18],

$$F = C - P + 2, \tag{2.1a}$$

where  $P$  is the number of phases present under the specific condition.  $F$  is also termed the *number of thermodynamic degrees of freedom* of the system because the absolute size of the system is irrelevant for thermodynamic considerations. If the pressure is

fixed at  $p = 1$  atm, the number of degrees of freedom reduces to [18]

$$F = C - P + 1. \quad (2.1b)$$

If liquid and crystalline phase ( $P = 2$ ) co-exist in a single component system ( $C = 1$ ) in equilibrium, Eq. (2.1b) yields  $F = 0$ . Hence, there are no degrees of freedom, i. e., a single component systems (e. g., an element) exhibits a single melting point  $T_m$ . For a binary alloy ( $C = 2$ ), in contrast, liquid and crystal can coexist over a range of temperatures in equilibrium:  $F = 2 - 2 + 1 = 1$ . This single degree of freedom means that the temperature can be changed while the two-phase state of the system is maintained. However, the temperature change induces a composition change of the individual phases, i. e., temperature and composition are dependent variables. For the case that the binary system is entirely crystalline (or entirely liquid), i. e.,  $P = 1$ , Eq. (2.1b) yields  $F = 2 - 1 + 1 = 2$ . Hence, temperature and composition can be varied independently.

### 2.1.2 The phase diagram

The Gibbs phase rule can be visualized most easily by means of a *phase diagram*. The simplest phase diagram, the binary phase diagram with complete solid and liquid solution, is represented in Fig. 2.1. At sufficiently high temperatures (above the *liquidus temperature*  $T_l$ ), any composition is molten completely in equilibrium. Similarly, at sufficiently low temperatures (below the *solidus temperature*  $T_s$ ), any composition is completely crystalline in equilibrium. Between  $T_s$  and  $T_l$ , there is a two-phase region, in which crystal and liquid co-exist in equilibrium. The associated degrees of freedom  $F$  [cf. Eq. (2.1b)] are given in Fig. 2.2 for various regions of the phase diagram. In the two-phase region, an A-rich liquid ( $L_1$ ) is in equilibrium with a B-rich solid ( $S_1$ ). Their compositions are determined by the horizontal line as shown in Fig. 2.3. The conservation of the overall system composition determines unambiguously the relative amount of the two phases (lever rule): If the phase diagram in Fig. 2.3 were thought to be in an upright position and if the pivot point of a hypothetical lever were fixed in the state point (open circle), the relative amount of the phases put onto the lever at the black points ( $L_1$  and  $S_1$ ) would keep the lever in equilibrium (i. e., in horizontal

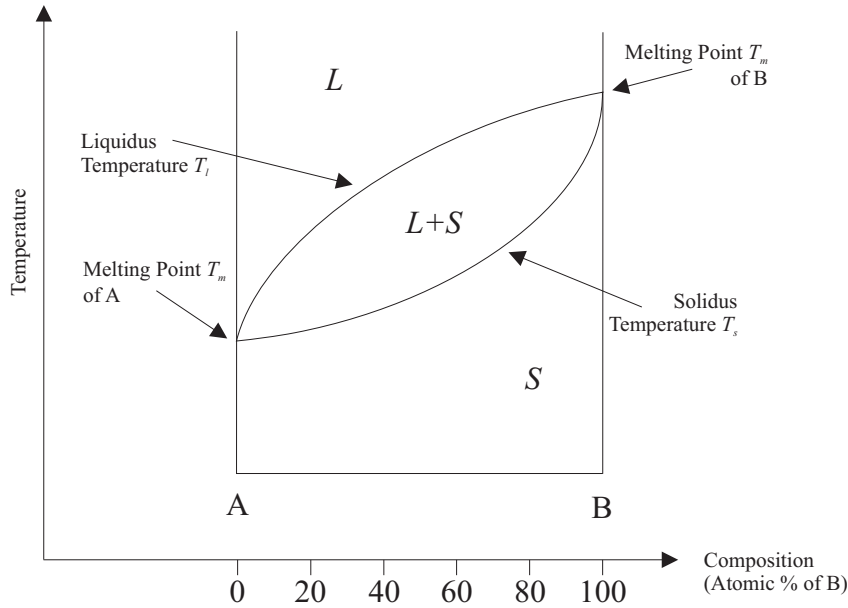


**Figure 2.1:** Binary phase diagram showing complete solid solution ( $S$ ) and complete liquid solution ( $L$ ). The two components A and B have a single melting point  $T_m$ , but for the other compositions the solid and liquid phase can co-exist between the solidus and the liquidus line ( $L + S$  region).

position) [18]. Hence, in the example of Fig. 2.3, the amount of liquid (in atomic %<sup>1</sup>) is higher than the amount of solid because the state point (open circle) is closer to the liquidus line than to the solidus line.

The simple phase diagram with complete solid solubility in Figs. 2.1–2.2 qualitatively applies to binary alloys of chemically similar components. Important examples are the binary Si–Ge and Cu–Ni phase diagrams [19]. In most cases, however, a solid solution only exists over a limited range of composition. An example is the Ge–Sb phase diagram [19]. On the other hand, liquid solubility for all compositions is common, but there are also exceptions. For instance, the Cu–Pb and Ag–Ni phase diagrams exhibit a miscibility gap in the liquid state [19].

For the alloys studied in this work,  $\text{Ge}_{12}\text{Sb}_{88}$  (binary,  $C = 2$ ), GeSbTe alloys of various stoichiometries (ternary,  $C = 3$ ), and  $\text{Ag}_{5.5}\text{In}_{6.5}\text{Sb}_{59}\text{Te}_{29}$  (quaternary,  $C = 4$ ), the phase diagrams look more complicated than in Figs. 2.1–2.2. This is discussed in Chap. 9.

<sup>1</sup>The same applies to weight % if the horizontal axis in Fig. 2.3 were given in weight %.

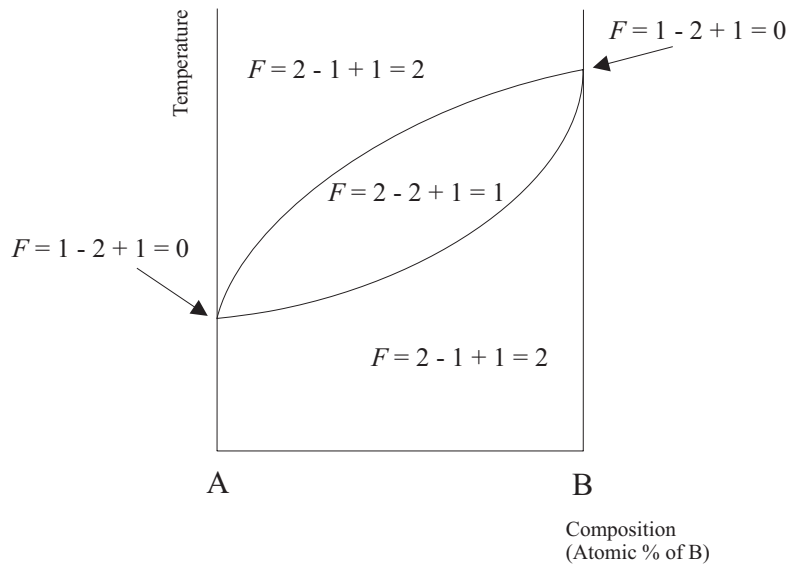


**Figure 2.2:** Degrees of freedom for various locations in the phase diagram calculated from the Gibbs phase rule [Eq. (2.1b)].

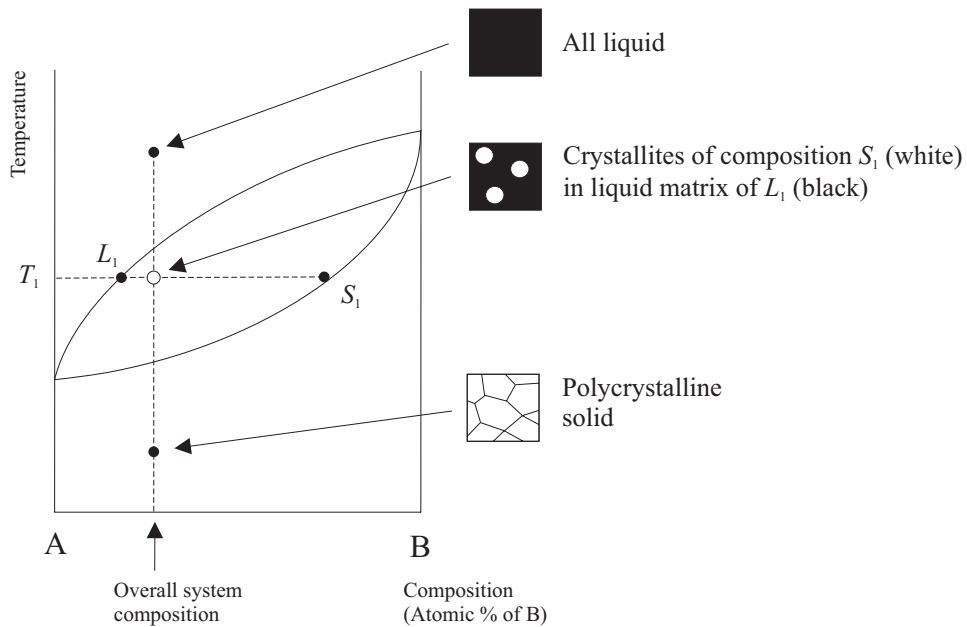


**Figure 2.3:** Determination of the composition of the B-rich solid  $S_1$  and the A-rich liquid  $L_1$  from a state point (open circle) within the two-phase region at temperature  $T_1$  in a binary phase diagram of complete solid solution.

## 2.2 The undercooled liquid and the glass transition

### 2.2.1 Configurational freezing of undercooled liquids

The phase diagrams discussed in Sec. 2.1.2 apply only in (global) thermodynamic equilibrium. Furthermore, these diagrams only map the *stable* phases for a given temperature and composition. This point needs further discussion: When a liquid is cooled below the liquidus temperature  $T_l$ , it should immediately undergo crystallization according to the phase diagram discussed in Sec. 2.1.2. However, this is rarely observed because the formation of a crystal nucleus requires the creation of a solid-liquid interface, which is energetically not favorable (this will be discussed in detail in Sec. 3.1). Therefore, the liquid phase is usually maintained to a certain degree of undercooling, when crystal nucleation is finally initiated. Upon cooling, the liquid hardens continuously, which is observed by a large but continuous increase in its shear viscosity  $\eta$  (hereafter: viscosity) that reflects the slowing dynamics in the liquid with decreasing temperature (Fig. 2.4). The undercooled liquid<sup>2</sup> is *metastable* with respect to the (stable) crystalline phase but remains in *internal equilibrium*. Hence, the undercooled liquid is said to be in *metastable equilibrium*. Its molecular mobility is still large enough (i. e., its viscosity still low enough) to sample all thermodynamically accessible configurations. For some materials, the probability of crystal nucleation is so low that they can be undercooled to the *glass transition temperature*  $T_g$  (Fig. 2.4), which is defined as the temperature at which the time scale necessary for atomic rearrangements becomes larger than the experimentally imposed time window<sup>3</sup>. Therefore, the undercooled liquid is configurationally frozen at  $T_g$  and goes out of internal equilibrium. As a consequence, the viscosity rises less quickly upon further cooling (Fig. 2.4) [20, 21]. For  $T < T_g$ , the liquid is called a *glass*. X-ray diffraction (XRD) experiments have shown that glasses exhibit neither long-range translational order nor long-range orientational order. They exhibit the statistical structure of a liquid at a fixed time. This structure is commonly called *amorphous*. The glass transition usually occurs at the point where the viscosity  $\eta$  approaches a value on the order of  $10^{12}$  Pa s

---

<sup>2</sup>The expressions *undercooled liquid* and *supercooled liquid* are equally used and equivalent.

<sup>3</sup>Even though they are not *thermodynamic* quantities, the viscosity  $\eta$  and the glass transition temperature  $T_g$  are discussed in Chap. 2 because their knowledge is useful to understand the following sections better.

$= 10^{13}$  poise [22, 23, 20, 21]. This can be understood as follows: For diffusion-limited kinetics (Sec. 3.1.1.4.1 below), the liquid diffusivity  $D$  and the liquid jump frequency per atom  $\Gamma_D$  are related by [24, 25]

$$D = \frac{1}{6}\Gamma_D\lambda^2, \quad (2.2)$$

where  $\lambda$  is the interatomic distance. Diffusivity  $D$  and viscosity  $\eta$  are inversely related by the *Stokes-Einstein equation* [20, 26, 24, 25]

$$\eta D = \frac{k_B T}{3\pi\lambda}. \quad (2.3)$$

Combining Eq. (2.2) and (2.3) gives

$$\eta = \frac{k_B T}{3\pi\lambda D} \simeq \frac{k_B T}{\Gamma_D\lambda^3} \simeq \frac{k_B T}{\Gamma_D\Omega}, \quad (2.4)$$

where  $\Omega \simeq \lambda^3$  is the atomic volume. Hence,

$$\Gamma_D = \frac{k_B T}{\eta\Omega}, \quad (2.5)$$

or

$$\tau_D := \frac{1}{\Gamma_D} = \frac{\eta\Omega}{k_B T} = \frac{\eta\bar{V}}{RT}, \quad (2.6)$$

where  $\bar{V} = N_{\text{Av}}\Omega$  is the molar volume and  $R = N_{\text{Av}}k_B$  the Gas constant ( $N_{\text{Av}}$ : Avogadro's number). Taking  $\eta = 10^{12}$  Pa s,  $\bar{V} \sim 10^{-5} \frac{\text{m}^3}{\text{mol}}$  and  $RT \sim 10^3 \frac{\text{J}}{\text{mol}}$  yields

$$\tau_D \sim 10^4 \text{ s} \sim 1 \text{ hour}. \quad (2.7)$$

Hence, a viscosity on the order of  $10^{12}$  Pa s =  $10^{13}$  poise corresponds to  $\Gamma_D \sim \frac{1}{\text{hour}}$ , i. e., about one jump per hour. Such a low jump frequency leads to configurational freezing. At even lower temperatures, the glass seems to show no apparent permanent change in its shape any more on experimental time scales due to its large viscosity. Macroscopically, it is solid.

Equation (2.6) shows that the glass transition temperature depends on the time scale of the experiment: For high cooling rates, a few jumps per hour cannot maintain equilibrium. Therefore, the glass transition temperature occurs at a higher value for  $\Gamma_D$ , i. e., at a lower value for  $\eta$  or at a higher temperature [path (a) in Fig. 2.4]. Slower cooling allows more time for equilibration upon cooling and results in path (b). Therefore, the glass transition is a *kinetic* and not a *thermodynamic* phenomenon.

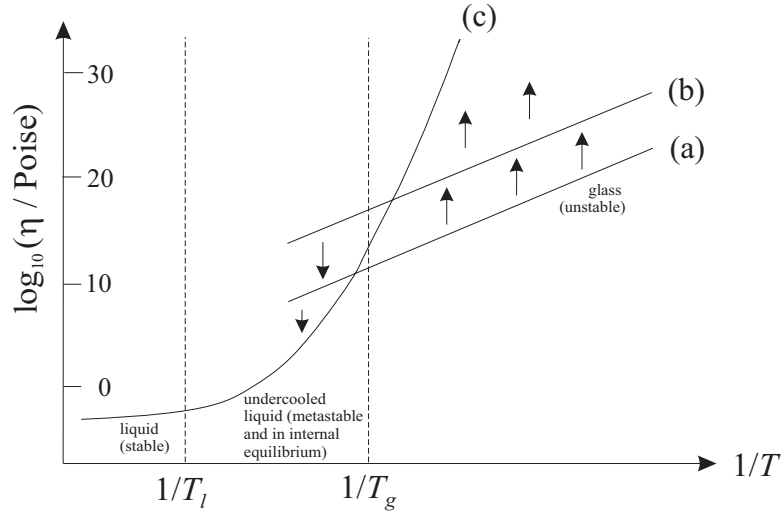


**Figure 2.4:** Viscosity  $\eta$  in various stability regimes: stable equilibrium for  $T > T_l$ , metastable equilibrium for  $T_g < T < T_l$  and isoconfigurational states (unstable with respect to structural relaxation) for  $T < T_g$ . (a) Fast cooling. (b) Slow cooling. (c) Ininitively slow cooling. The isoconfigurational states [glass, states (a) and (b)] experience structural relaxation towards the undercooled liquid (c), which is in internal equilibrium. This is indicated by the arrows.

If the undercooled liquid is cooled infinitively slowly, it would not undergo a glass transition, i. e., internal equilibrium would be maintained at all times [path (c) in Fig. 2.4]. In this hypothetical (and experimentally inaccessible) case the imposed time window upon cooling would be infinitively large, and hence, the system would have sufficient time for atomic rearrangements at arbitrary temperature or viscosity value.

A system that has gone out of (internal) equilibrium tends to approach equilibrium again. Glasses do this by *structural relaxation* towards the undercooled liquid state. Hence, glasses are *unstable with respect to structural relaxation*. This is indicated by the arrows in Fig. 2.4: Below  $T_g$ , the viscosity of the glass continuously increases with time. On the other hand, if the glass is quickly heated above  $T_g$ , internal equilibrium might not yet be reached and the viscosity *decreases* with time (Fig. 2.4). States (a) and (b) in Fig. 2.4 are called *isoconfigurational states*. The atomic configuration in each of those states is identical to an *instantaneous* atomic configuration of the undercooled liquid at that temperature where the two curves cross.

As a result of structural relaxation, each material property of a glass that depends on atomic configuration is time-dependent at constant temperature and depends on the

thermal history of the glass [27]. This causes serious problems in studying properties of amorphous materials experimentally. For example, electrical resistivity changes of about 1%, Young's modulus changes of about 5 – 10%, and mass density changes of about 0.5% have been reported [28]. However, atomic transport coefficients exhibit the most significant changes: viscosity and diffusivity changes of several orders of magnitude have been observed [29, 30, 31, 32].

At the end of the 1950s, Cohen and Turnbull [33] made the important prediction of the *universality of the glass transition*: They postulated that all liquids exhibit the glass transition if crystallization upon cooling can be avoided. Indeed, glasses have been formed by continuous melt cooling from materials of every bond type (covalent, ionic, metallic, van der Waals or hydrogen bonded) in the subsequent decades.

It should be mentioned that materials with amorphous structure have also been formed by other methods, e. g., by vapor condensation, electrodeposition or sputtering. However, the term 'glass' is usually only reserved for those materials that were formed by continuous cooling from the melt through the glass transition.

### 2.2.2 The temperature dependence of the viscosity in the undercooled liquid

The temperature dependence of the viscosity in the amorphous phase (i. e., in the isoconfigurational states) is usually of the Arrhenius type over a relatively large temperature range<sup>4</sup> [20, 21]. This is indicated by straight lines in Fig. 2.4. The temperature dependence of the undercooled liquid, in contrast, does not necessarily show an Arrhenius temperature dependence (Fig. 2.4). Those liquids for which the temperature dependence of  $\eta$  in the undercooled liquid closely resembles an Arrhenius behavior over a *large* temperature range have been termed *strong* liquids [34]. Strong liquids tend to have tetrahedral network structure. Examples are  $\text{SiO}_2$  and  $\text{GeO}_2$ . Some metallic glass formers are also fairly strong [34]. Liquids for which the temperature dependence of  $\eta$  in the undercooled liquid significantly deviates from the Arrhenius type have been termed *fragile* [34]. The viscosity for these liquids can usually only

---

<sup>4</sup>The temperature dependence of a quantity  $A$  is usually called *Arrhenius* if it can be described by an equation of the form  $A = A_0 \exp\left(\pm \frac{E}{k_B T}\right)$ .  $E$  is the *activation energy* and  $k_B$  the Boltzmann constant.

be approximated *locally* with an Arrhenius equation. Fragile liquids tend to be highly coordinated ionic liquids, van der Waals bonded liquids, molecular liquids or aromatic hydrocarbons [34, 23]. Molecules of fragile liquids exert largely non-directional, dispersive forces on each other [35, 23]. The term *intermediate* is also widely used for liquids that deviate from the Arrhenius law more than strong liquids but less than fragile liquids (Fig. 2.5). Most of the common liquids of the geochemical and technological world are either strong or intermediate [34]. Angell showed that the magnitude of the *kinetic fragility*  $m$ , defined as

$$m = \left. \frac{\partial \log_{10} \eta(T)}{\partial \left(\frac{T_g}{T}\right)} \right|_{T=T_g}, \quad (2.8)$$

(the partial derivative is taken in the undercooled liquid, not in the amorphous phase) scales with the ‘degree of deviation’ of  $\eta$  from Arrhenius behavior in the undercooled liquid (Fig. 2.5) [34, 36]. In other words, the more fragile a liquid is, the more its viscosity in the undercooled liquid deviates from Arrhenius behavior and the higher is the parameter  $m$ . Fragilities between around 20 and 120 have been reported in the literature [34, 36, 37].

Several fitting equations have been proposed to describe the temperature dependence of the viscosity in the undercooled liquid [34, 38]. The one that is used most widely is the Vogel-Fulcher-Tammann equation [39, 40, 41, 34],

$$\eta(T) = \eta_0 \cdot \exp\left(\frac{DT_{FV}}{T - T_{FV}}\right) \quad (T > T_{FV}), \quad (2.9)$$

where  $\eta_0$ ,  $D$ , and  $T_{FV} < T_g$  are constants. Equation (2.9) has been found to perform very well for strong and intermediate liquids over many orders of magnitude of viscosity. For fragile liquids, in contrast, this equation usually only works over some 2–4 orders of magnitude of viscosity [34, 38].

Substituting  $\eta(T)$  from Eq. (2.9) into Eq. (2.8) yields after differentiation

$$m = \frac{D}{\ln(10)} \frac{T_g T_{FV}}{(T_g - T_{FV})^2}. \quad (2.10)$$

According to Ref. [42],  $D$  is a decreasing function of fragility  $m$ . This statement is not necessarily in contradiction with Eq. (2.10), since the term  $(T_g - T_{FV})^2$  in the denominator of Eq. (2.10) is small for fragile liquids and large for strong liquids.

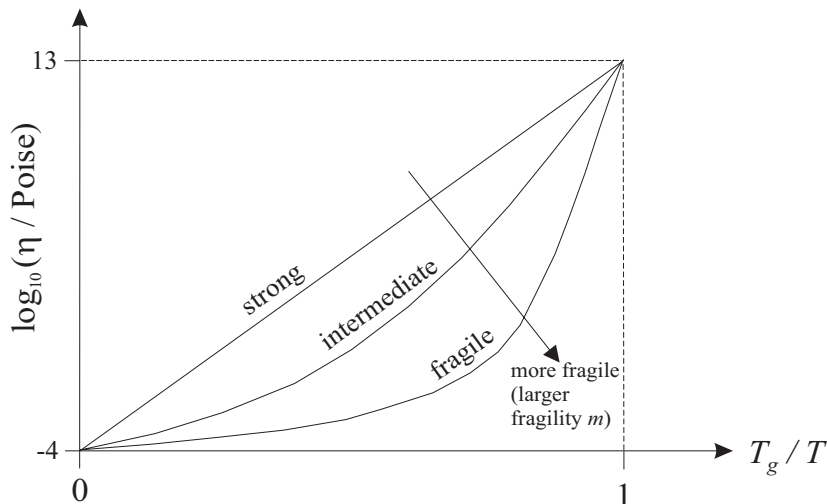


**Figure 2.5:** Qualitative temperature dependence of the viscosity  $\eta$  in the undercooled liquid for strong, intermediate, and fragile liquids ( $T_g$  scaled plot). Extrapolations of measured viscosity data in the liquid phase to high temperatures frequently yield  $\lim_{T \rightarrow \infty} \eta(T) \sim 10^{-4}$  poise [36].

## 2.3 Thermodynamics of the undercooled liquid

For simplicity, the theory in Sec. 2.3 is presented only for a single component system ( $C = 1$ ), which exhibits a single melting point  $T_m$ . The theory is qualitatively valid also for multi-component systems ( $C > 1$ ), like the binary, ternary, and quaternary alloys studied in this work. However, quantitative extensions are more complicated and would go beyond the scope of this study. The central point of interest is the effect of those extensions on the magnitude of the Gibbs free energy change  $\Delta G$  upon crystallization (Sec. 2.3.2 below): in a multi-component system, a crystal nucleus can have a composition different from the liquid, which affects the calculation of the crystal nucleation rate (Sec. 3.1 below). An excellent review on this issue is given by Baker and Cahn [43]. An approximate analytical expression for the Gibbs free energy change upon crystallization in binary metallic liquids was derived by Thompson and Spaepen from regular solution models for the liquid and the solid [44].

Describing a metastable state such as the undercooled liquid by equilibrium thermodynamics requires an explanation: Within the interpretation of statistical physics, the macroscopic thermodynamics can only be applied to systems for which each microstate

is accessible within a time  $t < \infty$ . However, as demonstrated first by Turnbull [45], the state of the undercooled liquid can be maintained over an extended period of time. This will also be the subject of Chap. 9. Hence, the system is able to sample all of its microstates within the experimental time window, i. e., as stated before, it is in internal equilibrium.

### 2.3.1 The Heat Capacity at constant pressure $C_p$

Figure 2.6 qualitatively displays the heat capacity  $C_p$  for the undercooled liquid, the crystal, and the glass<sup>5</sup>. The heat capacity is usually higher for the undercooled liquid than for the crystal due to additional configurational degrees of freedom [46, 23, 47, 38]. Frequently, but not always, the heat capacity of the undercooled liquid increases with increasing undercooling (as shown in Fig. 2.6). Chen and Turnbull suggested that this behavior is the manifestation of the loss of configurational entropy of the liquid [48].

Characteristic for the glass transition temperature  $T_g$  is a sudden drop in the heat capacity  $C_p$  upon cooling due to the freezing of the configurational degrees of freedom of the liquid. For  $T < T_g$  the heat capacity of glass and crystal become approximately equal [46, 23, 47, 38]. The drop in heat capacity in Fig. 2.6 is shown for two cooling rates: The curves (a) and (b) correspond to those shown in the viscosity diagram (Fig. 2.4).

### 2.3.2 Enthalpy $H$ , Entropy $S$ , and Gibbs Free Energy $G$

The heat capacity  $C_p$  and the enthalpy  $H$  are related by

$$dH = C_p dT . \quad (2.11)$$

Therefore, the difference in enthalpy  $\Delta H_{lc}$  between liquid and the crystal is given by

$$\Delta H_{lc}(T) = H_l(T) - H_c(T) = \Delta H_f + \int_{T_m}^T \Delta C_{p,lc}(T') dT' , \quad (2.12)$$

where  $H_l$  and  $H_c$  are the enthalpy of the liquid and the crystal, respectively, and  $\Delta C_{p,lc} = C_{p,l} - C_{p,c}$  the difference in heat capacity between liquid and crystal. The

---

<sup>5</sup>The index  $p$  in the quantity  $C_p$  refers to the heat capacity at constant *pressure*.

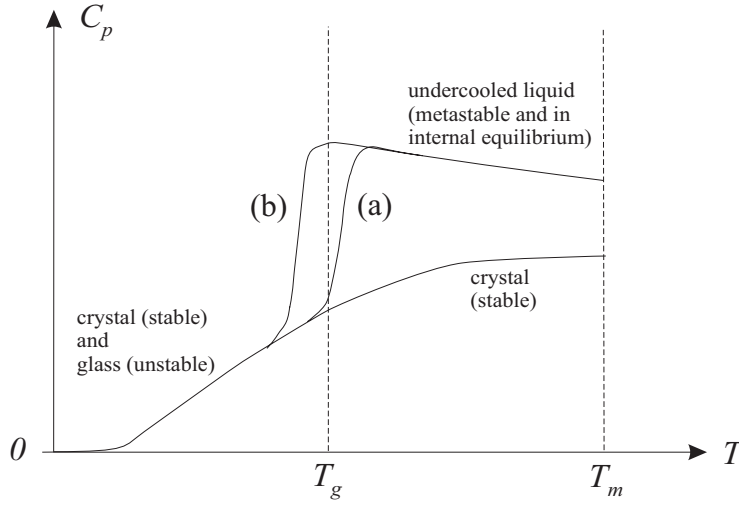


**Figure 2.6:** Heat Capacity  $C_p$  of a glass former in various stability regimes. The two cooling paths (a – fast cooling) and (b – slow cooling) correspond to those shown in Fig. 2.4.

integration constant  $\Delta H_f = H_l(T_m) - H_c(T_m)$  is called the *heat of fusion*. It is the amount of heat that has to be provided to rearrange bonds upon melting of a crystal. The result of the integration is shown qualitatively in Fig. 2.7. Slower cooling (b) leads to a lower value of  $\Delta H_{lc}$  below  $T_g$ . Curve (c) is obtained by extrapolating the equilibrium curve of the undercooled liquid, which corresponds to the (theoretical) case of infinitively slow cooling (cf. Fig. 2.4c). Structural relaxation is indicated by the arrows in Fig. 2.7.

The total differential of the enthalpy

$$dH = TdS + VdP \quad (2.13)$$

yields an expression for the entropy. Assuming constant pressure ( $dP = 0$ ) and using Eq. (2.11), this results in

$$dS = C_p \frac{dT}{T}. \quad (2.14)$$

The difference in entropy  $\Delta S_{lc}$  between liquid and crystal is obtained by integration:

$$\Delta S_{lc}(T) = S_l(T) - S_c(T) = \Delta S_f + \int_{T_m}^T \frac{\Delta C_{p,lc}(T')}{T'} dT', \quad (2.15)$$

where  $S_l$  and  $S_c$  are the entropy of liquid and crystal, respectively, and the integration constant  $\Delta S_f = S_l(T_m) - S_c(T_m)$  the *entropy of fusion*. A relation between  $\Delta H_f$

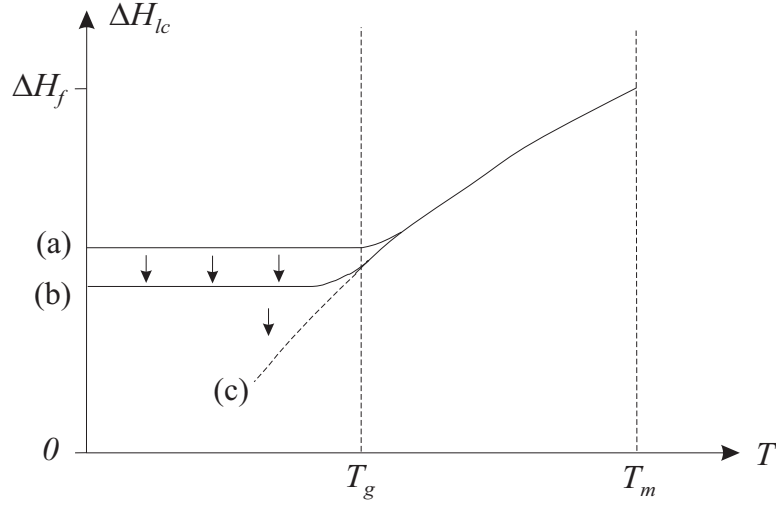


**Figure 2.7:** Difference in enthalpy  $H$  between liquid and crystal from Eq. (2.12). (a) Fast cooling. (b) Slow cooling. (c) Infinitively slow cooling. The isoconfigurational states [glass, states (a) and (b)] experience structural relaxation towards the undercooled liquid (c), which is in internal equilibrium. This is indicated by the arrows.

and  $\Delta S_f$  can be derived from the definition of the Gibbs free energy  $G$  (hereafter: free energy<sup>6</sup>),

$$G = H - TS. \quad (2.16)$$

Hence,

$$\Delta G_{lc}(T) = \Delta H_{lc}(T) - T\Delta S_{lc}(T). \quad (2.17)$$

At the melting point  $T_m$ , the free energy of liquid and crystal are equal:

$$\Delta G_{lc}(T_m) = 0, \quad (2.18)$$

and therefore,

$$\Delta S_f = \frac{\Delta H_f}{T_m}. \quad (2.19)$$

Figure 2.8 displays the temperature dependence of the entropy obtained from integration. According to Kauzmann [46], both  $\Delta S_{lc}$  and  $\Delta H_{lc}$  decrease upon cooling from  $T_m$  to  $T_g$  by a factor of two or more. Based on undercooled liquid heat capacity measurements on a variety of materials of different bond type, extrapolations of the

<sup>6</sup>The Helmholtz free energy  $F = E - TS$  ( $E$ : energy) will not be used throughout this thesis because it is the pressure and not the volume that is usually externally imposed in experiments.

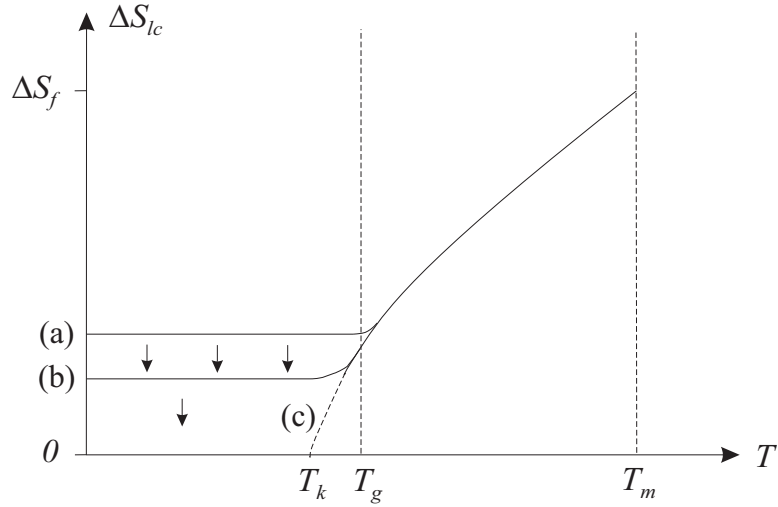


**Figure 2.8:** Difference in entropy  $S$  between liquid and crystal from Eq. (2.15). See caption of Fig. 2.7 for more details.

equilibrium curve to temperatures  $T < T_g$  yields  $\Delta S_{lc} = 0$  at a temperature  $T_k > 0$ , usually not far below  $T_g$  (Fig. 2.8c) [46].  $T_k$  is commonly called the *Kauzmann temperature*. Kauzmann postulated that  $T_k$  presents the ultimate limit for the undercooling of a liquid. He argued that the liquid entropy should never be lower than the crystal entropy. Moreover, the crystal entropy vanishes at  $T = 0$ , and negative entropies violate the third law of thermodynamics. The physical reason for a quickly decreasing liquid entropy around  $T_g$  is that the excess entropy  $\Delta S_{lc}$  of the undercooled liquid compared to the crystal is mainly of configurational (not vibrational) nature [49, 50, 25]. Hence, due to the rapid increase in configurational order associated with the rise in viscosity in the undercooled liquid,  $\Delta S_{lc}$  decreases quickly around  $T_g$ .

That the extrapolation of liquid entropy below  $T_k$  adopts values lower than the crystal entropy was called an ‘apparent paradox’ by Kauzmann [46]. A resolution was suggested by Gibbs and DiMarzio [51], who predicted an underlying second-order thermodynamic phase transition at  $T_k$  to an ideal glass with a unique configuration. This point of view is however controversial (e.g., Ref. [35] and references therein). Experimental proof of the existence of this second-order phase transition is difficult since the postulated transition at  $T_k$  cannot be reached experimentally upon cooling due to an intervening kinetic phenomenon, the glass transition.

Adam and Gibbs [52] have proposed a correlation between the configurational en-

ropy  $S_c$  of an undercooled liquid and its viscosity  $\eta$ :

$$\eta(T) = \eta'_0 \cdot \exp \frac{M}{TS_c(T)}, \quad (2.20)$$

where  $\eta'_0$  is a constant. The parameter  $M$  is related to the minimum entropy required for a region to undergo a transformation. It depends on composition and type of chemical bonding [53].  $S_c(T)$  can be obtained by a computer simulation. It has frequently been assumed that  $S_c(T)$  can be approximated by the excess entropy  $\Delta S_{lc}(T)$  of the undercooled liquid compared to the crystal [curve (c) in Fig. 2.8]. This approximation is, however, controversial since  $\Delta S_{lc}(T)$  contains vibrational contributions as well (e. g., Ref. [54] and references therein). For instance, according to Spaepen [49], the excess entropy in pure metals at  $T_m$  [i. e., the entropy of fusion, Eq. (2.19)] can be broken into about 17% of vibrational and about 83% of configurational contribution. The vibrational part is due to the fact that the atomic volume in the liquid is larger than in the crystal. It is however interesting to note that Eq. (2.20) reduces to the Vogel-Fulcher-Tammann equation [Eq. (2.9)] if vibrational contribution to  $\Delta S_{lc}$  is neglected and if the difference in heat capacity between undercooled liquid and crystal is assumed to vary inversely with temperature,

$$\Delta C_{p,lc}(T) = \frac{K}{T}, \quad (2.21)$$

where  $K$  is a constant [55, 42]. The configurational entropy is then given by

$$\begin{aligned} S_c(T) \approx \Delta S_{lc}(T) &= \int_{T_k}^T \frac{\Delta C_{p,lc}(T')}{T'} dT' \\ &= K \int_{T_k}^T \frac{1}{(T')^2} dT' \\ &= K \left( \frac{1}{T_k} - \frac{1}{T} \right). \end{aligned} \quad (2.22)$$

Substituting the lower line of Eq. (2.22) into Eq. (2.20) gives

$$\eta(T) = \eta'_0 \cdot \exp \frac{MT_k}{K(T - T_k)}. \quad (2.23)$$

Equation (2.23) coincides with Eq. (2.9) for

$$D = M/K, \quad \eta_0 = \eta'_0, \quad \text{and} \quad T_{FV} = T_k. \quad (2.24)$$

Equation (2.20) implies that a pronounced temperature dependence of  $S_c$  around  $T_g$  yields a pronounced temperature dependence of  $\eta$  around  $T_g$  and therefore fragile behavior [according to the definition in Eq. (2.8)]. As a consequence of the relation

$$\left(\frac{\partial S_c(T)}{\partial T}\right)_p \approx \left(\frac{\partial \Delta S_{lc}(T)}{\partial T}\right)_p = \frac{\Delta C_{p,lc}(T)}{T} \quad (2.25)$$

[cf. Eq. (2.14)], a pronounced temperature dependence of  $S_c$  around  $T_g$  also implies a large difference in heat capacity  $\Delta C_{p,lc}(T_g)$  between undercooled liquid and crystal around the glass transition temperature [23]. For this reason,  $\Delta C_{p,lc}(T_g)$  is frequently termed the *thermodynamic* fragility [in order to distinguish it clearly from the *kinetic* fragility  $m$  defined in Eq. (2.8)]. A correlation between the kinetic fragility and the thermodynamic fragility among different materials is, however, controversial since the parameter  $M$  in Eq. (2.20) varies between materials (Ref. [56] and references therein). However, it is frequently observed that materials with a large kinetic fragility also exhibit a large thermodynamic fragility [23].

Combining Eq. (2.21) with Eq. (2.24) yields

$$D = \frac{M}{T_g \cdot \Delta C_{p,lc}(T_g)}. \quad (2.26)$$

Substituting Eq. (2.26) into Eq. (2.10) gives a connection between the thermodynamic and the kinetic fragility if the parameters  $M$ ,  $T_g$ , and  $T_{FV}$  are known:

$$m = \frac{M}{\Delta C_{p,lc}(T_g) \cdot \ln(10)} \cdot \frac{T_{FV}}{(T_g - T_{FV})^2}. \quad (2.27)$$

It should however be emphasized that Eq. (2.27) has only limited validity since it was derived under the assumption that Eqs. (2.21) and (2.24) hold. Equation (2.27) is not necessarily in contradiction with the statement that  $m$  is frequently an increasing function of  $\Delta C_{p,lc}(T_g)$  since the term  $(T_g - T_{FV})^2$  in the denominator of Eq. (2.27) is small for fragile liquids and large for strong liquids.

Figure 2.8 shows that the glass exhibits a residual entropy  $S > 0$  at  $T = 0$ . This is not in contradiction with the third law of thermodynamics, which does not apply for a non-equilibrium system.

Figure 2.9 displays the free energy  $G$ , which can be obtained in two ways. One way is to substitute Eqs. (2.12) and (2.15) into Eq. (2.17). Using Eq. (2.19), this yields the

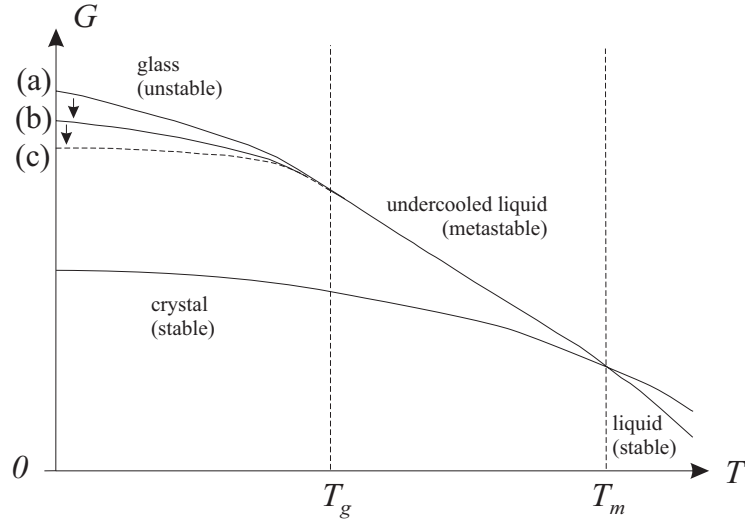


**Figure 2.9:** Gibbs free energy  $G$  in various stability regimes. See caption of Fig. 2.7 for more details.

difference in free energy  $\Delta G_{lc}$  between liquid and the crystal,

$$\begin{aligned}\Delta G_{lc}(T) &= G_l(T) - G_c(T) \\ &= \frac{\Delta H_f \Delta T}{T_m} + \int_{T_m}^T \Delta C_{p,lc}(T') dT' - T \int_{T_m}^T \frac{\Delta C_{p,lc}(T')}{T'} dT',\end{aligned}\quad (2.28)$$

where  $G_l$  and  $G_c$  are the free energy of liquid and crystal, respectively, and  $\Delta T := (T_m - T)$ . The other way is to consider the total differential for  $G$ ,

$$dG = -SdT + VdP. \quad (2.29a)$$

For  $dP = 0$ ,

$$dG = -SdT. \quad (2.29b)$$

Hence,

$$\Delta G_{lc}(T) = - \int_{T_m}^T \Delta S_{lc}(T') dT'. \quad (2.30)$$

Following Eq. (2.18), the integration constant vanishes here. Using Eq. (2.15), this yields

$$\Delta G_{lc}(T) = \frac{\Delta H_f \Delta T}{T_m} - \int_{T_m}^T \int_{T_m}^{T'} \frac{\Delta C_{p,lc}(T'')}{T''} dT'' dT'. \quad (2.31)$$

Equations (2.28) and (2.31) are equivalent.

### 2.3.3 Approximations of the free energy change on crystallization

The free energy change on crystallization  $\Delta G_{lc}$  of an undercooled liquid [Eqs. (2.28) or (2.31)] is an important parameter for the kinetics of crystallization (Chap. 3 below).  $\Delta G_{lc}$  can be calculated from Eqs. (2.28) or (2.31) if the heat capacity  $C_p$  for liquid and crystal is known as a function of temperature. However, unfortunately, the heat capacity of the undercooled liquid is difficult to determine experimentally for most materials due to interfering crystallization. Hence, one has to rely on approximations for  $\Delta G_{lc}$ . For the case that no heat capacity data are available, three approximations to Eqs. (2.28) or (2.31) have been proposed for  $T < T_m$ :

The oldest and simplest approximation, as used, for example, by Turnbull [57], assumes  $\Delta C_p = 0$  over the range of the undercooled liquid. For this case, Eqs. (2.28) or (2.31) yield

$$\Delta G_{lc}(T) = \frac{\Delta H_f \Delta T}{T_m}. \quad (2.32a)$$

Hence,  $\Delta G_{lc}$  is proportional to the undercooling  $\Delta T$ . Equation (2.32a) usually works well for metals, for which the difference in specific heat between liquid and crystal near the melting point is close to zero (e. g., [58]).

Another approximation was proposed by Thompson and Spaepen [59]. They assume

1.  $\Delta C_p = \text{const.}$  over the range of the undercooled liquid and
2.  $\Delta S_{lc} = 0$  for  $T = T_k$ .

Substituting these conditions into Eqs. (2.28) and (2.15), and performing further simplifications [59] eliminates both  $\Delta C_p$  and  $T_k$  and yields

$$\Delta G_{lc}(T) = \frac{\Delta H_f \Delta T}{T_m} \cdot \left( \frac{2T}{T_m + T} \right). \quad (2.32b)$$

As shown in Ref. [59], Eq. (2.32b) works best for materials for which  $\Delta C_p$  can be approximated as a constant of magnitude  $\Delta C_p = \frac{\Delta H_f}{T_m}$ .

The third approximation, as proposed by Hoffman [60], assumes

1.  $\Delta C_p = \text{const.}$  over the range of the undercooled liquid and
2.  $\Delta H_{lc} = 0$  for a temperature  $T_\infty$ , not far below  $T_g$ .

Substituting these conditions into Eqs. (2.28) and (2.12), and performing further simplifications [59, 60] eliminates both  $\Delta C_p$  and  $T_0$  and yields

$$\Delta G_{lc}(T) = \frac{\Delta H_f \Delta T}{T_m} \cdot \left( \frac{T}{T_m} \right). \quad (2.32c)$$

As shown in Ref. [59], Eq. (2.32c) does not work well for metals but works well for materials for which  $\Delta C_p$  at  $T_m$  is large.

Comparison of Eqs. (2.32a)–(2.32c) reveals that the Turnbull approximation yields the largest and the Hoffman approximation the lowest  $\Delta G_{lc}$  for all temperatures.

The advantage of Eqs. (2.32a)–(2.32c) over Eq. (2.28) or (2.31) is that they do not require knowledge of temperature dependent thermodynamic quantities of the undercooled liquid. Only the melting temperature  $T_m$  and the heat of fusion  $\Delta H_f$  are needed, which can, in most cases, easily be determined by calorimetric measurements.

## 2.4 The link between thermodynamics and kinetics

The second law of thermodynamics states the direction of a spontaneous transition:

$$\Delta S > 0 \quad (\text{closed system, energy } E \text{ and volume } V \text{ externally imposed}). \quad (2.33)$$

An equivalent statement is [61]

$$\Delta G < 0 \quad (\text{temperature } T \text{ and pressure } p \text{ externally imposed}). \quad (2.34)$$

The latter statement is usually more useful for the experimentalist as the temperature and the pressure are imposed in most experiments. Hence, under these conditions, it is valid:

- $\Delta G < 0$ : process *can* occur spontaneously,
- $\Delta G = 0$ : process occurs reversible (equilibrium),
- $\Delta G > 0$ : process *cannot* occur spontaneously.

Therefore,  $\Delta G$  is called the *driving force* for a transition, giving the direction of a spontaneous transition. The words *can* and *cannot* in above itemization are crucial, as they build the bridge from thermodynamics to kinetics: Thermodynamics can only tell what *cannot* happen spontaneously, but it can do this with absolute certainty. Hence, “*thermodynamics is the science of the impossible*”, as pointed out concisely by Baker and Cahn [43]. On the other hand, thermodynamics is noncommittal about the things that are possible. It is unable to tell if an allowed transition ( $\Delta G < 0$ ) *indeed* occurs or not, and *when* or *how* it occurs. These predictions can only be made by *kinetic theories*.

While the above paragraph applies to *any* transition, this concept will be applied to metastable phases in the following. Figure 2.10 shows the *molar* free energy of the liquid phase and various crystalline phases  $\gamma$ ,  $\delta$ ,  $\mu$ , and  $\nu$ . The  $\gamma$  phase is stable for  $T < T_m^\gamma$  (since its *molar* free energy is lowest), whereas the  $\delta$ ,  $\mu$ , and  $\nu$  phases are metastable. The liquid is stable for  $T > T_m^\gamma$  and metastable for  $T < T_m^\gamma$ . Thermodynamics can predict the following statements with certainty [Eq. (2.34)]:

1. The  $\gamma$  phase *cannot* form spontaneously from the liquid for  $T > T_m^\gamma$ .
2. The  $\delta$  phase *cannot* form spontaneously from the liquid for  $T > T_m^\delta$ .
3. The  $\mu$  phase *cannot* form spontaneously from the liquid for  $T > T_m^\mu$ .
4. The  $\nu$  phase *cannot* form spontaneously from the liquid at any temperature.

Hence, the number of possible crystallization paths increases with undercooling. If the liquid is undercooled below  $T_m^\mu$ , all of the three phases  $\gamma$ ,  $\delta$  and  $\mu$  can form from the liquid. However, thermodynamics is unable to tell *which* phase will crystallize for  $T < T_m^\mu$  or if *any* of them will crystallize and *when* and *how*. This prediction can only be made by kinetic theories of nucleation and growth, which will be the subject of Chap. 3. From the viewpoint of thermodynamics, in contrast, the metastable equilibrium is a full equilibrium. As long as another phase of lower free energy does not nucleate, the metastable equilibrium cannot be distinguished from the full equilibrium by any experiment. All thermodynamic measurements that have been performed on stable phases can also be performed on metastable phases.

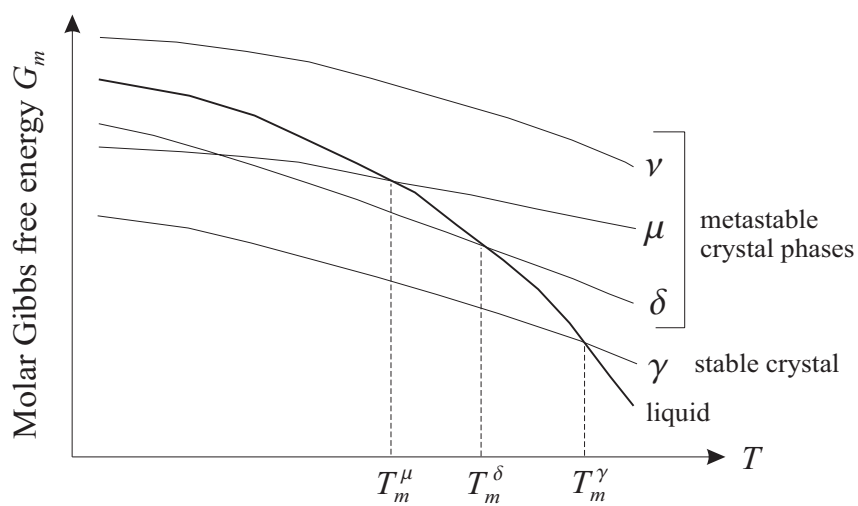


**Figure 2.10:** Molar Gibbs free energy  $G_m$  for various phases.  $T_m^\gamma$ ,  $T_m^\delta$ , and  $T_m^\mu$  are the melting points of the crystalline phases  $\gamma$ ,  $\delta$ , and  $\mu$ , respectively.



# Chapter 3

## Theory: Kinetics of solidification

Two processes are involved in the crystallization of a liquid. First, crystallization is initiated by crystal nucleation (Sec. 3.1). Subsequently, a stable crystal cluster grows to macroscopic size (crystal growth, Sec. 3.2).

### 3.1 Crystal nucleation

In the simplest case, nucleation occurs in the interior of the metastable phase, i. e., without the involvement of a ‘foreign’ substance. This is called *homogeneous nucleation* (Sec. 3.1.1). If a foreign substance is involved that acts as a preferred nucleation site (like an impurity or a container wall), nucleation is called *heterogeneous* (Sec. 3.1.2).

#### 3.1.1 Homogeneous nucleation

The basic concept for nucleation theory was provided by Gibbs in 1878 [62, 63, 64]. This early treatment is still purely thermodynamic (more precisely: thermostatic) and describes cluster formation of a new phase. Using this approach, the first kinetic model for nucleation was proposed by Volmer and Weber in 1926 [65, 63, 64], who treated the condensation of a supersaturated vapor. Their simple model has served as a basis for a further improvement by Becker and Döring in 1935 [66, 63, 64]. Finally, in 1949, Turnbull and Fisher applied the concept of the Becker-Döring theory to crystal nucleation in undercooled liquids [67, 63, 64]. Today, the theory is collectively known as the *classical nucleation theory* by Volmer, Weber, Becker, Döring, Turnbull, and Fisher.

### 3.1.1.1 Thermodynamics of cluster formation (Gibbs, 1878)

In a liquid, atoms approach each other statistically, forming crystal-like clusters by thermodynamic fluctuations<sup>1</sup>. For simplicity, the clusters are assumed spherical with radius  $r$ . The probability  $P^{equ}(r)$  to obtain a cluster of the new phase depends on the reversible work (free energy change) for cluster formation  $\Delta G_{\text{cluster}}(r)$  and is obtained from the theory of thermodynamic fluctuations (Boltzmann statistics) [68],

$$P^{equ}(r) \propto \exp\left(-\frac{\Delta G_{\text{cluster}}(r)}{k_B T}\right), \quad (3.1)$$

where  $k_B$  is the Boltzmann constant. The equilibrium cluster distribution is then

$$N^{equ}(r) = N_0 \cdot \exp\left(-\frac{\Delta G_{\text{cluster}}(r)}{k_B T}\right), \quad (3.2)$$

where  $N_0$  is the total number of atoms in the liquid and  $N^{equ}(r)$  is the equilibrium number of clusters of radius  $r$  (both quantities per unit volume, dimension:  $\frac{1}{\text{m}^3}$ ).  $\Delta G_{\text{cluster}}(r)$  can be expressed as a sum of two contributions [62, 63, 64]:

$$\Delta G_{\text{cluster}}(r) = \Delta G_{lc,V} \cdot \frac{4}{3}\pi r^3 + \sigma \cdot 4\pi r^2. \quad (3.3)$$

$\Delta G_{lc,V}$  is the free energy difference between the liquid and the crystalline phase (cf. Fig. 2.9), normalized *per unit volume*. It is defined to be positive above  $T_m$  and negative below  $T_m$ . The second term in Eq. (3.3) results from the creation of an interface between the cluster and the liquid. This term is always positive, and hence, it is energetically favorable neither for  $T > T_m$  nor for  $T < T_m$ . The quantity  $\sigma > 0$  is the interfacial free energy (hereafter: interfacial energy). Equation (3.3) is based on two assumptions:

1. There is a sharp interface between cluster and liquid.
2. The interfacial energy is independent of cluster size and can therefore be obtained from macroscopic measurements. This is called the *capillarity approximation*.

Figure 3.1 qualitatively displays the evolution of  $\Delta G_{\text{cluster}}(r)$ . For  $T > T_m$ ,  $\Delta G_{\text{cluster}}(r) > 0$  for any radius  $r$ . Hence, the clusters spontaneously decay. For  $T < T_m$ ,

---

<sup>1</sup>It should be noted that the distinction between a cluster and a liquid is purely artificial: All configurations that can be obtained by fluctuations in the liquid are possible microstates that are accessible in the equilibrium liquid.

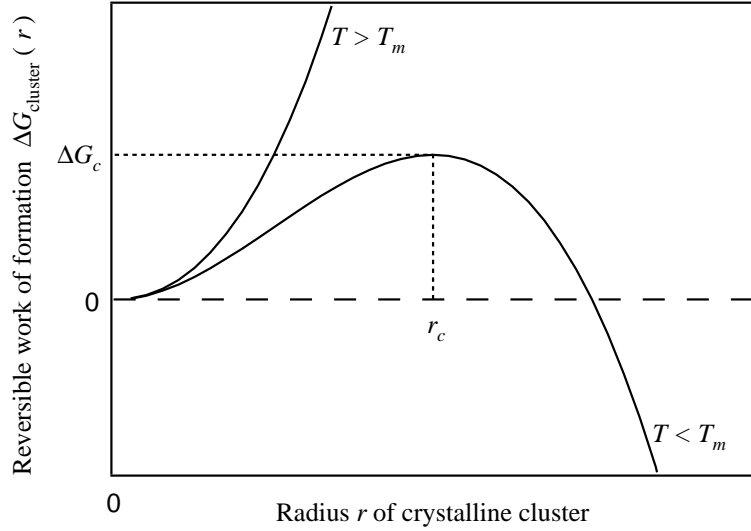


**Figure 3.1:** Reversible work (free energy change)  $\Delta G_{\text{cluster}}(r)$  for the formation of crystalline clusters of radius  $r$  in a liquid. For  $T > T_m$ , clusters spontaneously decay at any radius. For  $T < T_m$ , in contrast, clusters decay for  $r < r_c$  and grow for  $r > r_c$ .

however, the curve for  $\Delta G_{\text{cluster}}$  passes through a maximum (Fig. 3.1), which can be obtained by equating  $\frac{\partial \Delta G_{\text{cluster}}(r)}{\partial r} = 0$ . The maximum occurs because the surface-to-volume ratio is large for small clusters. The position of the maximum is (Fig. 3.1)

$$r_c = -\frac{2\sigma}{\Delta G_{lc,V}}, \quad (3.4)$$

and the height of the maximum is

$$\Delta G_c := \Delta G_{\text{cluster}}(r_c) = \frac{16\pi}{3} \frac{\sigma^3}{(\Delta G_{lc,V})^2}. \quad (3.5)$$

The quantity  $r_c$  is called the *critical radius*. A cluster of radius  $r_c$  is called a *critical cluster*.  $\Delta G_c$  is called the *critical work for cluster formation*. For  $T < T_m$ ,  $\Delta G_{\text{cluster}}(r)$  increases for  $r < r_c$ . Hence, clusters of size  $r < r_c$  spontaneously decay. However, for  $r > r_c$  and  $T < T_m$ , clusters would grow due to a gain in free energy. Therefore,  $\Delta G_c$  forms an activation barrier against crystallization and is crucial for undercooling of a liquid. Simply speaking, nucleation is the formation of post-critical clusters of size  $r > r_c$ .

It should be noted that the theory outlined above does not only apply to the formation of crystal-like clusters in undercooled liquids, but also to condensation in su-

persaturated vapors. For this case, the melting point  $T_m$  in Fig. 3.1 would have to be replaced by the boiling point. However, an additional term would be required in Eq. (3.3) that describes gravitation effects, i. e., that takes into account that the vapor is compressible. This term is negligible for crystal nucleation in liquids. The additional term affects the calculation of the critical radius [Eq. (3.4)] and the critical work [Eq. (3.5)] from Eq. (3.3).

Similarly, an additional term would be required in Eq. (3.3) if the parent phase was solid (e. g., for a crystal-to-crystal transformation). In this case, the change in volume, which accompanies most phase transformations, cannot be neglected. The additional term describes the increase in elastic strain energy per atom [63]. This term can be neglected for nucleation in a vapor or a liquid due to flow in the surrounding fluid. Similarly, it can be neglected for crystal nucleation in a glass if the temperature is sufficiently high.

### 3.1.1.2 Model based on equilibrium distribution of clusters (Volmer and Weber, 1926)

Volmer and Weber developed the first *kinetic* model for nucleation in a supersaturated vapor (condensation of either liquid or crystalline clusters - depending on temperature and pressure) [65, 63, 64]. Their model is based on the equilibrium cluster distribution [Eq. (3.2)]. As a function of cluster size  $i$  ( $i$  is the number of atoms in the cluster<sup>2</sup>), Eq. (3.2) can be rewritten as

$$N_i^{equ} = N_0 \cdot \exp\left(-\frac{\Delta G_{\text{cluster}}(i)}{k_B T}\right), \quad (3.6)$$

where  $N_0$  is the total number of atoms in the vapor and  $N_i^{equ}$  the equilibrium number of clusters of size  $i$  (both quantities per unit volume, dimension:  $\frac{1}{\text{m}^3}$ ). This cluster distribution function is shown in Fig. 3.2. For  $i = i_c$  ( $i_c$ : number of atoms in a critical cluster),

$$N_{i_c}^{equ} = N_0 \cdot \exp\left(-\frac{\Delta G_{\text{cluster}}(i_c)}{k_B T}\right) = N_0 \cdot \exp\left(-\frac{\Delta G_c}{k_B T}\right). \quad (3.7)$$

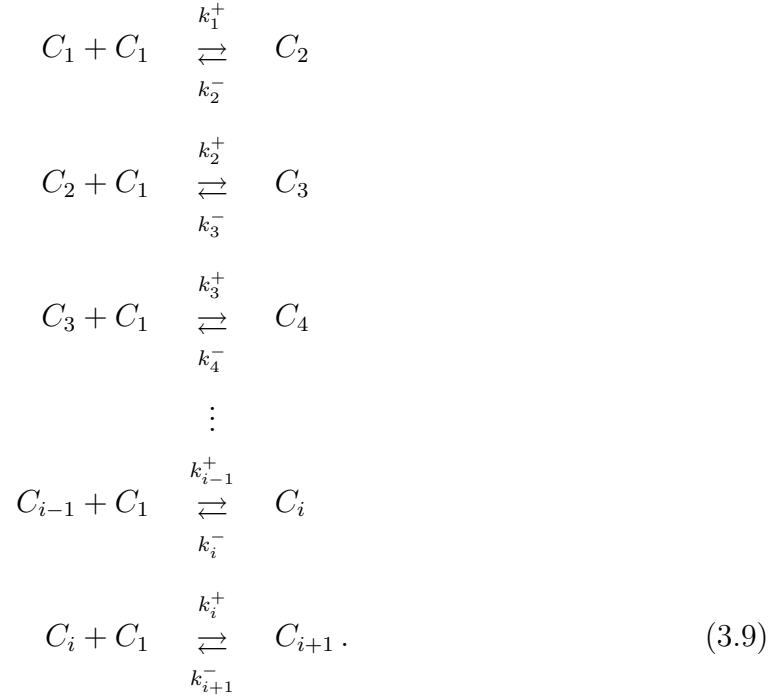
---

<sup>2</sup>Apparently, the description of spherical clusters by their number of atoms  $i$  is equivalent to the description by their radius  $r$  [Eq. (3.2)]. For the conversion from one to the other description, the knowledge of the atomic volume  $\Omega$  is required.

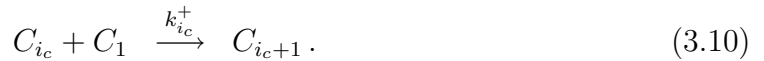
For  $i > i_c$ , the distribution becomes unphysical (as it diverges for large  $i$ ) and was therefore ignored by Volmer and Weber. Hence, the Volmer-Weber equilibrium cluster distribution becomes [63, 64]

$$\begin{aligned} i \leq i_c : \quad N_i^{equ} &= N_0 \cdot \exp\left(-\frac{\Delta G_{\text{cluster}}(i)}{k_B T}\right) \\ i > i_c : \quad N_i^{equ} &= 0. \end{aligned} \quad (3.8)$$

The development of clusters is assumed to occur by a sequence of bimolecular reactions [63, 64]:



$C_i$  is a cluster that contains  $i$  atoms.  $k_i^+$  is the arrival rate from the vapor to a cluster of size  $i$  (number of arrivals per atom on the cluster surface per unit time, dimension:  $\frac{1}{s}$ ).  $k_i^-$  is the corresponding evaporation or sublimation rate from a cluster of size  $i$ . Volmer and Weber assumed that nucleation occurs when a critical cluster  $C_{i_c}$  acquires one more atom:



The nucleation rate  $I^{equ}$  (dimension:  $\frac{1}{m^3 s}$ ) in the Volmer-Weber model is then given by [63, 64]

$$I^{equ} = s_{i_c} \cdot k_{i_c}^+ \cdot N_{i_c}^{equ} = s_{i_c} \cdot k_{i_c}^+ \cdot N_0 \cdot \exp\left(-\frac{\Delta G_c}{k_B T}\right), \quad (3.11)$$

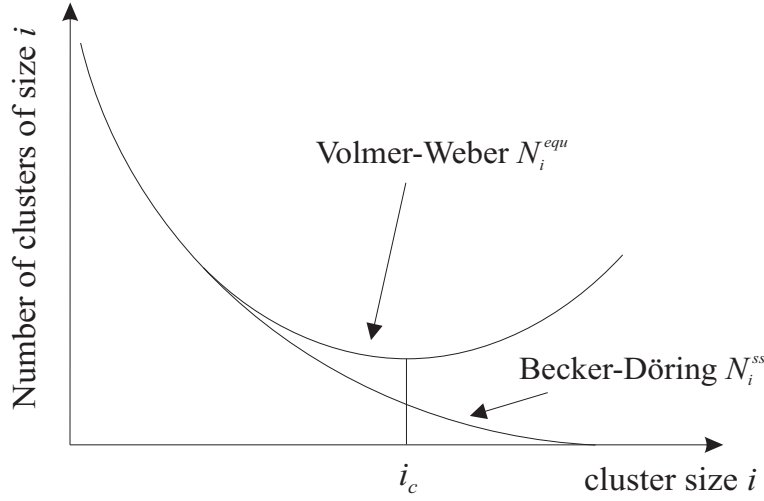


**Figure 3.2:** Statistical cluster distribution function (number of clusters of size  $i$ , where  $i$  is the number of atoms in the cluster).  $N_i^{equ}$ : Volmer-Weber model.  $N_i^{ss}$ : Becker-Döring model. The number of atoms in the critical cluster [cluster of radius  $r = r_c$  (cf. Fig. 3.1)] is  $i_c$ .

where  $s_{i_c}$  is the number of surface atoms in the critical cluster (dimensionless), which is on the order of 10–100 [24]. Clusters  $C_{i_c+1}$  are assumed to grow to macroscopic size and are taken out of the ensemble. Particle conservation requires that they are replaced by an equivalent number of  $(i_c + 1)$  vapor atoms.

### 3.1.1.3 Steady state model (Becker and Döring, 1935)

The Volmer-Weber model assumes that a critical cluster grows to macroscopic size as soon as it becomes post-critical by the condensation of an additional vapor atom. However, in reality, there can be a back-flux according to Eq. (3.9) also for a post-critical cluster and hence, it can decay again with a certain probability. This is the main deficit of the Vomer-Weber theory. Hence, Becker and Döring [66, 63, 64] assumed that a steady state cluster distribution  $N_i^{ss}$  is more reasonable than the equilibrium distribution  $N_i^{equ}$  employed by Volmer and Weber [Eq. (3.6)]. Both distributions are shown in Fig. 3.2. The particle conservation requires the integral over the cluster distribution to converge, so that  $N_i^{ss}$  becomes essentially zero at large cluster sizes  $i$ . For small cluster sizes,  $N_i^{ss}$  approaches  $N_i^{equ}$  (Fig. 3.2). The steady state nucleation

rate  $I^{ss}$  employed by Becker and Döring, taking care of the back flux, is

$$I^{ss} = s_i \cdot k_i^+ \cdot N_i^{ss} - s_{i+1} \cdot k_{i+1}^- \cdot N_{i+1}^{ss}, \quad (3.12)$$

where  $s_i$  is the number of surface atoms in a cluster of size  $i$  (dimensionless).  $I^{ss}$  should be independent of cluster size  $i$  for a true steady-state condition. In their treatment, Becker and Döring obtain after making a few assumptions [25, 63, 64]:

$$I^{ss} = s_{i_c} \cdot k_{i_c}^+ \cdot N_0 \cdot \underbrace{\frac{1}{i_c} \cdot \left( \frac{\Delta G_c}{3\pi k_B T} \right)^{\frac{1}{2}}}_{\Gamma_z} \cdot \exp \left( -\frac{\Delta G_c}{k_B T} \right). \quad (3.13)$$

Equation (3.13) differs by the Volmer-Weber equation [Eq. (3.11)] only by the Zeldovich factor  $\Gamma_z$ , which only has a weak temperature dependence and which takes into account the post-critical clusters of size  $i > i_c$ :

$$I^{ss} = \Gamma_z \cdot I^{equ}. \quad (3.14)$$

Based on analytical and numerical studies,  $\Gamma_z$  is between  $\frac{1}{100}$  and  $\frac{1}{10}$  in most cases [63, 64, 26].

As the nucleation rate is far more sensitive to slight changes in  $\Delta G_c$  than to the exact value of the pre-exponential factor [63], the expression from the Becker-Döring theory [Eq. (3.13)] is essentially the same as that from the Volmer-Weber theory [Eq. (3.11)] for practical purposes. However, the importance of the Becker-Döring theory is that the kinetic problem has been treated correctly [63].

The prefactor  $k_{i_c}^+$  in Eq. (3.13) is readily obtained by kinetic theory of gases. Under the assumption that each vapor atom that collides with the cluster indeed condenses,  $k_{i_c}^+$  is approximately given by the product of an atomic area  $\Omega^{2/3}$  ( $\Omega$ : atomic volume) and the kinetic theory collision factor  $\frac{p}{\sqrt{2\pi m k_B T}}$  [63]:

$$k_{i_c}^+ = \frac{p}{\sqrt{2\pi m k_B T}} \cdot \Omega^{2/3}, \quad (3.15)$$

where  $p$  is the vapor pressure and  $m$  the atomic mass. Hence, the steady state nucleation rate becomes

$$I^{ss} = \underbrace{s_{i_c} \cdot \Omega^{2/3}}_{a_c} \cdot \frac{p}{\sqrt{2\pi m k_B T}} \cdot N_0 \cdot \Gamma_z \cdot \exp \left( -\frac{\Delta G_c}{k_B T} \right), \quad (3.16)$$

where  $a_c = 4\pi r_c^2$  is the surface area of the critical cluster.

The steady state model by Becker and Döring [Eq. (3.13) or (3.16)] applies if the experimental time window has been large enough to establish the steady state distribution of clusters  $N_i^{ss}$  (Fig. 3.2). If this is not the case, this distribution may not be reached and transient effects have to be taken into account (Sec. 3.1.3).

### 3.1.1.4 The kinetic factor in liquid-crystal transformations (Turnbull and Fisher, 1949)

Turnbull and Fisher were the first to extend the Becker-Döring model to crystal nucleation in undercooled liquids [67, 63, 64]. They obtained the corresponding prefactor  $k_{i_c}^+$  in Eq. (3.13) for two cases: diffusion-limited crystallization kinetics (Sec. 3.1.1.4.1 below) and collision-limited crystallization kinetics (Sec. 3.1.1.4.2 below).

**3.1.1.4.1 Diffusion-limited crystallization** The first case (diffusion-limited crystallization) applies if changes of neighbors by diffusive motions are necessary for crystallization. This usually applies to metallic alloys, ionic materials, and covalent materials. In ionic materials, the charge topology has to change, and in covalent materials the bonds have to rearrange upon crystallization. The frequency of diffusive jumps across the liquid-crystalline interface per atom is [24, 25]

$$k_{i_c}^+ = \frac{6D}{\lambda^2} \quad (\text{diffusion-limited}), \quad (3.17)$$

where  $D$  is usually associated with the diffusivity in the undercooled liquid (not in the crystal). The parameter  $\lambda = \Omega^{1/3}$  is the average interatomic distance [24, 25]. Equation (3.17) is equivalent to Eq. (2.2), where  $k_{i_c}^+ \equiv \Gamma_D$ . Substituting Eq. (3.17) into Eq. (3.13) gives the nucleation rate for diffusion-limited crystallization [24, 25]:

$$\begin{aligned} I^{ss} &= s_{i_c} \cdot k_{i_c}^+ \cdot N_0 \cdot \Gamma_z \cdot \exp\left(-\frac{\Delta G_c}{k_B T}\right) \\ &= s_{i_c} \cdot \frac{6D}{\lambda^2} \cdot N_0 \cdot \Gamma_z \cdot \exp\left(-\frac{\Delta G_c}{k_B T}\right). \end{aligned} \quad (3.18)$$

Using the Stokes-Einstein equation [Eq. (2.3)], this gives

$$I^{ss} = s_{i_c} \cdot \frac{2k_B T}{\eta \pi \lambda^3} \cdot N_0 \cdot \Gamma_z \cdot \exp\left(-\frac{\Delta G_c}{k_B T}\right). \quad (3.19)$$

The Stokes-Einstein equation states the relation between the macroscopic viscosity  $\eta$  and the microscopic diffusivity  $D$ . It is expected to be valid if viscous flow and atomic diffusion are governed by the *same* physical process. The Stokes-Einstein equation has been found to hold for a large variety of undercooled liquids. Violations of this relation have been reported for some fragile liquids below  $T_c$  ( $\approx 1.2T_g$ ), the mode coupling theory critical temperature, due to a decoupling of diffusivity from viscosity [38, 35, 34, 69]. For this group of fragile liquids, the diffusivity has been reported to slow down less rapidly than the fluidity  $f$  (inverse of the viscosity:  $f \equiv \frac{1}{\eta}$ ) for  $T < T_c$  [34, 69].

Substituting  $N_0 = \frac{1}{\lambda^3} = \frac{1}{\Omega}$  in Eq. (3.19) gives

$$I^{ss} = s_{i_c} \cdot \frac{2k_B T}{\eta \pi} \cdot N_0^2 \cdot \Gamma_z \cdot \exp\left(-\frac{\Delta G_c}{k_B T}\right). \quad (3.20)$$

The pre-exponential factor in Eq. (3.20) may be estimated by setting  $N_0 \sim 10^{28} \frac{1}{\text{m}^3}$ ,  $s_{i_c} \sim 10$ ,  $T \sim 1000$  K, and  $\Gamma_z \sim \frac{1}{100}$ . This gives

$$I^{ss} = \frac{10^{35}}{\eta} \exp\left(-\frac{\Delta G_c}{k_B T}\right) \quad \frac{\text{J}}{\text{m}^6}. \quad (3.21)$$

Setting  $\eta = \hat{\eta} \text{ poise} = \hat{\eta} \cdot \frac{1}{10} \text{ Pa s}$  (i. e.,  $\hat{\eta}$  is the numerical value of the viscosity in poise), this yields

$$I^{ss} = \frac{10^{36}}{\hat{\eta}} \exp\left(-\frac{\Delta G_c}{k_B T}\right) \quad \frac{1}{\text{m}^3 \text{ s}}. \quad (3.22a)$$

Using Eq. (3.5), this can be rewritten as

$$I^{ss} = \frac{10^{36}}{\hat{\eta}} \exp\left(-\frac{16\pi}{3k_B T} \frac{\sigma^3}{(\Delta G_{lc,V})^2}\right) \quad \frac{1}{\text{m}^3 \text{ s}}. \quad (3.22b)$$

The uncertainty of the pre-exponential factor of  $10^{36}$  is about two to four orders of magnitude [63]. However, as the variation of the exponential term in Eq. (3.22) changes so rapidly with  $\Delta G_c$  upon undercooling, the value of  $\Delta G_c$  that is required to give a fixed nucleation rate at a specific temperature is insensitive to the exact value of the pre-exponential factor [63, 64]. This applies even more to the interfacial energy  $\sigma$ , since it is raised to the third power in the exponential.

The nucleation rate  $I^{ss}$  in Eq. (3.22) becomes negligibly small close to the melting point, where  $\Delta G_{lc,V}$  becomes small (cf. Fig. 2.9), and close to the glass transition

temperature  $T_g$ , where the viscosity strongly increases (cf. Fig. 2.4). Hence, glass formation should be possible in any material that is governed by diffusion-limited kinetics since the kinetics slow down at low temperature due to the involvement of diffusion. However, depending on the cooling rate and the height of the maximum in  $I^{ss}$ , which is located between glass transition and melting temperature, crystallization can interfere and thereby prevent glass formation. The height of the maximum, and hence the ease of glass formation, depends on the parameters  $\sigma$ ,  $\Delta G_{lc,V}$ , and  $\hat{\eta}$ . This will be discussed in more detail in Chap. 9.

**3.1.1.4.2 Collision-limited crystallization** The second case (collision-limited crystallization) applies to a situation, where atomic neighbors generally do not have to change by diffusive rearrangements upon crystallization. Instead, atomic movement from the liquid to the crystalline phase can be accomplished by thermal vibration. Hence, crystallization is governed by the collision of the atoms. This is usually expected in pure metals<sup>3</sup> and in van der Waals bonded materials. The arrival rate constant  $k_{i_c}^+$  is then equal to the collision rate at which the atoms attempt to join the nucleus:

$$k_{i_c}^+ = \frac{u_{\text{sound}}}{\lambda} \quad (\text{collision-limited}). \quad (3.23)$$

$u_{\text{sound}}$  is the sound velocity in the liquid, which is characteristic for the vibrational motion of the atoms. Substituting Eq. (3.23) into Eq. (3.13) gives

$$\begin{aligned} I^{ss} &= s_{i_c} \cdot k_{i_c}^+ \cdot N_0 \cdot \Gamma_z \cdot \exp\left(-\frac{\Delta G_c}{k_B T}\right) \\ &= s_{i_c} \cdot \frac{u_{\text{sound}}}{\lambda} \cdot N_0 \cdot \Gamma_z \cdot \exp\left(-\frac{\Delta G_c}{k_B T}\right). \end{aligned} \quad (3.24)$$

The pre-exponential factor in Eq. (3.24) may be estimated by setting  $N_0 \sim 10^{28} \frac{1}{\text{m}^3}$ ,  $s_{i_c} \sim 10$ ,  $\lambda \sim 3 \text{ \AA}$ ,  $u_{\text{sound}} \sim 1000 \text{ ms}^{-1}$ , and  $\Gamma_z \sim \frac{1}{100}$ . This gives

$$I^{ss} = 10^{39} \exp\left(-\frac{\Delta G_c}{k_B T}\right) \quad \frac{1}{\text{m}^3 \text{ s}}. \quad (3.25a)$$

Substitution of  $\Delta G_c$  from Eq. (3.5) gives

$$I^{ss} = 10^{39} \exp\left(-\frac{16\pi}{3k_B T} \frac{\sigma^3}{(\Delta G_{lc,V})^2}\right) \quad \frac{1}{\text{m}^3 \text{ s}}. \quad (3.25b)$$

---

<sup>3</sup>The word ‘pure’ denotes that the metal consists only of one element.

The discussion in the paragraph underneath Eq. (3.22b) on the uncertainty of the pre-exponential factor is equally valid for collision-limited crystallization.

The nucleation rate  $I^{ss}$  in Eq. (3.25) becomes negligibly small close to the melting point, where  $\Delta G_{lc,V}$  becomes small (cf. Fig. 2.9), and increases continuously upon cooling. Hence, glass formation is very difficult for purely collision-limited kinetics. However, it is not necessarily impossible since the collision rate [Eq. (3.23)] involves quantum mechanical effects at low temperatures. Also, free volume is required for atomic rearrangements upon crystallization. With a little bit of free volume, these rearrangements are easy, and the limiting factor is the collision rate [Eq. (3.23)]. If this is not the case, the structural change may become impossible, which can favor glass formation [53]. Experimentally, however, there is no evidence of any pure metal having been quenched into a glass from the liquid. Pure amorphous metals have indeed been prepared by electrodeposition or vapor deposition, but their crystallization temperature is often lower than for the same element when it is alloyed.

Equations (3.22) and (3.25) roughly coincide for low undercoolings, where the viscosity is roughly independent of temperature (Fig. 2.4) and usually on the order of  $10^{-1} - 10^{-3}$  poise. Both equations have been used widely and successfully to model experimental data on crystal nucleation in undercooled liquids [70, 44, 71, 72, 73, 63, 74, 41, 24]. Equations (3.22) or (3.25) can finally predict which of the three phases  $\gamma$ ,  $\delta$ , or  $\mu$  back in Fig. 2.10 will nucleate for  $T < T_m^\mu$ : It will be the phase for which the nucleation rate (i. e., the probability for nucleation) is highest. This will be determined by

1. the interfacial energy  $\sigma$  between the liquid and each of the crystalline  $\gamma$ ,  $\delta$ , and  $\mu$  phase and
2. the magnitude of the driving force  $\Delta G_{lc,V}$  per unit volume.

Considering the parameters  $\sigma$  and  $\Delta G_{lc,V}$  collectively, it is the quantity  $\Delta G_c$  that determines which phase nucleates [Eqs. (3.22a) and (3.25a)] since the viscosity  $\hat{\eta}$  of the parent state is the same for all possible transitions at the same temperature.

It is worth emphasizing that the magnitude of the driving force per unit volume determines the nucleation rate, whereas the magnitude of the driving force per mole determines which phase is the *stable* phase: In Fig. 2.10, the  $\gamma$  phase has the largest

driving force *per mole* for its formation, but if its density is low, it does not necessarily have the largest driving force *per unit volume*. Hence, for  $T < T_m^\mu$ , nucleation of the metastable  $\delta$  or  $\mu$  phase might be preferred [43].

### 3.1.2 Heterogeneous nucleation

The homogeneous nucleation rate [Eqs. (3.22b) and (3.25b)] depends on the interfacial energy  $\sigma$  and the free energy change  $\Delta G_{lc,V}$ , and for diffusion-limited crystallization also on the viscosity  $\eta$ . Those parameters are *intrinsic* properties of the material. Hence, homogeneous nucleation is an intrinsic process. In practice, however, homogeneous nucleation is difficult to observe. Usually, foreign phases like container walls and impurities take part in the nucleation process. In this case, nucleation is called *heterogeneous*. Heterogeneous nucleation is therefore an *extrinsic* process and can be influenced by the experimental conditions [26].

The simplest model for heterogeneous nucleation is due to Volmer [75, 76]. It describes the thermodynamics of heterogeneous cluster formation in a similar way as the Gibbs model for homogeneous cluster formation (Sec. 3.1.1.1), but with a flat substrate involved, which acts as a heterogeneous nucleation site. Like Gibbs' model, Volmer's model can be applied to both nucleation in a supersaturated vapor (condensation) and to crystal nucleation in an undercooled liquid. For simplicity, the indices in the following treatment just refer to the latter case.

Under the assumption that the phases are isotropic, the interface between the crystalline cluster and the liquid parent phase must have the same curvature everywhere. Hence, the crystalline cluster grows on the flat substrate like a spherical cap of radius  $r$  (Fig. 3.3). As a function of the wetting angle  $\theta$  (Fig. 3.3), the exposed volume fraction  $f(\theta)$  and the exposed surface fraction  $s(\theta)$  relative to a sphere of the same radius  $r$  are [76]

$$f(\theta) = \frac{(2 + \cos \theta)(1 - \cos \theta)^2}{4}, \quad (3.26a)$$

$$s(\theta) = \frac{1 - \cos \theta}{2}. \quad (3.26b)$$

Figure 3.4 displays the functions  $f$  and  $s$ .  $\theta = 0^\circ$  represents complete wetting of the substrate, whereas  $\theta = 180^\circ$  corresponds to no wetting (homogeneous cluster formation).

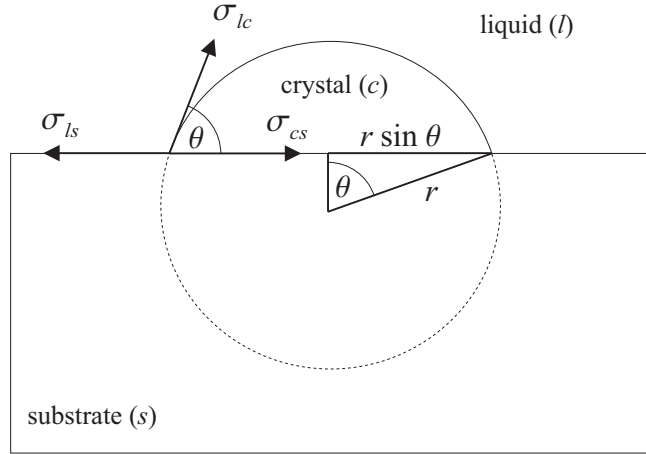


**Figure 3.3:** Volmer's spherical cap model for heterogeneous cluster formation. The exposed crystal cluster has the shape of a spherical cap, whose volume and surface fraction relative to the entire sphere,  $f(\theta)$  and  $s(\theta)$ , respectively, are given in Eq. (3.26). The dashed circle segment is a guide for the eye.

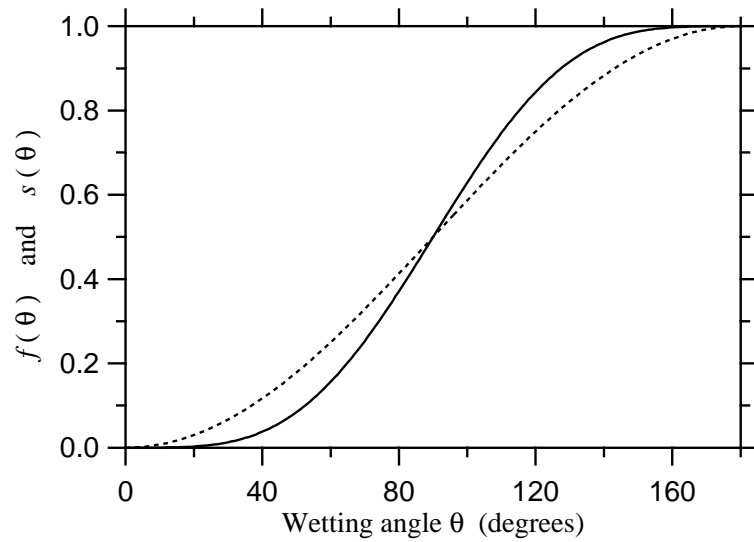


**Figure 3.4:** Heterogeneous cluster formation: Exposed volume fraction  $f(\theta)$  (solid curve) and exposed surface fraction  $s(\theta)$  (dotted curve) [Eq. (3.26)] relative to a sphere of the same radius  $r$  as a function of wetting angle  $\theta$  (cf. Fig. 3.3).

The reversible work for heterogeneous cluster formation  $\Delta G_{\text{cluster}}^{\text{het}}(r)$  is then readily obtained from Fig. 3.3 in a similar way as for the homogeneous case:

$$\Delta G_{\text{cluster}}^{\text{het}}(r) = \Delta G_{lc,V} \cdot f(\theta) \cdot \frac{4}{3}\pi r^3 + \sigma_{lc} \cdot s(\theta) \cdot 4\pi r^2 + \underbrace{\pi(r \sin \theta)^2}_{\text{supporting area}} (\sigma_{cs} - \sigma_{ls}), \quad (3.27)$$

where the indices  $c$ ,  $l$ , and  $s$  denote crystal, liquid, and substrate, respectively [76]. The first term in Eq. (3.27) corresponds to the free energy change per unit volume [cf. Eq. (3.3) for the homogeneous case]. The second term results from the interface between crystalline cluster and liquid, and the third term results from the replacement of a liquid-substrate interface by a crystal-substrate interface, where  $\pi(r \sin \theta)^2$  is the circular supporting area of the crystalline cluster on the substrate (Fig. 3.3). If

$$\sigma_{cs} - \sigma_{ls} < \sigma_{lc} \quad (3.28)$$

the free energy of cluster formation *per atom* is lower than if the circular cluster surface  $\pi(r \sin \theta)^2$  were exposed to the liquid. This is the main idea of the spherical cap model for heterogeneous nucleation as it lowers the critical work for cluster formation. Using Young's equation [76],

$$\sigma_{cs} - \sigma_{ls} = -\sigma_{lc} \cos \theta, \quad (3.29)$$

Eq. (3.27) can be written as

$$\begin{aligned} \Delta G_{\text{cluster}}^{\text{het}}(r) &= \Delta G_{lc,V} \cdot f(\theta) \cdot \frac{4}{3}\pi r^3 + \sigma_{lc} \cdot s(\theta) \cdot 4\pi r^2 - \pi(r \sin \theta)^2 \sigma_{lc} \cos \theta \\ &= \Delta G_{lc,V} \cdot f(\theta) \cdot \frac{4}{3}\pi r^3 + \sigma_{lc} \cdot 4\pi r^2 \underbrace{\left( s(\theta) - \frac{1}{4} \sin^2 \theta \cos \theta \right)}_{=f(\theta)} \\ &= \left( \Delta G_{lc,V} \cdot \frac{4}{3}\pi r^3 + \sigma_{lc} \cdot 4\pi r^2 \right) f(\theta). \end{aligned} \quad (3.30)$$

Hence, the free energy for *heterogeneous* cluster formation can be written as

$$\Delta G_{\text{cluster}}^{\text{het}}(r) = \Delta G_{\text{cluster}}^{\text{hom}}(r) \cdot f(\theta), \quad (3.31)$$

where  $\Delta G_{\text{cluster}}^{\text{hom}}(r)$  is the free energy for *homogeneous* cluster formation [denoted as  $\Delta G_{\text{cluster}}(r)$  in Eq. (3.3)]. Hence, the critical radius for heterogeneous nucleation, obtained by equating  $\frac{\partial \Delta G_{\text{cluster}}^{\text{het}}(r)}{\partial r} = 0$ , is the *same* as for homogeneous nucleation:

$$r_c^{\text{het}} = r_c^{\text{hom}}. \quad (3.32)$$

However, apparently, the *number of atoms* in the critical cluster  $i_c$  differs by the factor  $f(\theta)$  for homogeneous and heterogeneous nucleation:

$$i_c^{\text{het}} = i_c^{\text{hom}} \cdot f(\theta). \quad (3.33)$$

Both  $i_c$  and  $\Delta G_{\text{cluster}}$  are therefore reduced by the factor  $f(\theta)$  in the case of heterogeneous nucleation (Fig. 3.5). The critical work for heterogeneous cluster formation is

$$\Delta G_c^{\text{het}} := \Delta G_{\text{cluster}}^{\text{het}}(r_c) = \frac{16\pi}{3} \underbrace{\frac{\sigma^3}{(\Delta G_{lc,V})^2}}_{\Delta G_c \equiv \Delta G_c^{\text{hom}}} \cdot f(\theta), \quad (3.34)$$

where  $\Delta G_c$  is the critical work for homogeneous cluster formation [Eq. (3.5)]. Hence, if there is no wetting ( $\theta = 180^\circ$ ,  $f = 1$ ), the above equations reduce to the homogeneous equations, i. e., the substrate does not aid in the nucleation process. On the other hand, for perfect wetting ( $\theta = 0^\circ$ ,  $f = 0$ ), the critical work is zero and the liquid cannot be undercooled at all. It is interesting to relate the latter statement to the melting of a crystal: For this case, perfect wetting ( $\theta = 0^\circ$ ,  $f = 0$ ) always occurs, and the surface of the crystal forms an ideal nucleation site for the melting process. Consequently, in contrast to undercooling effects, superheating effects are rarely observed, i. e., materials melt at their equilibrium melting temperature [26].

The classical theory for homogeneous nucleation can equally be applied to the case of heterogeneous nucleation [63, 26]. The only difference is the lower work for critical cluster formation [Eq. (3.34)] and the reduced number of atoms that can act as a nucleation site: While any atom can act as a nucleation site for homogeneous nucleation, only those atoms in contact with the impurity can act as a nucleation site for heterogeneous nucleation. If  $\epsilon$  is the fraction of atoms in contact with the heterogeneity (usually  $\epsilon \ll 1$ ), then the steady state nucleation rate for heterogeneous nucleation  $I^{ss,\text{het}}$  is readily obtained from the Becker-Döring model [Eq. (3.13)] [63]:

$$\begin{aligned} I^{ss,\text{het}} &= s_{i_c} \cdot k_{i_c}^+ \cdot \epsilon \cdot N_0 \cdot \Gamma_z \cdot \exp\left(-\frac{\Delta G_c}{k_B T} \cdot f(\theta)\right) \\ &= s_{i_c} \cdot k_{i_c}^+ \cdot \epsilon \cdot N_0 \cdot \Gamma_z \cdot \exp\left(-\frac{16\pi}{3k_B T} \frac{\sigma^3}{(\Delta G_{lc,V})^2} \cdot f(\theta)\right) \\ &= s_{i_c} \cdot k_{i_c}^+ \cdot \epsilon \cdot N_0 \cdot \Gamma_z \cdot \exp\left(-\frac{\Delta G_c^{\text{het}}}{k_B T}\right), \end{aligned} \quad (3.35)$$

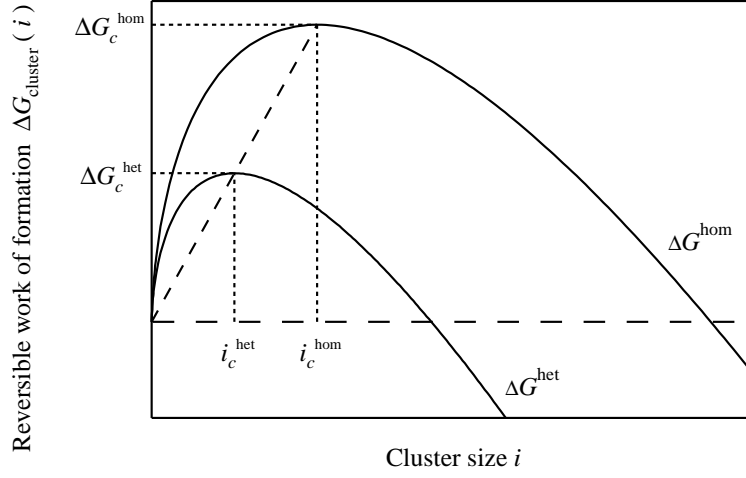


**Figure 3.5:** The reversible work (free energy change) for *heterogeneous* cluster formation  $\Delta G_{\text{cluster}}^{\text{het}}(i)$  for  $T < T_m$  as a function of the number of atoms in the cluster  $i$  can be obtained from the *homogeneous* work of cluster formation  $\Delta G_{\text{cluster}}^{\text{hom}}(i)$  [Eq. (3.3)] by multiplying both axes with the factor  $f(\theta)$ , which is the volume fraction of the spherical cap relative to the entire sphere of radius  $r$  (Fig. 3.3). Here  $f(\theta) = \frac{1}{2}$ .

where the product  $\epsilon \cdot N_0$  is the *absolute* number of atoms in contact with the heterogeneity. The heterogeneous nucleation rate in undercooled liquids is then for diffusion-limited crystallization [cf. Eq. (3.22)]

$$\begin{aligned}
 I^{ss,\text{het}} &= \epsilon \cdot \frac{10^{36}}{\hat{\eta}} \exp\left(-\frac{\Delta G_c}{k_B T} \cdot f(\theta)\right) \frac{1}{\text{m}^3 \text{s}} \\
 &= \epsilon \cdot \frac{10^{36}}{\hat{\eta}} \exp\left(-\frac{16\pi}{3k_B T} \frac{\sigma^3}{(\Delta G_{lc,V})^2} \cdot f(\theta)\right) \frac{1}{\text{m}^3 \text{s}} \\
 &= \epsilon \cdot \frac{10^{36}}{\hat{\eta}} \exp\left(-\frac{\Delta G_c^{\text{het}}}{k_B T}\right) \frac{1}{\text{m}^3 \text{s}} \tag{3.36}
 \end{aligned}$$

and for collision-limited crystallization [cf. Eq. (3.25)]

$$\begin{aligned}
 I^{ss,\text{het}} &= \epsilon \cdot 10^{39} \exp\left(-\frac{\Delta G_c}{k_B T} \cdot f(\theta)\right) \\
 &= \epsilon \cdot 10^{39} \exp\left(-\frac{16\pi}{3k_B T} \frac{\sigma^3}{(\Delta G_{lc,V})^2} \cdot f(\theta)\right) \\
 &= \epsilon \cdot 10^{39} \exp\left(-\frac{\Delta G_c^{\text{het}}}{k_B T}\right) \tag{3.37}
 \end{aligned}$$

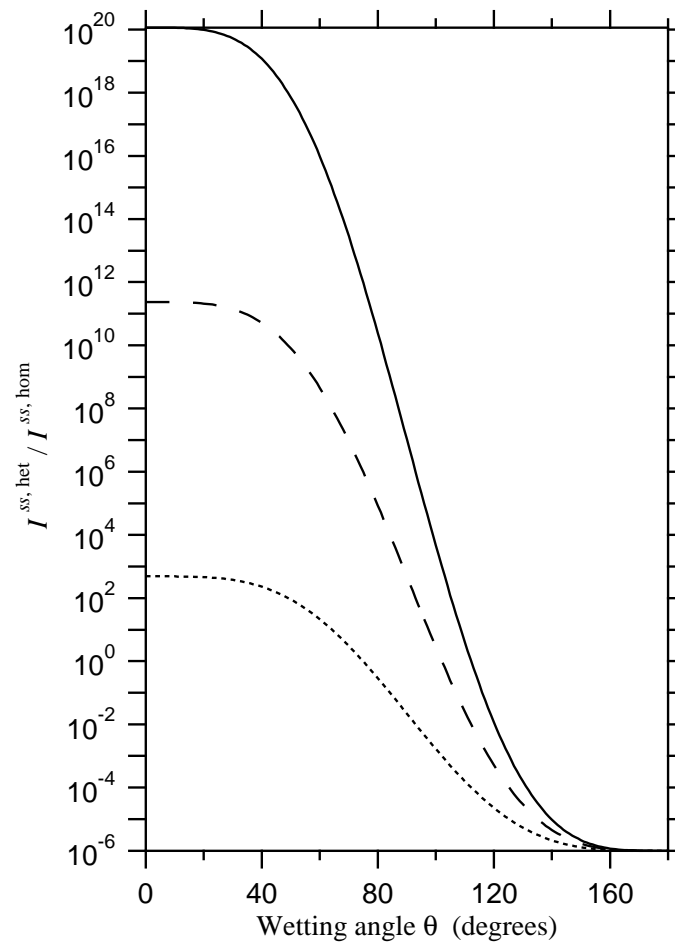


**Figure 3.6:** Ratio of heterogeneous to homogenous nucleation rate  $\frac{I^{ss,het}}{I^{ss,hom}}$  (dimensionless) at constant temperature, calculated from Eqs. (3.38) and (3.26a) for  $\epsilon = 10^{-6}$ . Solid line:  $\Delta G_c = 60k_B T$ . Dashed line:  $\Delta G_c = 40k_B T$ . Dotted line:  $\Delta G_c = 20k_B T$ .

[63, 26, 73, 77]. The ratio of heterogeneous to homogenous nucleation rate (dimensionless) at constant temperature is then for all cases given by

$$\frac{I^{ss,het}}{I^{ss,hom}} = \epsilon \cdot \exp\left(\frac{\Delta G_c}{k_B T} \cdot [1 - f(\theta)]\right). \quad (3.38)$$

Figure 3.6 shows a plot of Eq. (3.38) for a reasonable parameter of  $\epsilon = 10^{-6}$  [26, 73] for three values of the critical work  $\Delta G_c$ . This illustrates the drastic influence of heterogeneities on the nucleation rate by several orders of magnitude.

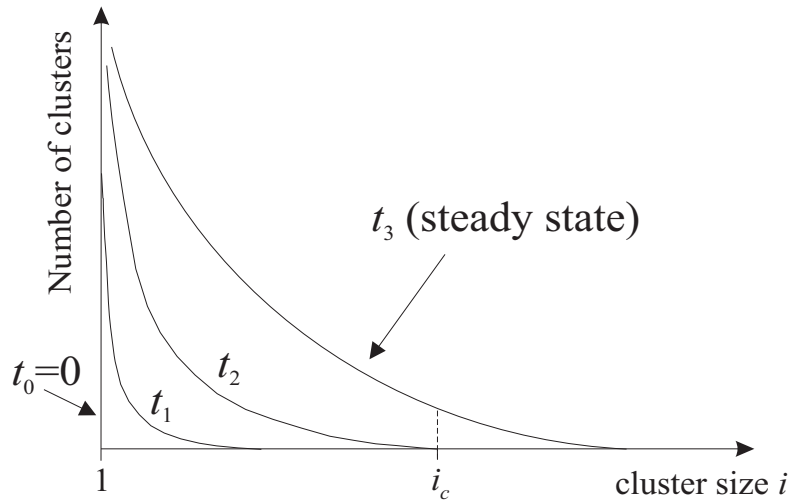


**Figure 3.7:** Statistical cluster distribution function  $N_i$  for transient nucleation for several times steps ( $t_0 = 0 < t_1 < t_2 < t_3$ ) at constant temperature. In an idealized model, only clusters  $C_1$  of size  $i = 1$  (i. e., atoms) are present at  $t = 0$ . As the time increases, clusters  $C_i$  of increasing size develop according to Eq. (3.9). For large times ( $t = t_3$ ), the steady state distribution from the Becker-Döring model (Fig. 3.2) is attained.

### 3.1.3 Transient nucleation

The derivation of the steady state nucleation rate for the homogeneous case [Eq. (3.13)] and the heterogeneous case [Eqs. (3.35)] was based on the assumption of a steady-state distribution of clusters  $N_i^{ss}$ . This does not necessarily have to be the case. Equation (3.9) shows that clusters develop by a sequence of bimolecular reactions. Hence, if the liquid is quickly cooled from above to below the melting point, the steady state cluster distribution  $N_i^{ss}$  has to be established first. The same applies to a glass or an undercooled liquid for which the temperature is suddenly changed since the cluster distribution  $N_i^{ss}$  depends on temperature. Figure 3.7 qualitatively shows the cluster distribution function  $N_i$  for several time steps at isothermal observation<sup>4</sup>.

The nucleation rate is a function of time until the steady state distribution of clusters is attained. This is called *transient nucleation* and is important unless the transient times are short compared to the period of observation. As the nucleation rate depends essentially on the number of critical clusters, there is a characteristic

<sup>4</sup>The superscript ‘ss’ in the distribution function  $N_i$  is omitted now to describe the general case in which the steady state is not necessarily established.

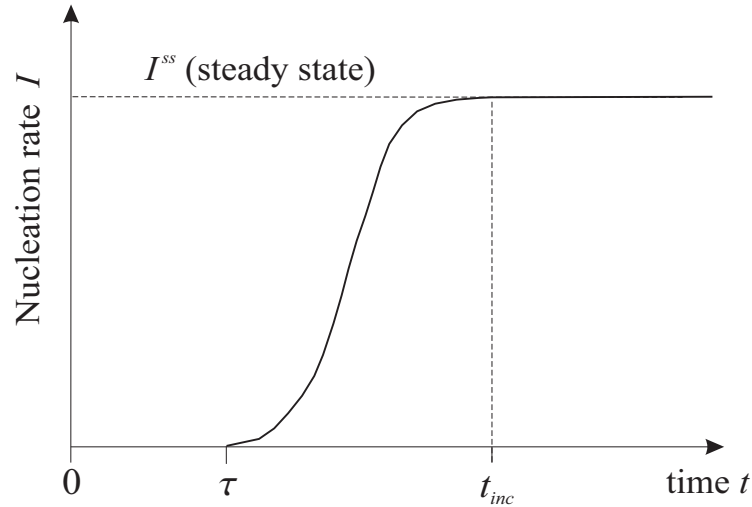


**Figure 3.8:** Time dependence of the nucleation rate. For  $t < \tau$  ( $\tau$ : time lag), no nucleation is observed. The steady state nucleation rate  $I^{ss}$  is attained after the incubation time  $t_{inc}$  has elapsed. Note that  $\tau$  approximately corresponds to  $t_2$  in Fig. 3.7 since the nucleation rate depends essentially on the number of critical clusters. Furthermore,  $t_{inc}$  corresponds to  $t_3$  in Fig. 3.7.

time  $\tau$  before which nucleation cannot be observed experimentally, i. e., before which the probability for a nucleation event within a reasonable sample volume is too low to be observed (Fig. 3.8) [63].  $\tau$  is called the *time lag for nucleation*. Subsequently, for  $\tau < t < t_{inc}$ , nucleation can be observed, and the nucleation rate increases with time until the steady state rate  $I^{ss}$  is attained.  $t_{inc}$  is called the *incubation time for nucleation*<sup>5</sup>.

Transient time constants, like time lag and incubation time, scale with the number of atoms  $i_c$  in the critical cluster [76]. Hence, according to Eq. (3.33), transient times are shorter by a factor of  $f(\theta)$  for heterogeneous nucleation than for homogeneous nucleation.

---

<sup>5</sup>It should be noted that, apart from the expressions ‘time lag’ and ‘incubation time’, other expressions like ‘induction time’ are widely used. Transient time constants are frequently defined variationally. In this work, the transient time constants are only used as defined in Fig. 3.8.

## 3.2 Crystal growth

The nucleation theory describes the formation of stable crystal clusters. Those can grow to macroscopic size. There are two possibilities:

1. For partitionless crystallization, the composition of liquid and crystal are the same at all time. For this case, growth is controlled by rearrangement processes *only* at the liquid-crystalline interface. This growth mode is called *interface-controlled growth* [63]. The rearrangement frequency is then independent of the interface position so that the growth velocity  $u$  is time-independent (Sec. 3.2.1 below).
2. If there is a composition change upon crystallization, *long range* diffusive transport controls the growth velocity because the liquid depletes in certain components close to the liquid-crystalline interface. This depletion becomes more pronounced with increasing time, so that the growth velocity must decrease with time. The corresponding growth mode is called *diffusion-controlled growth* (Sec. 3.2.2 below).

### 3.2.1 Interface-controlled growth

The liquid-crystalline interface moves with the velocity [63, 25]

$$u = f_s \cdot \lambda \cdot k, \quad (3.39)$$

where  $0 \leq f_s \leq 1$  is the fraction of sites where a new atom can be incorporated.  $f_s$  increases with increasing interface roughness: Upon attachment on the crystal surface, an atom finds more energetically favorable sites on a rough interface than on a smooth interface since it can bind to more neighbors in the crystal. This makes a successful attachment more likely.  $\lambda$  is the average interatomic distance (i. e., the distance that the interface moves by each rearrangement).  $k$  is the *net* rearrangement frequency at the interface (net number of atomic transfers across the interface, per atom in the interface and per unit time, dimension:  $\frac{1}{s}$ ):

$$k = k^+ - k^-. \quad (3.40)$$

$k^+$  is the atomic transfer rate from the liquid to the crystalline phase, and  $k^-$  is the corresponding reverse transfer rate from the crystalline to the liquid phase.

If liquid and crystalline phase are in equilibrium (i. e.,  $G_l = G_c$ , where  $G_l$  and  $G_c$  are the free energies of the liquid and crystalline phases, respectively),  $k^+$  is equal to  $k^-$  [Fig. 3.9(a)]. Transition state theory gives [78]:

$$k^+ = k^- = k_0 \exp\left(-\frac{\Delta G^*}{k_B T}\right). \quad (3.41)$$

$\Delta G^*$  is the free energy of activation per atom to the transition state and  $k_0$  is a constant. In a multi-component system, the phase equilibrium  $G_l = G_c$  (under the constraint that liquid and crystal have the *same* composition) is established at a temperature  $T_0$  [43]:

$$\Delta G_{lc}(T_0) \equiv G_l(T_0) - G_c(T_0) = 0. \quad (3.42)$$

In the phase diagram (Sec. 2.1.2), the  $T_0$  line of equal free energy is located between the solidus line  $T_s$  and the liquidus line  $T_l$ . For a single-component system (i. e., an element or a congruently melting compound<sup>6</sup>),  $T_0$  is equal to the melting temperature  $T_m$  [cf. Eq. (2.18)]. Equations (3.39), (3.40), and (3.41) yield

$$u = 0 \quad (T = T_0). \quad (3.43)$$

For  $T < T_0$  [Fig. 3.9(b)],  $G_c$  is lower than  $G_l$  (cf. Fig. 2.9 for a single component system). For this case, transition state theory gives for the forward and reverse rate constants [25, 78]

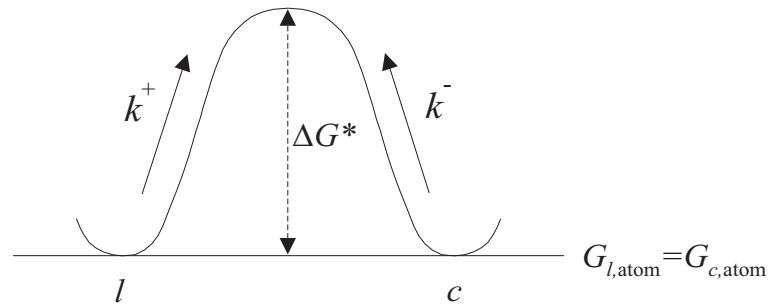
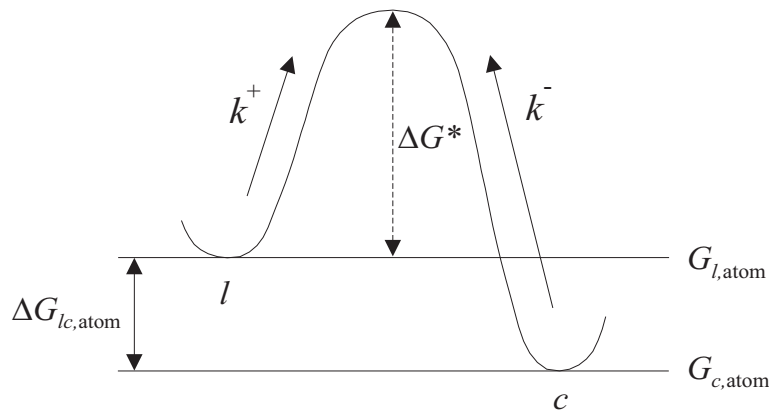
$$\begin{aligned} k^+ &= k_0 \exp\left(-\frac{\Delta G^*}{k_B T}\right), \\ k^- &= k_0 \exp\left(-\frac{\Delta G^* + |\Delta G_{lc,atom}|}{k_B T}\right) \\ &= k^+ \exp\left(-\frac{|\Delta G_{lc,atom}|}{k_B T}\right), \end{aligned} \quad (3.44)$$

where  $\Delta G_{lc,atom}$  is the difference in free energy between the liquid and crystalline phase *per atom*. Therefore, the net transfer rate is

$$\begin{aligned} k &= k^+ - k^- \\ &= k^+ \left[1 - \exp\left(-\frac{|\Delta G_{lc,atom}|}{k_B T}\right)\right], \end{aligned} \quad (3.45)$$

---

<sup>6</sup>A compound is said to melt *congruently* if the liquid formed upon melting in equilibrium has the same composition as the solid from which it was formed [18]. Hence, melting does not occur over a temperature range but at a single melting temperature  $T_m$  for this case.

(a)  $T = T_0$ (b)  $T < T_0$ 

**Figure 3.9:** Free energy  $G$  per atom versus position across the liquid-crystalline interface for interface-controlled growth.  $l$ : liquid phase;  $c$ : crystalline phase;  $G_{l,atom}$ : free energy of the liquid per atom;  $G_{c,atom}$ : free energy of the crystal per atom;  $\Delta G^*$ : free energy of activation per atom to the transition state;  $k^+$  and  $k^-$ : forward and reverse rate constants for atomic transfer across the interface (per atom in the interface per unit time).

and hence, the crystal growth velocity is [Eq. (3.39)]

$$u = f_s \cdot \lambda \cdot k^+ \left[ 1 - \exp \left( -\frac{|\Delta G_{lc,atom}|}{k_B T} \right) \right] \quad (T < T_0). \quad (3.46)$$

The value of the forward rate constant  $k^+$  in Eq. (3.46) depends on the type of crystallization kinetics (diffusion-limited crystallization versus collision-limited crystallization, Sec. 3.1.1.4) and is the same as for nucleation:

$$k^+ \equiv k_{i_c}^+, \quad (3.47)$$

where  $k_{i_c}^+$  is given in Eqs. (3.17) and (3.23) for the corresponding type of kinetics. This is discussed in detail in the following subsections.

### 3.2.1.1 Diffusion-limited crystallization

For diffusion-limited crystallization,  $k^+$  and  $k^-$  can be identified as the rates of thermally activated *diffusive jumps* across the interface. The growth velocity is obtained from Eqs. (3.46), (3.47) and (3.17):

$$u = f_s \cdot \frac{6D}{\lambda} \left[ 1 - \exp \left( -\frac{|\Delta G_{lc,atom}|}{k_B T} \right) \right] \quad (T < T_0) \quad (3.48)$$

[63, 25]. Using the Stokes-Einstein equation [Eq. (2.3)], this gives

$$u = f_s \cdot \frac{2k_B T}{\eta \pi \lambda^2} \left[ 1 - \exp \left( -\frac{|\Delta G_{lc,atom}|}{k_B T} \right) \right] \quad (T < T_0). \quad (3.49)$$

Close to  $T_0$ ,  $u$  is dominated by the term  $\left[ 1 - \exp \left( -\frac{|\Delta G_{lc,atom}|}{k_B T} \right) \right]$ , since  $\Delta G_{lc}(T_0) = 0$ . For this case, the exponential can be approximated to

$$\left[ 1 - \exp \left( -\frac{|\Delta G_{lc,atom}|}{k_B T} \right) \right] \approx \frac{|\Delta G_{lc,atom}|}{k_B T} \quad (T \approx T_0). \quad (3.50)$$

Hence, Eq. (3.49) simplifies to

$$u = f_s \cdot \frac{2k_B T}{\eta \pi \lambda^2} \cdot \frac{|\Delta G_{lc,atom}|}{k_B T} \quad (T \approx T_0). \quad (3.51)$$

Close to the glass transition temperature  $T_g$ ,  $u$  is dominated by the diffusive jump term  $6D/\lambda$ , which slows down rapidly as  $T_g$  is approached (equivalently, the viscosity rapidly increases, cf. Fig. 2.4). Hence,  $u$  exhibits a maximum between  $T_g$  and  $T_0$ , which is usually located at higher temperature than the maximum for the nucleation rate [Eq. (3.22)].

### 3.2.1.2 Collision-limited crystallization

For collision-limited crystallization, the growth velocity is obtained from Eqs. (3.46), (3.47) and (3.23):

$$u = f_s \cdot u_{\text{sound}} \left[ 1 - \exp \left( -\frac{|\Delta G_{lc, \text{atom}}|}{k_B T} \right) \right] \quad (T < T_0) \quad (3.52)$$

[25]. As for collision-limited *nucleation* (Sec. 3.1.1.4.2), collision-limited *growth* applies to the situation where atomic neighbors do not have to change by diffusive rearrangements upon crystallization, which is rarely the case for alloys or compounds. Collision-limited growth proceeds far more quickly than diffusion-limited growth since an atomic motion proceeds over a distance much less than an interatomic spacing and since a cooperative movement of neighboring atoms (as in diffusion) is not necessary.

The term  $\left[ 1 - \exp \left( -\frac{|\Delta G_{lc, \text{atom}}|}{k_B T} \right) \right]$  in Eq. (3.52) varies between unity at  $T = 0$  and zero at  $T = T_0$ . Hence, the growth velocity does not exhibit a maximum as for diffusion-limited growth but continuously increases upon cooling with increasing driving force  $\Delta G_{lc}$ . For pure metals,  $f_s$  is usually close to 1. Therefore, the ultimate limit for the crystal growth velocity is the sound velocity  $u_{\text{sound}}$  in the liquid.

### 3.2.2 Diffusion-controlled growth

If growth is controlled by *long-range* diffusion (diffusion-controlled growth), the growth velocity is parabolic in time, which can be seen from dimensional analysis of the diffusion equation [79]

$$\frac{\partial n_i}{\partial t} = D \left( \frac{\partial^2 n_i}{\partial x^2} + \frac{\partial^2 n_i}{\partial y^2} + \frac{\partial^2 n_i}{\partial z^2} \right), \quad (3.53)$$

where  $n_i$  is the concentration of a component  $i$ . The dimension of the diffusivity  $D$  is  $\frac{\text{m}^2}{\text{s}}$ . The component concentrations  $n_i$  enter into growth equations only in dimensionless combination because the diffusion equation and its boundary conditions are homogeneous in  $n_i$  [63]. Other quantities are not involved in Eq. (3.53). Under the simplifying assumption that the diffusivity  $D$  is the same for all components, a diffusion distance must be proportional to  $(Dt)^{1/2}$ . Therefore, the interface position is proportional to  $(Dt)^{1/2}$  as well, and hence, the growth velocity (the time derivative of the interface position) must be proportional to  $(D/t)^{1/2}$ .

### 3.3 Isothermal transformation curves

For isothermal crystallization of an undercooled liquid or an amorphous solid, Johnson and Mehl [80] and Avrami [81, 82, 83] derived a model that relates the three (time-dependent) quantities crystal nucleation rate  $I$ , crystal growth velocity  $u$ , and crystallized material fraction  $\chi$  ( $0 \leq \chi \leq 1$ ) at constant temperature  $T$  [63]. Using this model, any of those quantities can be accurately calculated as a function of time from the knowledge of the complete time dependence of the other two quantities. The problem is entirely geometrical.

The Johnson-Mehl-Avrami- (JMA-) model does not only apply to crystal nucleation but can be applied to any phase transformation that encompasses nucleation and growth. The parent phase can have an arbitrary (spatial) dimension. Section 3.3.1 assumes a dimension of 3 for the parent phase to provide a model for homogeneous nucleation. Section 3.3.2 assumes a dimension of 2 for the parent phase to provide a model for heterogenous nucleation at the 2-dimensional surface of the parent phase.

#### 3.3.1 Three-dimensional analysis

Let  $V$  be the total 3-dimensional volume of the parent phase (here: a liquid or an amorphous solid) before the beginning of the transformation. Within the parent phase, the daughter phase (here: crystal) nucleates and grows. For simplicity, any density change upon crystallization is neglected. The total volume of the liquid (or amorphous) phase at time  $t$  is denoted by  $V^l(t)$ , and the total volume of the crystalline phase by  $V^c(t)$ . Hence,

$$V = V^l(t) + V^c(t) = \text{const} . \quad (3.54)$$

The initial conditions at  $t = 0$  are then  $V^l(0) = V$  and  $V^c(0) = 0$ . Complete crystallization implicates  $V^l(\infty) = 0$  and  $V^c(\infty) = V$ . The number of the *new* crystals  $dN$  nucleated between time  $t'$  and  $t' + dt'$  is given by [63]

$$dN = I(t')V^l(t')dt' , \quad (3.55)$$

where  $I(t')$  is the crystal nucleation rate at time  $t'$  (number of new crystals per unit volume and unit time, dimension:  $\frac{1}{\text{m}^3\text{s}}$ ). On the right side of Eq. (3.55), the volume  $V^l$  (not  $V$ ) is used because crystals can only nucleate in the untransformed volume  $V^l$ .

Therefore, the transformed volume  $dV^c$  at time  $t$  resulting from regions nucleated between  $t'$  and  $t' + dt'$  is

$$dV^c = v(t, t')I(t')V^l(t')dt', \quad (3.56)$$

where  $v(t, t')$  is the volume of a crystal at time  $t$  that nucleated at time  $t'$ . For spherical crystals and for a time-independent crystal growth velocity  $u$  (interface-controlled growth<sup>7</sup>, Sec. 3.2.1),  $v(t, t')$  is given by

$$v(t, t') = v(t - t') = \begin{cases} 0 & (t < t') \\ \frac{4\pi}{3}u^3(t - t')^3 & (t > t') \end{cases}. \quad (3.57)$$

During the initial part of the transformation, it is valid  $V^l \approx V$ . Therefore, the crystallized volume fraction  $\chi = \frac{V^c}{V}$  can be obtained by integration [63]:

$$\begin{aligned} \chi(t) = \frac{V^c(t)}{V} &= \int_0^t v(t, t')I(t')dt' \\ &= \frac{4\pi}{3}u^3 \int_0^t (t - t')^3 I(t')dt' \quad (\chi \ll 1). \end{aligned} \quad (3.58)$$

This expression is incorrect for a later stage of the transformation, i. e., when crystals start to impinge each other and when  $V^l$  becomes remarkably smaller than  $V$ . This more general case can be treated as follows: Between time  $t'$  and  $t' + dt'$ , when  $I(t')V^l(t')dt'$  new crystals nucleate in the volume  $V^l$ , an additional number  $I(t')V^c(t')dt'$  would nucleate in the already transformed volume  $V^c$  if crystallization had not occurred there already. Avrami described those as *phantom nuclei* and proposed the definition of an *extended volume*  $V_e^c$  [63]

$$\begin{aligned} dV_e^c(t') &= v(t, t')I(t')V^l(t')dt' + v(t, t')I(t')V^c(t')dt' \\ &= v(t, t')I(t')[V^l(t') + V^c(t')]dt' \\ &= v(t, t')I(t')V dt'. \end{aligned} \quad (3.59)$$

Integration yields

$$\begin{aligned} V_e^c &= V \int_0^t v(t, t')I(t')dt' \\ &= \frac{4\pi V}{3}u^3 \int_0^t (t - t')^3 I(t')dt'. \end{aligned} \quad (3.60)$$

---

<sup>7</sup>The analysis would also work for an arbitrary time dependence of the crystal growth velocity. However, this is not considered here for simplicity.

$V_e^c$  differs by the real transformed volume  $V^c$  in two respects:

- Phantom nuclei, which nucleate in the already transformed volume, are included in  $V_e^c$  but not in  $V^c$ .
- In the expression for  $V_e^c$ , all crystals are treated as if they were growing ‘through’ each other, no matter if crystallization had already occurred there.

Hence, the extended volume includes transformed volume elements multiple times, so that  $V_e^c > V^c$  ( $V_e^c = V^c$  at the beginning of the transformation, when  $\chi \ll 1$ ).

A relation between  $V_e^c$  and  $V^c$  has to be found as a function of time: In any *random* region, a volume fraction  $(1 - \frac{V^c}{V}) = 1 - \chi$  is untransformed at time  $t'$ . Subsequently, between  $t'$  and  $t' + dt'$ , the true volume increases by  $dV^c$  and the extended volume by  $dV_e^c$ . Hence, a fraction  $(1 - \frac{V^c}{V})$  of the new volume elements that contribute to  $dV_e^c$  will *on average* lie in previously untransformed material and will therefore contribute to  $dV^c$ . Therefore [63],

$$dV^c = \left(1 - \frac{V^c}{V}\right) dV_e^c. \quad (3.61)$$

It is important to emphasize that Eq. (3.61) is only valid if nucleation centers are distributed *randomly* over the entire volume  $V$  of the liquid. Equation (3.61) does not apply if nucleation occurs at preferred sites that are not randomly distributed. Integrating Eq. (3.61) yields

$$V_e^c = -V \ln \left(1 - \frac{V^c}{V}\right). \quad (3.62)$$

Equating Eqs. (3.60) and (3.62) then yields

$$V \int_0^t v(t, t') I(t') dt' = -V \ln \left(1 - \frac{V^c}{V}\right) \quad (3.63)$$

and hence

$$\chi(t) = \frac{V^c(t)}{V} = 1 - \exp \left[ - \int_0^t v(t, t') I(t') dt' \right]. \quad (3.64)$$

Using Eq. (3.57), this yields then

$$\chi(t) = 1 - \exp \left[ - \frac{4\pi}{3} u^3 \int_0^t (t - t')^3 I(t') dt' \right]. \quad (3.65)$$

For small times (when  $\chi \ll 1$ ), the exponential can be approximated as  $\exp(-x) = 1 - x$ , and Eq. (3.65) reduces to Eq. (3.58).

Equation (3.65) can only be computed if the time dependence of the nucleation rate  $I$  is known. However, for three special time dependencies of  $I$ , Eq. (3.65) can be rewritten in the simplified form

$$\chi(t) = 1 - \exp[-(kt)^n], \quad (3.66)$$

where  $k$  is the Avrami rate constant and  $n$  the Avrami exponent.

In the first case,  $I$  is constant in time (steady-state nucleation), i. e.,

$$I(t') = I_0. \quad (3.67a)$$

This yields an Avrami exponent of  $n = 4$ :

$$\begin{aligned} \chi(t) &= 1 - \exp\left[-\frac{4\pi}{3}u^3I_0 \int_0^t (t-t')^3 dt'\right] \\ &= 1 - \exp\left[-\underbrace{\frac{\pi u^3 I_0}{3}}_{=k^4} \cdot t^4\right]. \end{aligned} \quad (3.67b)$$

In the second case,  $N_0$  crystals nucleate at time  $t = 0$  (per unit volume, dimension of  $N_0 : \frac{1}{\text{m}^3}$ ). For  $t > 0$ , no nucleation occurs. The corresponding nucleation rate is

$$I(t') = N_0 \cdot \delta(t'). \quad (3.68a)$$

This gives an Avrami exponent of  $n = 3$ :

$$\begin{aligned} \chi(t) &= 1 - \exp\left[-\frac{4\pi}{3}u^3N_0 \int_0^t \delta(t')(t-t')^3 dt'\right] \\ &= 1 - \exp\left[-\underbrace{\frac{4\pi}{3}u^3N_0}_{=k^3} \cdot t^3\right]. \end{aligned} \quad (3.68b)$$

In the third case,  $I(t')$  exhibits a time dependence according to

$$I(t') = I_0 \cdot \left(\frac{t'}{s}\right)^{\hat{n}}. \quad (3.69a)$$

**Table 3.1:** Values of the Avrami exponent  $n$  in Eq. (3.66) for different time dependencies of the nucleation rate  $I$  for interface-controlled growth. The parameter  $d$  denotes the spatial dimension that the model is constrained to.  $d = 3$  serves as a model for homogeneous nucleation in a 3-dimensional parent phase.  $d = 2$ , in contrast, applies to heterogeneous nucleation at the 2-dimensional surface of the parent phase.

Conditions	$d = 3$	$d = 2$
$I$ increases with time	$n > 4$	$n > 3$
$I$ is time-independent	$n = 4$	$n = 3$
$I$ decreases with time	$n = 3 - 4$	$n = 2 - 3$
Crystals only nucleate at $t = 0$ (saturation of sites)	$n = 3$	$n = 2$

$I_0$  is a time-independent (but temperature-dependent) prefactor (dimension:  $\frac{1}{\text{m}^3\text{s}}$ ), and  $s$  denotes the dimension ‘second’.  $\hat{n}$  can be any real number greater than  $(-1)$ :

$$\hat{n} > -1. \quad (3.69b)$$

Hence,  $I(t')$  in Eq. (3.69a) increases with time for  $\hat{n} > 0$  (this may be a very crude model for transient nucleation) and decreases with time for  $-1 < \hat{n} < 0$ . For  $\hat{n} = 0$ , Eq. (3.69a) reduces to Eq. (3.67a). The nucleation rate given in Eq. (3.69a) yields an Avrami exponent of  $n = 4 + \hat{n}$ :

$$\begin{aligned} \chi(t) &= 1 - \exp \left[ -\frac{4\pi}{3} u^3 I_0 \int_0^t \left( \frac{t'}{s} \right)^{\hat{n}} (t - t')^3 dt' \right] \\ &= 1 - \exp \left[ -\frac{4\pi}{3} u^3 I_0 \underbrace{\frac{6}{(1 + \hat{n})(2 + \hat{n})(3 + \hat{n})(4 + \hat{n})s^{\hat{n}}}}_{=k^{4+\hat{n}}} \cdot t^{4+\hat{n}} \right]. \quad (3.69c) \end{aligned}$$

Table 3.1 summarizes the values of the Avrami exponent  $n$  for the different time dependencies of the nucleation rate  $I(t')$ .

### 3.3.2 Two-dimensional analysis

If the spatial dimension of the parent phase is 2, the derivation of the model is entirely analogous to Sec. 3.3.1. 3-dimensional volumes have to be replaced by 2-dimensional surfaces, e. g., spherical crystals are replaced by circular crystals. For interface-controlled growth, the ‘area’  $a$  of a circular crystal at time  $t$  that nucleated at time  $t'$  is in analogy to Eq. (3.57) given by

$$a(t, t') = a(t - t') = \begin{cases} 0 & (t < t') \\ \pi u^2 (t - t')^2 & (t > t') \end{cases}. \quad (3.70)$$

Under the assumption that the (heterogeneous) nucleation sites are distributed *randomly* at the surface of the parent phase, the crystallized *surface* fraction  $\chi(t)$  is then in analogy to Eq. (3.65) given by

$$\chi(t) = 1 - \exp \left[ -\pi u^2 \int_0^t (t - t')^2 I(t') dt' \right], \quad (3.71)$$

where  $I(t')$  is the *surface* nucleation rate (number of nucleated crystals per unit *area* per unit time, dimension:  $\frac{1}{\text{m}^2\text{s}}$ ).

In analogy to Sec. 3.3.1, Eq. (3.71) can be reduced to the simplified form

$$\chi(t) = 1 - \exp [-(kt)^n] \quad (3.72)$$

for three special time dependencies of  $I(t')$ .

In the first case,  $I$  is constant in time (steady-state nucleation), i. e.,

$$I(t') = I_0. \quad (3.73a)$$

This yields an Avrami exponent of  $n = 3$ :

$$\begin{aligned} \chi(t) &= 1 - \exp \left[ -\pi u^2 I_0 \int_0^t (t - t')^2 dt' \right] \\ &= 1 - \exp \left[ - \underbrace{\frac{\pi u^2 I_0}{3}}_{=k^3} \cdot t^3 \right]. \end{aligned} \quad (3.73b)$$

In the second case,  $N_0$  crystals are nucleated at time  $t = 0$  (per unit volume, dimension of  $N_0$  :  $\frac{1}{\text{m}^2}$ ). For  $t > 0$ , no nucleation occurs. This case corresponds to a

simultaneous exhaustion of heterogeneous nucleation sites at  $t = 0$ . The corresponding nucleation rate is

$$I(t') = N_0 \cdot \delta(t'). \quad (3.74a)$$

This gives an Avrami exponent of  $n = 2$ :

$$\begin{aligned} \chi(t) &= 1 - \exp \left[ -\pi u^2 N_0 \int_0^t \delta(t') (t - t')^2 dt' \right] \\ &= 1 - \exp \left[ -\underbrace{\pi u^2 N_0}_{=k^2} \cdot t^2 \right]. \end{aligned} \quad (3.74b)$$

In the third case,  $I(t')$  exhibits a time dependence according to

$$I(t') = I_0 \cdot \left( \frac{t'}{s} \right)^{\hat{n}}. \quad (3.75a)$$

$I_0$  is a time-independent (but temperature-dependent) prefactor (dimension:  $\frac{1}{\text{m}^2\text{s}}$ ), and  $s$  denotes the dimension ‘second’.  $\hat{n}$  can be any real number greater than (-1). The nucleation rate given in Eq. (3.75a) yields an Avrami exponent of  $n = 3 + \hat{n}$ :

$$\begin{aligned} \chi(t) &= 1 - \exp \left[ -\pi u^2 I_0 \int_0^t \left( \frac{t'}{s} \right)^{\hat{n}} (t - t')^2 dt' \right] \\ &= 1 - \exp \left[ -\pi u^2 I_0 \underbrace{\frac{2}{(1 + \hat{n})(2 + \hat{n})(3 + \hat{n})s^{\hat{n}}}}_{=k^{3+\hat{n}}} \cdot t^{3+\hat{n}} \right]. \end{aligned} \quad (3.75b)$$

Table 3.1 summarizes the values of the Avrami exponent  $n$  for the different time dependencies of the nucleation rate  $I(t')$ .



# Chapter 4

## Scientific instruments

This chapter reviews the scientific instruments used throughout this work. The purpose of this review is to give a simple but concise overview. For more detailed information, the reader may be referred to the extensive literature available for each instrument. The description is not product-related, and also not related to the purpose for which an individual instrument is used in this work. This is described in detail in the ‘Experimental methods’ sections in the subsequent chapters.

### 4.1 The sputter chamber

A sputter chamber is used to deposit thin films (thickness range: between a few nanometers and a few micrometers) of *precise* and *specified* composition. This process is called *sputter deposition*.

A vacuum chamber (Fig. 4.1) is pumped down to low pressure and back filled with a usually inert gas (frequently: Ar). A small fraction of the Ar atoms are ionized by random processes (collisions between atoms or interactions with cosmic radiation). A large negative voltage with respect to the chamber (usually a few hundred volts) is applied to the water-cooled ‘target’, which consists of the material that needs to be deposited. The Ar ions are attracted by the target and dislodge target atoms upon impingement. Those ‘sputtered’ atoms are ejected from the target due to the momentum transfer. As they are not in their thermodynamic equilibrium state, they tend to condense back into the solid state upon collision with any surface. This results

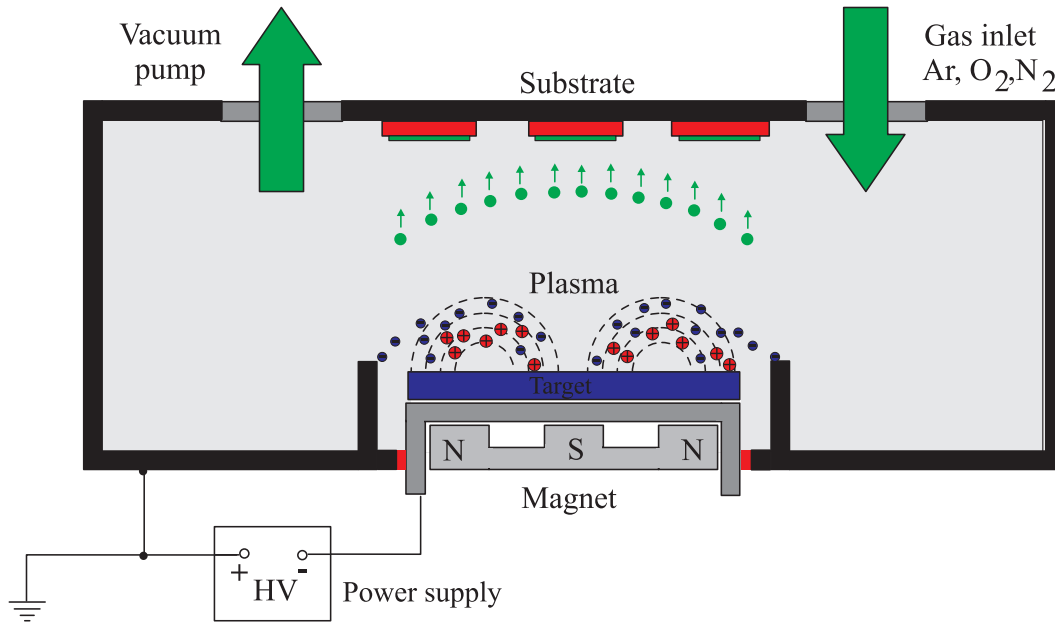


**Figure 4.1:** (Color). Schematic view of a magnetron sputter chamber. Substrates (red) are located above the sputter target (blue). Red circles: Positively charged ionized molecules (frequently: Ar, O<sub>2</sub>, or N<sub>2</sub>). Blue circles: electrons. Green circles: sputtered atoms.

in deposition of the sputtered material on all surfaces inside the chamber, including the substrates for film deposition, which are located opposite the target (Fig. 4.1).

In order to obtain a noteworthy deposition rate, the number of Ar ions in the chamber needs to be significantly larger than the small number produced by random processes. Increasing the Ar pressure would increase the number of Ar ions, but as a secondary effect, the sputtered atoms would be scattered at the Ar atoms more frequently, which would lower the deposition rate again. Additionally, a higher Ar pressure would increase the number of Ar atoms incorporated in the film. The large number of Ar ions required for an efficient sputter process is supplied by an Ar plasma that is created by a *steady state* electric glow discharge inside the sputter chamber during the sputter process: Upon the impingement of an Ar ion at the sputter target, not only atoms, but also electrons, are ejected. Due to the negative target voltage, those electrons are accelerated away from the target and ionize more Ar atoms by collisions. A magnet is located underneath the target to constrain the electrons on cyclotron paths. This lengthens the electron path and increases the number of ionization processes close

to the target ('magnetron sputtering').

If the applied voltage is a direct current (DC) voltage, only electrically conducting materials can be sputtered. Otherwise, the target surface would be electrically charged by the impinging Ar ions, which would create an electric field that acts opposite to the externally applied voltage. Insulators can be sputtered by using a radio frequency (RF) voltage instead of the DC voltage. This allows a periodic charge compensation on the target surface by collection of electrons in the plasma.

Usually, the sputter deposition is performed at room temperature. The substrates can be either fixed above the target (static sputtering) or moved periodically above an aperture that is located above the target (dynamic sputtering). While the former process yields higher deposition rates, the latter process yields a more homogeneous film thickness.

The advantage of magnetron sputtering versus other deposition techniques is that the composition of the prepared films is the same as that of the target. Hence, the composition can usually be specified precisely. Moreover, sputtering can be used to deposit large areas, and the target material can have a high melting temperature. Additionally, films of low surface roughness can be prepared.

## 4.2 The differential scanning calorimeter (DSC)

A differential scanning calorimeter (DSC) is a thermoanalytical instrument in which the *difference* between the amount of heat required to increase the temperature of a sample and that of a reference system are measured as a function of temperature. In the power-compensated design, sample and reference are heated in two *separate* but ideally identical furnaces<sup>1</sup> (Fig. 4.2). Those furnaces keep the sample and the reference holders at the *same* temperature throughout the experiment, which is performed either at constant heating rate or isothermally. If the sample undergoes a thermal transformation (either exothermic or endothermic), more or less heat will need to flow into the sample holder than into the reference holder to maintain both holders at the same

---

<sup>1</sup>A heat-flux design is also widely used, in which sample and reference are heated in the *same* furnace on a common heat-conducting plate. This design is similar to the DTA described in Sec. 4.3 but is not described in this section because it is not used in this work.

temperature. The reference should not undergo a transformation in the temperature range of interest<sup>2</sup>. This way, the heat of transformation and the corresponding transition temperature of the sample can be measured. The measured signal  $\delta\dot{H}$  at constant heating rate  $\dot{T}$  is

$$\begin{aligned}\delta\dot{H}(T) &:= \dot{H}_s(T) - \dot{H}_r(T) \\ &= C_{p,s}(T) \cdot \dot{T} + \dot{H}_{\text{trans}}(T) - C_{p,r}(T) \cdot \dot{T} + \dot{H}_{\text{base}}(T).\end{aligned}\quad (4.1)$$

$\dot{H}_s = dH_s/dt$  and  $\dot{H}_r = dH_r/dt$  ( $H$ : enthalpy) is the heat flow into the sample holder and reference holder, respectively (in units of power).  $C_{p,s}$  and  $C_{p,r}$  are the heat capacity at constant pressure of the sample and reference, respectively.  $\dot{H}_{\text{trans}}$  is the heat flow into the *sample* associated with a thermal transformation. For exothermic transformations, it is  $\dot{H}_{\text{trans}} > 0$ , and for endothermic transformations  $\dot{H}_{\text{trans}} < 0$ . If no transformation occurs,  $\dot{H}_{\text{trans}} = 0$ . The term  $\dot{H}_{\text{base}}$  represents a temperature dependent baseline that depends on the different heat loss coefficients and heat capacities of the two holders and pans (which are in practice never entirely identical). A thermal transformation (e. g., melting or crystallization) is therefore indicated by a peak in the measured heat flow signal due to the term  $\dot{H}_{\text{trans}}$ . The heat of transformation  $\Delta H_{\text{trans}}$  (in units of energy) is then obtained by the area enclosed by the peak and the interpolated baseline ( $[C_{p,s} - C_{p,r}]\dot{T} + \dot{H}_{\text{base}}$ ):

$$\Delta H_{\text{trans}} = \int_{\text{peak}} \dot{H}_{\text{trans}} dt = \int_{\text{peak}} \dot{H}_{\text{trans}} \frac{dT}{\dot{T}}. \quad (4.2)$$

The term  $(\dot{H}_{\text{base}} - C_{p,r}\dot{T})$  in Eq. (4.1) can be obtained from a calibration experiment [84, 85, 86, 87], so that the heat capacity  $C_{p,s}$  of the sample can also be measured in those temperature ranges where no thermal transformation occurs (i. e., where  $\dot{H}_{\text{trans}} = 0$ ).

During continuous heating, the glass transition temperature  $T_g$  of an amorphous sample can be measured due to the enthalpy change associated with structural relaxation (Fig. 2.7), which occurs rapidly around  $T_g$ . If the sample does not crystallize, the difference in heat capacity between undercooled liquid and amorphous phase (Fig. 2.6) is a further indication for the glass transition.

---

<sup>2</sup>Frequently, no reference material is used, i. e., the pan in the reference furnace remains empty.

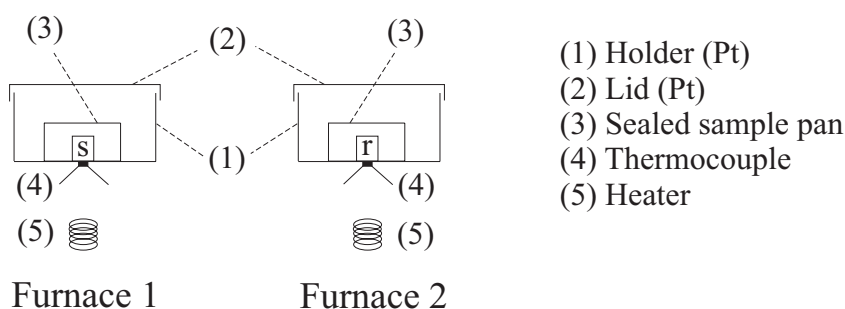


**Figure 4.2:** Schematic view of the two (ideally identical) furnaces in a power-compensated differential scanning calorimeter (DSC). Sample material ‘s’ and reference material ‘r’ are placed in a (usually sealed) sample pan, which is itself placed in a Pt holder. A thermocouple is attached to the lower side of each Pt holder to control a feedback loop that maintains sample and reference holder at the same temperature throughout the entire experiment.

Because of the small furnace volume and mass (usually less than  $1 \text{ mm}^3$  and about 1 g for each furnace in the power-compensated design), the DSC is highly sensitive both in terms of temperature and heat flow measurement. The response of the system to changes in the heating rate is also very fast as a result of the small furnace size (time constant: a few seconds). Due to the temperature gradient between the thermocouple and the sample (as a result of a non-zero distance, Fig. 4.2), the DSC has to be calibrated as a function of heating (or cooling) rate [84, 85, 86, 87].

The maximum temperature in a power-compensated DSC is usually around 700–750°C, limited by the sensitivity of the electronics. For temperatures lower than around 600°C, Al sample pans are usually used [item (3) in Fig. 4.2]. Al melts at around 660°C, and reactions between the Pt holder [item (1) in Fig. 4.2] and the Al pan can occur above 600°C. Therefore, Pt, Au, Cu, graphite, or ceramic sample pans are usually used above 600°C. The latter two cannot be sealed and are therefore not suitable for volatile samples.

### 4.3 The differential thermal analyzer (DTA)

The differential thermal analyzer (DTA) shares much in common with the DSC and provides similar information. The main difference is that sample and reference are heated in a *common* furnace, which is usually more than a hundred times larger and

heavier than one of the power-compensated DSC furnaces. Both sample and reference holder are equipped with a separate thermocouple. In this design, sample and reference holder are not constrained to have the same temperature during the experiment. Upon heating at a constant heating rate (or in an isothermal experiment), a thermal process in the sample causes a difference in temperature between sample and reference due to the transfer of the heat of transformation to or from the sample. A calibration with materials for which the heat of transformation is well known [84, 85, 86, 87] is used to convert the temperature difference to heat flow.

Some differential thermal analyzers include a thermogravimeter (TG). The TG measures the mass of both sample and reference holder during heating. This allows a detection of a mass loss as a consequence of, e. g., evaporation. An exhaust attached to the furnace can drain the vapor.

The advantage of the DTA over the DSC is that it allows significantly higher temperatures (1000–1500 °C depending on the model) because it is much simpler than the DSC: Due to the large furnace size, the temperature sensitive electronics can be insulated better from the heat source. The DTA (but not the DSC) is also ideal to study volatile samples since the evaporation cannot harm the electronics due to their large separation from the sample. In the DSC, volatile samples would additionally contaminate the *sample furnace*, but not the *reference furnace*. Hence, the two furnaces in the DSC would not be identical any more, which induces strong baseline curvatures [last term in Eq. (4.1)] and therefore hampers the detection of small signals. The disadvantage of the DTA is, however, that the heat flow measurement is significantly less precise than in the DSC because the heat flow is not measured *directly* as in the power-compensated DSC. On the other hand, the *temperature* measurement in the DTA is equally precise as in the DSC. Another disadvantage of the DTA is that it reacts much slower to a heating rate change than the DSC (time constant: a few minutes). The DSC is therefore preferred over the DTA whenever this is possible in terms of experimental conditions.

A more detailed introduction to DSC, DTA, and TG can be found, e. g., in the textbooks in Refs. [88, 89].

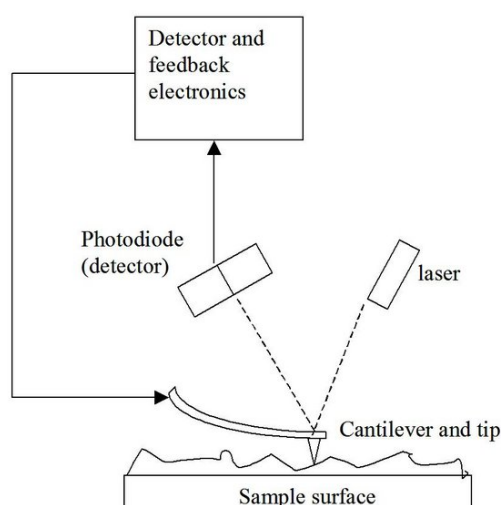


**Figure 4.3:** Measurement principle of an atomic force microscope (AFM).

## 4.4 The atomic force microscope (AFM)

The atomic force microscope (AFM) can reconstruct the three-dimensional topography of a sample surface in nanometer resolution. The sample has to be very flat, i. e., the height difference between the lowest and highest point must not be greater than a few micrometers.

Two piezoelectric scanners are used to scan the cantilever in lateral (x and y) direction over the sample (Fig. 4.3). A very fine tip is located underneath the cantilever to scan the topography. A laser is reflected at the back side of the cantilever towards a position-sensitive split photodiode detector that measures the deflection of the cantilever, which is related to the topography. A feedback loop controls a third piezoelectric scanner to re-adjust the height of the cantilever (z coordinate).

Two operational modes are most frequently used:

**Contact mode (constant force mode):** The tip is in continuous contact with the sample surface during scanning. The feedback loop maintains a constant cantilever deflection ('setpoint') and therefore a constant force on the sample. For instance, a hillock on the surface would induce a larger force and therefore a stronger deflection. The feedback loop however counteracts by lifting the scanner by the height of the hillock. Similarly, the feedback loop lowers the scanner by a

distance equal to the depth of a depression. Hence, the movement of the scanner exactly reproduces the surface topography. Silicon nitride cantilevers are usually used for contact mode.

**Tapping mode (constant amplitude mode):** The cantilever is oscillated vertically (normal to the sample surface) by an external periodic force at or near its resonance frequency of about 300 kHz. The oscillation amplitude typically ranges between 20 and 100 nm. The tip ‘taps’ on the sample surface at each oscillation minimum, which leads to a damping of its oscillation amplitude. The feedback loop maintains this amplitude (‘setpoint’) at a constant level and therefore, the movement of the scanner reproduces the surface topography as in contact mode: If a *hillock* occurs, the scanner *lifts* the cantilever to prevent an amplitude decrease due to an *increased* damping. On the other hand, if a *depression* occurs, the scanner *lowers* the cantilever to prevent an amplitude *increase* due to a *decreased* damping. For tapping mode, the cantilever and the tip are usually an integrated assembly of single crystal silicon.

The advantage of contact mode is that it can yield atomic resolution. Moreover, mechanical properties of the sample can be measured. However, the disadvantage of this mode is that the tip can damage (scrape) soft samples easily. Hence, contact mode is usually only used for hard samples.

Tapping mode can be used for softer samples because it applies marginal (usually non-damaging) forces to the sample, still at a good resolution.

## 4.5 The transmission electron microscope (TEM)

The transmission electron microscope (TEM) can be used to image a sample with a beam of monochromatic coherent electrons. Since the microscope works in transmission mode, the sample has to be very thin in order to be electron transparent ( $\lesssim 100$  nm). Magnifications between about  $10\,000\times$  and  $1\,000\,000\times$  can be obtained. Additionally, the TEM provides local information about the crystal structure of the sample because the electrons experience Bragg diffraction at the crystal lattice planes.

It is instructive to compare a TEM to an optical microscope in transmission mode: In the optical microscope, visible light is focussed by convex glass lenses. In the TEM,

in contrast, the electrons are focussed by magnetic coils due to the Lorentz force. Otherwise, the TEM has much in common with an optical microscope in transmission mode since electron lenses act like convex glass lenses to a reasonable approximation<sup>3</sup>.

Fig. 4.4 shows the two basic operations of the TEM: diffraction mode (A) and image mode (B). The diffraction mode displays the diffraction pattern of the sample on the fluorescent screen, whereas the image mode displays an image of the sample on the screen. The magnetic lenses are represented like convex glass lenses, which illustrates the similarity to an optical microscope in transmission mode that is placed upside down. The electron source and the condensor lenses are located above the sample (not shown). In many applications, the condensor lenses create a parallel electron beam at the location of the sample specimen. This is assumed in the following.

**Diffraction mode, Fig. 4.4(A):** The specimen is located in the object plane of the objective lens. A circular selected area diffraction (SAD) aperture is inserted in the image plane of the objective lens. Hence, the objective lens creates an image of this aperture back in its object plane where the specimen is located. Therefore, only the circular region of the specimen within this aperture image contributes to the information visible on the screen. The objective lens creates the diffraction pattern of this region in its back focal plane [three circles near the top of Fig. 4.4(A)]. The object plane of the intermediate lens is chosen to coincide with the back focal plane of the objective lens. Hence, the intermediate lens reproduces the diffraction pattern in its image plane, i. e., between the intermediate lens and the projector lens. The projector lens is just used for further magnification of the diffraction pattern. The image plane of the projector plane is the screen.

**Image mode, Fig. 4.4(B):** The SAD aperture is removed in order to observe a larger area than the circular area confined by this aperture. A circular objective aperture (OA) is inserted in the back focal plane of the objective lens to select either the direct beam [bright field (BF) image, Fig. 4.5(A)] or one of the diffracted beams [dark field (DF) image, Fig. 4.5(B)] in the diffraction pattern. The crucial point is that the strength of the intermediate lens is changed upon switching

---

<sup>3</sup>That the electrons spiral through the coils due to the Lorentz force is not of importance to understand the basic principle of a TEM.

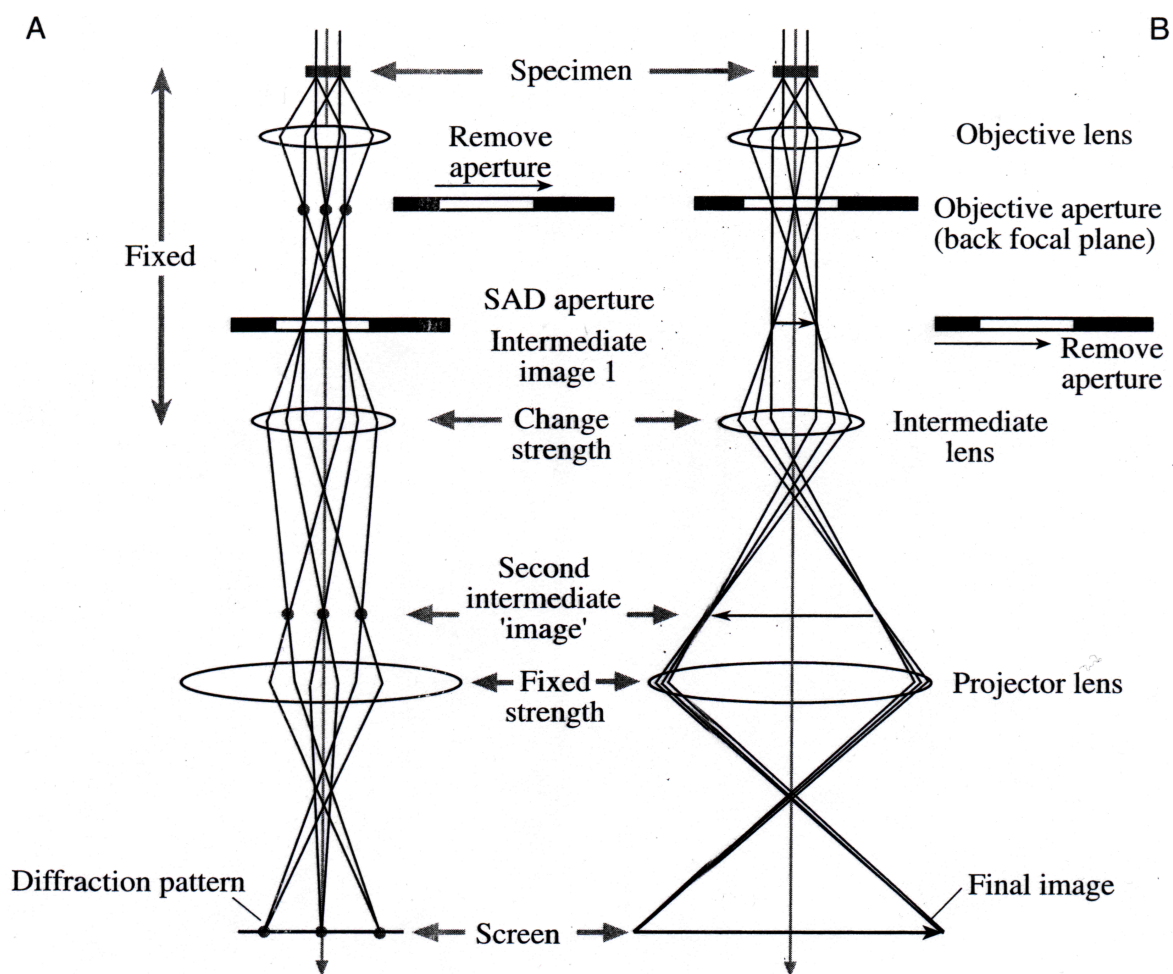


**Figure 4.4:** Schematic drawing of the two basic operation modes of the transmission electron microscope (TEM): diffraction mode (A) and image mode (B). The diffraction pattern in (A) is indicated by three circles and the image of the sample in (B) by a horizontal arrow. The location of the objective aperture in (B) is shown in more detail in Fig. 4.5. From [90].

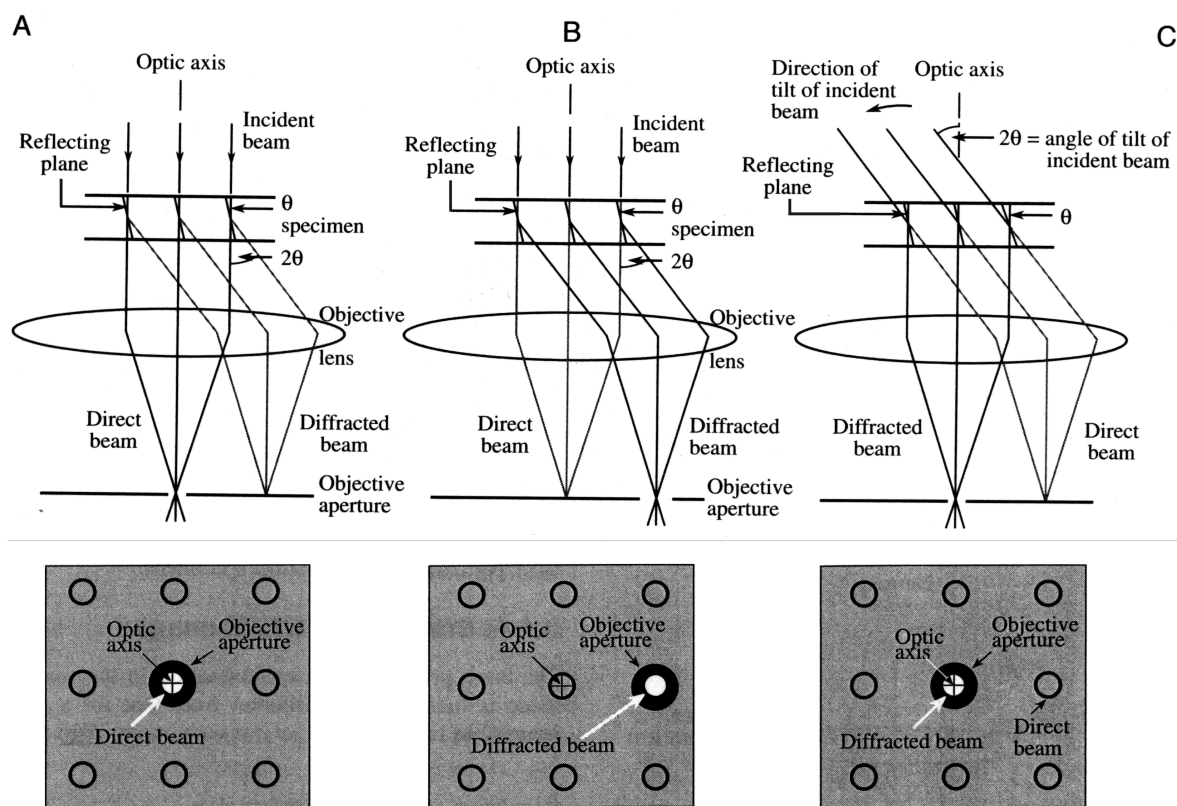


**Figure 4.5:** Schematic diagram showing how the objective aperture in a TEM forms a bright field image by selecting the direct beam (A), a dark field image by selecting a diffracted off-axis beam (B) and a centered dark field image by selecting a diffracted beam on the optic axis (C). The position of the objective aperture in the diffraction pattern in the back focal plane of the objective lens is shown underneath each diagram. From [90].

from diffraction mode to image mode: In image mode, the object plane of the intermediate lens is equal to the *image plane* of the objective lens. This produces an image of the specimen on the screen.

DF images are frequently difficult to focus because the off-axis electrons suffer from spherical aberrations. For this reason, centered dark field [CDF, Fig. 4.5(C)] is frequently used instead of DF. For CDF, the incident beam is tilted by  $2\theta$  ( $\theta$  : Bragg diffraction angle), so that the diffracted beam is aligned on the optic axis.

Some TEMs are equipped with an energy dispersive x-ray spectroscopy (EDS) de-

tector, which can be used to identify the chemical composition of the specimen. In order to perform EDS, the electron beam is usually converged to a small spot on the specimen by the condenser lenses. Within the area of this spot, the converged beam ‘displaces’ electrons from the inner atomic shells of the imaged material. An atom returns to its state of lowest energy by a transition of an electron from an outer atomic shell to the vacancy in the inner atomic shell (Fig. 4.6). The energy release is emitted in the form of an x-ray photon. The EDS detector collects the photons and sorts them by energy. Since the energy of each photon is characteristic of the element which produced it, the chemical composition of the material within the irradiated spot can be identified. This allows a *local* analysis of chemical composition.

Newer TEMs can be operated in a scanning transmission electron microscopy (STEM) mode. In this mode, a converged beam scans the sample, while the image is ‘recorded’ by an electron sensitive detector, which is inserted into a plane that is conjugate with the back focal plane of the objective lens. The diameter of the STEM beam within the specimen is significantly smaller (down to 0.1 nm) than in conventional converged beam TEM. Therefore, the resolution in an EDS analysis is better in STEM mode than in converged beam TEM mode. That the beam automatically scans the sample in STEM mode additionally facilitates the generation of composition maps (i. e., the chemical composition as a function of position along a line or within an area).

A more detailed introduction to TEM, STEM, and EDS can be found, e. g., in the textbook in Ref. [90].

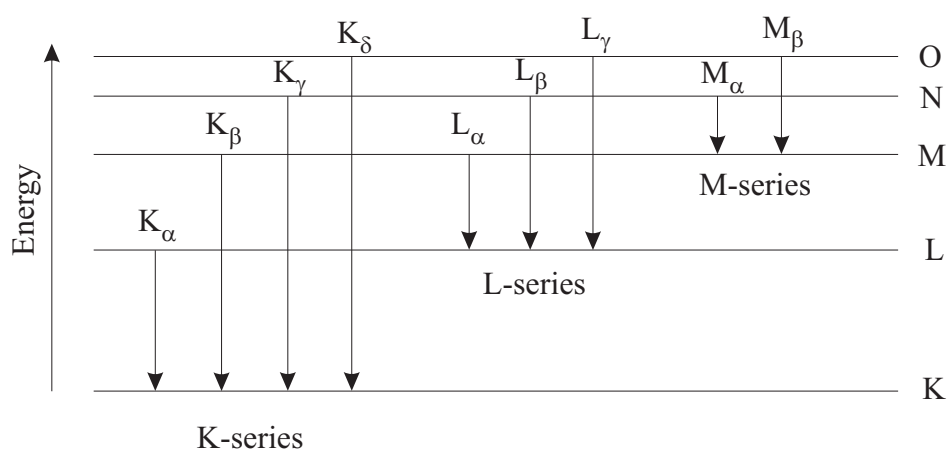


**Figure 4.6:** Characteristic x-rays are emitted by the transition of an electron from a higher atomic shell to a vacancy in a lower atomic shell. The corresponding transition (‘x-ray line’, indicated by an arrow) is usually labeled by the Latin capital letter identifying the shell of the final state (K, L, M, N, O) and by a Greek index identifying the shell of the initial state (relative to the final state). X-ray lines that share the same final state are collectively termed a ‘series’. The diagram is simplified since it does not include atomic subshells as a result of fine structure (more details can be found, e. g., in Ref. [90]).



## Part II

**Nucleation and growth parameters  
in thin films measured around the  
glass transition temperature**



# Chapter 5

## The crystal growth velocity

### 5.1 Preface

As pointed out in Sec. 1.2.1, the goal of this work is to understand crystallization kinetics of phase change materials better. According to Chap. 3, crystallization consists of the two processes nucleation and growth. This chapter will deal with the experimental determination of the crystal growth velocity  $u$  around the glass transition temperature  $T_g$ . The experimental determination of the nucleation rate  $I$  will be the subject of Chaps. 7 and 9 (cf. Table 1.1).

The general idea of the growth velocity measurements presented in this chapter is to employ a high-resolution microscope in combination with a high-precision furnace to *directly* observe the growth of crystals in thin films of amorphous phase change materials as a function of temperature and re-crystallization mechanism (Fig. 1.2). Measurements of crystal sizes as a function of anneal time at constant temperature would directly yield the isothermal crystal growth velocity.

Excerpts of this chapter have also been published elsewhere [91, 92].

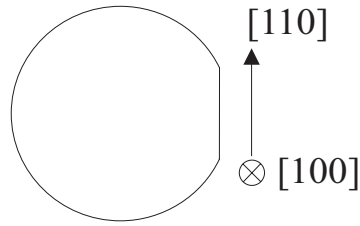


**Figure 5.1:** Schematic top view of a commercial (100) Silicon wafer. The flat side indicates the [110] direction.

## 5.2 Experimental methods

### 5.2.1 Sample preparation

(100) Silicon wafers (thickness: 640  $\mu\text{m}$ ) were cleaved with a diamond scribe in squares of size 25 mm by 25 mm in order to serve as substrates for thin film deposition. Silicon cleaves most easily in the [110] direction<sup>1</sup>, which is indicated by a flat side on a round commercial wafer (Fig. 5.1). The cleaved substrates were cleaned carefully with distilled water and commercial dish-washing liquid.

Thin films of various compositions (thickness: 30 nm and 350 nm for  $\text{Ge}_4\text{Sb}_1\text{Te}_5$ ; 30 nm for  $\text{AgIn-Sb}_2\text{Te}$  and  $\text{Ge}_2\text{Sb}_2\text{Te}_5$ ; 40 nm for  $\text{Ge}_1\text{Sb}_2\text{Te}_4$ ) were prepared by dynamic direct current magnetron sputtering (Sec. 4.1) on those substrates from a single commercial sputter target<sup>2</sup>. A commercially available lab sputter system was used for this purpose (company: Von Ardenne; model: LS 320 S). The background pressure was approximately  $10^{-6}$  mbar and the working pressure during sputtering in Ar ambient was  $7 \times 10^{-3}$  mbar. The sputtering power was 100 W ( $\text{Ge}_4\text{Sb}_1\text{Te}_5$ ,  $\text{AgIn-Sb}_2\text{Te}$ , and  $\text{Ge}_2\text{Sb}_2\text{Te}_5$ ) and 80 W ( $\text{Ge}_1\text{Sb}_2\text{Te}_4$ ). The deposition rate was approximately 0.5 nm/s ( $\text{Ge}_4\text{Sb}_1\text{Te}_5$ ,  $\text{AgIn-Sb}_2\text{Te}$ , and  $\text{Ge}_2\text{Sb}_2\text{Te}_5$ ) and 0.4 nm/s ( $\text{Ge}_1\text{Sb}_2\text{Te}_4$ ). The diameter of the sputter target was 10 cm and the target-substrate distance 5 cm for all alloys. The samples were prepared without additional capping layers, i. e., the films were exposed to natural oxidation after the sputter process. However, all samples were stored in vacuum

<sup>1</sup>[110] indicates a *crystal direction* here and *not* reference number 110.

<sup>2</sup>The films were sputter-deposited by H. Dieker. The nucleation and growth parameters for  $\text{Ge}_1\text{Sb}_2\text{Te}_4$  presented in Chaps. 5 and 7 were obtained by M. Klein in a Diploma work that was advised within this PhD project [93].

until used for the measurement to reduce oxidation and to keep away moisture. Earlier studies by x-ray reflectometry (XRR) on similarly prepared samples revealed that the saturation thickness of the oxidation layer is on the order of 2 nm for all alloys [94].

As confirmed by transmission electron microscopy (TEM, Sec. 4.5), the structure of the as-deposited films was entirely amorphous, i. e., no evidence of partial crystallization during deposition was found (Sec. 6.3.1.1 below). This is in line with earlier studies by X-ray diffraction (XRD) on similarly prepared amorphous films [94, 8, 9, 7].

### 5.2.2 Microscopic methods

Optical microscopy (Nikon Eclipse ME 600) turned out to be a useful tool to monitor the progress of crystallization of furnace-annealed films. Due to the reflectivity change upon crystallization [2] (cf. also Sec. 1.1), crystals could be identified as little bright dots in the amorphous matrix. However, the resolution of the optical microscope ( $\sim 500$  nm, comparable to the wavelength of visible light) was not large enough to quantitatively determine crystal sizes of partially crystallized films. Hence, optical microscopy is not suitable to measure the growth velocity in thin films of phase change alloys.

TEM yields a significantly larger resolution than optical microscopy ( $\sim 1$  nm). It was reported frequently (e. g., Ref. [95]) that TEM is a powerful tool to observe crystals in thin films of amorphous Te alloys. The isothermal crystal growth velocity as a function of temperature has been measured by *in situ*<sup>3</sup> TEM for  $\text{Ge}_2\text{Sb}_2\text{Te}_5$  [96, 97] by counting crystals and measuring their change in size. This method, however, has two major uncertainties:

- Precise temperature control (which is essential due to the strong temperature dependence of thermally activated processes) is often very difficult for TEM measurements [96]. This is because the temperature in the thin foil can deviate significantly from the measured holder temperature. Non-uniform heating of the amorphous film has also been reported [98, 99]. Moreover, it is difficult to heat the holder rapidly and without overshoot to the desired anneal temperature.

---

<sup>3</sup>In this work, the expression *in situ* is used for observations that are made simultaneously upon annealing. In contrast, *ex situ* observations are made subsequent to the anneal.

- The electron beam significantly triggers crystallization of phase change materials by local heating of the foil [100, 101], which can add artifacts to the observation.

Ex situ atomic force microscopy (AFM, Sec. 4.4) was identified as the method of choice in this project as it avoids these two difficulties if the annealing is performed precisely (cf. Sec. 5.2.3 below). Due to the mass density increase upon crystallization, which induces a reduction in film thickness on the order of 5% [102, 94, 9, 7, 103], crystals could be directly observed as depressions in the amorphous film with a Digital Instruments 3100 AFM in tapping mode<sup>4</sup> (Sec. 4.4). The samples were alternately *ex situ* annealed and scanned in the AFM. A specific sample was always annealed at the *same* temperature and rescanned in the AFM at the *same* microscopic location (this was possible by scratching the film with a fine needle and using the optical microscope attached to the AFM to relocate the site). Using several samples, these annealing/rescanning cycles were performed at several temperatures, 5°C apart. The isothermal crystal growth velocity was determined from two subsequent AFM scans from the ratio of the increase in crystal radius (average over 10–20 crystals) and the annealing time. Depending on the temperature, between 2 and 9 annealing/rescanning cycles were performed. This could reveal the time dependence of the growth velocity for up to 8 stages of the transformation.

### 5.2.3 Ex-situ anneal methods (isothermal)

Due to the pronounced temperature dependence of the processes studied here, a very precise temperature control is crucial for the experiment.

#### 5.2.3.1 Lower temperatures

For the lower temperatures, where crystallization proceeded on a timescale of hours to about a minute, isothermal annealing was performed in a high-precision furnace of a Perkin Elmer Pyris 1 differential scanning calorimeter (DSC, power-compensated design, Sec. 4.2) in an argon atmosphere<sup>5</sup>. The temperature of the DSC furnace was

---

<sup>4</sup>Contact mode did not yield satisfactory results.

<sup>5</sup>Caloric information (heat of crystallization) could not be obtained due to the low mass of the thin film. Hence, the DSC was *only* used as a furnace for the experiments presented in this chapter.

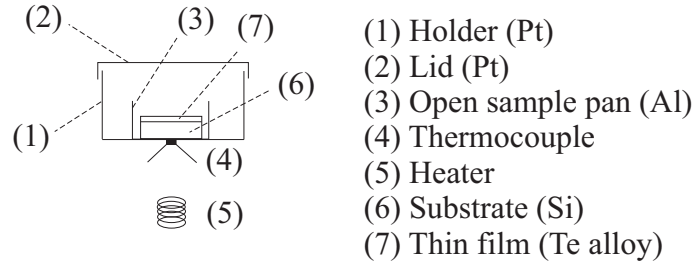


**Figure 5.2:** Schematic view of a substrate in the DSC furnace inside an open Al sample pan. The thin film is located at the top of the substrate. The thermocouple is located underneath the Pt holder and above the heating coil. A substrate of similar size (with no film) was placed in an open Al pan in the reference furnace (not shown, cf. Fig. 4.2).

calibrated [84, 85, 86, 87] for isothermal operation using the melting points of indium ( $T_m = 156.60^\circ\text{C}$ ), tin ( $T_m = 231.88^\circ\text{C}$ ), and zinc ( $T_m = 419.47^\circ\text{C}$ ). The temperature uncertainty was less than  $0.1^\circ\text{C}$ .

Samples were annealed in the commercial aluminum DSC sample pans [item (3) in Figs. 4.2 or 5.2], which were also used for the calibration experiments. The pans were not sealed but left open at the top. Due to the small sample pan size (cylindrical, diameter: 6 mm, height: 1.5 mm), the sputtered samples of size 25 mm by 25 mm (Sec. 5.2.1) had to be cleaved to small pieces of approximate size 4 mm by 4 mm.

A heating rate of 50 K/min was used to ramp up to the isothermal anneal temperature. The proportional integral derivative (PID) controller of the DSC was adjusted in a way that no temperature overshoot occurred. This is crucial because of the strong thermal activation of the growth velocity. At the end of the isothermal anneal, the sample was cooled to room temperature at 50 K/min.

Both heater and thermocouple are located underneath the Pt holder of the DSC furnace. The film is located on the top side of the substrate (Fig. 5.2). As the substrate is very thick (640  $\mu\text{m}$ ), it had to be established if heat conduction effects through the thickness of the substrate have a significant effect on the annealing time *of the film*. The time for heat transfer by thermal conduction can be estimated by dimensional analysis of the heat conduction equation [104]

$$\frac{\partial T}{\partial t} = D_{th} \left( \frac{\partial^2 T}{\partial x^2} + \frac{\partial^2 T}{\partial y^2} + \frac{\partial^2 T}{\partial z^2} \right), \quad (5.1)$$

**Table 5.1:** Thermal constants of silicon [105].  $\lambda$  is the heat conductivity,  $\rho$  the mass density, and  $c_p^{(m)}$  the specific heat at constant pressure per unit mass.

$\lambda$ (25 °C)	$\lambda$ (100 °C)	$\rho$	$c_p^{(m)}$
$\left(\frac{\text{W}}{\text{mK}}\right)$	$\left(\frac{\text{W}}{\text{mK}}\right)$	$\left(\frac{\text{kg}}{\text{m}^3}\right)$	$\left(\frac{\text{J}}{\text{kg K}}\right)$
149	108	2330	705

where

$$D_{th} = \frac{\lambda}{\rho c_p^{(m)}} \quad (5.2)$$

is the thermal diffusivity (dimension:  $\frac{\text{m}^2}{\text{s}}$ ).  $\lambda$  is the heat conductivity,  $\rho$  the mass density, and  $c_p^{(m)}$  the specific heat at constant pressure per unit mass. Equation (5.1) has the same form as the diffusion equation [Eq. (3.53)]. The time for heat transfer by conduction along a distance  $l$  must therefore be on the order of

$$\tau = \frac{l^2}{D_{th}} = \frac{l^2 \rho c_p^{(m)}}{\lambda}. \quad (5.3)$$

This is the only possibility to attain the dimension of a time by combining all quantities involved in Eq. (5.1) with the distance  $l$  over which heat conduction occurs. Taking  $l = 640 \mu\text{m}$  and using the thermal constants of silicon (Table 5.1) yields

$$\tau \sim 6 \text{ ms}. \quad (5.4)$$

This is orders of magnitude shorter than a typical isothermal anneal time in the experiments (between about a minute and several hours). Hence, the influence of heat conduction along the thickness of the substrate on the anneal time is clearly negligible. This is due to the excellent thermal conductivity of silicon (Table 5.1).

For test purposes, a sample was placed into the DSC furnace with its film located at its lower side (i. e., the film was in direct contact with the Aluminum pan). As a result, the progress of crystallization as observed in the AFM was the same as for those anneals where the film was located at the top of the sample (using the same anneal temperature and anneal time). This shows that the upper surface of the sample in the DSC always exhibits the same temperature as the lower surface, i. e., there is no significant heat loss at the upper surface by convection or radiation. Hence, the temperature of the

upper and the lower side of the sample are the same for all purposes of this study. All data presented in this work result from anneals where the film was located on the top side of the substrate in the DSC furnace as shown in Fig. 5.2.

The DSC furnace was used for isothermal anneals in the following temperature ranges:

- AgIn-Sb<sub>2</sub>Te: 140 °C – 170 °C
- Ge<sub>4</sub>Sb<sub>1</sub>Te<sub>5</sub>: 140 °C – 170 °C
- Ge<sub>2</sub>Sb<sub>2</sub>Te<sub>5</sub>: 115 °C – 145 °C
- Ge<sub>1</sub>Sb<sub>2</sub>Te<sub>4</sub>: 95 °C – 125 °C .

### 5.2.3.2 Higher temperatures

The DSC furnace could not be used for annealing times shorter than about half a minute. This is because the PID controller had to be adjusted in a way that temperature overshoot could not occur. As a consequence, the system approaches the isothermal temperature setpoint from below. If the anneal time is too short, the temperature setpoint is not reached. Hence, an immersion experiment was constructed to perform anneals on timescales between a few seconds and about a minute. The sample was immersed manually into a hot liquid of the desired temperature for a few seconds and subsequently quenched into a cold liquid.

Safflower oil was used as the hot liquid as its smoke point is significantly higher than for many other oils (Table 5.2). The smoke point of an oil is the temperature at which the oil begins to decompose (e. g., polymerize) and when visible smokes are given off. Each time an oil is heated above its smoke point, the viscosity increases irreversibly, and the smoke point decreases irreversibly. Hence, a high smoke is important for the experiments to establish good thermal conduction in the oil due to a low viscosity. Also, the oil can be re-used for subsequent anneals without loss of reproducibility. For any oil, the smoke is still significantly below its flash point (around 320 °C for most oils), when tiny wisps of fire begin to leap from its surface. Above the fire point (around 400 °C for most oils) the oil surface starts to burn. Hence, care had to be taken not to heat the oil accidentally to high temperatures.



**Figure 5.3:** (Color). Experimental setup of the immersion experiment. Safflower oil (in a large jar on the hot plate) is used to anneal a sample on short timescales by immersion. Subsequently, the sample is immersed rapidly into ethylene glycol (liquid on the left of the hot plate in the small jar). The oil temperature is measured with a mercury thermometer. The thermometer is immersed into the oil up to the calibration line, which is indicated on the thermometer. The scale is read through a magnifying glass for higher precision. A timer is located in the front.

**Table 5.2:** Smoke points of various oils taken from several cookbooks. Due to its high smoke point, safflower oil is most appropriate for the immersion experiments.

Oil	Smoke point (°C)
Safflower oil	265
Sunflower oil	246
Soybean oil	241
Canola oil	238
Corn oil	236
Peanut oil	231
Sesame oil	215
Olive oil	190

The experimental setup is shown in Fig. 5.3. Before the anneal, the oil was heated on a hot plate to a temperature of about 5–10 °C higher than the desired anneal temperature. Subsequently, the hotplate temperature was decreased slightly and the oil was stirred continuously with a teaspoon, so that its temperature decreased *slowly*. Once the desired anneal temperature was reached (usually after about 10 minutes of stirring), the sample was immersed into the oil for the desired amount of time. The sample (dimensions: about 8 mm by 4 mm) was held by a copper wire (0.5 mm diameter), which was coiled two or three times around the sample (Fig. 5.4). To obtain a homogeneous temperature distribution in the oil by convection, the oil was stirred further while the sample was immersed<sup>6</sup>. The oil temperature was measured by a calibrated mercury thermometer (temperature uncertainty: less than 0.5 °C).

The cold liquid needed to have a boiling point higher than the sample temperature in order to obtain the highest possible quench rate: If the boiling point were significantly lower than the sample temperature, the sample could evaporate the liquid locally upon immersion, so that the sample would be surrounded by a vapor layer. This would

<sup>6</sup>The random movement of the teaspoon in the oil avoids artifacts in the temperature distribution, which might occur with the use of an automatic stirring device.

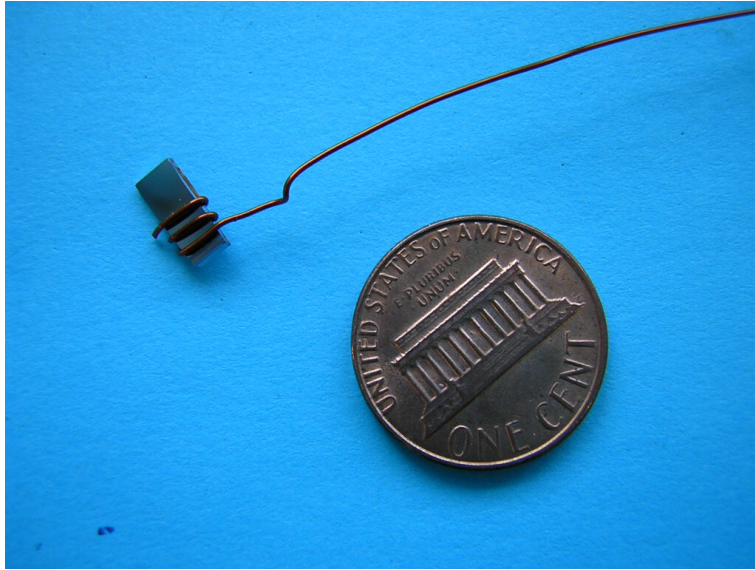


**Figure 5.4:** (Color). Copper wire used as a sample holder for the immersion experiment. The wire was coiled around the sample. A cent coin is shown to serve as a reference scale.

yield far slower cooling rates<sup>7</sup>. Hence, ethylene glycol ( $\text{HOCH}_2\text{CH}_2\text{OH}$ , boiling point:  $198^\circ\text{C}$ ) was chosen.

Oil residues on the sample were cleaned off with an isopropanol-soaked soft cloth after each anneal.

Equation (5.4) also applies to the immersion experiment as the substrate material and thickness are the same. Hence, the time that the sample needs to adopt the liquid temperature after immersion is clearly negligible provided that the thermal contact between liquid and sample is good.

The immersion experiment was used for isothermal anneals in the following temperature ranges:

- $\text{AgIn-Sb}_2\text{Te}$ :  $172.8^\circ\text{C} - 185^\circ\text{C}$
- $\text{Ge}_4\text{Sb}_1\text{Te}_5$ :  $170.7^\circ\text{C} - 186^\circ\text{C}$ .

No immersion experiments were performed on  $\text{Ge}_2\text{Sb}_2\text{Te}_5$  and  $\text{Ge}_1\text{Sb}_2\text{Te}_4$  for reasons which will become clear below (the crystal density was too high to allow an analysis at high temperatures).

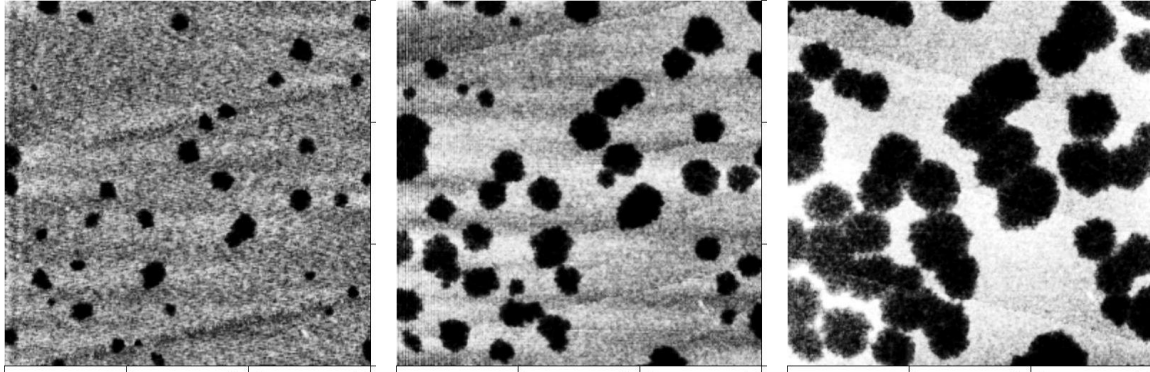
---

<sup>7</sup>For this reason, liquid nitrogen would yield poor cooling rates.

## 5.3 Results

Figures 5.5–5.12 shows a series AFM scans for two temperatures per alloy. Scans on  $\text{Ge}_4\text{Sb}_1\text{Te}_5$ ,  $\text{Ge}_2\text{Sb}_2\text{Te}_5$  and  $\text{Ge}_1\text{Sb}_2\text{Te}_4$  look qualitatively similar. The scans on  $\text{AgIn-Sb}_2\text{Te}$  differ from those on the  $\text{GeSbTe}$  alloys in two major respects:

1. At a given time and temperature (represented by a single AFM scan), the crystal diameter distribution is rather sharp for  $\text{AgIn-Sb}_2\text{Te}$  but broad for the  $\text{GeSbTe}$  alloys. Since the isothermal crystal growth velocity of neighboring crystals was observed to be identical, this implies that all (heterogeneous) nucleation sites are approximately simultaneously exhausted for  $\text{AgIn-Sb}_2\text{Te}$ . In contrast, the isothermal nucleation rate remains non-zero at all times for the  $\text{GeSbTe}$  alloys.
2. The total number of crystals  $N_c$  per unit area, which would be observed after complete crystallization of the sample surface, increases with increasing temperature for the  $\text{GeSbTe}$  alloys, but adopts a temperature-independent value of  $N_c = (5.0 \pm 0.3) \mu\text{m}^{-2}$  for  $\text{AgIn-Sb}_2\text{Te}$ . This behavior was observed in the entire temperature range investigated (but Figs. 5.5–5.12 show only two temperatures per alloy).

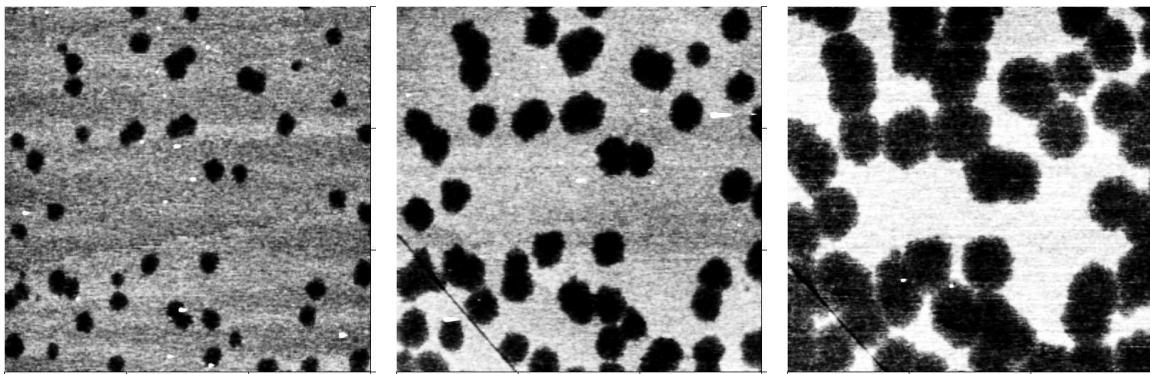


(a) 5 min

(b) 5 + 2 = 7 min

(c) 5 + 2 + 2 = 9 min

**Figure 5.5:** AFM scans on AgIn-Sb<sub>2</sub>Te. Dimensions: 3  $\mu\text{m}$  by 3  $\mu\text{m}$ . Anneal temperature: 160  $^{\circ}\text{C}$  (DSC furnace). Film thickness: 30 nm. Crystals (dark) are visible in amorphous surrounding (bright). The height scale is shown in Fig. 5.13. The dimension of the anneal time underneath the images is left out in some cases for better readability (this applies to the other AFM scans below as well).

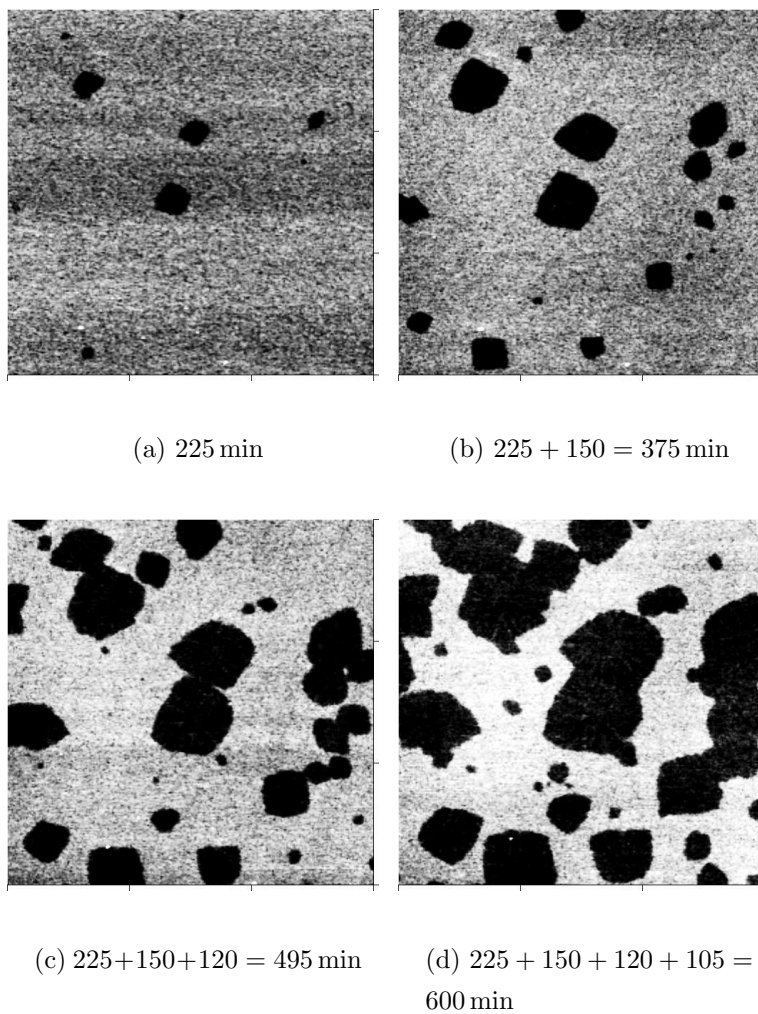


(a) 4 s

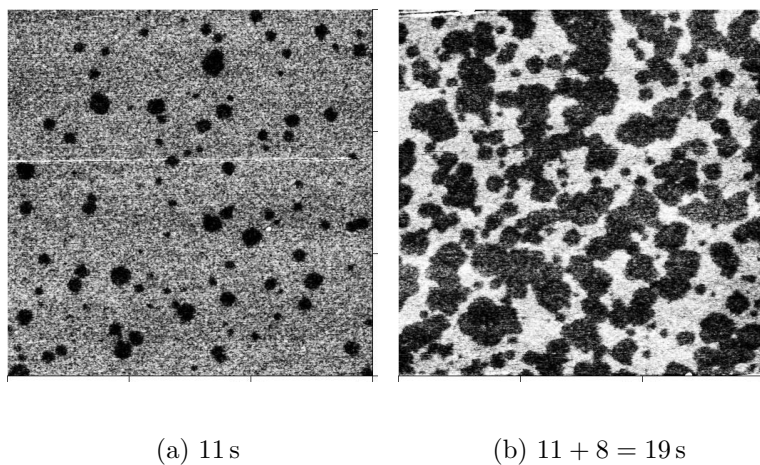
(b) 4 + 2 = 6 s

(c) 4 + 2 + 2 = 8 s

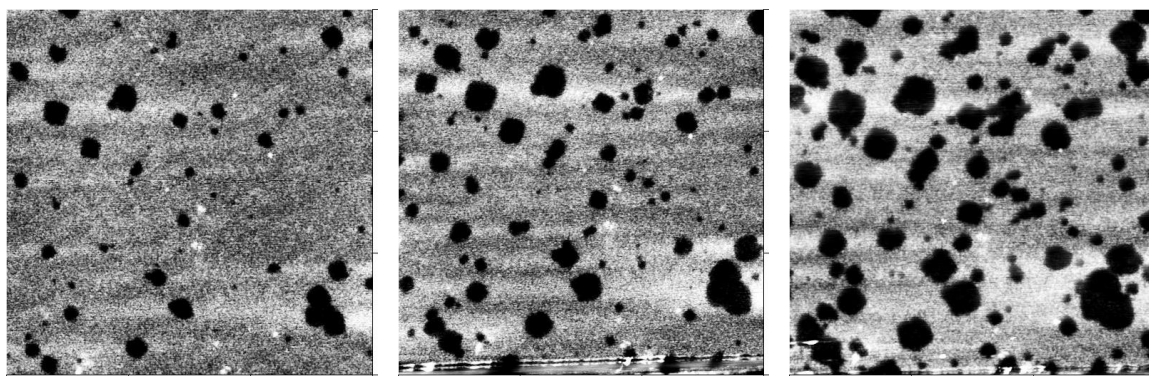
**Figure 5.6:** AFM scans on AgIn-Sb<sub>2</sub>Te. Dimensions: 3  $\mu\text{m}$  by 3  $\mu\text{m}$ . Anneal temperature: 185  $^{\circ}\text{C}$  (immersion experiment). Film thickness: 30 nm. Crystals (dark) are visible in amorphous surrounding (bright). The height scale is shown in Fig. 5.13.



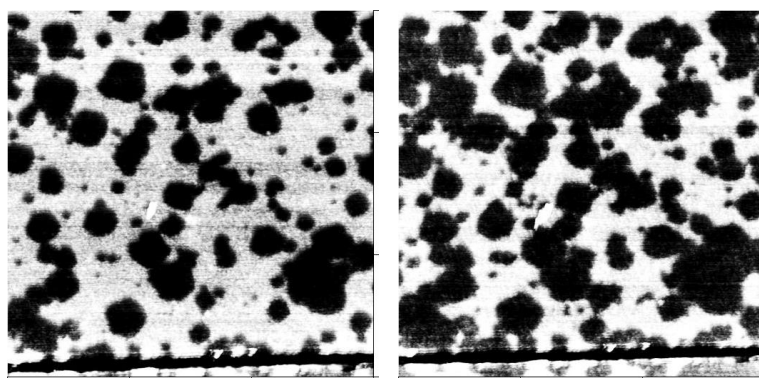
**Figure 5.7:** AFM scans on  $\text{Ge}_4\text{Sb}_1\text{Te}_5$ . Dimensions:  $3\ \mu\text{m}$  by  $3\ \mu\text{m}$ . Anneal temperature:  $140^\circ\text{C}$  (DSC furnace). Film thickness:  $30\ \text{nm}$ . Crystals (dark) are visible in amorphous surrounding (bright). The height scale is shown in Fig. 5.13.



**Figure 5.8:** AFM scans on  $\text{Ge}_4\text{Sb}_1\text{Te}_5$ . Dimensions:  $3\ \mu\text{m}$  by  $3\ \mu\text{m}$ . Anneal temperature:  $180^\circ\text{C}$  (immersion experiment). Film thickness:  $30\ \text{nm}$ . Crystals (dark) are visible in amorphous surrounding (bright). The height scale is shown in Fig. 5.13.



(a) 570 min

(b)  $570 + 80 = 650$  min(c)  $570 + 80 + 80 = 730$  min(d)  $570 + 80 + 80 + 80 =$   
810 min(e)  $570 + 80 + 80 + 80 + 80 =$   
890 min

**Figure 5.9:** AFM scans on  $\text{Ge}_2\text{Sb}_2\text{Te}_5$ . Dimensions:  $3\ \mu\text{m}$  by  $3\ \mu\text{m}$ . Anneal temperature:  $115^\circ\text{C}$  (DSC furnace). Film thickness: 30 nm. Crystals (dark) are visible in amorphous surrounding (bright). The height scale is shown in Fig. 5.13. The line that is visible on the lower side of the scans is a scratch in the film.

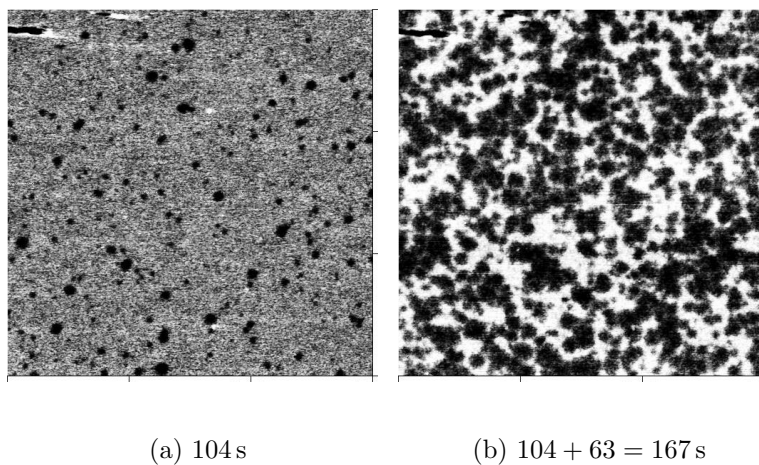


**Figure 5.10:** AFM scans on  $\text{Ge}_2\text{Sb}_2\text{Te}_5$ . Dimensions:  $3\ \mu\text{m}$  by  $3\ \mu\text{m}$ . Anneal temperature:  $145\ ^\circ\text{C}$  (DSC furnace). Film thickness:  $30\ \text{nm}$ . Crystals (dark) are visible in amorphous surrounding (bright). The height scale is shown in Fig. 5.13.

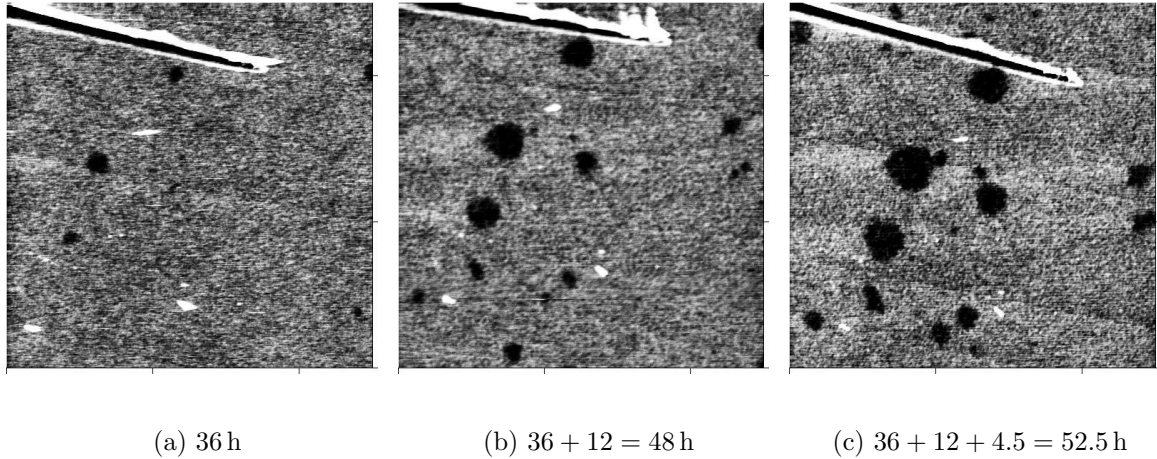


**Figure 5.11:** AFM scans on  $\text{Ge}_1\text{Sb}_2\text{Te}_4$ . Dimensions:  $2.5\ \mu\text{m}$  by  $2.5\ \mu\text{m}$ . Anneal temperature:  $95\ ^\circ\text{C}$  (DSC furnace). Film thickness:  $40\ \text{nm}$ . Crystals (dark) are visible in amorphous surrounding (bright). The height scale is shown in Fig. 5.13. The scratch in the film was used to relocate the site.

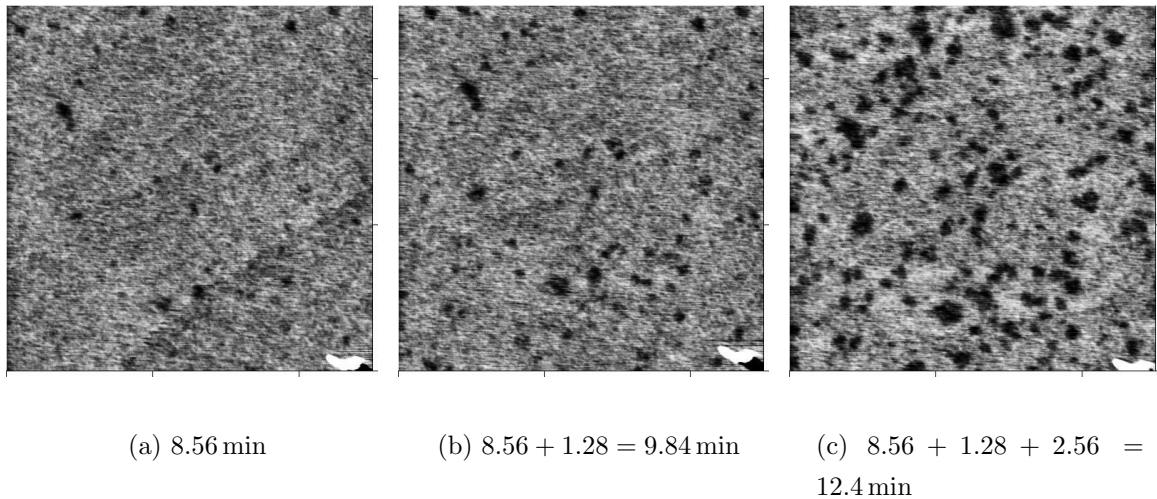


**Figure 5.12:** AFM scans on  $\text{Ge}_1\text{Sb}_2\text{Te}_4$ . Dimensions:  $2.5\ \mu\text{m}$  by  $2.5\ \mu\text{m}$ . Anneal temperature:  $125\ ^\circ\text{C}$  (DSC furnace). Film thickness:  $40\ \text{nm}$ . Crystals (dark) are visible in amorphous surrounding (bright). The height scale is shown in Fig. 5.13. The scratch in the film (lower right side of the images) was used to relocate the site.

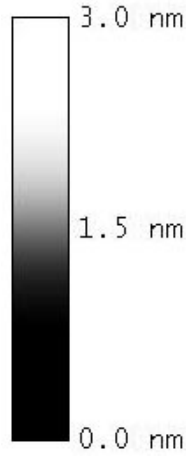


**Figure 5.13:** Height scale for the AFM scans shown in Figs. 5.5–5.12.

Cross-sectional transmission electron microscopy shows that crystals nucleate only heterogeneously at the (naturally oxidized) film surface (this is discussed in Chap. 6 below). Heterogeneous nucleation at the film-substrate interface and homogeneous nucleation does not occur.

Figure 5.14 is an Arrhenius plot of the crystal growth velocities,  $u$ . For AgIn-Sb<sub>2</sub>Te, Ge<sub>4</sub>Sb<sub>1</sub>Te<sub>5</sub> and Ge<sub>2</sub>Sb<sub>2</sub>Te<sub>5</sub>, each of the data points results from the crystal growth velocity obtained from two *consecutive* AFM scans (between 2 and 9 scans per temperature; Figs. 5.5–5.10 only show a sequence for two temperatures per alloy). The data points in Fig. 5.14 coincide within error for a given temperature and alloy. Therefore, over the entire temperature range investigated, the isothermal crystal growth velocity is time-independent within error. The same was also observed for Ge<sub>1</sub>Sb<sub>2</sub>Te<sub>4</sub>, but Fig. 5.14 just shows the average growth velocity for each temperature.

Growth velocities of AgIn-Sb<sub>2</sub>Te and Ge<sub>4</sub>Sb<sub>1</sub>Te<sub>5</sub> are similar at a given temperature. Crystal growth is thermally activated. The fitting parameters obtained from the Arrhenius fits are given in Table 5.3. For Ge<sub>2</sub>Sb<sub>2</sub>Te<sub>5</sub>, the value of  $E_u = 2.35 \pm 0.05$  eV agrees well with that of Privitera and co-workers,  $E_u = 2.4 \pm 0.3$  eV [97], but differs slightly from that of Ruitenbergh and co-workers,  $E_u = 1.6 \pm 0.6$  eV [96]. Both literature values were obtained in about the same temperature range by *in situ* TEM. The deviation between the latter value and the value of this work (Table 5.3) may be due to the large temperature uncertainty of  $\pm 10^\circ\text{C}$  reported in Ref. [96]. For AgIn-Sb<sub>2</sub>Te, Ge<sub>4</sub>Sb<sub>1</sub>Te<sub>5</sub>, and Ge<sub>1</sub>Sb<sub>2</sub>Te<sub>4</sub>, no values of  $E_u$  have been reported in the literature.

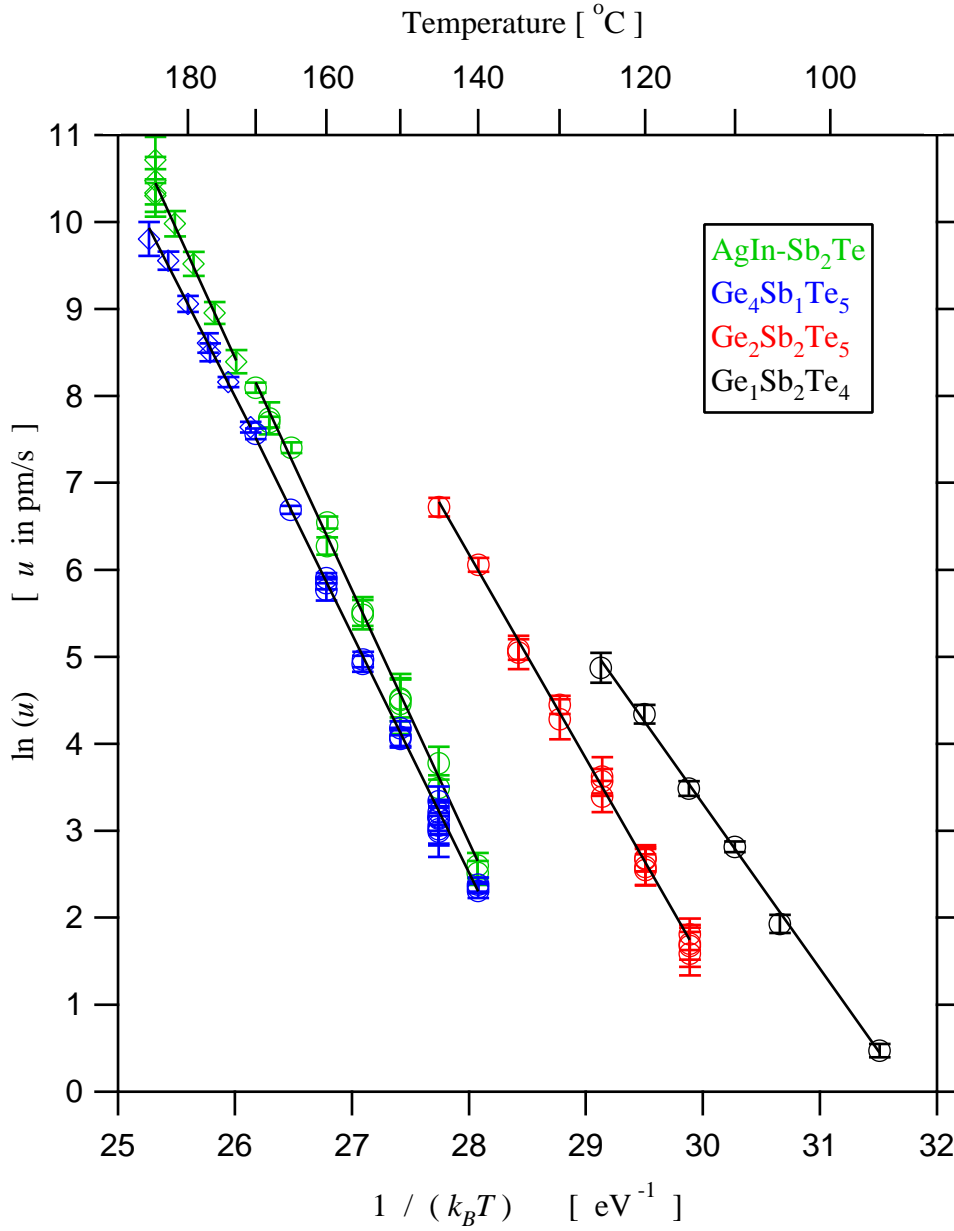


**Figure 5.14:** (Color). Crystal growth velocity  $u$  as a function of temperature  $T$ : AgIn-Sb<sub>2</sub>Te (green), Ge<sub>4</sub>Sb<sub>1</sub>Te<sub>5</sub> (blue), Ge<sub>2</sub>Sb<sub>2</sub>Te<sub>5</sub> (red), and Ge<sub>1</sub>Sb<sub>2</sub>Te<sub>4</sub> (black). Circles: DSC furnace anneal. Diamonds: Immersion anneal. For Ge<sub>2</sub>Sb<sub>2</sub>Te<sub>5</sub> and Ge<sub>1</sub>Sb<sub>2</sub>Te<sub>4</sub>, the crystal density was too high to allow measurements using immersion anneals. The data were fitted with an Arrhenius equation (Table 5.3). For AgIn-Sb<sub>2</sub>Te and Ge<sub>4</sub>Sb<sub>1</sub>Te<sub>5</sub>, DSC and immersion anneal data were fitted separately, and the fitting parameters were subsequently averaged. These averaged values (Table 5.3) are less sensitive to possible small systematic errors in the temperature calibration of the two annealing methods.

**Table 5.3:** Arrhenius fit parameters for the crystal growth velocity in Fig. 5.14. The fit equation is  $\ln(u) = \ln(u_0) - \frac{E_u}{k_B T}$ .

Alloy	$\ln(u_0)$ ( $u_0$ in pm/s)	$E_u$ (eV)
AgIn-Sb <sub>2</sub> Te	$84.00 \pm 1.22$	$2.90 \pm 0.05$
Ge <sub>4</sub> Sb <sub>1</sub> Te <sub>5</sub>	$79.15 \pm 0.79$	$2.74 \pm 0.03$
Ge <sub>2</sub> Sb <sub>2</sub> Te <sub>5</sub>	$71.95 \pm 1.46$	$2.35 \pm 0.05$
Ge <sub>1</sub> Sb <sub>2</sub> Te <sub>4</sub>	$60.11 \pm 1.53$	$1.89 \pm 0.05$

For the DSC furnace anneals, due to the finite heating and cooling rate of 50 K/min, the crystals do not only grow upon annealing at the isothermal setpoint temperature  $T^{sp}$ , but they also grow upon heating and cooling, when the temperature is close to  $T^{sp}$ . Hence, the data in Fig. 5.14 had to be corrected for this effect, which becomes most important at the highest annealing temperatures. A computer simulation was performed that interpolated this correction: During a short time interval  $\Delta t$ , the interface grows by the distance

$$s(t + \Delta t) - s(t) = \Delta t \cdot u_0 \cdot \exp\left(-\frac{E_u}{k_B T(t)}\right), \quad (5.5)$$

where  $s(t)$  is the total distance that the interface has grown during a particular anneal at time  $t$  (as an average over 10–20 crystals). Hence,  $s(0) = 0$  is used as an initial value (at  $t = 0$ , the thermal program starts to heat the sample that may already contain a few crystals from the preceding anneal).  $T(t)$  is the *measured* temperature at time  $t$ , which is recorded by the DSC computer.  $s(t)$  is then calculated recursively from Eq. (5.5):  $s(0) = 0$  yields  $s(\Delta t)$ ;  $s(\Delta t)$  yields  $s(2 \cdot \Delta t)$  and so on. This simulation is performed over the entire temperature-time curve  $T(t)$ , until a value  $s(n \cdot \Delta t) = s_{\text{final}}$  is obtained, where  $n \cdot \Delta t$  is the total duration of the recorded  $T(t)$  curve, and  $s_{\text{final}}$  is the distance the interface grew during one anneal (as an average over 10–20 crystals). For starting values in the simulation, the activation energy  $E_u^{(0)}$  and the prefactor  $u_0^{(0)}$  from a fit similar to the one shown in Fig. 5.14 (that did not yet include this correction) was used. Then, the simulated value of  $s_{\text{final}}$  is matched to the corresponding measured value (as an average over about 10–20 crystals) by keeping  $E_u^{(0)}$  fixed but varying the

prefactor  $u_0$  in the simulation (the time interval  $\Delta t$  was decreased until no change in the result was obtained any more). This yields a new value  $u_0^{(0')}$ . Then, the crystal growth velocity at the corresponding setpoint temperature  $T^{sp}$  is computed using the values  $u_0^{(0')}$  and  $E_u^{(0)}$ :

$$u(T^{sp}) = u_0^{(0')} \exp\left(-\frac{E_u^{(0)}}{k_B T^{sp}}\right). \quad (5.6)$$

This procedure is done for all anneals at all temperatures. The new values  $u(T^{sp})$  are plotted in a graph similar to Fig. 5.14, and the data are fitted with an Arrhenius equation. New fit parameters  $E_u^{(1)}$  and  $u_0^{(1)}$  are obtained, which are used again for the simulation in Eq. (5.5), i. e., the entire procedure is repeated for all anneals at all temperatures. The simulation is terminated after multiple cycles of this procedure once self-consistent values are obtained (i. e., once the values for  $E_u$  and  $u_0$  obtained in the simulation matched those obtained from the subsequent Arrhenius fit). As a result of the simulation, this correction increased the effective anneal time by about 15 s and decreased the activation energy  $E_u$  by around 0.1 eV. The correction is included in the data shown in Fig. 5.14 and Table 5.3.

The data presented in Figs. 5.5–5.12, Fig. 5.14, and Table 5.3 were taken on films of thickness 30 nm for AgIn-Sb<sub>2</sub>Te, Ge<sub>4</sub>Sb<sub>1</sub>Te<sub>5</sub>, and Ge<sub>2</sub>Sb<sub>2</sub>Te<sub>5</sub> (40 nm for Ge<sub>1</sub>Sb<sub>2</sub>Te<sub>4</sub>). In an additional experiment (not shown), the growth velocity was measured on 350 nm thick films for Ge<sub>4</sub>Sb<sub>1</sub>Te<sub>5</sub> at 155 °C. As a result, the growth velocity did not depend on the film thickness as expected.

## 5.4 Discussion

### 5.4.1 Type of crystallization kinetics

The time-independent growth velocity implies interface-controlled growth (Sec. 3.2.1) for all four alloys (in contrast to diffusion-controlled growth, where the position of the interface is proportional to the square root of time, cf. Sec. 3.2.2).

The crystal growth velocity  $u$  is observed to *increase* with increasing temperature for all alloys (Fig. 5.14). Hence, as usually expected in alloys, diffusion-limited kinetics (not collision-limited kinetics) should apply. For the latter case,  $u$  would *decrease* with increasing temperature (Sec. 3.2.1). As a further indication, experience indicates that

the crystal growth velocities observed for the Te alloys are too small to be the result of collision-limited kinetics [53].

### 5.4.2 Activation energy for diffusion

Substituting the upper line of Eq. (3.44) into Eq. (3.46) yields the following expression for the crystal growth velocity:

$$\begin{aligned} u &= f_s \cdot \lambda \cdot k^+ \left[ 1 - \exp \left( -\frac{|\Delta G_{lc,atom}|}{k_B T} \right) \right] \\ &= f_s \cdot \lambda \cdot k_0 \exp \left( -\frac{\Delta G^*}{k_B T} \right) \left[ 1 - \exp \left( -\frac{|\Delta G_{lc,atom}|}{k_B T} \right) \right]. \end{aligned} \quad (5.7)$$

The free energy of activation to the transition state  $\Delta G^*$  (Fig. 3.9) can be broken into an activation enthalpy  $\Delta H^*$  and an activation entropy  $\Delta S^*$  to the transition state [78]:

$$\Delta G^* = \Delta H^* - T \Delta S^*. \quad (5.8)$$

Combining Eqs. (5.7) and (5.8) gives

$$u = \underbrace{f_s \cdot \lambda \cdot k_0 \exp \left( \frac{\Delta S^*}{k_B} \right)}_{=: \hat{u}} \exp \left( -\frac{\Delta H^*}{k_B T} \right) \left[ 1 - \exp \left( -\frac{|\Delta G_{lc,atom}|}{k_B T} \right) \right], \quad (5.9)$$

where  $\hat{u}$  is a constant, which is temperature-independent to a good approximation. The activation enthalpy  $\Delta H^*$  can again be broken into an activation energy  $\Delta E^*$  and an activation volume  $\Delta V^*$  to the transition state:

$$\Delta H^* = \Delta E^* + p \Delta V^*. \quad (5.10)$$

For  $p = 1$  bar, the term  $p \Delta V^*$  is entirely negligible compared to  $\Delta E^*$ . Hence,

$$\Delta H^* = \Delta E^* \quad (p = 1 \text{ bar}). \quad (5.11)$$

The crystal growth velocity then becomes

$$u = \hat{u} \exp \left( -\frac{\Delta E^*}{k_B T} \right) \left[ 1 - \exp \left( -\frac{|\Delta G_{lc,atom}|}{k_B T} \right) \right] \quad (p = 1 \text{ bar}). \quad (5.12)$$

Comparison of Eq. (5.12) with Eq. (3.48) yields

$$f_s \cdot \frac{6D}{\lambda} = \hat{u} \exp \left( -\frac{\Delta E^*}{k_B T} \right) \quad (5.13)$$

or

$$D = \hat{D} \exp\left(-\frac{\Delta E^*}{k_B T}\right), \quad (5.14)$$

where  $\hat{D}$  is a temperature-independent constant. The quantity  $D$  in Eqs. (3.17) and (3.48) is usually associated with the diffusivity in the undercooled liquid or in the amorphous phase (not in the crystal). Hence, also the activation energy  $\Delta E^*$  to the transition state can be associated with the activation energy for diffusion in the undercooled liquid or in the amorphous phase<sup>8</sup>.

The experimentally determined activation energy  $E_u$  for the crystal growth velocity (Table 5.3) can contain contributions from  $\Delta E^*$  and  $\Delta G_{lc,atom}$  [cf. Eq. (5.12)]. In Refs. [106, 107],  $\Delta G_{lc,atom}$  was estimated from heat capacity measurements to be about 44 meV around 180°C for AgIn-Sb<sub>2</sub>Te. Similar values of less than 100 meV are obtained for the other alloys in this temperature range by the free energy approximations [Eq. (2.32)], using typical values of heat of fusion and melting temperature (Chap. 9 below and Refs. [106, 107]). This is significantly smaller than the activation energies  $E_u$  for the crystal growth velocity (Table 5.3). Therefore, significantly below the melting temperature (which is around 550°C–650°C, cf. Chap. 9), the temperature dependence of the growth velocity is dominated by the diffusive jump term  $f \frac{6D}{\lambda}$ , whereas the thermodynamic factor  $\left[1 - \exp\left(-\frac{|\Delta G_{lc,atom}|}{k_B T}\right)\right]$  is just a temperature independent constant to a good approximation<sup>9</sup>. Therefore,

$$E_u = \Delta E^*, \quad (5.15)$$

or

$$u = B \cdot D, \quad (5.16)$$

where  $B$  is a temperature independent constant. Hence, the growth velocity measurements determine the activation energy for diffusion in the undercooled liquid or in the amorphous phase.

---

<sup>8</sup>Note that  $\Delta E^*$  can be temperature-dependent.

<sup>9</sup>This statement would not be correct any more if the melting temperature is approached, where  $\Delta G_{lc,atom}$  approaches zero.

### 5.4.3 Structural relaxation

The data in Fig. 5.14 appear to be taken in the undercooled liquid (not in the amorphous phase) because the crystal growth velocity was observed to be time-independent. In the amorphous phase, atomic transport coefficients would experience significant changes in time in an isothermal experiment due to structural relaxation (Sec. 2.2.1). The viscosity increases with time (Fig. 2.4), and similarly, the diffusivity decreases with time (Fig. 5.15). According to Eq. (5.16),  $u$  would also decrease with time in the amorphous phase (Fig. 5.15).

It should be noted, however, that this argument is *in general* not sufficient to conclude that the measurements were taken in the undercooled liquid: Far away from equilibrium, the increase in viscosity (or equivalently, the decrease in diffusivity) is usually observed to occur *linearly* with time [28, 108, 109, 110, 111, 112, 113, 114, 107]. If the viscosity is very high (note the *logarithmic* representation in Figs. 2.4 and 5.15), a further increase in viscosity due to structural relaxation in the amorphous phase may not be observable any more within the experimental timescale even though the equilibrium state of the undercooled liquid may not yet be reached. This argument, however, should not apply to the crystal growth velocity measurements in the present work: Viscosity measurements in the amorphous phase on the alloys studied in this work have shown [114, 107] that structural relaxation can clearly be observed on timescales of a few hours at temperatures between 60°C and 100°C, which is lower than the temperature range used for the growth velocity measurements in the present work (Fig. 5.14). Between 60°C and 100°C, the viscosity should even higher than in the present measurements (cf. Fig. 2.4). Hence, if structural relaxation is observable between 60°C and 100°C, it should certainly also be observable at temperatures higher than 100°C on the same timescales. At the lowest temperatures, the anneals for the growth velocity measurements were performed on timescales up to about 12 hours, but structural relaxation was not observable. Hence, it appears that in the present work the equilibrium state of the undercooled liquid is reached after the first anneal on any sample for all temperatures investigated (Fig. 5.16). Subsequent anneals, which are used to determine the crystal growth velocity, are then performed in the undercooled liquid state (Fig. 5.16). That the calorimetric glass transition is observed in the same temperature range that is used for the growth velocity measurements further underlines this statement (Chap. 8

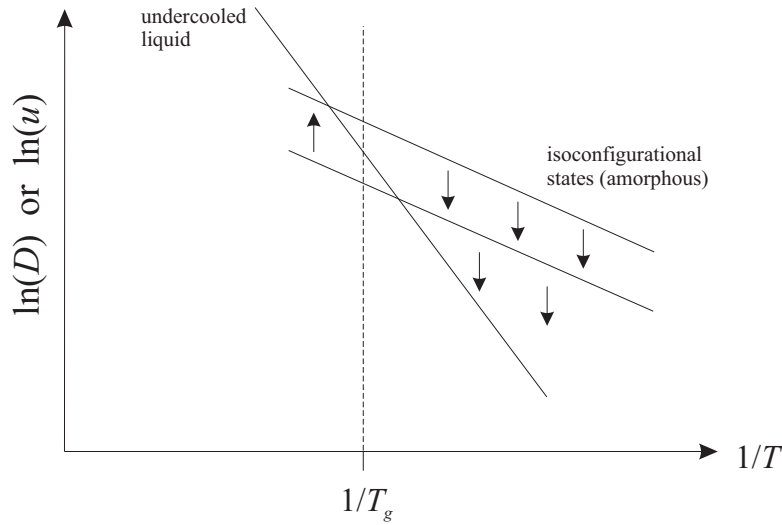


**Figure 5.15:** Schematic drawing of diffusivity  $D$  [or equivalently, crystal growth velocity  $u$ , cf. Eq. (5.16)] as a function of reciprocal temperature around the glass transition temperature  $T_g$ . Structural relaxation from the isoconfigurational states towards the undercooled liquid is indicated by arrows (cf. Figs. 2.4 and 2.9).

below).

It should be noted that the observed Arrhenius temperature dependence of the crystal growth velocity (Fig. 5.14) is not necessarily inconsistent with a Vogel-Fulcher-Tammann temperature dependence [Eq. (2.9)] since the data were taken within a relatively small temperature range of less than 50 K. Hence, a temperature dependence that is non-Arrhenius over a large temperature range can appear Arrhenius-like within a small temperature range and within the uncertainty of the measurement. Moreover, Elliott indeed points out that the Vogel-Fulcher-Tammann temperature dependence usually observed for the viscosity in undercooled liquids often becomes Arrhenius-like near  $T_g$  [23]. Finally, it should also be noted that the measured crystal growth velocity might not even be related to the viscosity if the Stokes-Einstein equation [Eq. (2.3)] is invalid below the mode coupling theory critical temperature [cf. the paragraph below Eq. (3.19)]. For this case, a Vogel-Fulcher-Tammann temperature dependence would not be expected *a priori* for the crystal growth velocity in the studied temperature range.

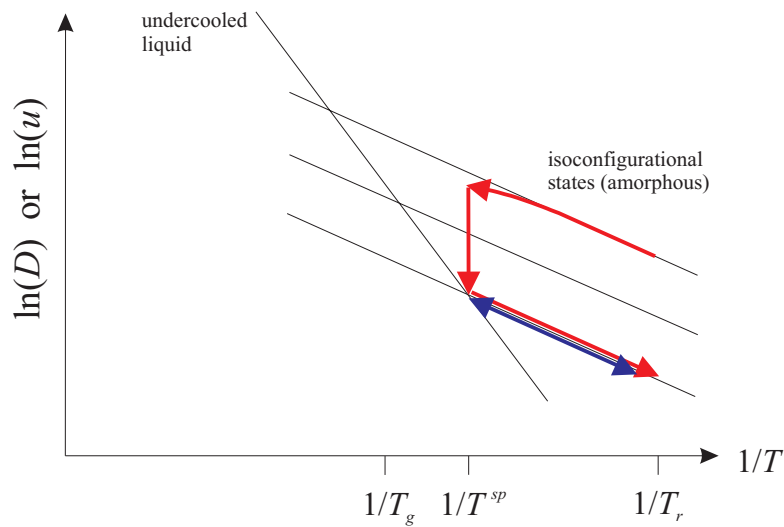


**Figure 5.16:** (Color). Schematic drawing of the evolution of the diffusivity  $D$  (or crystal growth velocity  $u$ ) in the anneals used for the experiments in Chap. 5.  $T^{sp}$  is the anneal (setpoint) temperature;  $T_r$  is the room temperature. During the first anneal at  $T^{sp}$ , the amorphous phase relaxes entirely towards the undercooled liquid (red arrows). During the subsequent anneals at  $T^{sp}$ , the undercooled liquid state is already reached immediately once the sample has been heated to  $T^{sp}$  (blue arrows). The glass transition temperature  $T_g$  shown in this plot corresponds to the value obtained by differential scanning calorimetry (DSC) measurements at a scanning rate of 40 K/min (Chap. 8). It is instructive to compare this figure to Fig. 8.2 below.

## 5.5 Conclusions

1. It was demonstrated that the combination of an AFM and a high-precision furnace provides an accurate method to determine isothermal crystallization parameters as a function of time and temperature. This method should be generally applicable to thin films that exhibit heterogeneous crystal nucleation at the film surface and a density change upon crystallization of a few percent. It *may* also be applicable to films that exhibit homogeneous nucleation or heterogeneous nucleation at the interface to the substrate.
2. All alloys exhibited interface-controlled growth (diffusion-limited kinetics) and activation energies for the growth velocity between 1.9 eV and 2.9 eV. The activation energy is largest for AgIn-Sb<sub>2</sub>Te, which exhibits growth-dominated re-crystallization of amorphous marks (Fig. 1.2). However, the difference in nucleation behavior between AgIn-Sb<sub>2</sub>Te and the GeSbTe alloys appears to be much more pronounced than this relatively small difference in growth characteristics. This suggests that the different re-crystallization mechanisms observed upon laser heating (Sec. 1.1, Fig. 1.2) can be ascribed to the significant difference in crystal nucleation behavior rather than to the smaller difference in crystal growth velocity. The continuous nucleation and the increase of the crystal density with increasing temperature as observed in the GeSbTe alloys is reflected in the nucleation-dominated re-crystallization of laser-heated amorphous marks. In contrast, the saturation of nucleation and the temperature independent crystal density observed in AgIn-Sb<sub>2</sub>Te corresponds to the growth-dominated re-crystallization of the marks.
3. The crystal growth parameters determined in this chapter can be used to model crystallization kinetics.



# Chapter 6

## The crystal morphology

### 6.1 Preface

The AFM images presented in Chap. 5 do not only allow an extraction of growth parameters, but also an extraction of nucleation parameters. However, for a correct determination of nucleation parameters, a detailed knowledge of the crystal morphology is required first, which is the focus of this chapter. The extraction of the nucleation parameters from the AFM images will be the focus of Chap. 7.

The morphology was studied by transmission electron microscopy (TEM, Sec. 4.5). The main questions to be answered are:

1. Are the growth formations in the AFM images (dark features in Figs. 5.5–5.12) single crystals or polycrystals?
2. Is nucleation heterogeneous or homogeneous?
3. In case nucleation is heterogeneous: Where are the nucleation sites located? Are they located at the film-substrate interface or at the surface of the film?

Item (1.) will be answered by plan view studies, whereas items (2.) and (3.) will be answered by cross-sectional studies. These findings will allow the determination of nucleation parameters around 150°C from the AFM images presented in Chap. 5. This will be the subject of Chap. 7.

Excerpts of Chap. 6 have also been published elsewhere [115].

## 6.2 Experimental methods

### 6.2.1 Sample preparation

The same samples that were prepared for the growth velocity measurements (films of composition  $\text{Ge}_4\text{Sb}_1\text{Te}_5$ ,  $\text{Ge}_2\text{Sb}_2\text{Te}_5$ , and  $\text{AgIn-Sb}_2\text{Te}$ , sputter-deposited on Si wafers, cf. Sec. 5.2.1 for details) were also used for the study of the crystal morphology. However, the crystal morphology for the  $\text{Ge}_1\text{Sb}_2\text{Te}_4$  films was not analyzed.

Those samples were partially crystallized by annealing in a differential scanning calorimeter (DSC) as described in Sec. 5.2.3.1. The progress of crystallization was monitored by atomic force microscopy (AFM) as described in Sec. 5.2.2.

#### 6.2.1.1 Plan view TEM sample preparation

Self-supporting discs for TEM plan view measurements were prepared from the partially crystallized samples (film thickness: 30 nm) by ultrasonic disc cutting (Gatan Model 601), dimple grinding (Gatan Model 656), and ion beam milling (Gatan Model 691) [90]:

Initially, the 640  $\mu\text{m}$ -thick sample was glued on a glass slide using superglue (the *film* side of the sample was glued to the glass). Superglue was used because it hardens at room temperature. Therefore, the sample does not have to be heated, which would induce further crystallization. A cylindrical disk of 3 mm diameter was cut from the sample using the ultrasonic disk cutter. A mixture of silicon carbide powder and water was used for cutting. Once the cut was finished, the sample was removed from the glass by dissolving the superglue in acetone for about 1 hour.

Subsequently, the disk was superglued on a glass cylinder, which acts as a sample holder for the dimple grinding step (the *film* side of the sample was glued to the glass cylinder). In this condition, the Si wafer was first polished manually from the original thickness of 640  $\mu\text{m}$  to around 150–200  $\mu\text{m}$  using silicon carbide polishing paper. The thickness was measured using a caliper gage. Subsequently, the dimple grinder was used to thin the sample in the center of the disk. A rotating wheel above the sample in combination with a diamond compound paste and water was used for thinning. The sample was rotated underneath this wheel. The final thickness in the center of the disk should be less than 20  $\mu\text{m}$ . At the rim of the disk, the thickness remained around

150–200  $\mu\text{m}$ . Afterwards, the sample was removed from the glass by dissolving the superglue in acetone for about 1 hour.

In the next step, the edges of the sample were superglued on a copper holder, which acts as a sample holder for the ion milling step (the *film* side of the sample was glued to the copper holder). The ion miller ‘bombards’ the thin specimen with energetic ions until it is thin enough to be studied by TEM. Two Ar ion guns at an angle of incidence of  $8^\circ$  were used (measured from a plane parallel to the sample). *Both* guns were aligned at the *substrate* side of the sample, not at the *film* side. The accelerating voltage during *continuous* milling was 4 kV and the beam current 2–3  $\mu\text{A}$  for each gun. The background pressure was  $10^{-6}$  Torr and the pressure during milling  $3 \times 10^{-5}$  Torr. The sample was rotated at 4 rpm during milling to avoid the formation of grooves on the surface. No cooling device was used for the sample. Once a hole was visible in the sample by a magnifying camera attached to the ion miller (typically after around 10–30 min depending on the initial thickness), the ion guns were switched off immediately. The rim of the hole is typically thin enough ( $\sim 20$ – $80$  nm) to be electron transparent. Subsequently, the superglue was dissolved in acetone for about 1 hour.

In addition to the TEM samples prepared from partially crystallized films, a TEM sample was prepared from an as-deposited  $\text{Ge}_2\text{Sb}_2\text{Te}_5$  film (i. e., from a sample that was not heated in the DSC). This sample was also analyzed by TEM in order to prove that the sample preparation did not cause artifacts. A possible artifact would be heating of the sample to elevated temperatures during ion milling, which could induce partial or complete crystallization of the film.  $\text{Ge}_2\text{Sb}_2\text{Te}_5$  was chosen because it exhibits a lower crystallization temperature than the other two alloys studied in this chapter (Fig. 5.14).

### 6.2.1.2 Cross-sectional TEM sample preparation

For  $\text{Ge}_4\text{Sb}_1\text{Te}_5$ , additional cross-sectional TEM samples on copper washers were prepared<sup>1</sup> from partially crystallized samples (film thickness: 350 nm) by mechanical tripod polishing followed by ion beam milling (Gatan Model 691) [90]. Such thick films were chosen to enable heterogeneous nucleation at the substrate and/or the film surface to be distinguished from homogeneous nucleation in the cross-sectional images.

The *film* sides of two 640- $\mu\text{m}$ -thick samples were glued face to face. Four additional

---

<sup>1</sup>The cross-sectional TEM samples were prepared by C. Y. Wen.

Si wafers of similar thickness were glued to the stack for better stability. Subsequently, the stack of six wafers was mechanically thinned from both sides (perpendicular to the planes of the wafers) using a tripod and a rotating grinding wheel (100 rpm) under running water. The final thickness of about 10  $\mu\text{m}$  was reached once the silicon became transparent for red light<sup>2</sup>. The resulting thin slice was glued between two copper washers (outer diameter: 3 mm) for stability reasons.

Subsequently, the sample was ion milled to TEM specimen thickness as described in Sec. 6.2.1.1. However, the ion guns were inclined at *opposite* sides of the specimen at an angle of 10°. The accelerating voltage was 5 kV and the beam current 8–9  $\mu\text{A}$  for each gun. The sample was rotated at 3 rpm. The beam was not operated continuously but in *pulsed* mode (using the same frequency as for the sample rotation) because the glue between the two films thins faster than the silicon.

Both plan view and cross-sectional samples were stored in vacuum after preparation until used for the measurement to reduce oxidation and to keep away moisture.

## 6.2.2 The transmission electron microscope (TEM)

A Philips TEM Model EM 420 T (thermionic electron source) operated at 100 kV was used to study the crystal morphology on the plan view samples in both bright field (BF) and centered dark field (CDF) mode (Sec. 4.5). CDF was preferred towards displaced aperture dark field (DF) for better resolution.

A JEOL 2010 FEG TEM/STEM operated at 200 kV was used to study the cross-sectional samples in BF mode<sup>3</sup>. This microscope was also used to perform high resolution transmission electron microscopy (HRTEM) and energy dispersive x-ray spectroscopy (EDS) on the plan view samples<sup>4</sup>.

---

<sup>2</sup>Below a thickness of about 10  $\mu\text{m}$ , Si is transparent for red light.

<sup>3</sup>FEG: field emission gun; STEM: scanning transmission electron microscope

<sup>4</sup>The JEOL 2010 FEG TEM/STEM was operated by C. Y. Wen.

## 6.3 Results

### 6.3.1 Plan view analysis

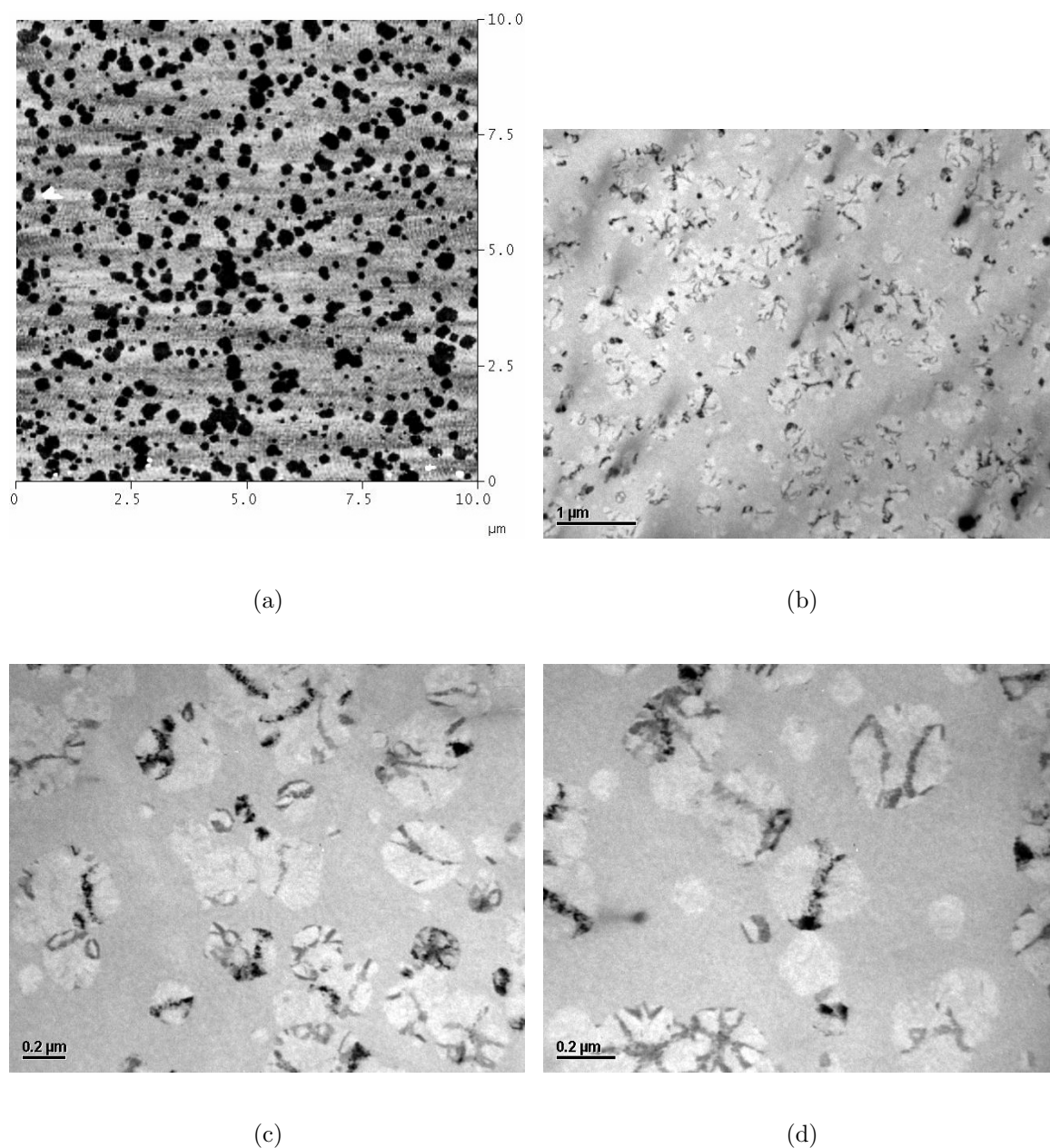
#### 6.3.1.1 Low magnification TEM

Figure 6.1 shows an AFM image and three TEM BF images, all taken on the same  $\text{Ge}_4\text{Sb}_1\text{Te}_5$  sample (the AFM image was taken before the TEM sample preparation). Approximately circular crystals are observed by either bright or dark diffraction contrast in the TEM images (depending on the alignment of the diffracting planes with respect to the incident electron beam). A comparison of Fig. 6.1(a) with Figs. 6.1(b)–6.1(d) shows that the dark features observed in the AFM image exhibit the same size and number density as the crystals observed in the TEM images. The same was observed for  $\text{Ge}_2\text{Sb}_2\text{Te}_5$  and  $\text{AgIn-Sb}_2\text{Te}$  (not shown). This unequivocally shows that the dark features observed by AFM (e. g., Figs. 5.5–5.12) are *indeed* crystals. Additionally, this shows that the TEM sample preparation (in particular, the ion milling step) did not heat the sample to temperatures higher than around 120°C. Otherwise, the crystals observed in the TEM would be larger than the crystals observed in the AFM.

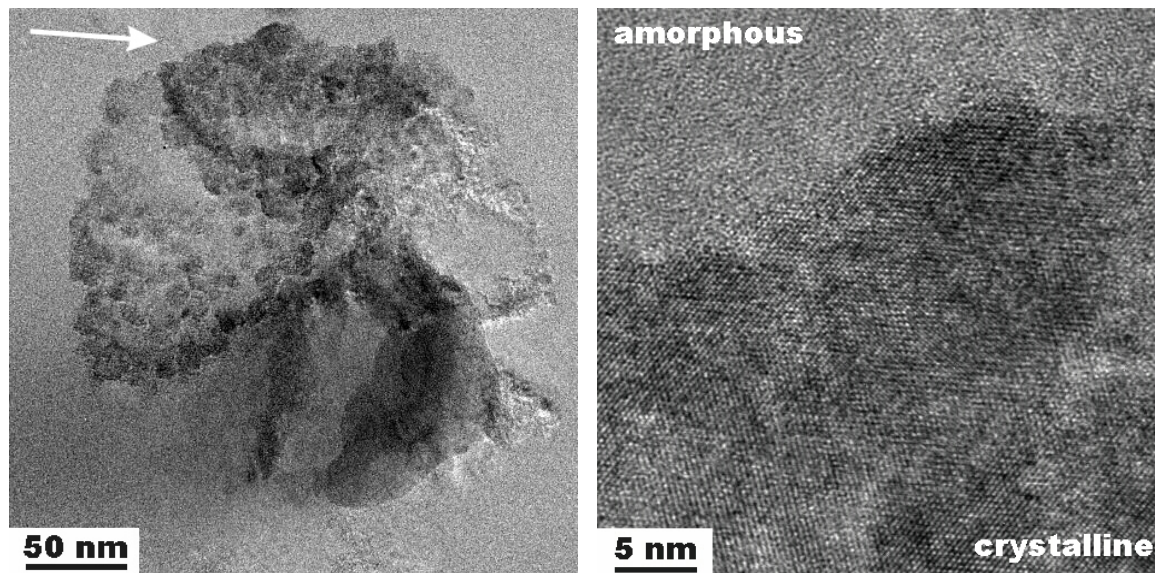
The TEM sample prepared from the as-deposited  $\text{Ge}_2\text{Sb}_2\text{Te}_5$  film did not show any evidence of partial crystallization: No crystals were observed in the BF images (not shown). The corresponding selected area electron diffraction (SAD) patterns showed those rings (‘halos’) that are typically observed for an amorphous structure (not shown) [90]. This additionally shows that the sample preparation did not heat the sample to elevated temperatures, where crystallization occurs. This also shows that the sputter deposition method (Sec. 5.2.1) produces *entirely* amorphous samples, which is in agreement with earlier studies by X-ray diffraction (XRD) on similarly prepared amorphous films in the same sputter chamber [8, 94].

#### 6.3.1.2 High magnification TEM

HRTEM images were taken on a  $\text{Ge}_4\text{Sb}_1\text{Te}_5$  crystal (Fig. 6.2). Figures 6.2(b) and 6.2(c) show the phase contrast [90] resulting from the lattice planes for the crystal shown in Fig. 6.2(a).

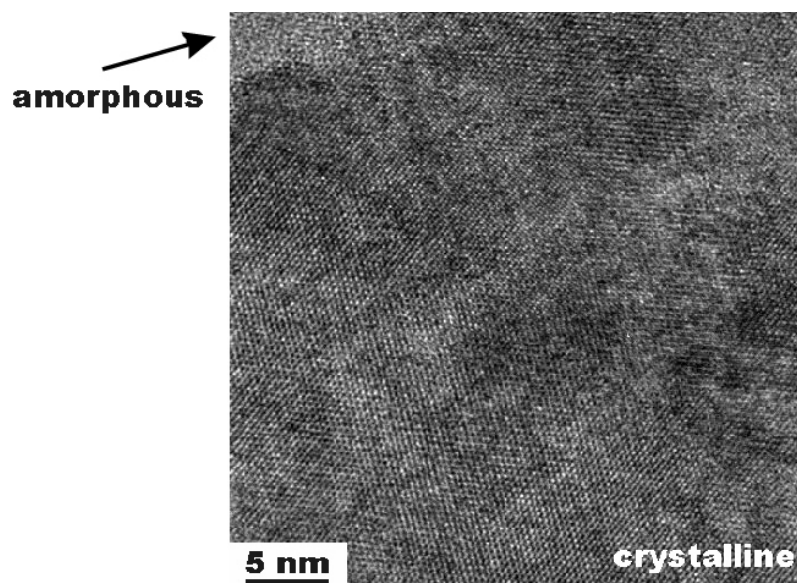


**Figure 6.1:** (a) AFM image (dimensions: 10  $\mu\text{m}$  by 10  $\mu\text{m}$ ) of a  $\text{Ge}_4\text{Sb}_1\text{Te}_5$  sample that was annealed for 8.7 min at 160  $^\circ\text{C}$ . The height scale is shown in Fig. 5.13. (b)–(d) BF TEM images of the *same* sample after thinning to electron transparency (Sec. 6.2.1.1). The large dark features in (b) are artifacts (probably as a result of contamination during the TEM sample preparation). A comparison of the size and the number density of the depressions in (a) with the crystals in (b)–(d) reveals that the AFM indeed probes crystals: All four images show maximum crystal diameters of about 500 nm and a crystallized surface fraction on the order of 25%. Microscope [(b)–(d)]: Philips EM 420 T.



(a)

(b)



(c)

**Figure 6.2:** (a) BF TEM image of a  $\text{Ge}_4\text{Sb}_1\text{Te}_5$  crystal. The top left location indicated by the arrow was used for the BF HRTEM images shown in (b) and (c). Microscope: JEOL 2010 FEG.

### 6.3.1.3 Crystal curvature

Figures 6.3–6.5 show a crystal for each of the three alloys in both BF and CDF mode. Upon tilting the sample in *image mode* (both BF and CDF), the contrast moved *continuously* over the crystal. This was observed for all three alloys on many crystals and is demonstrated in Figs. 6.3–6.5 for one crystal per alloy at three tilting angles. Upon tilting the sample in *selected area electron diffraction mode* (SAD), the location of the diffraction spots did not change on any crystal for any of the alloys. Therefore, in all three alloys each observed growth formation is a single crystal (not a polycrystal) that is curved *continuously* (bend contours [90]). Using a double tilt holder, it was demonstrated for all alloys and for each crystal that this curvature is present for *any* tilt axis in the film plane. Figures 6.3–6.5 show only one example for one tilt axis. Independent of its crystallographic orientation, each crystal, therefore, is shaped like a *spherical* cap. The bend contours are an intrinsic property of the crystal rather than a sample preparation artifact such as bending of the entire foil. The radius of crystal curvature, as shown in Fig. 6.6, is on the order of 1  $\mu\text{m}$  ( $\text{Ge}_4\text{Sb}_1\text{Te}_5$  and  $\text{AgIn-Sb}_2\text{Te}$ ) and 2  $\mu\text{m}$  ( $\text{Ge}_2\text{Sb}_2\text{Te}_5$ ), far smaller than the dimensions of the observable film. Hence, the observed magnitude of crystal curvature cannot continue in the amorphous surrounding. Crystal curvatures of similar magnitude as shown in Fig. 6.6 were reported by Kooi and co-workers for  $\text{Ge}_2\text{Sb}_2\text{Te}_5$  [101] and  $\text{Sb}_{3,6}\text{Te}$  [116]. The sign of the curvature was carefully checked for many crystals on all three alloys and was always found to be the same (see Figs. 6.3–6.6). The same sign was also observed by Kooi and De Hosson [116].

### 6.3.1.4 Diffraction contrast and amorphous-crystalline interface

For  $\text{AgIn-Sb}_2\text{Te}$ , the amorphous-crystalline interface appears very rough, and the BF and CDF images exhibit a spotted diffraction contrast (features with size on the order of 10 nm, Fig. 6.5). This is also true to a lesser extent for  $\text{Ge}_4\text{Sb}_1\text{Te}_5$  (Fig. 6.3), but not for  $\text{Ge}_2\text{Sb}_2\text{Te}_5$  (Fig. 6.4). In agreement with the discussion above (continuous crystal curvature) this contrast cannot be due to grains of size 10 nm having slightly different orientations because no arcs are visible in the SAD pattern (very short segments of the rings that are typically observed in poly-crystalline films, Fig. 6.7) [90, 117]. The spotted diffraction contrast and the rough interface may be due to local strain fields

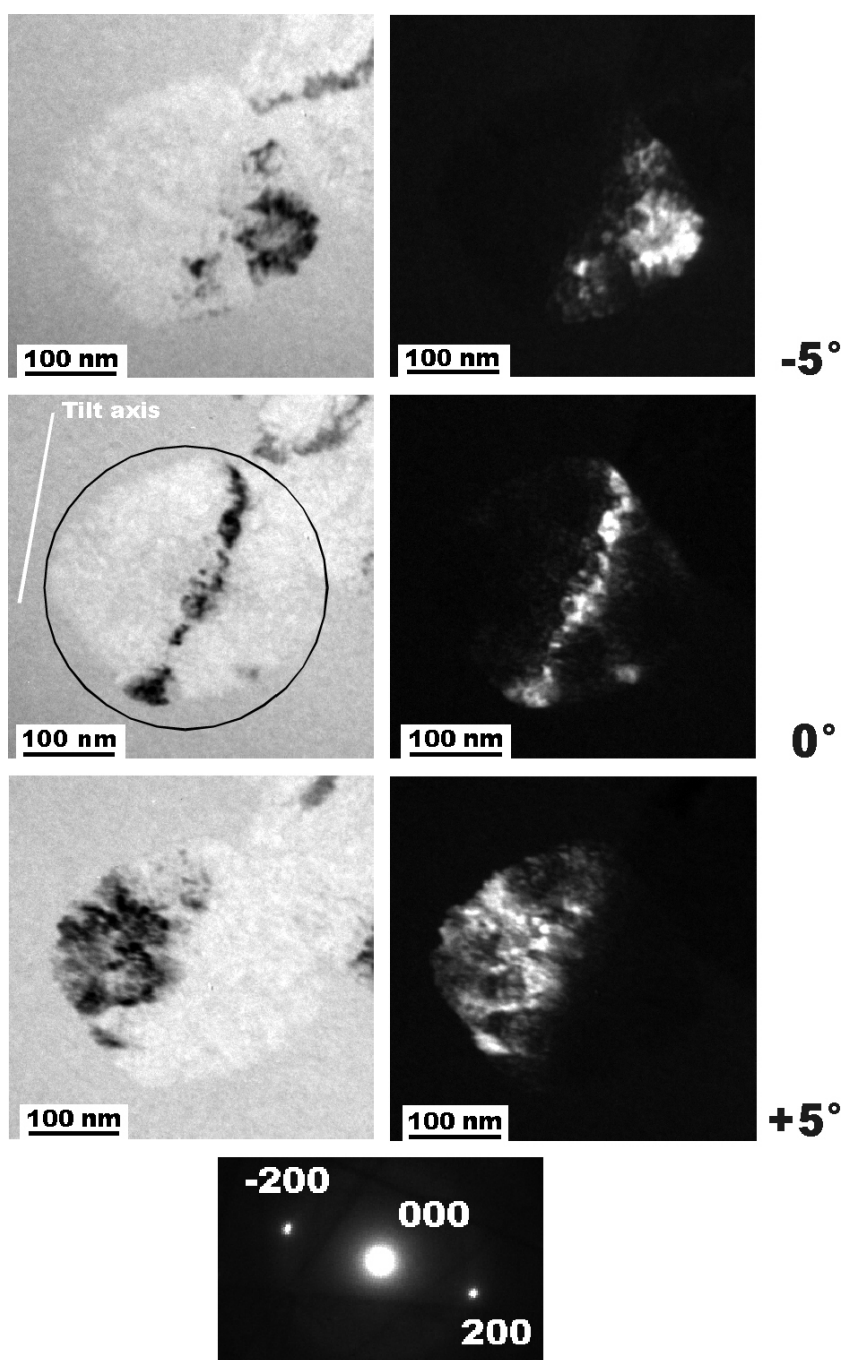


**Figure 6.3:** Bright field (BF, left) and centered dark field (CDF, right) images of a  $\text{Ge}_4\text{Sb}_1\text{Te}_5$  crystal for three tilting angles,  $5^\circ$  apart. The corresponding rotation-calibrated selected area diffraction (SAD) pattern is shown underneath. The location of the SAD aperture and the direction of the sample tilt axis are indicated in the BF image for  $0^\circ$ . The 200-diffraction was used for the CDF images. Before the TEM specimen preparation, the sample was annealed for 8.7 min at  $160^\circ\text{C}$ . Microscope: Philips EM 420 T.

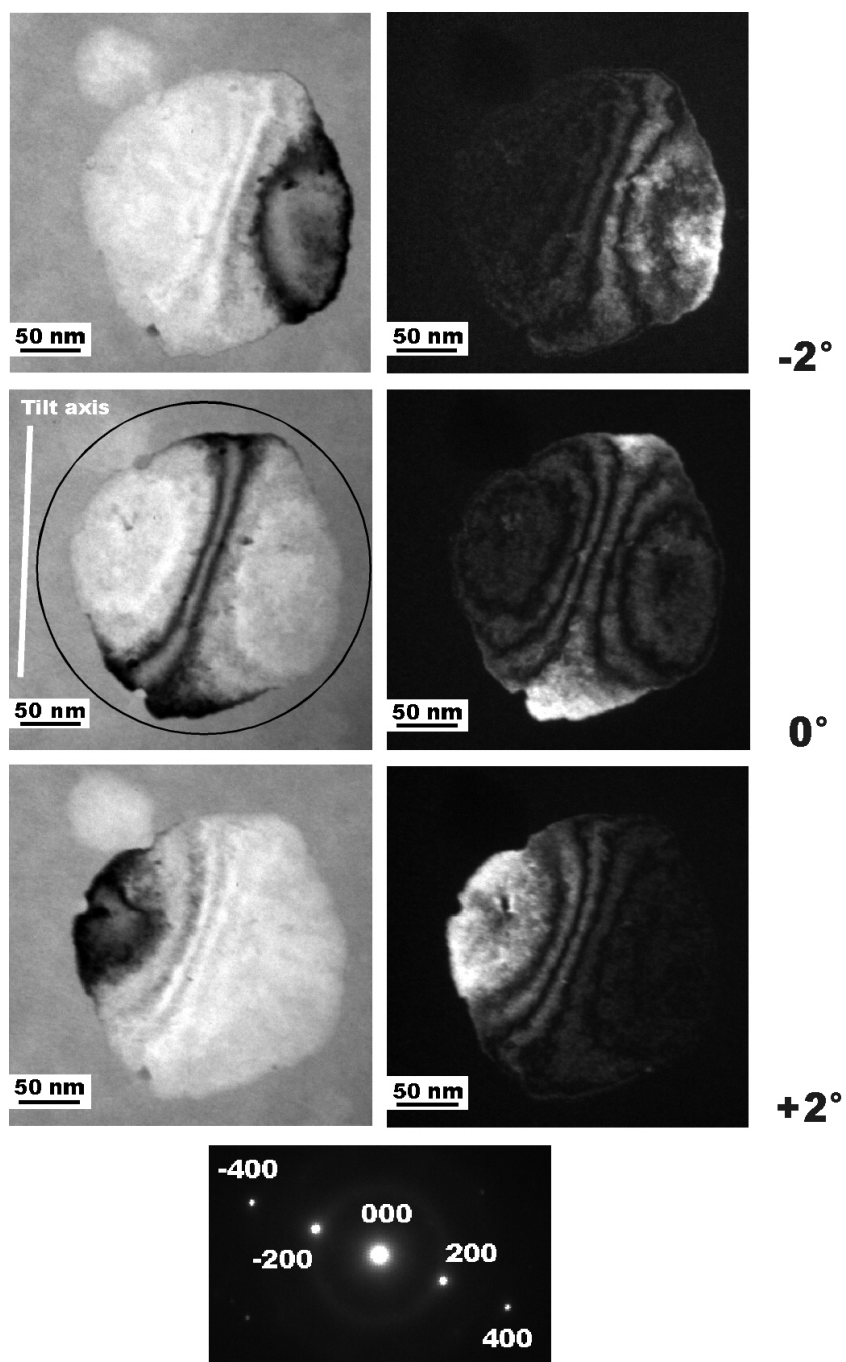


**Figure 6.4:** Bright field (BF, left) and centered dark field (CDF, right) images of a  $\text{Ge}_2\text{Sb}_2\text{Te}_5$  crystal for three tilting angles,  $2^\circ$  apart. The corresponding rotation-calibrated selected area diffraction (SAD) pattern is shown underneath. The location of the SAD aperture and the direction of the sample tilt axis are indicated in the BF image for  $0^\circ$ . The 200-diffraction was used for the CDF images. Before the TEM specimen preparation, the sample was annealed for 600 min at  $115^\circ\text{C}$ . Microscope: Philips EM 420 T.

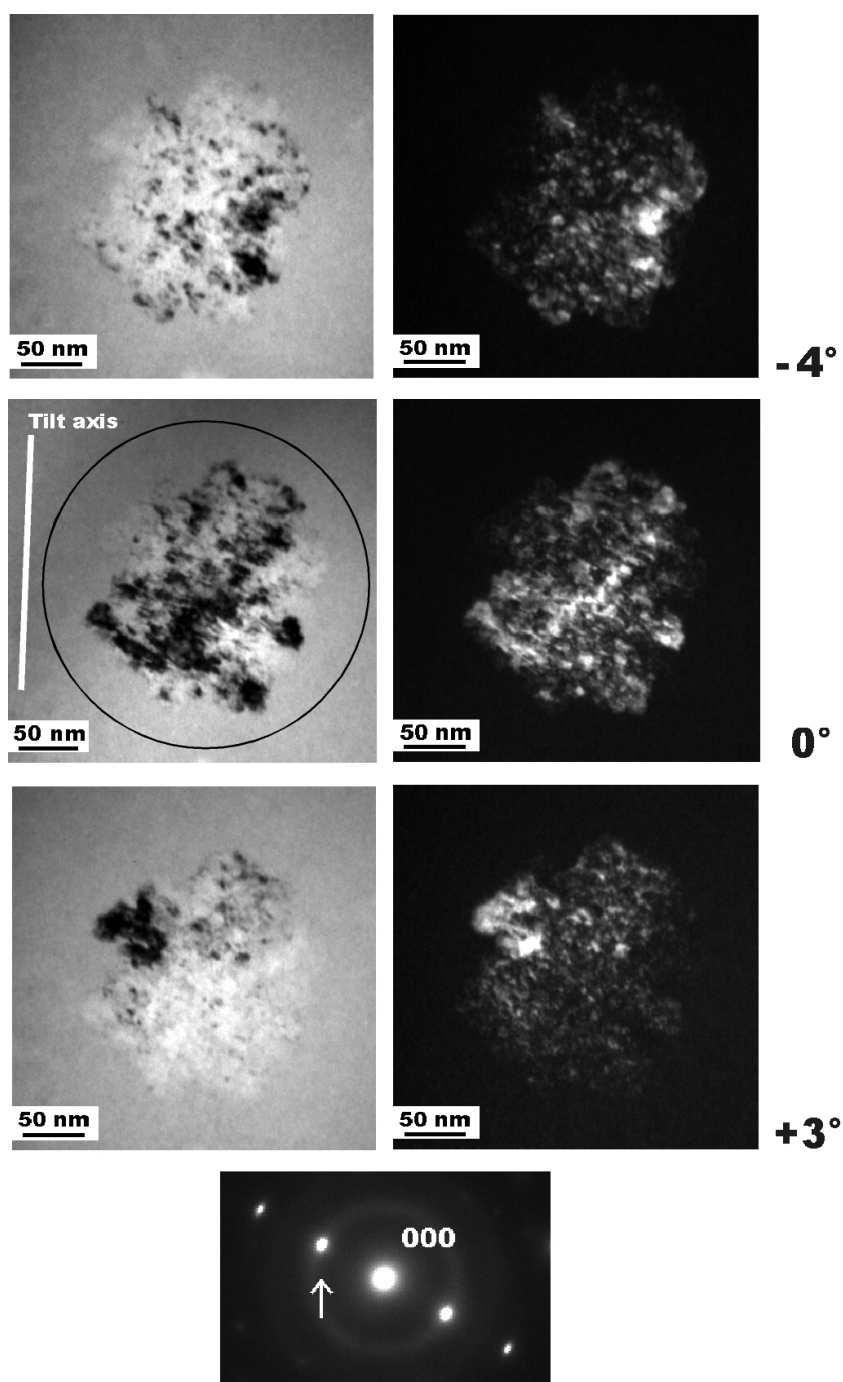


**Figure 6.5:** Bright field (BF, left) and centered dark field (CDF, right) images of a AgInSb<sub>2</sub>Te crystal for three tilting angles. The corresponding rotation-calibrated selected area diffraction (SAD) pattern is shown underneath. The location of the SAD aperture and the direction of the sample tilt axis are indicated in the BF image for 0°. The diffraction indicated by an arrow (Miller indices were not determined) was used for the CDF images. Before the TEM specimen preparation, the sample was annealed for 5.9 min at 160°C. Microscope: Philips EM 420 T.

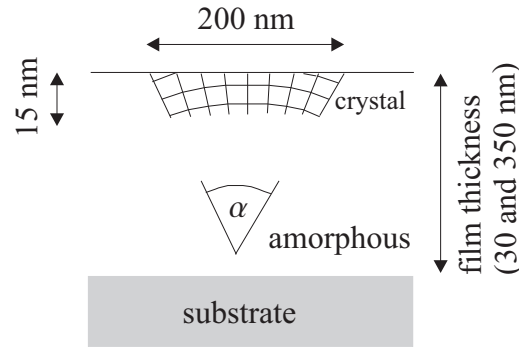


**Figure 6.6:** Schematic illustration of heterogeneous crystal nucleation at the film surface. The crystals are only 15 nm thick normal to the film surface, but more than one order of magnitude wider in lateral direction. A typical tilt angle  $\alpha$  for a 200-nm-wide crystal in a 30-nm-thick film is  $(11 \pm 2)^\circ$  [ $\text{Ge}_4\text{Sb}_1\text{Te}_5$  and  $\text{AgIn-Sb}_2\text{Te}$ ], and  $(5 \pm 2)^\circ$  [ $\text{Ge}_2\text{Sb}_2\text{Te}_5$ ]. The decrease in film height upon crystallization of 1-2 nm [e. g., Figs. 5.5–5.12] is not shown here for simplicity. The sign of the curvature is the same for all alloys.

caused by stacking faults, which tilt the diffraction planes locally into and out of the Bragg condition (Fig. 6.8) [90, 117]. For  $\text{AgIn-Sb}_2\text{Te}$ , the stacking faults are probably due to the  $\text{AgIn}$  doping. Kooi and co-workers [101] observed this spotted diffraction contrast also for  $\text{Ge}_2\text{Sb}_2\text{Te}_5$ . This discrepancy with our observations may be the result of slight differences in stoichiometry and their effect on the formation of stacking faults. It should be noted that Kooi and co-workers use the terminology “colony of grains with a size 10nm” rather than “spotted diffraction contrast” for this observation [101]. This terminology is not quite accurate, because the crystals are curved continuously. However, private communication with the authors revealed that their terminology was indeed used to describe the same “spotted diffraction contrast”.

The rougher interface for  $\text{AgIn-Sb}_2\text{Te}$  may be related to the fact that a higher crystal growth velocity is observed for this alloy than for the other two alloys upon laser-induced crystallization [3]: The factor  $f_s$  in Eq. (3.39) increases with increasing interface roughness.

The BF image in Fig. 6.4 for  $0^\circ$  shows *two* parallel dark lines because the Bragg condition for the (200) planes is satisfied *exactly* in two locations due to the sample curvature (Fig. 6.9) [90]. The CDF image in Fig. 6.4 shows more bright lines because (a) double diffraction occurs, (b) diffraction occurs both at the front and at the back

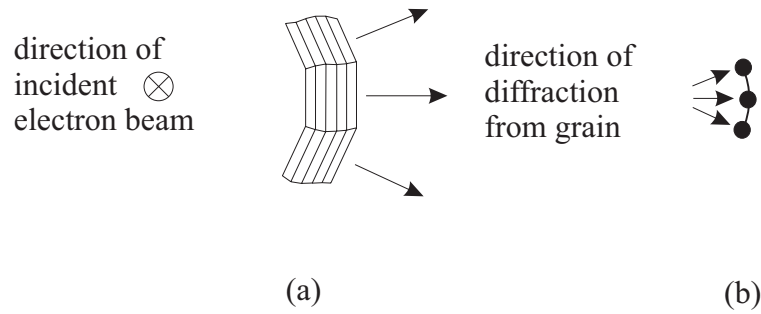


**Figure 6.7:** Schematic illustration of diffraction from grains in the TEM (top view of the sample). (a) Three grains having slightly different orientation are exposed to diffraction. The parallel lines within each grain represent diffraction planes. (b) The corresponding rotation-calibrated SAD pattern. Each of the three diffraction spots (full circles) result from the diffraction from one grain. Together, those spots appear as an arc (a segment of a ring).

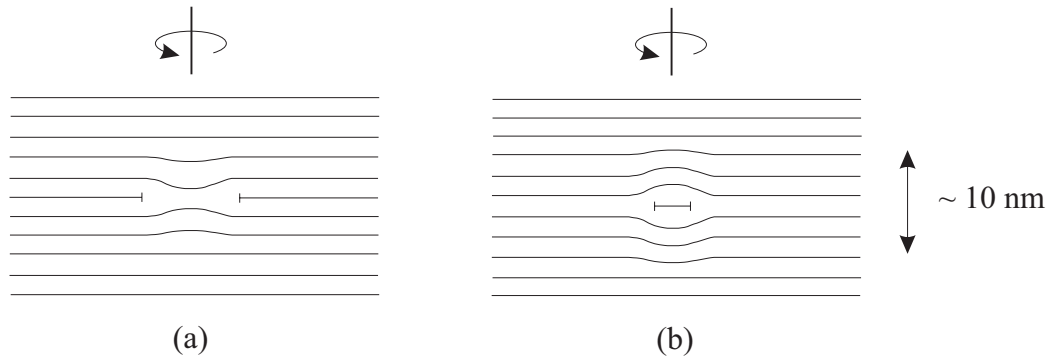


**Figure 6.8:** Schematic illustration of stacking faults (*local* dislocations, two possibilities), which can tilt the diffraction planes locally into and out of the Bragg condition, and which are therefore assumed to induce the spotted diffraction contrast observed in the BF and CDF images (Figs. 6.3 and 6.5). The stacking faults are rotationally symmetric with respect to the axes drawn on top of the illustrations.

of the planes and (c) CDF was used rather than DF for better image resolution. The pair of parallel dark lines in the BF images of Fig. 6.4 should also appear in the BF images for the other two alloys (Figs. 6.3 and 6.5) but cannot be separated because (a) the crystal curvature is larger for these alloys (cf. Fig. 6.6) so that these lines move closer together in space (cf. Fig. 6.9), and (b) the spotted diffraction contrast (as discussed above) prevents their resolution. Two parallel dark lines were also observed by Kooi and De Hosson [116] in BF images on  $\text{Sb}_{3.6}\text{Te}$  crystals doped with 5% of Ge. Therefore, this fits well with the explanation given above: this alloy did not show spotted diffraction contrast so that these lines are revealed. Similarly, these lines were not observed by Kooi and co-workers [101] for  $\text{Ge}_2\text{Sb}_2\text{Te}_5$  due to the spotted diffraction contrast in their images.

### 6.3.1.5 Crystal structure and texture

Analysis of the SAD patterns of many crystals showed that no obvious crystallographic texture was present in any of the alloys studied here. The SAD patterns match perfectly with a face-centered cubic crystal structure for the GeSbTe alloys [lattice parameter:  $a = (6.02 \pm 0.04) \text{ \AA}$  for  $\text{Ge}_4\text{Sb}_1\text{Te}_5$ , and  $a = (6.04 \pm 0.03) \text{ \AA}$  for  $\text{Ge}_2\text{Sb}_2\text{Te}_5$ ], in agreement with other studies of these alloys [7, 8, 101, 118, 94]. The camera length was calibrated using the SAD pattern of the Si substrate. Kooi and co-workers [101] observed texture in their TEM studies of  $\text{Ge}_2\text{Sb}_2\text{Te}_5$ : crystals with the  $\{111\}$  planes parallel to the surface were most abundant. The reason for this difference is unclear.

### 6.3.1.6 Energy dispersive x-ray spectroscopy (EDS)

EDS line scans were performed across several crystals for all alloys. For this purpose, the JEOL 2010 FEG microscope was operated in the STEM mode (cf. Sec. 4.5). The result is shown for one crystal per alloy in Figs. 6.10–6.12. Each data curve in Figs. 6.10–6.12 represents one characteristic x-ray *series* (cf. Fig. 4.6). For instance, the Te-K curve represents the relative number of x-ray photon counts resulting from electrons that undergo a transition from *any* atomic shell to the K-shell. In other words, the Te-K curve illustrates joint contributions from the  $\text{K}_\alpha$ ,  $\text{K}_\beta$ , and  $\text{K}_\gamma$  lines, and so on (cf. Fig. 4.6). The photon energy in the M series is too low to be detected. Si and C were also detected (from the substrate and as a result of the hydrocarbon build-up during

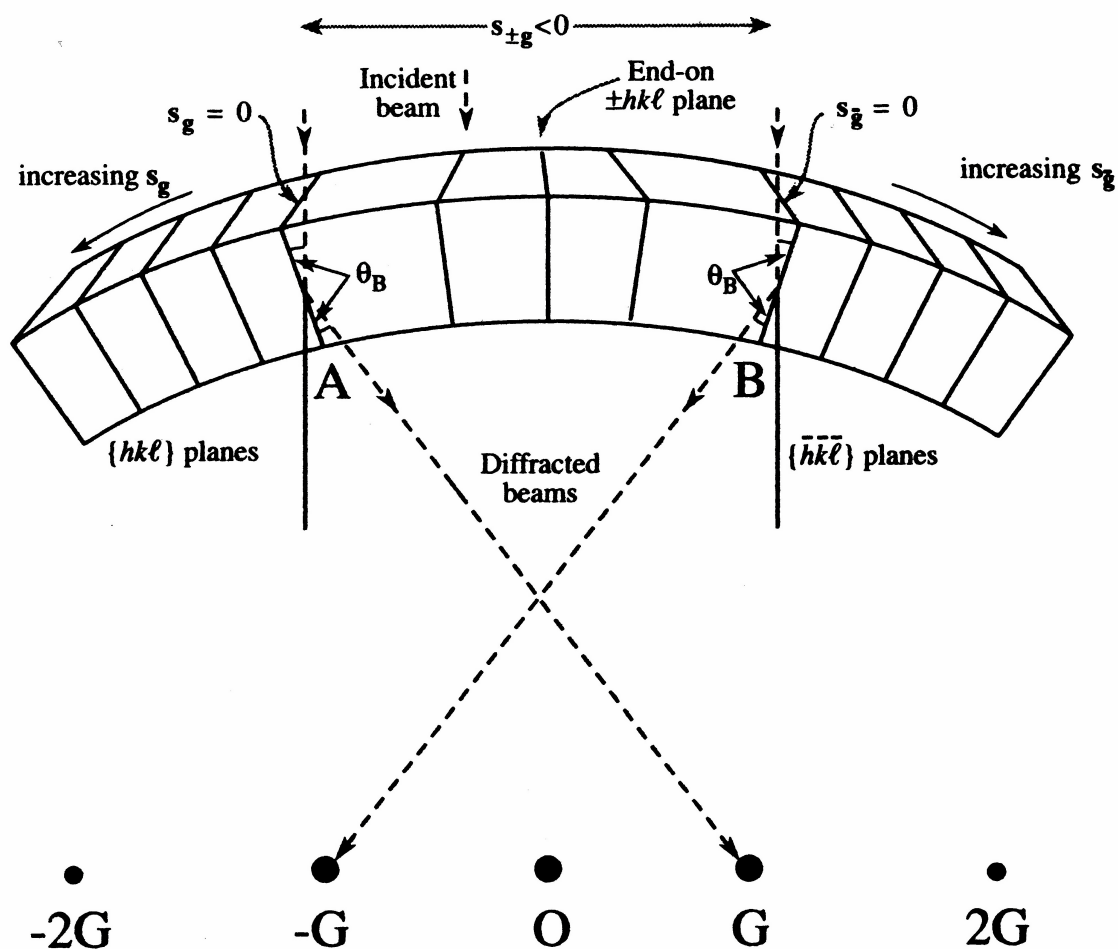


**Figure 6.9:** Schematic illustration of a bent TEM specimen. The Bragg condition for the  $(hkl)$  planes is satisfied *exactly* in two locations (at points A and B). The corresponding Bragg angle is  $\theta_B$ , and the corresponding diffractions in the diffraction pattern underneath (equivalently: the reciprocal lattice) are labelled as  $G$  and  $-G$ . The direct beam in the diffraction pattern (i.e., the origin of the reciprocal lattice) is labelled as  $O$ . The vector  $s_g$ , which is not discussed in this work, is the excitation error that corresponds to the diffraction  $G$ . From [90].

scanning, respectively), but were not included in Figs. 6.10–6.12 for the calculation of the *relative* number of counts.

The spatial resolution in EDS is theoretically only limited by the beam diameter in the STEM mode, i. e., as good as 0.1 nm [90]. However, this may only be reached for ideal (very thin) samples. A more likely value for less ideal samples is a few nanometers. In these experiments, the resolution is also limited by the distance of the data points in Figs. 6.10–6.12, i. e., about 12–24 nm depending on the alloy (see captions). Within this resolution, no composition change upon crystallization could be observed, i. e., crystal and amorphous surrounding exhibit the same chemical composition. This is in line with the observation of a time-independent crystal growth velocity and confirms that interface-controlled (not diffusion-controlled) growth occurs (cf. Sec. 5.4.1). The same was reported by Kooi and De Hosson [116] on their  $\text{Sb}_{3.6}\text{Te}$  films.

The x-ray analysis (Figs. 6.10–6.12) remains *qualitative*, i. e., it shows that the overall film composition does not change along the line scan. A *quantitative* analysis, which is not necessary for this argument, would involve a determination of this composition from the data in Figs. 6.10–6.12. This is more complicated and was not performed.

### 6.3.2 Cross-sectional analysis

Cross-sectional TEM on the alloy  $\text{Ge}_4\text{Sb}_1\text{Te}_5$  (Figs. 6.13 and 6.14) showed that crystals only nucleate heterogeneously at the (naturally oxidized) film surface. The HRTEM micrograph in Fig. 6.14 shows the phase contrast resulting from the lattice planes. This figure also shows a Moiré pattern<sup>5</sup>, probably as a result of the crystal curvature discussed in Sec. 6.3.1.3. As also confirmed by SAD, heterogeneous nucleation at the Si substrate (Fig. 6.15) and homogeneous nucleation were not observed. The same was reported by Jeong and co-workers [119] for  $\text{Ge}_2\text{Sb}_2\text{Te}_5$  films sputter-deposited on Si substrates (without the use of a capping layer, i. e., exposed to natural oxidation as well).

Crystals are more than ten times wider than they are thick (Figs. 6.6 and 6.13). As the crystallographic orientations were observed to be random, this strong anisotropy cannot be the result of texture. It may be related to local strain fields (due to the

---

<sup>5</sup>A Moiré pattern is an interference pattern created when two grids are overlaid at an angle, or when they have slightly different mesh sizes.

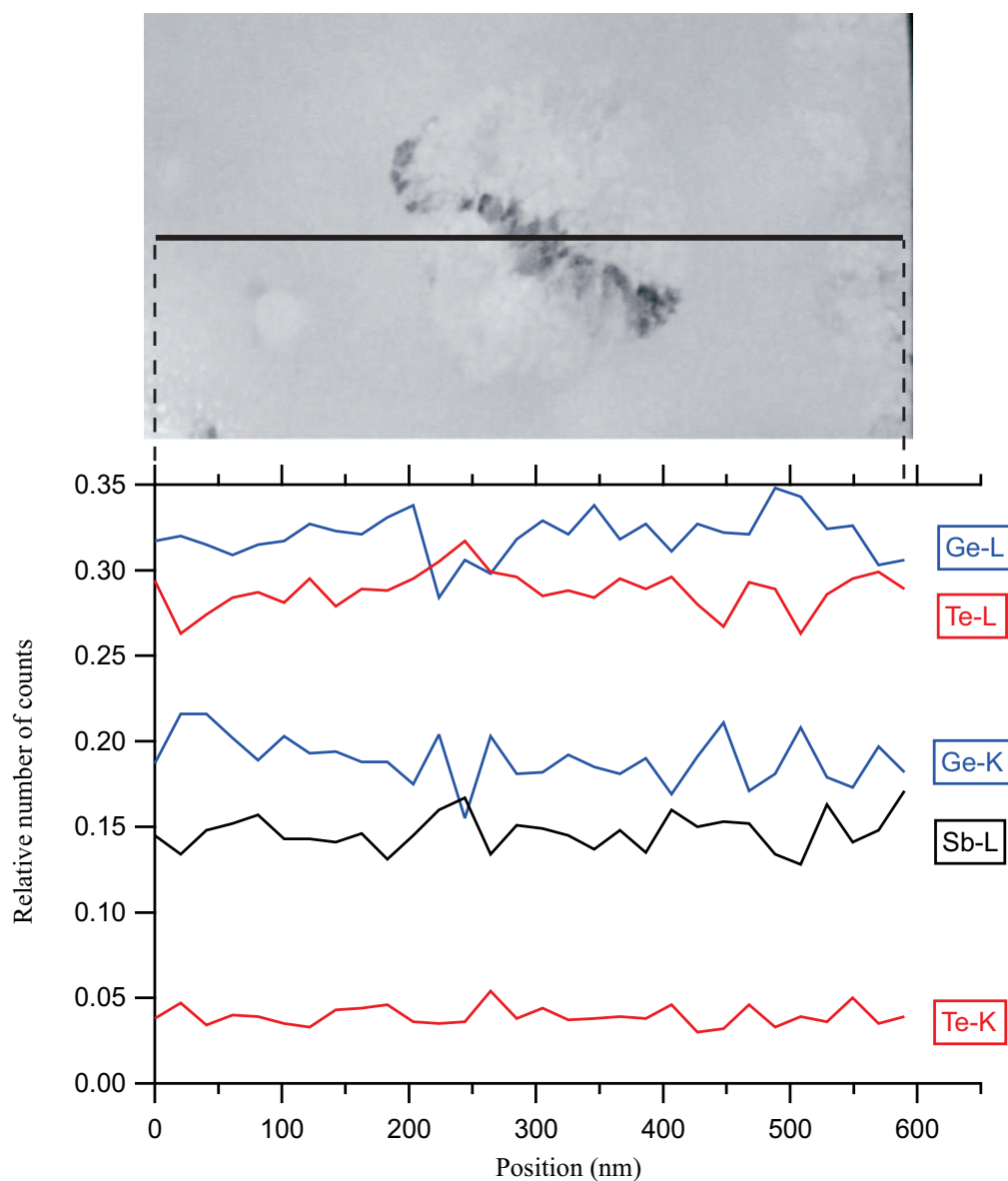


**Figure 6.10:** (Color). EDS line scan across a  $\text{Ge}_4\text{Sb}_1\text{Te}_5$  crystal (total length: 590 nm). The scan was performed along the black horizontal line shown in the BF STEM image at the top. Photons were counted for 15 s at each of the 30 equidistant locations, 20.3 nm apart. Microscope: JEOL 2010 FEG.

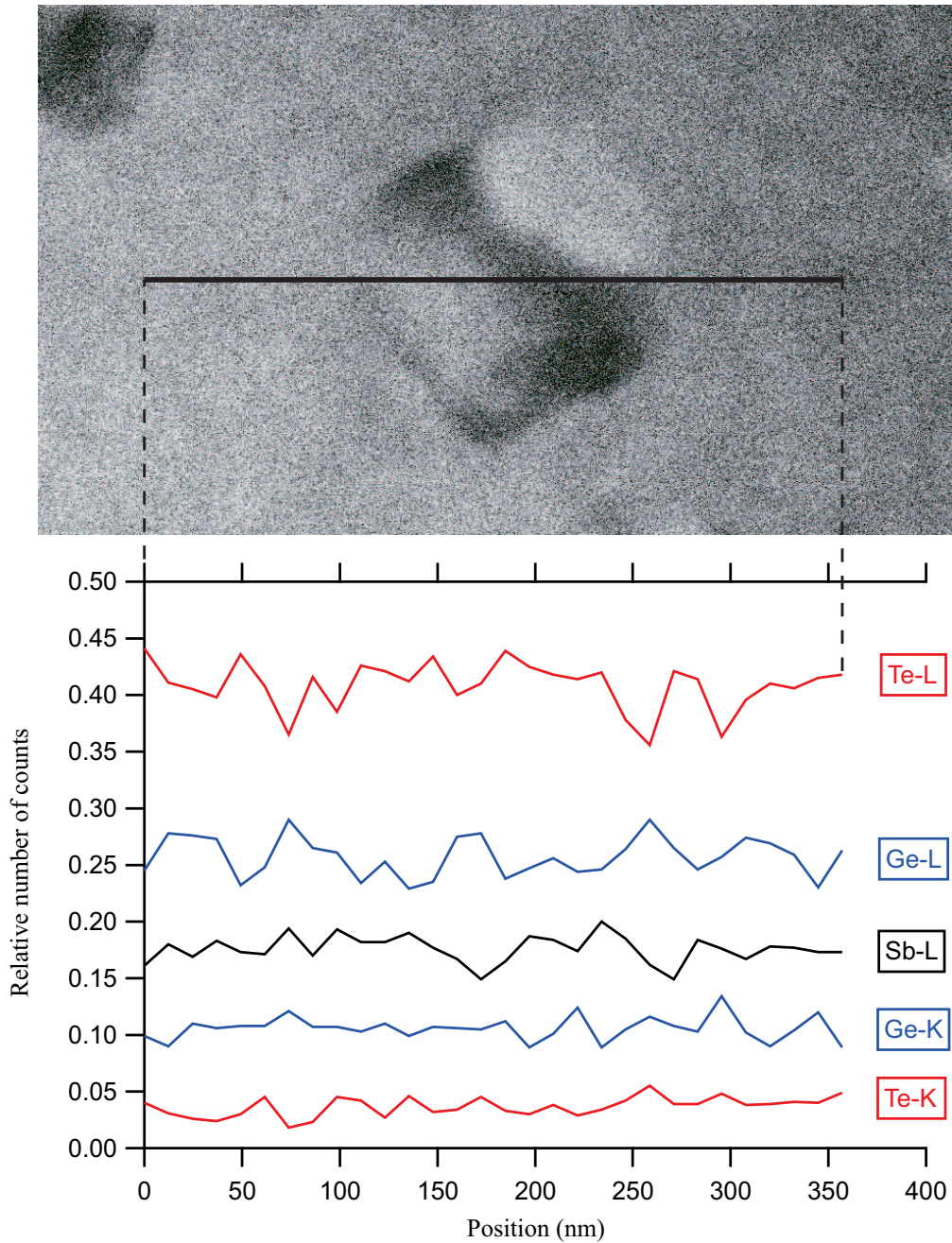


**Figure 6.11:** (Color). EDS line scan across a  $\text{Ge}_2\text{Sb}_2\text{Te}_5$  crystal (total length: 357 nm). The scan was performed along the black horizontal line shown in the BF STEM image at the top. Photons were counted for 30 s at each of the 30 equidistant locations, 12.3 nm apart. The quality of the STEM image is lower than in Fig. 6.10, probably as a result of a thicker (i. e., less ideal) sample. Microscope: JEOL 2010 FEG.

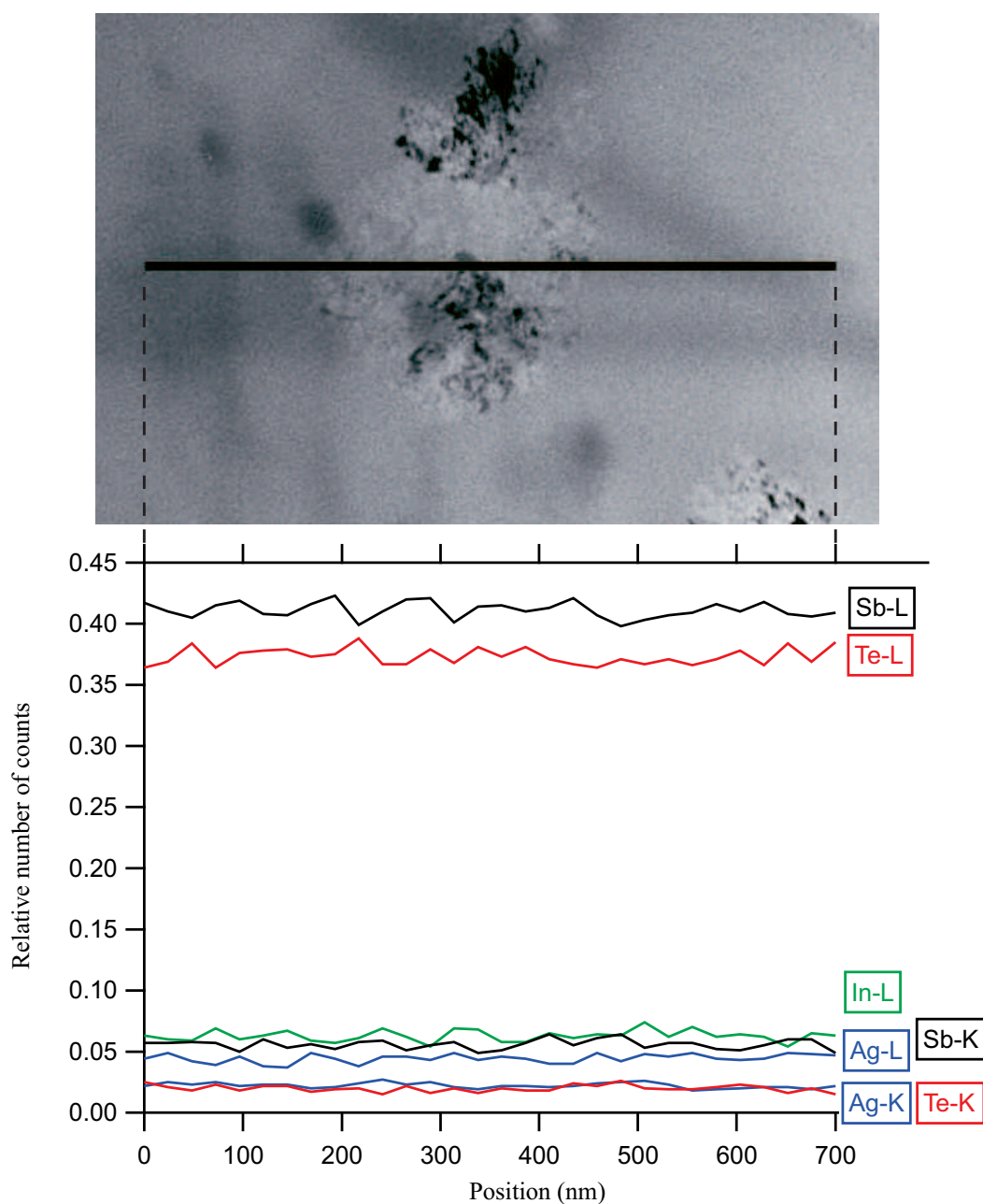


**Figure 6.12:** (Color). EDS line scan across a  $\text{AgIn-Sb}_2\text{Te}$  crystal (total length: 700 nm). The scan was performed along the black horizontal line shown in the BF TEM (*not* STEM) image at the top. The BF TEM image was taken after the EDS measurement and is shown instead of the STEM image because its resolution is better. Photons were counted for 30 s at each of the 30 equidistant locations, 24.1 nm apart. Microscope: JEOL 2010 FEG.

density change upon crystallization [7, 9, 102, 94]) that favor growth in the lateral direction and inhibit growth in the normal direction.

## 6.4 Discussion

### 6.4.1 Heterogeneous nucleation sites

Heterogeneous nucleation was only observed at the film surface (Sec. 6.3.2). X-ray reflectometry (XRR) measurements on both as-deposited films as well as on films annealed at temperatures between 100°C and 200°C revealed an oxidation layer with a thickness between about 0.5 and 2 nm for  $\text{Ge}_4\text{Sb}_1\text{Te}_5$ ,  $\text{Ge}_2\text{Sb}_2\text{Te}_5$ , and  $\text{AgIn-Sb}_2\text{Te}$  [94]. For the GeSbTe alloys, it is likely that either GeO or  $\text{GeO}_2$  is formed since the free energy of formation is lower for these oxides compared to all other oxides that can form from the elements contained in the GeSbTe alloys<sup>6</sup> (Fig. 9.1 below). For this case, the GeSbTe film depletes in germanium in the vicinity of the GeO or  $\text{GeO}_2$  layer, which could favor crystal nucleation. Indeed, it was observed by Yamada and co-workers [120] that a decreasing germanium concentration in amorphous GeSbTe films lowers the crystallization temperature upon furnace heating at a constant heating rate.

As an alternative or additional explanation, nucleation might be triggered by the atomic structure of the oxide (which for this explanation does not necessarily need to be GeO or  $\text{GeO}_2$ ). In order to catalyze nucleation, the oxide needs to be crystalline or at least nanocrystalline: Heterogeneous nucleation sites are usually crystalline. This was quantitatively first demonstrated by Turnbull and Cech, who undercooled liquid metallic droplets on glass surfaces by as much as 20% below their melting temperature  $T_m$  [121]. In a later study, Devaud and Turnbull undercooled liquid Si droplets on a glass surface by 17% [122, 123]. It will also be shown in Chap. 9 that the alloys studied in this work can be undercooled significantly by embedding them in a liquid flux.

Heterogeneous nucleation at the film-substrate interface was not observed in the cross-sectional analysis above. Indeed, this would not be expected: all Si substrates used throughout this work (layer 2 in Figs. 6.13 and 6.15) are covered by a natural  $\text{SiO}_2$

---

<sup>6</sup>However, it should be noted that not only thermodynamic, but also kinetic aspects determine which oxide forms. Hence, the formation of other oxides cannot be excluded.

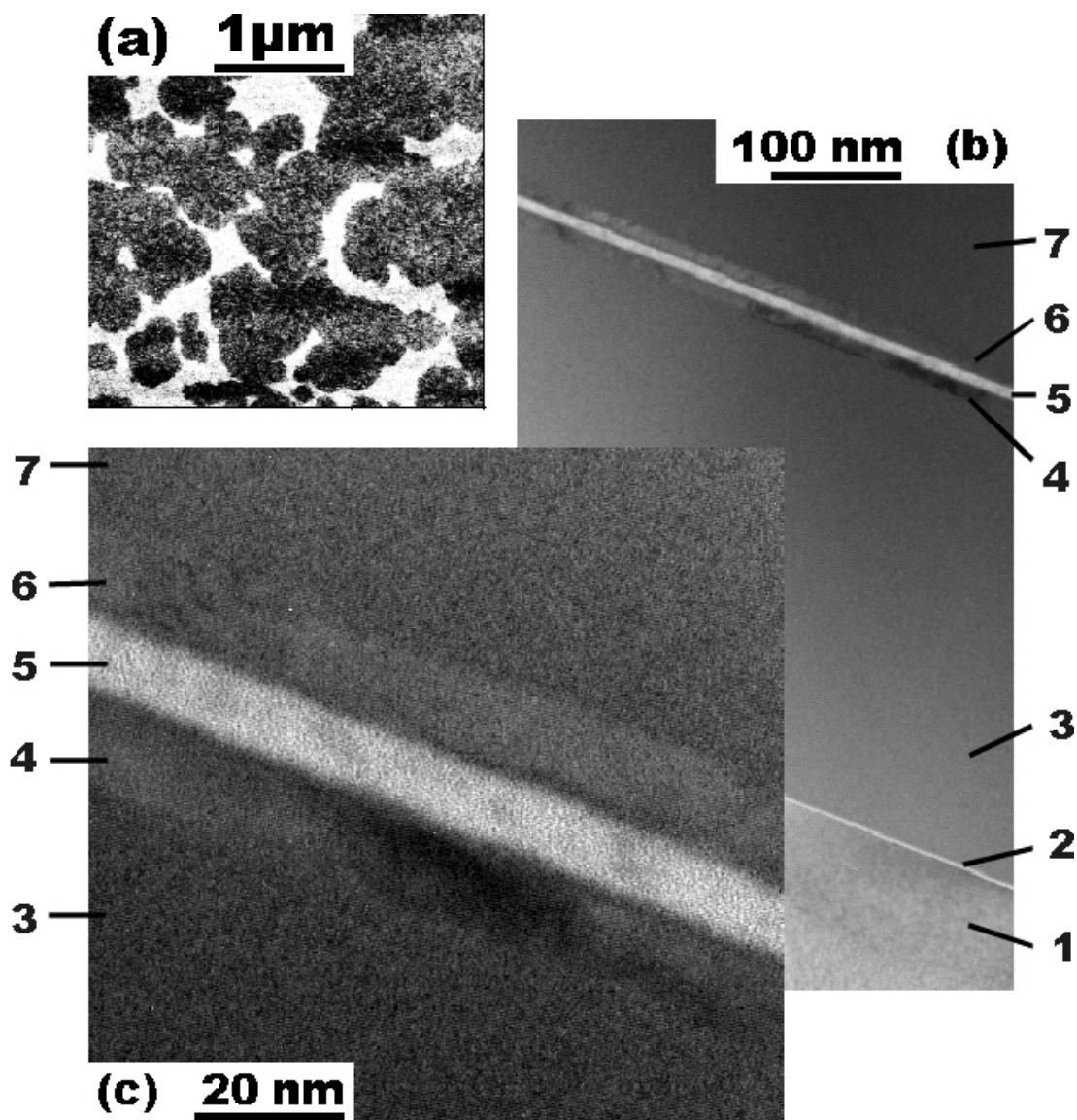


**Figure 6.13:**  $\text{Ge}_4\text{Sb}_1\text{Te}_5$  sample (film thickness: 350 nm) that was annealed for 36 min at  $155^\circ\text{C}$ . (a) AFM image of the surface. Crystals (dark, height:  $-1$  to  $-2$  nm) are visible in the amorphous surrounding (bright, zero height). The corresponding height scale is shown in Fig. 5.13. Note that the sample appears more than 70% crystallized. Crystals have a diameter of up to 500 nm. (b) and (c): Cross-sectional BF TEM micrographs of the sample shown in (a). Two samples are glued face to face (cf. Sec. 6.2.1.2). 1: Si substrate (sample 1); 2: natural  $\text{SiO}_2$  layer (thickness 2 nm, sample 1); 3: amorphous  $\text{Ge}_4\text{Sb}_1\text{Te}_5$  (sample 1); 4: crystalline  $\text{Ge}_4\text{Sb}_1\text{Te}_5$  (sample 1); 5: glue; 6: crystalline  $\text{Ge}_4\text{Sb}_1\text{Te}_5$  (sample 2); 7: amorphous  $\text{Ge}_4\text{Sb}_1\text{Te}_5$  (sample 2). Normal to the film surface, the crystals are only about 15 nm thick. Comparison of (a) and (c) reveals that crystals are more than an order of magnitude wider than thick. Microscope [(b) and (c)]: JEOL 2010 FEG.

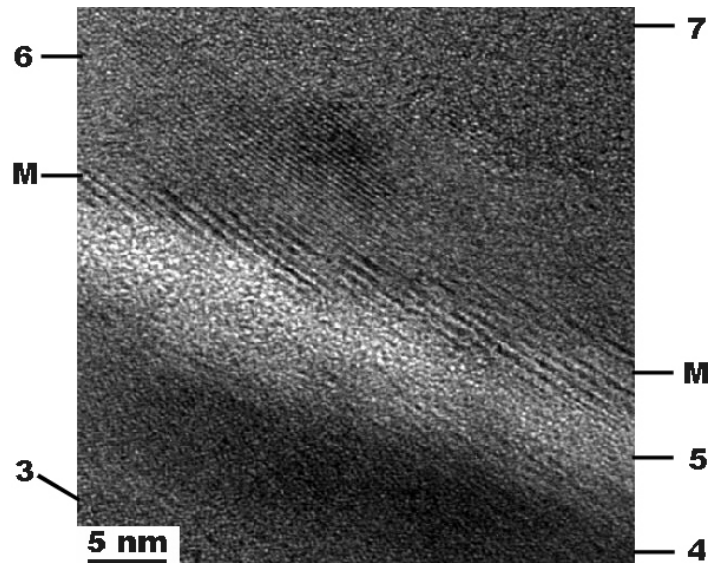


**Figure 6.14:** Cross-sectional BF HRTEM micrograph of the crystallized film surface for  $\text{Ge}_4\text{Sb}_1\text{Te}_5$  (same sample as in Fig. 6.13). The numbers are specified in the caption of Fig. 6.13. The phase contrast resulting from the lattice planes in region 6 is visible as parallel ‘lines’. A Moiré pattern (labeled as ‘M’) is visible in region 6 close to the interface with glue, where the distance of the parallel lines appears larger. Microscope: JEOL 2010 FEG.

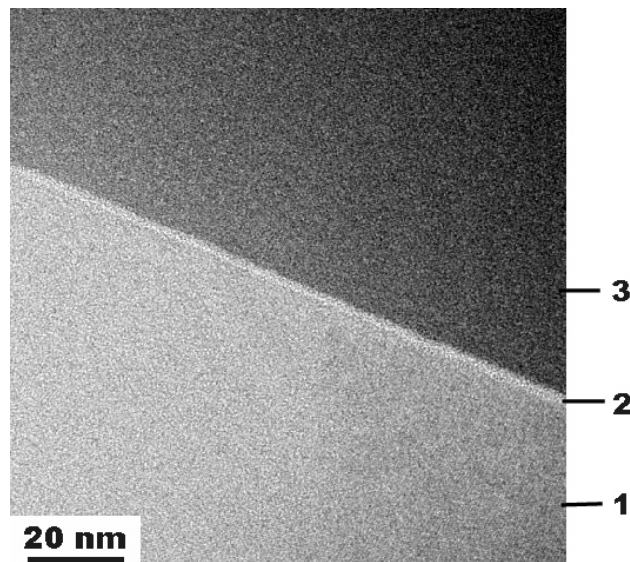


**Figure 6.15:** Cross-sectional BF TEM micrograph of the film-substrate interface for  $\text{Ge}_4\text{Sb}_1\text{Te}_5$  (same sample as in Fig. 6.13). The numbers are specified in the caption of Fig. 6.13. No heterogeneous nucleation is visible at this interface. Microscope: JEOL 2010 FEG.

layer. As the  $\text{SiO}_2$  layer is amorphous, it is unlikely that its structure triggers nucleation as explained above. Stress-induced crystal nucleation at the film-substrate interface is also unlikely since mechanical stresses in the amorphous phase are relaxed prior to crystallization in the temperature range of interest for the present study [103, 107].

No cross-sectional analysis was performed on  $\text{AgIn-Sb}_2\text{Te}$ . However, it is probable that crystals only nucleate heterogeneously at the (naturally oxidized) film surface for this alloy as well: The observation of an exhaustion of nucleation sites in the AFM images (Figs. 5.5 and 5.6) excludes the occurrence of homogeneous nucleation. Hence, only heterogeneous nucleation at either film surface or film-substrate interface can occur, while the latter is unlikely to occur as described above. Njoroge and co-workers have indeed shown that the crystallization kinetics (crystallization temperature and Kissinger activation energy for crystallization) for  $\text{AgIn-Sb}_2\text{Te}$  are different for uncapped films and films capped with a 5 nm-thin dielectric layer [94, 124]. Therefore, it is very likely that  $\text{AgIn-Sb}_2\text{Te}$  behaves in the same way as  $\text{Ge}_4\text{Sb}_1\text{Te}_5$  and  $\text{Ge}_2\text{Sb}_2\text{Te}_5$ , i. e., that heterogeneous nucleation occurs only at the film surface.

### 6.4.2 Density change and bend contours

Kooi and De Hosson argue [116] that the large density change upon crystallization [7, 9, 102, 94], which induces a local change in film height [103], causes the appearance of bend contours for crystals that nucleate heterogeneously at the film surface. Their explanation (Fig. 10 in [116]) should apply to the alloys studied in this work as well.

## 6.5 Conclusions

1. Plan view TEM confirmed for all alloys that the depressions in the amorphous films, which occur after annealing and which were observed by AFM (Chap. 5), are indeed crystals.
2. Earlier observations by Kooi and co-workers [101, 116] and Jeong and co-workers [119] on similar Te alloys were confirmed: only heterogeneous nucleation of bent single crystals occurs.
3. The crystals are much wider than thick. Their thickness is much less than the

film thickness for 350 nm-thick-films so that most of the film remains amorphous during the crystallization of the surface.

4. For AgIn-Sb<sub>2</sub>Te, the crystals exhibited a rough amorphous-crystalline interface and a spotted diffraction contrast (probably as a result of stacking faults). This was observed to a far lesser extent for Ge<sub>4</sub>Sb<sub>1</sub>Te<sub>5</sub>, but not for Ge<sub>2</sub>Sb<sub>2</sub>Te<sub>5</sub>. It was suggested that the interface roughness is related to the different magnitude of the crystal growth velocity among these alloys as observed, e.g., for laser-induced crystallization, since the crystal growth velocity increases with increasing interface roughness.
5. EDS line scans across crystals revealed that there is no lateral composition change upon crystallization for all alloys within resolution. This is in line with the interface-controlled growth mode reported in Chap. 5.

# Chapter 7

## The crystal nucleation rate

### 7.1 Preface

In this chapter, the AFM measurements presented in Chap. 5 will be analyzed with respect to their crystal nucleation rate. A qualitative analysis has already been given in Sec. 5.3: For the GeSbTe alloys, nucleation was observed to be continuous in time, and the crystal density was observed to increase with increasing temperature. For AgIn-Sb<sub>2</sub>Te, in contrast, an approximate simultaneous exhaustion of heterogeneous nucleation sites was observed, and the number of those sites was  $(5.0 \pm 0.3) \mu\text{m}^{-2}$  independent of temperature.

These observations will be analyzed in more detail in this chapter. The main open questions to be answered are:

- Is there a time dependence in the nucleation rate? Is there a time lag and an incubation time for nucleation (Sec. 3.1.3)?
- What is the temperature dependence of the nucleation rate?
- Why does the number of crystals increase with increasing temperature for the GeSbTe alloys? Can this behavior be related to nucleation and growth parameters for these alloys?

The nucleation rate determination in this chapter will mainly focus on the GeSbTe alloys. For AgIn-Sb<sub>2</sub>Te, the situation is more straightforward: It is apparent from

the AFM images that the isothermal nucleation rate first increases in time towards a maximum. Subsequently, it decreases with time and approaches zero at large times, when the sites are exhausted.

Excerpts of this chapter have also been published elsewhere [115].

## 7.2 Computational methods

The nucleation rate analysis was performed by two methods. Both of them look at the problem from a different perspective. The first method (Sec. 7.2.1) employs the Johnson-Mehl-Avrami (JMA) analysis presented in Sec. 3.3. The other method (Sec. 7.2.2) employs an analysis used by Köster and Blanke [125]. Both methods exhibit advantages and disadvantages, which are discussed below in Sec. 7.4.

The nucleation rate analysis presented below is based on the observations of Sec. 6.3 in two respects: First, the crystal density and the crystal nucleation rate were normalized *per unit area* of film surface rather than *per unit volume* of the film because crystals only nucleate heterogeneously at the film surface. Second, each growth formation is a bent *single* crystal (not a polycrystal), so that the number of growth formations are equal to the number of nucleation centers.

### 7.2.1 Johnson-Mehl-Avrami analysis

The main idea of employing the JMA analysis (Sec. 3.3) in this chapter is to calculate the crystal nucleation rate  $I$  as a function of time and temperature from the measured crystal growth velocity  $u$  (Sec. 5.3) and the measured crystallized material fraction  $\chi$ .

As crystallization was observed to occur heterogeneously at the film surface (Sec. 6.3.2), the 2-dimensional JMA model was used for this analysis (Sec. 3.3.2). Therefore,  $\chi = 1$  corresponds to a complete crystallization of the film *surface*, irrespective of the possibility that the film underneath may still be amorphous (Fig. 6.13).

The crystallized *surface* fraction was therefore measured for each AFM image and used for the calculation of the nucleation rate  $I$ .

The condition for the applicability of the JMA model (random distribution of nucleation centers, Sec. 3.3) is fulfilled because the analysis is performed *two-dimensionally*

for the film surface. Within the film surface, heterogeneous nucleation centers appear randomly distributed (e. g., Figs. 5.5 – 5.12).

### 7.2.2 Back calculation of crystal diameters

The diameter of each crystal in the AFM images (Sec. 5.3) was determined. Using the measured value of the time-independent crystal growth velocity  $u$  at the corresponding temperature, the time at which each crystal nucleated was determined by back calculation [125]. In other words, there is a clear relation between crystal size and nucleation time: The larger a crystal is, the earlier it nucleated.

Hence, whereas the JMA method (Sec. 7.2.1) only calculates the nucleation rate *indirectly* from the growth velocity and the crystallized surface fraction, the back calculation method determines the nucleation rate *directly* from the observation of individual crystals.

An AFM image area of 3  $\mu\text{m}$  by 3  $\mu\text{m}$  ( $\text{Ge}_2\text{Sb}_2\text{Te}_5$ ) and 2.5  $\mu\text{m}$  by 2.5  $\mu\text{m}$  ( $\text{Ge}_1\text{Sb}_2\text{Te}_4$ ) was used for both JMA and back calculation analysis. For  $\text{AgIn-Sb}_2\text{Te}$  and  $\text{Ge}_4\text{Sb}_1\text{Te}_5$ , an area of 9-60  $\mu\text{m}^{-2}$  was used depending on the temperature for better statistics due to the lower crystal density.

## 7.3 Results

### 7.3.1 Back calculation of crystal diameters: time lag determination

The largest crystal within the observed area is the one that nucleated first as the crystal growth velocity  $u$  was observed to be the same for all crystals. The nucleation time of the largest crystal, counted from the beginning of the first isothermal anneal, is therefore equal to the time lag  $\tau$  (Sec. 3.1.3).  $\tau$  was determined by the method explained in Sec. 7.2.2 and is shown as a function of temperature in Fig. 7.1. For  $\text{AgIn-Sb}_2\text{Te}$ , the approximate time  $\tilde{\tau}$  when the last crystal (the one with the smallest diameter) nucleates is also shown in Fig. 7.1. Data for  $\tau$  and  $\tilde{\tau}$  for  $\text{AgIn-Sb}_2\text{Te}$  from the immersion anneals are omitted because the errors on the data points were too large to allow a reliable analysis. According to Table 7.1, the activation energy for  $\tilde{\tau}$  is larger

**Table 7.1:** Fit parameters for the time lag for nucleation  $\tau$  [Arrhenius fit:  $\ln(\tau) = \ln(\tau_0) + E_\tau/(k_B T)$ ] and the approximate time  $\tilde{\tau}$  when the last crystal nucleated [Arrhenius fit:  $\ln(\tilde{\tau}) = \ln(\tilde{\tau}_0) + E_{\tilde{\tau}}/(k_B T)$ ] in Fig. 7.1.

Alloy	$\ln(\tau_0)$ ( $\tau_0$ in s)	$E_\tau$ (eV)	$\ln(\tilde{\tau}_0)$ ( $\tilde{\tau}_0$ in s)	$E_{\tilde{\tau}}$ (eV)
AgIn-Sb <sub>2</sub> Te	$-57.75 \pm 4.86$	$2.33 \pm 0.18$	$-67.99 \pm 1.56$	$2.74 \pm 0.06$
Ge <sub>4</sub> Sb <sub>1</sub> Te <sub>5</sub>	no data	no data	n/a	n/a
Ge <sub>2</sub> Sb <sub>2</sub> Te <sub>5</sub>	$-72.36 \pm 3.77$	$2.74 \pm 0.13$	n/a	n/a
Ge <sub>1</sub> Sb <sub>2</sub> Te <sub>4</sub>	$-60.19 \pm 1.97$	$2.27 \pm 0.06$	n/a	n/a

than for  $\tau$  for this alloy, so that the crystal diameter distribution becomes ‘sharper’ with increasing temperature. This can also clearly be seen from the comparison of Fig. 5.5 and Fig. 5.6. The appearance of a non-zero time lag for AgIn-Sb<sub>2</sub>Te implies that the crystals in Figs. 5.5 and 5.6 were not grown from crystalline clusters that were already present before the anneal but were nucleated during the isothermal anneal. The time lag for Ge<sub>4</sub>Sb<sub>1</sub>Te<sub>5</sub> was zero within the uncertainty of measurement and is therefore not indicated in Fig. 7.1. A time lag on the order of 100 ns was observed by laser irradiation experiments for all alloys (including Ge<sub>4</sub>Sb<sub>1</sub>Te<sub>5</sub>) at temperatures significantly above 200 °C (estimates of the exact temperature in the laser experiments are difficult) [126, 127, 128, 129, 130]. Therefore, it is expected that the time lag for Ge<sub>4</sub>Sb<sub>1</sub>Te<sub>5</sub> is greater than zero also for temperatures below 200 °C but too small to be revealed in the isothermal experiments discussed in this chapter due to insufficient time resolution.

For Ge<sub>2</sub>Sb<sub>2</sub>Te<sub>5</sub>, time lags of similar duration in the same temperature range have also been observed by Ruitenbergh et al. [96] and Privitera et al. [97]. Both studies were performed by *in-situ* TEM. A time lag for Ge<sub>48</sub>Te<sub>52</sub> was reported by Lu and Libera, who employed time-resolved hot-stage transmission *optical* microscopy in a similar temperature range [98, 99].

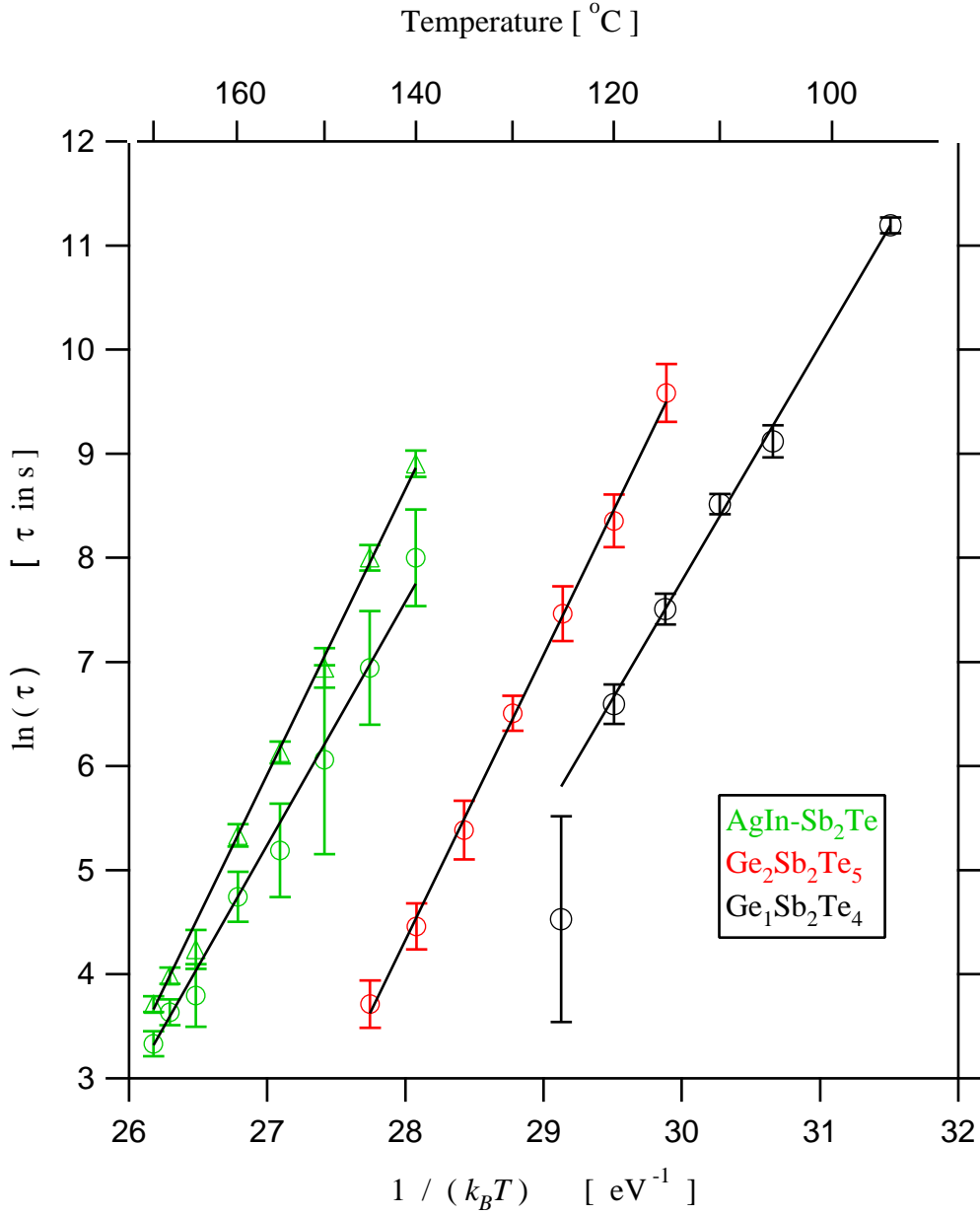


**Figure 7.1:** (Color). Time lag for nucleation  $\tau$  for AgIn-Sb<sub>2</sub>Te (green circles), Ge<sub>2</sub>Sb<sub>2</sub>Te<sub>5</sub> (red circles), and Ge<sub>1</sub>Sb<sub>2</sub>Te<sub>4</sub> (black circles). For the AgIn-Sb<sub>2</sub>Te alloy, in which nucleation sites are exhausted in the early stage of the transformation (cf. Sec. 5.3), the approximate time  $\tilde{\tau}$  when the *last* crystal nucleates is also indicated (green triangles). For Ge<sub>2</sub>Sb<sub>2</sub>Te<sub>5</sub> and Ge<sub>1</sub>Sb<sub>2</sub>Te<sub>4</sub>, crystals nucleate throughout the entire transformation so that a statement on  $\tilde{\tau}$  is not applicable. Ge<sub>4</sub>Sb<sub>1</sub>Te<sub>5</sub> is not included because the time lag was zero within the uncertainty of measurement. Fit parameters are listed in Table 7.1.

**Table 7.2:** Arrhenius fit parameters for the Avrami rate constant  $k$  in Fig. 7.7 and the nucleation rate prefactor  $I_0$  in Fig. 7.8. The fit equations are  $\ln(k) = \ln(k_0) - \frac{E_k}{k_B T}$  and  $\ln(I_0) = \ln(I_{0,0}) - \frac{E_{I_0}}{k_B T}$ . Errors for  $\text{Ge}_2\text{Sb}_2\text{Te}_5$  are larger than for  $\text{Ge}_4\text{Sb}_1\text{Te}_5$  due to the additional uncertainty in the time lag  $\tau$ .

Alloy	$\ln(k_0)$ ( $k_0$ in $\frac{1}{\text{s}}$ )	$E_k$ (eV)	$\ln(I_{0,0})$ ( $I_{0,0}$ in $\frac{1}{\mu\text{m}^2\text{s}}$ )	$E_{I_0}$ (eV)
$\text{Ge}_4\text{Sb}_1\text{Te}_5$	$76.04 \pm 0.28$	$3.09 \pm 0.01$	$167.35 \pm 9.51$	$6.58 \pm 0.37$
$\text{Ge}_2\text{Sb}_2\text{Te}_5$	$69.94 \pm 0.74$	$2.69 \pm 0.03$	$164.77 \pm 18.30$	$6.08 \pm 0.68$

### 7.3.2 Johnson-Mehl-Avrami-Analysis

The crystallized surface fraction (relative number of dark pixels) was calculated from all AFM images for all temperatures for  $\text{Ge}_4\text{Sb}_1\text{Te}_5$  and  $\text{Ge}_2\text{Sb}_2\text{Te}_5$ . Figures 7.2–7.4 show the result in a specific logarithmic representation<sup>1</sup>. A straight line was fitted to the data points for each temperature. The linear fit is motivated by the JMA equation

$$\chi(t) = \begin{cases} 0 & (t \leq \tau) \\ 1 - \exp[-\{k(t - \tau)\}^n] & (t > \tau) \end{cases} \quad (7.1)$$

so that the slope of the straight lines in Figs. 7.2–7.4 is equal to the Avrami exponent  $n$ , whereas the intersection with the vertical axis [at  $\ln(t - \tau) = 0$ ] is equal to  $n \cdot \ln(k)$ . Hence,  $n$  is assumed to be time-independent<sup>2</sup>, but different for each temperature. Equation (7.1) differs from Eq. (3.72) by the incorporation of the time lag  $\tau$  (which is zero for  $\text{Ge}_4\text{Sb}_1\text{Te}_5$  but larger than zero for  $\text{Ge}_2\text{Sb}_2\text{Te}_5$  – cf. Sec. 7.3.1). In general, the JMA analysis can be performed both ways, i. e., according to Eq. (3.72) and Eq. (7.1). However, it is more insightful to base the analysis on Eq. (7.1) because of  $\chi = 0$  and  $I = 0$  for  $t \leq \tau$ . Equation (7.1) is used for the analysis in this chapter. Hence,  $t$  is replaced by  $(t - \tau)$  in the lower lines of Eqs. (3.67b), (3.68b), (3.69c), (3.73b), (3.74b), and (3.75b). Similarly,  $t'$  is replaced by  $(t' - \tau)$  in Eqs. (3.68a), (3.69a), (3.74a), and (3.75a). Hence, the zero point in time is shifted by the length  $\tau$ .

<sup>1</sup>The data for  $\chi$  in Figs 7.2–7.4 were measured by successive anneals of the same sample. The same values were obtained for single anneals of the same overall length (not shown).

<sup>2</sup>This approximation will be discussed in Sec. 7.4.5.

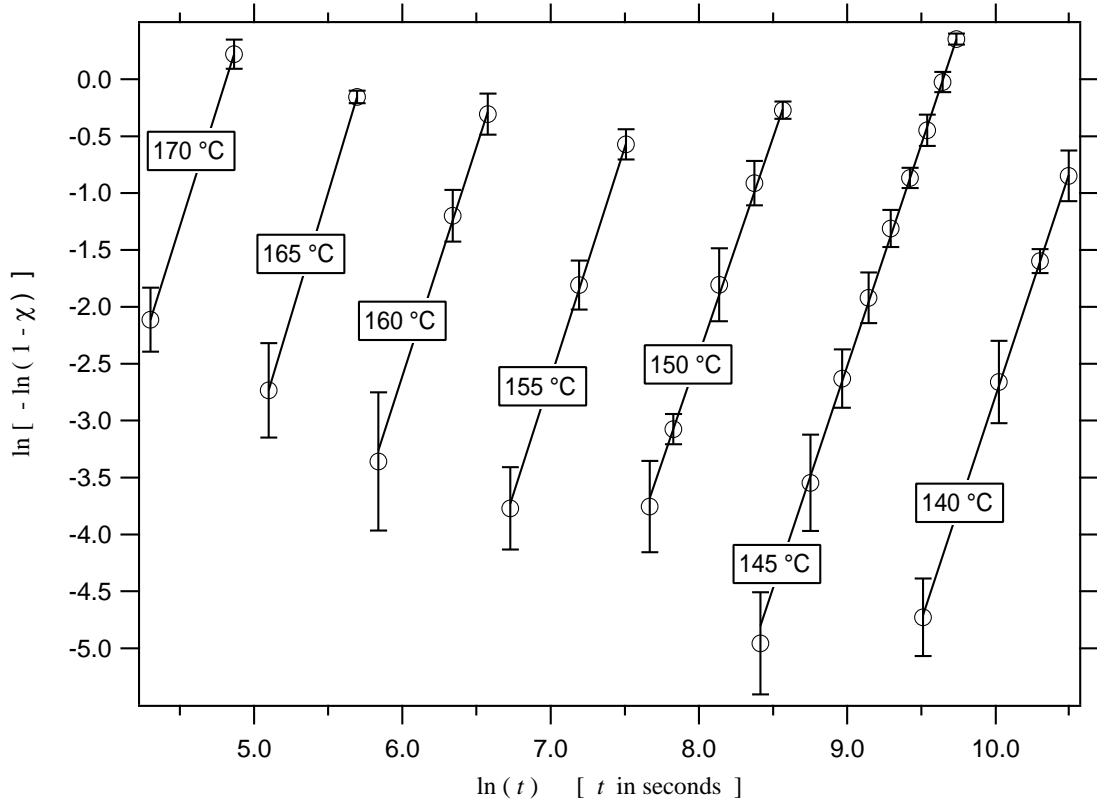


**Figure 7.2:** Johnson Mehl Avrami (JMA) plot for  $\text{Ge}_4\text{Sb}_1\text{Te}_5$  (DSC furnace anneals). Each data point corresponds to one AFM image. For each temperature, all data points result from the *same* sample at the *same* location. For instance, at  $145^\circ\text{C}$ , 9 subsequent AFM images were taken on the same sample at the same location.  $\chi$  denotes the crystallized fraction of the film *surface*. Straight lines are fitted for each temperature. Comparison with Eq. (7.1) ( $\tau = 0$  for  $\text{Ge}_4\text{Sb}_1\text{Te}_5$ ) yields that the slope of the lines are equal to the Avrami exponent  $n$  and that the intersection with the vertical axis [at  $\ln(t - \tau) = 0$ ] is equal to  $n \cdot \ln(k)$ . The parameters  $n$  and  $\ln(k)$  obtained from the fits (including their errors) are plotted in Figs. 7.5 and 7.7.

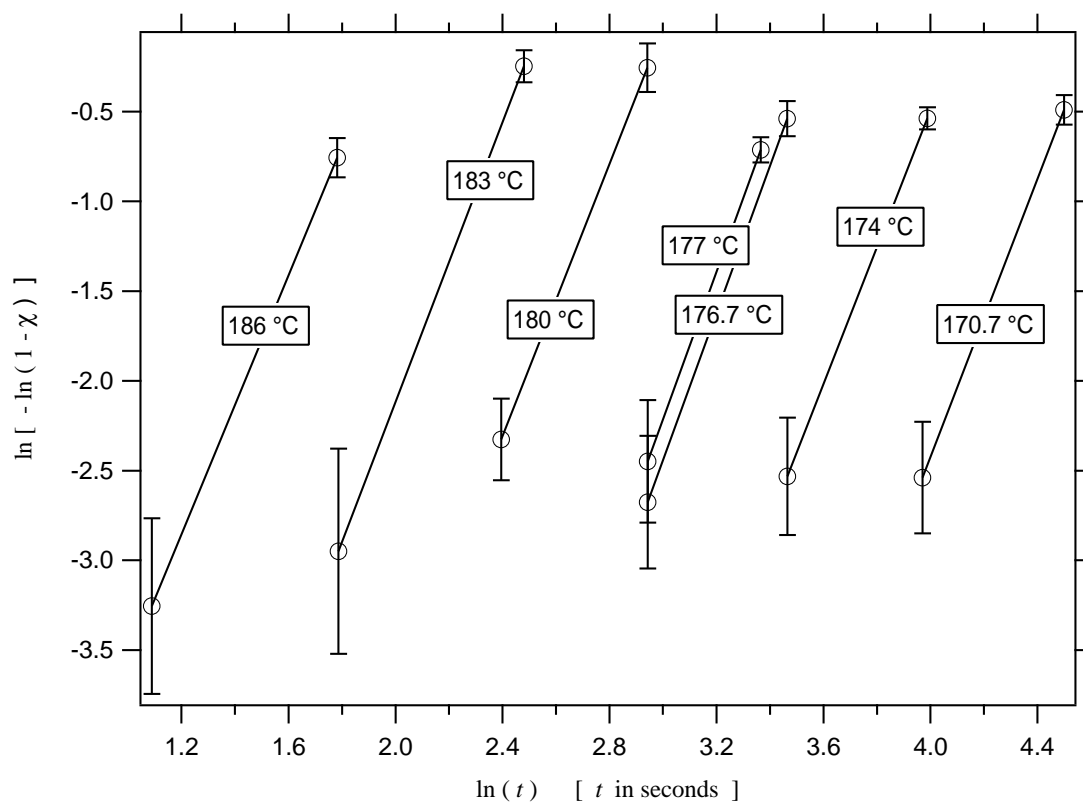


**Figure 7.3:** JMA plot for Ge<sub>4</sub>Sb<sub>1</sub>Te<sub>5</sub> (Immersion anneals). For more information see caption of Fig. 7.2.

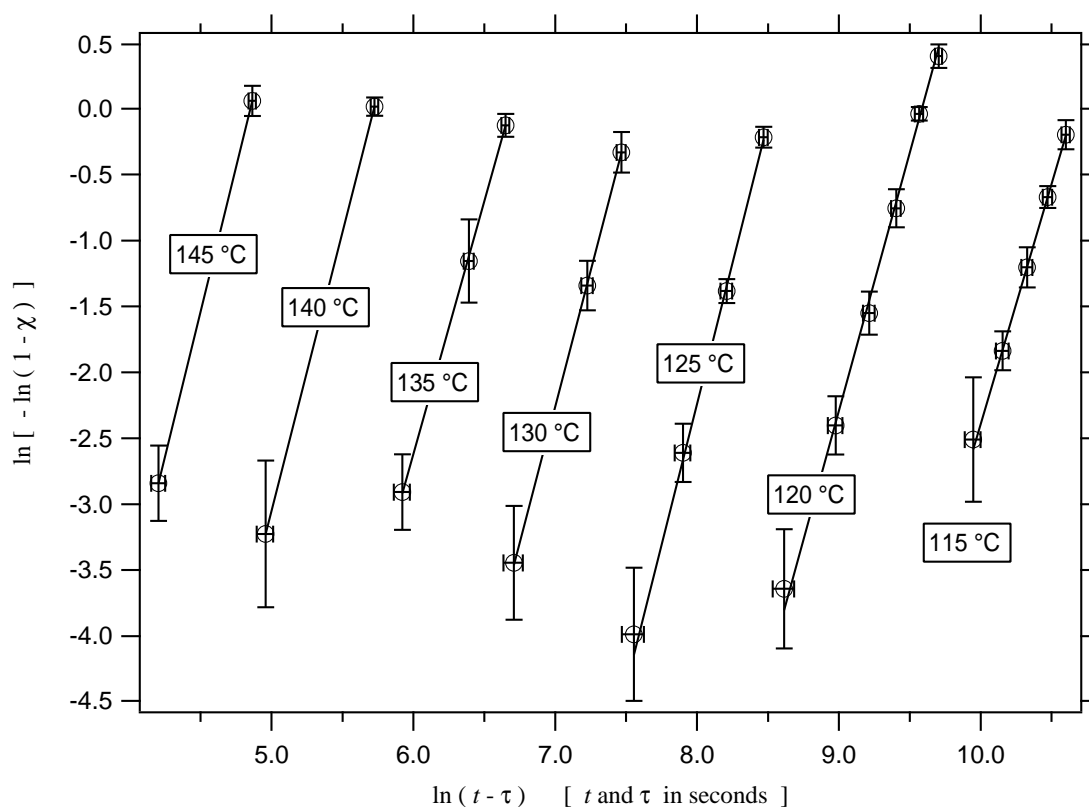


**Figure 7.4:** JMA plot for Ge<sub>2</sub>Sb<sub>2</sub>Te<sub>5</sub> (DSC furnace anneals). For more information see caption of Fig. 7.2. However, note that the time zero point on the horizontal axis was shifted by the time lag  $\tau$ , i.e., the horizontal axis shows  $\ln(t - \tau)$ . Error bars in vertical direction result from the uncertainty in  $\tau$ . This uncertainty is included in the errors for  $n$  and  $\ln(k)$  in Figs. 7.6 and 7.7.

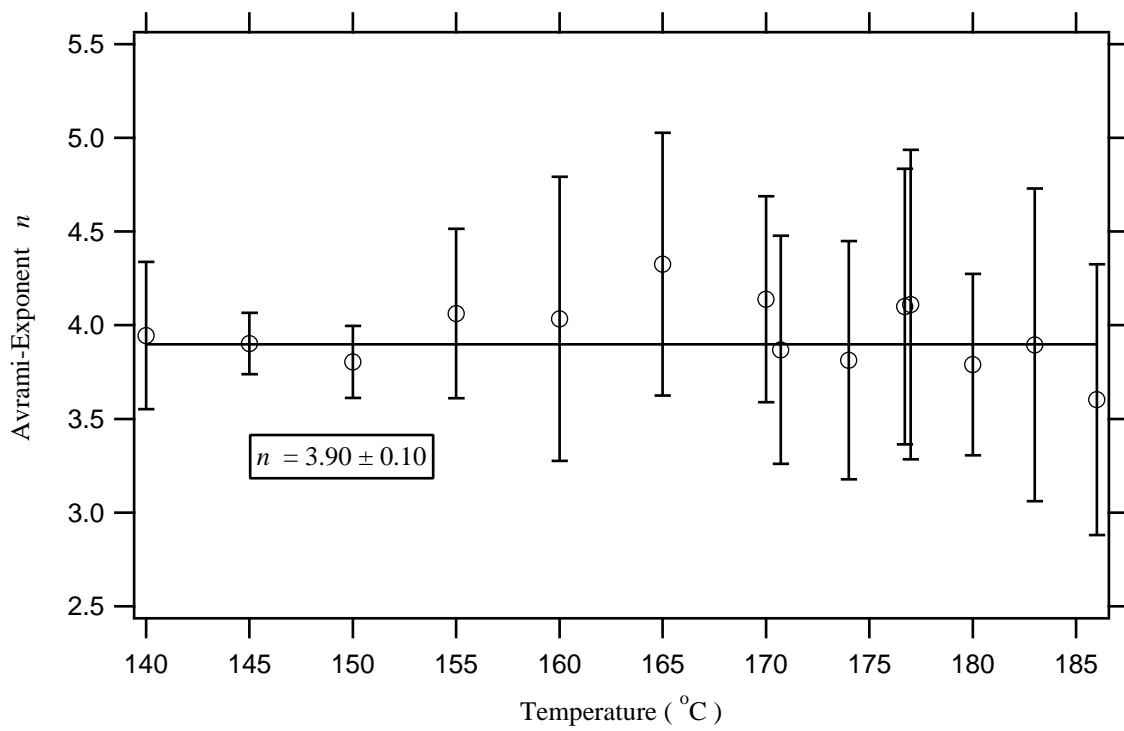


**Figure 7.5:** Avrami exponent  $n$  [Eq. (7.1)] as a function of temperature  $T$  for  $\text{Ge}_4\text{Sb}_1\text{Te}_5$  obtained from the slope of the straight lines in Figs. 7.2 and 7.3.  $n$  was averaged to a temperature independent value of  $3.90 \pm 0.10$ .

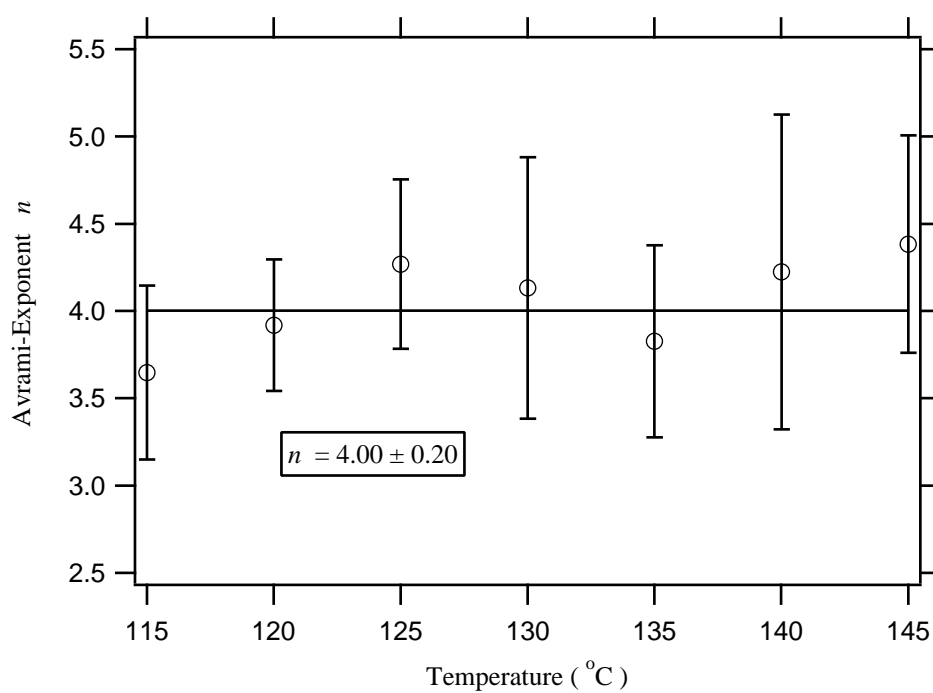


**Figure 7.6:** Avrami exponent  $n$  [Eq. (7.1)] as a function of temperature  $T$  for  $\text{Ge}_2\text{Sb}_2\text{Te}_5$  obtained from the slope of the straight lines in Fig. 7.4.  $n$  was averaged to a temperature independent value of  $4.00 \pm 0.20$ .

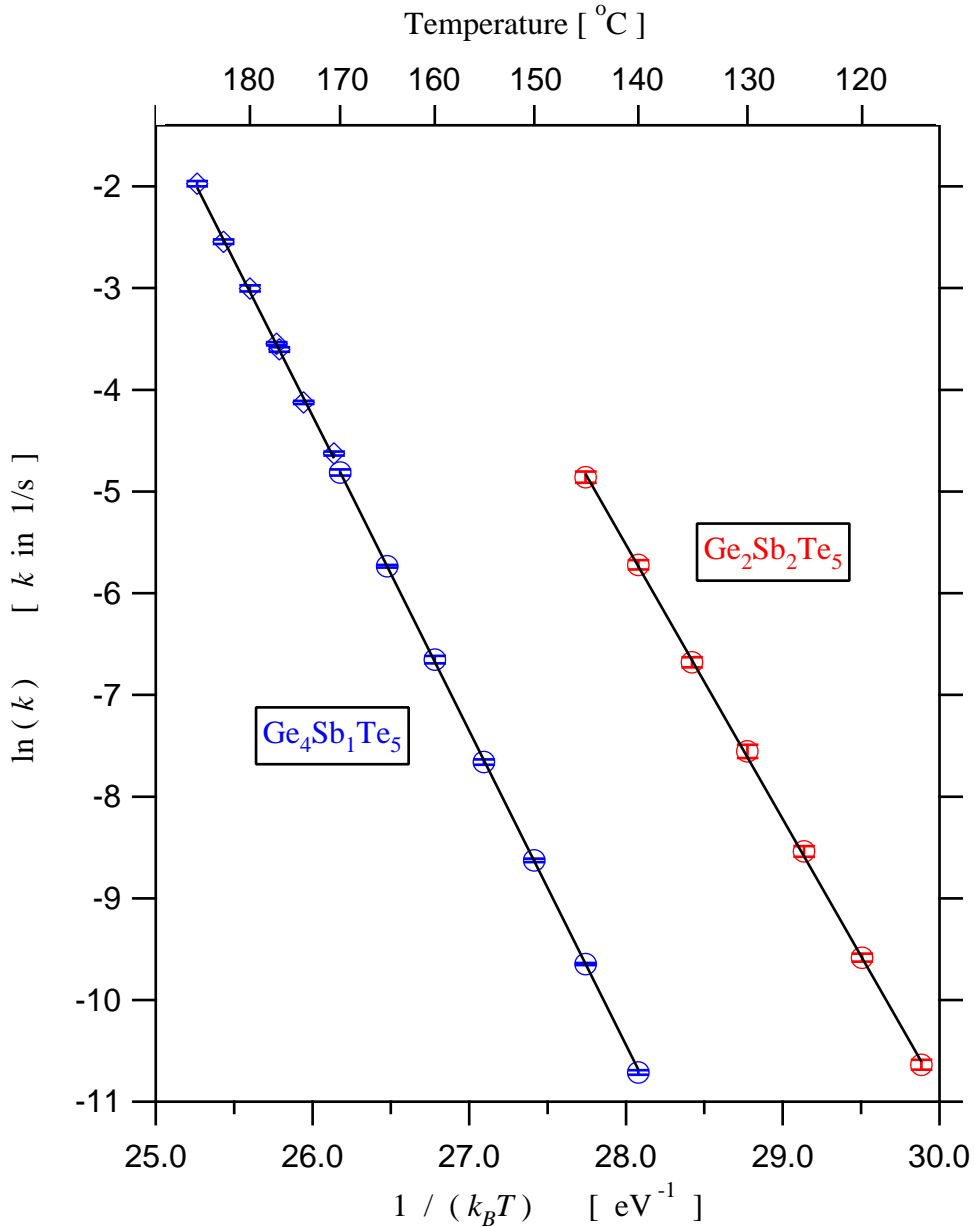


**Figure 7.7:** (Color). Logarithm of the Avrami rate constant  $k$  [Eq. (7.1)] as a function of temperature  $T$ .  $\ln(k)$  was obtained from the fit parameters of the straight lines in Figs. 7.2–7.4. Blue: Ge<sub>4</sub>Sb<sub>1</sub>Te<sub>5</sub>. Red: Ge<sub>2</sub>Sb<sub>2</sub>Te<sub>5</sub>. Circles: DSC furnace anneals. Diamonds: Immersion anneals. The data were fitted with an Arrhenius equation (Table 7.2). For Ge<sub>4</sub>Sb<sub>1</sub>Te<sub>5</sub>, DSC and immersion anneal data were fitted separately, and the fitting parameters were subsequently averaged. These averaged values (Table 7.2) are less sensitive to possible small systematic errors in the temperature calibration of the two annealing methods.

The Avrami exponent  $n$  is plotted in Figs. 7.5 and 7.6. No clear temperature dependence of  $n$  is observed within error, so that it was assumed to be temperature independent. The logarithm of the rate constant  $\ln(k)$  is plotted in Fig. 7.7.  $\ln(k)$  is extremely insensitive towards a variation in  $n$ : For instance, if  $n$  is constrained to a specific value in the fits in Figs. 7.2–7.4 (even as small as  $n = 3$  or as large as  $n = 5$ ), the same value will be obtained for  $\ln(k)$  to a very good approximation because the intersection of the straight lines with the vertical axis is a *product* of  $n$  and  $\ln(k)$ . For this reason, the error bars for  $\ln(k)$  in Fig. 7.7 are extremely small, and all data points for  $\ln(k)$  are almost perfectly located on a straight line.

Comparison of the Avrami exponent  $n$  obtained for the two alloys (Figs. 7.5 and 7.6) with the general JMA theory (Sec. 3.3.2) yields that an effective nucleation rate can be found that is of the form

$$I(t') = \begin{cases} 0 & (t' \leq \tau) \\ I_0 \cdot \left(\frac{t'-\tau}{s}\right)^{\hat{n}} & (t' > \tau) \end{cases} \quad (7.2)$$

for all temperatures, where  $\hat{n} = n - 3 = 0.90$  for  $\text{Ge}_4\text{Sb}_1\text{Te}_5$  and  $\hat{n} = n - 3 = 1.00$  for  $\text{Ge}_2\text{Sb}_2\text{Te}_5$ . Hence, this effective nucleation rate increases approximately linearly with time after the time lag  $\tau$  has elapsed ( $\tau = 0$  for  $\text{Ge}_4\text{Sb}_1\text{Te}_5$ ). The word ‘effective’ emphasizes that such a nucleation rate yields the same transformation curve  $\chi(t)$  as the true (unknown) nucleation rate within the limited amount of data points in Figs. 7.2–7.4.

The temperature dependence of  $I$  is included in the prefactor  $I_0$  [Eq. (7.2)].  $I_0$  can be obtained by solving the exponential part for the crystallized fraction

$$\chi(t) = \begin{cases} 0 & (t \leq \tau) \\ 1 - \exp \left[ - \underbrace{\pi u^2 I_0 \frac{2}{(1 + \hat{n})(2 + \hat{n})(3 + \hat{n})s^{\hat{n}}}}_{=k^{3+\hat{n}}=k^n} \cdot (t - \tau)^{3+\hat{n}} \right] & (t > \tau) \end{cases} \quad (7.3)$$

to the parameter  $I_0$ . Apart from the incorporation of the time lag  $\tau$ , Eq. (7.3) is identical to Eq. (3.75b). Rearranging yields

$$I_0 = \frac{k^n (n - 2)(n - 1)ns^{n-3}}{2\pi u^2}, \quad (7.4)$$

where  $\hat{n} = n - 3$  was used.

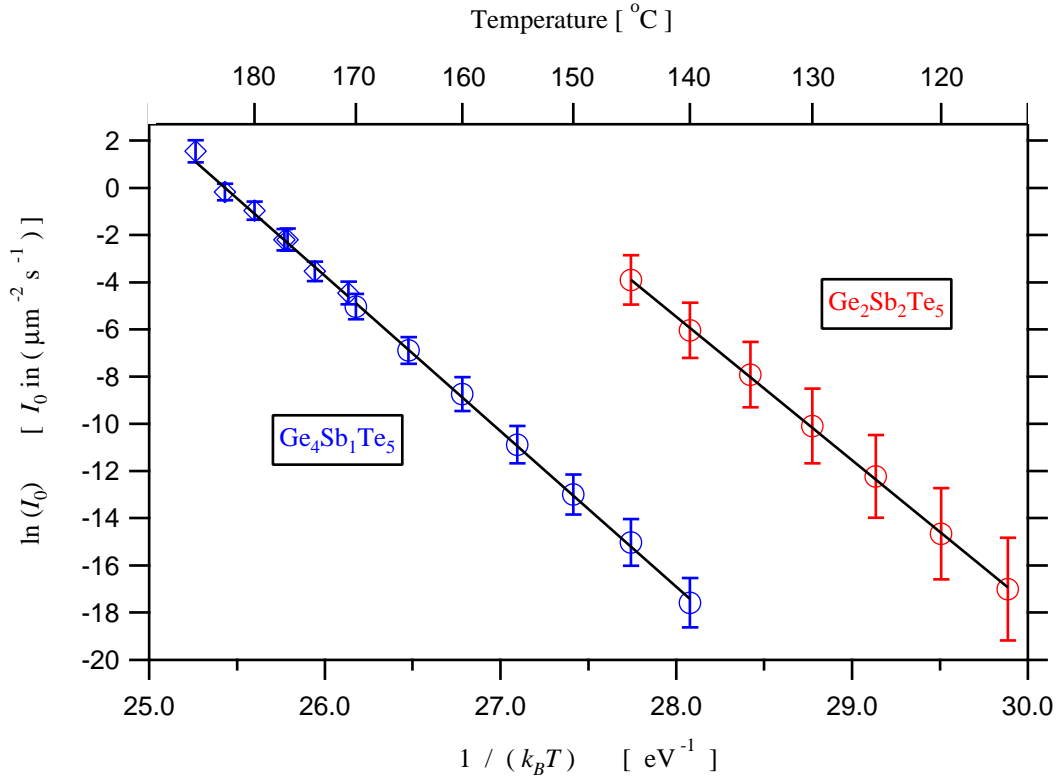


**Figure 7.8:** (Color). Logarithm of the nucleation rate prefactor  $I_0$  [Eq. (7.4)] as a function of temperature  $T$ . Blue:  $\text{Ge}_4\text{Sb}_1\text{Te}_5$ . Red:  $\text{Ge}_2\text{Sb}_2\text{Te}_5$ . Circles: DSC furnace anneals. Diamonds: Immersion anneals. The data were fitted with an Arrhenius equation (Table 7.2). For  $\text{Ge}_4\text{Sb}_1\text{Te}_5$ , DSC and immersion anneal data were fitted separately, and the fitting parameters were subsequently averaged. These averaged values (Table 7.2) are less sensitive to possible small systematic errors in the temperature calibration of the two annealing methods.

$I_0$  was calculated for all temperatures, using the averaged (temperature-independent) values for  $n$  (Figs. 7.5 and 7.6), the rate constant  $k$  (Fig. 7.7), and the growth velocity  $u$  (Fig. 5.14). The result is displayed in Fig. 7.8 and the fitting parameters in Table 7.2.

For a temperature-independent Avrami exponent  $n$  (Figs. 7.5 and 7.6), it follows from Eq. (7.4):

$$k^n \propto u^2 I_0. \quad (7.5)$$

Hence, the activation energies of the three quantities  $k$ ,  $u$ , and  $I_0$  are related by

$$E_k = \frac{2}{n} E_u + \frac{1}{n} E_{I_0}. \quad (7.6)$$

Using the experimentally determined activation energies (Tables 5.3 and 7.2) and the temperature-independent Avrami exponent (Figs. 7.5 and 7.6), this relation is

$$\underbrace{E_k}_{(3.09 \pm 0.01) \text{ eV}} = \underbrace{\frac{2}{n} E_u}_{(1.40 \pm 0.05) \text{ eV}} + \underbrace{\frac{1}{n} E_{I_0}}_{(1.69 \pm 0.05) \text{ eV}} \quad (\text{Ge}_4\text{Sb}_1\text{Te}_5), \quad (7.7a)$$

and

$$\underbrace{E_k}_{(2.69 \pm 0.03) \text{ eV}} = \underbrace{\frac{2}{n} E_u}_{(1.17 \pm 0.09) \text{ eV}} + \underbrace{\frac{1}{n} E_{I_0}}_{(1.52 \pm 0.09) \text{ eV}} \quad (\text{Ge}_2\text{Sb}_2\text{Te}_5). \quad (7.7b)$$

Equation (7.7) just represents a test as all activation energies have been determined before (Tables 5.3 and 7.2). However, Eq. (7.7) quantitatively demonstrates the relative contributions of the activation energy for nucleation  $E_{I_0}$  and the activation energy for growth  $E_u$  to the total activation energy for crystallization  $E_k$ . For both alloys, the nucleation contribution is larger. This explains why the number of crystals increases with increasing temperature for both alloys (Figs. 5.7 – 5.10).

The number of crystals  $N_c$  (per unit area, dimension:  $\frac{1}{\text{m}^2}$ ) that would be observed after complete crystallization of the sample surface is given by

$$N_c = \int_0^{\infty} I(t)[1 - \chi(t)] dt. \quad (7.8)$$

The normalization factor  $[1 - \chi(t)]$  appears because crystals can only nucleate in the untransformed (amorphous) part of the sample surface. Using Eqs. (7.1) and (7.2) and performing a variable transformation

$$(kt)^n = x \quad (7.9)$$

yields

$$N_c = \underbrace{\frac{\Gamma(1 - \frac{2}{n})}{nS^{n-3}}}_{\text{temperature independent}} \cdot I_0 \cdot k^{(2-n)}, \quad (7.10)$$

where

$$\Gamma(z) = \int_0^{\infty} x^{z-1} \exp(-x) dx \quad (7.11)$$

is the Euler Gamma function (here:  $z = 1 - 2/n$ ). Equation (7.10) is valid in general for an Avrami exponent  $n > 3$ .

Using the temperature dependencies  $I_0 \propto \exp\left(-\frac{E_{I_0}}{k_B T}\right)$  and  $k \propto \exp\left(-\frac{E_k}{k_B T}\right)$ , and using Eq. (7.6), Eq. (7.10) can be written as

$$N_c = \text{const.} \cdot \exp \left[ -\frac{1}{k_B T} \underbrace{\left( \frac{2}{n} [E_{I_0} - E_u(n-2)] \right)}_{:=E_{N_c}} \right]. \quad (7.12)$$

In general, the quantity  $E_{N_c}$  can be greater or smaller than zero.  $E_{N_c}$  is greater than zero (i. e., the number of crystals  $N_c$  increases with increasing temperature), if and only if

$$\frac{E_{I_0}}{n-2} > E_u. \quad (7.13)$$

Substituting  $E_u$ ,  $E_{I_0}$  (Tables 5.3 and 7.2), and the (temperature independent) Avrami exponent  $n$  (Figs. 7.5 and 7.6) in Eq. (7.13) yields

$$\underbrace{\frac{E_{I_0}}{n-2}}_{(3.47 \pm 0.07) \text{ eV}} > \underbrace{E_u}_{(2.74 \pm 0.03) \text{ eV}} \quad (\text{Ge}_4\text{Sb}_1\text{Te}_5), \quad (7.14a)$$

and

$$\underbrace{\frac{E_{I_0}}{n-2}}_{(3.04 \pm 0.11) \text{ eV}} > \underbrace{E_u}_{(2.35 \pm 0.05) \text{ eV}} \quad (\text{Ge}_2\text{Sb}_2\text{Te}_5). \quad (7.14b)$$

Hence,  $E_{N_c} > 0$  for both alloys.

In summary, the *experimentally observed* fact that the number of crystals  $N_c$  (per unit area) increases with increasing temperature for  $\text{Ge}_4\text{Sb}_1\text{Te}_5$  and  $\text{Ge}_2\text{Sb}_2\text{Te}_5$  (Figs. 5.7 – 5.10) can be explained *mathematically* by relating the experimentally obtained activation energies  $E_u$  and  $E_{I_0}$  (Tables 5.3 and 7.2) with the measured Avrami exponent  $n$  (Figs. 7.5 and 7.6).

The number of crystals  $N_c$  after complete surface crystallization was calculated from Eq. (7.10) for all temperatures and is shown in Fig. 7.9. The corresponding fitting parameters are shown in Table 7.3.

The average grain area  $A$  after complete crystallization of the sample surface (dimension:  $\text{m}^2$ ) can be obtained from  $N_c$  [Eq. (7.10)] by

$$A = \frac{1}{N_c} = \pi \rho^2. \quad (7.15)$$

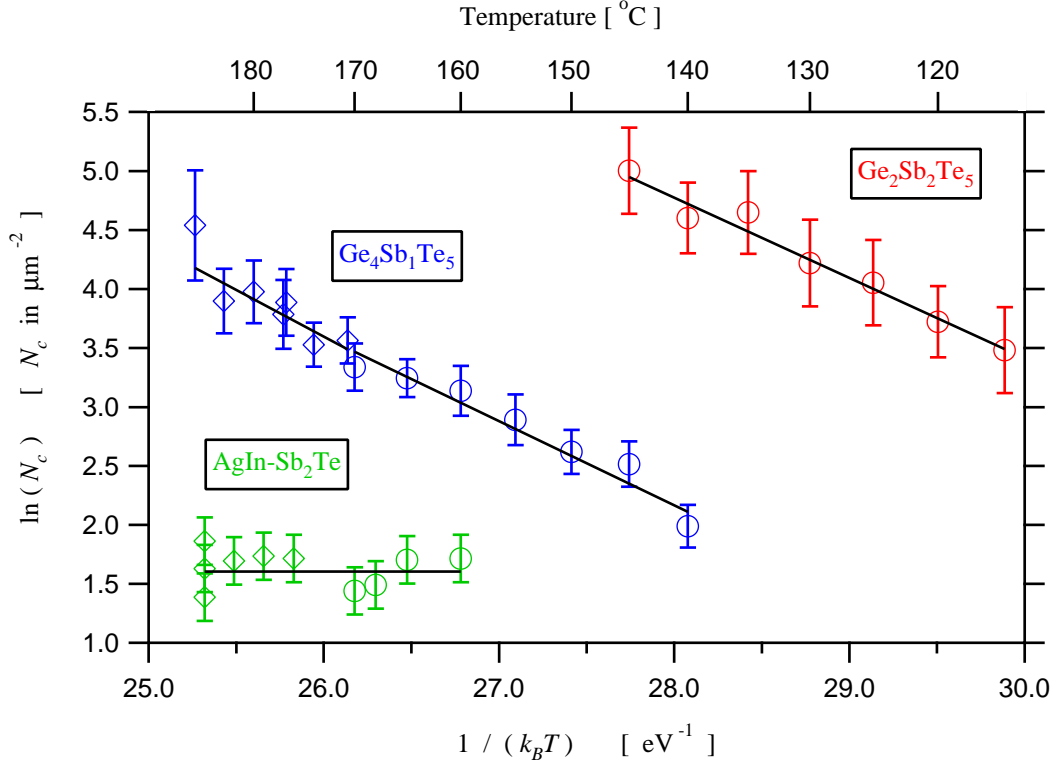


**Figure 7.9:** (Color). Number of crystals per unit area  $N_c$  [calculated from Eq. (7.10)] after complete crystallization of the film surface as a function of temperature  $T$ . Green: AgIn-Sb<sub>2</sub>Te. Blue: Ge<sub>4</sub>Sb<sub>1</sub>Te<sub>5</sub>. Red: Ge<sub>2</sub>Sb<sub>2</sub>Te<sub>5</sub>. Circles: DSC furnace anneals. Diamonds: Immersion anneals. The data for Ge<sub>4</sub>Sb<sub>1</sub>Te<sub>5</sub> and Ge<sub>2</sub>Sb<sub>2</sub>Te<sub>5</sub> were fitted with an Arrhenius equation (Table 7.3). For Ge<sub>4</sub>Sb<sub>1</sub>Te<sub>5</sub>, DSC and immersion anneal data were fitted separately, and the fitting parameters were subsequently averaged. These averaged values (Table 7.3) are less sensitive to possible small systematic errors in the temperature calibration of the two annealing methods. Due to the exhaustion of nucleation sites for AgIn-Sb<sub>2</sub>Te, the number of crystals could be determined directly from the AFM images (e. g., Figs. 5.5 – 5.6) for this alloy.  $N_c$  appears to be temperature-independent for AgIn-Sb<sub>2</sub>Te; the average value is  $N_c = (5.0 \pm 0.3) \mu\text{m}^{-2}$ .

**Table 7.3:** Arrhenius fit parameters for the number of crystals  $N_c$  and average grain radius  $\rho$  after complete surface crystallization in Figs. 7.9 and 7.10. The fit equations are  $\ln(N_c) = \ln(N_{c,0}) - \frac{E_{N_c}}{k_B T}$  and  $\ln(\rho) = \ln(\rho_0) + \frac{E_\rho}{k_B T}$ . Errors for  $\text{Ge}_2\text{Sb}_2\text{Te}_5$  are larger than for  $\text{Ge}_4\text{Sb}_1\text{Te}_5$  due to the additional uncertainty in the time lag  $\tau$ .

Alloy	$\ln(N_{c,0})$ ( $N_{c,0}$ in $\frac{1}{\mu\text{m}^2}$ )	$E_{N_c}$ (eV)	$\ln(\rho_0)$ ( $\rho_0$ in $\mu\text{m}$ )	$E_\rho$ (eV)
$\text{Ge}_4\text{Sb}_1\text{Te}_5$	$22.31 \pm 1.93$	$0.72 \pm 0.07$	$-11.72 \pm 0.97$	$0.36 \pm 0.04$
$\text{Ge}_2\text{Sb}_2\text{Te}_5$	$23.83 \pm 3.29$	$0.68 \pm 0.12$	$-12.49 \pm 1.65$	$0.34 \pm 0.06$

The average grain radius after complete surface crystallization  $\rho$  is then given by

$$\rho = \sqrt{\frac{A}{\pi}} = \sqrt{\frac{1}{N_c \pi}}. \quad (7.16)$$

Equations (7.15) and (7.16) assume circular crystals, which is approximately true for the crystals observed in this work (cf. Secs. 5.3 and 6.3.1). The radius  $\rho$  is shown as a function of temperature in Fig. 7.10, and the corresponding fitting parameters are shown in Table 7.3.

The experimentally observed and mathematically explained temperature dependence of  $N_c$  and  $\rho$  is qualitatively consistent with the re-crystallization mechanisms of amorphous marks observed upon laser annealing (Sec. 1.1). For  $\text{AgIn-Sb}_2\text{Te}$ , the number of crystals is small and temperature independent (Fig. 7.9). Hence, nucleation does not appear to be dominant in the crystallization process as compared to growth. This is in line with the observation that laser-induced re-crystallization is observed by the growth of the crystalline phase from the *rim* of the amorphous mark for this alloy [Fig. 1.2(a)]. For  $\text{Ge}_4\text{Sb}_1\text{Te}_5$  and  $\text{Ge}_2\text{Sb}_2\text{Te}_5$ , in contrast, the number of crystals  $N_c$  increases with increasing temperature (Fig. 7.9). Equivalently,  $\rho$  decreases with increasing temperature (Fig. 7.10). Therefore, it is expected that  $N_c$  will be even larger than all values shown in Fig. 7.9 for laser-induced re-crystallization, which occurs at higher temperatures than in the isothermal experiments presented in this work<sup>3</sup>. Hence, nucleation appears to be dominant as compared to growth in the crystallization process for higher temperatures. This is in line with the observation that laser-induced re-

<sup>3</sup>Exact statements on the temperature during laser annealing are difficult.

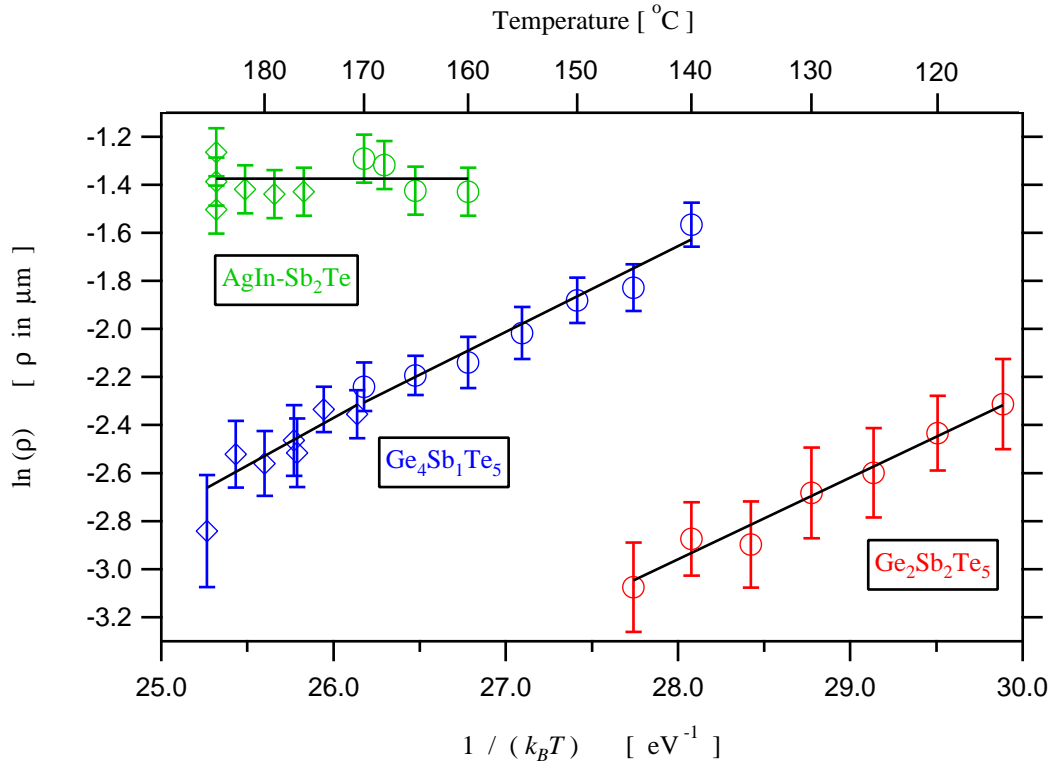


**Figure 7.10:** (Color). Average grain radius  $\rho$  after complete crystallization of the film surface as a function of temperature  $T$ . The radius  $\rho$  was calculated from the data for  $N_c$  in Fig. 7.9, using Eq. (7.16). Green: AgIn-Sb<sub>2</sub>Te. Blue: Ge<sub>4</sub>Sb<sub>1</sub>Te<sub>5</sub>. Red: Ge<sub>2</sub>Sb<sub>2</sub>Te<sub>5</sub>. Circles: DSC furnace anneals. Diamonds: Immersion anneals. The data for Ge<sub>4</sub>Sb<sub>1</sub>Te<sub>5</sub> and Ge<sub>2</sub>Sb<sub>2</sub>Te<sub>5</sub> were fitted with an Arrhenius equation (Table 7.3). For Ge<sub>4</sub>Sb<sub>1</sub>Te<sub>5</sub>, DSC and immersion anneal data were fitted separately, and the fitting parameters were subsequently averaged. These averaged values (Table 7.3) are less sensitive to possible small systematic errors in the temperature calibration of the two annealing methods. The average value for AgIn-Sb<sub>2</sub>Te is  $\rho = (0.25 \pm 0.01) \mu\text{m}$ .

crystallization of amorphous marks in  $\text{Ge}_4\text{Sb}_1\text{Te}_5$  and  $\text{Ge}_2\text{Sb}_2\text{Te}_5$  occurs by nucleation and subsequent growth of crystals *inside* the amorphous mark [Fig. 1.2(b)].

### 7.3.3 Back calculation of crystal diameters: nucleation rate determination

This section presents the nucleation rate analysis based on the back calculation method described in Sec. 7.2.2. The time dependence of the nucleation rate obtained below differs from the time dependence obtained in Sec. 7.3.2. A discussion of this issue follows in Sec. 7.4.5.

Figures 7.11(a) and 7.12(a) show the result of the back calculation of the time at which crystals nucleated for  $\text{Ge}_4\text{Sb}_1\text{Te}_5$  and  $\text{Ge}_2\text{Sb}_2\text{Te}_5$  for one temperature (circles). The data were plotted in a way that they all have the same distance in horizontal direction (equidistant time steps  $t_i$ ). For this reason, the original data points from the back calculation (which were not equidistant in time) had to be interpolated. The total number of points were not modified by this process. It will become clear below that this interpolation is necessary for a correct calculation of the nucleation rate [which is proportional to the derivative of the data, Eq. (7.20) below] from these data points. Plots similar to those shown in Figs. 7.11 and 7.12 were performed for other temperatures (140–160 °C for  $\text{Ge}_4\text{Sb}_1\text{Te}_5$  and 115–130 °C for  $\text{Ge}_2\text{Sb}_2\text{Te}_5$ ) but are not shown<sup>4</sup>. Figure 7.12 shows that no crystals nucleate for  $t < \tau \sim 13000$  s, where  $\tau$  is the time lag for nucleation for  $\text{Ge}_2\text{Sb}_2\text{Te}_5$  at 115 °C (cf. Fig. 7.1). For  $\text{Ge}_4\text{Sb}_1\text{Te}_5$ , the time lag appears to be zero within the resolution of the measurement (cf. Sec. 7.3.1). The intermediate curve of the three solid lines in Figs. 7.11(a) and 7.12(a) was calculated numerically from

$$N(t) = \begin{cases} 0 & (t \leq \tau) \\ \frac{\Gamma(1-\frac{2}{n}, \{k(t-\tau)\}^n)}{ns^{n-3}} \cdot I_0 \cdot k^{(2-n)} & (t > \tau) \end{cases}, \quad (7.17)$$

in the same way as  $N_c$  (Fig. 7.9) was calculated from Eq. (7.10), i. e., the same JMA parameters  $I_0$ ,  $k$ , and  $n$  that had been used for Eq. (7.10) were also used for Eq. (7.17). Equation (7.17) is the result of the integration in Eq. (7.8), where the upper integration

---

<sup>4</sup>For higher temperatures, the crystal density was too high to allow a reliable analysis.

boundary was chosen to be equal to  $t$ . The expression

$$\Gamma(z, x') = \int_0^{x'} x^{z-1} \exp(-x) dx \quad (7.18)$$

is the *incomplete* Gamma function. For  $x' \rightarrow \infty$  (i. e., for infinite times),  $\Gamma(z, x')$  is equal to  $\Gamma(z)$  [Eq. (7.11)]. In other words,

$$\lim_{t \rightarrow \infty} N(t) = N_c. \quad (7.19)$$

Hence, the saturation value for large times of the intermediate solid curve in Figs. 7.11(a) and 7.12(a) is identical to the value  $N_c$  plotted in Fig. 7.9 for the particular temperature. The other two solid curves in Figs. 7.11(a) and 7.12(a) represent worst case calculations from Eq. (7.17), which for large times correspond to the limit of the error bar to the value of  $N_c$  in Fig. 7.9 for the particular temperature.

Figures 7.11(a) and 7.12(a) show that the number of crystals  $N(t)$  as a function of time from the JMA model and from the back calculation coincide well within error.

The nucleation rate  $I(t_i)$  at each of the equidistant time steps  $t_i$  associated with each data point (circle) in Figs. 7.11(a) and 7.12(a) was obtained from

$$I(t_i) = \frac{\dot{N}(t_i)}{1 - \chi(t_i)}, \quad (7.20)$$

where  $N(t_i)$  is the crystal number in Figs. 7.11(a) and 7.12(a). The time derivative  $\dot{N}(t_i)$  at time  $t_i$  was obtained from the slope of a linear fit to five data points of  $N$  in the range  $[t_{i-2}, t_{i+2}]$  in Figs. 7.11(a) and 7.12(a).<sup>5</sup>  $\chi(t_i)$  is the crystallized surface fraction at time  $t_i$ , which was taken from Figs. 7.2 and 7.4 and is re-plotted on a linear scale in Figs. 7.11(b) and 7.12(b). The factor  $1/[1 - \chi(t_i)]$  normalizes  $\dot{N}(t_i)$  because crystals can only nucleate in the untransformed (amorphous) fraction  $[1 - \chi(t_i)]$  of the sample surface [this normalization is the same as the one used in

---

<sup>5</sup>In Refs. [131] and [132], Lee and co-workers used a similar analysis for the crystallization of NiTi films. They calculated  $\dot{N}(t_i)$  in Eq. (7.20) by the expression  $\dot{N}(t_i) = [N(t_i) - N(t_{i-1})]/[t_i - t_{i-1}]$ . Their method was found to give slightly noisier data than the five data point fit used for the nucleation rate plots in Figs. 7.11(c) and 7.12(c). However, the steady state nucleation rates  $I^{ss}$  obtained from both methods [average of the data for large times as shown in Figs. 7.11(c) and 7.12(c)] coincide closely with each other.

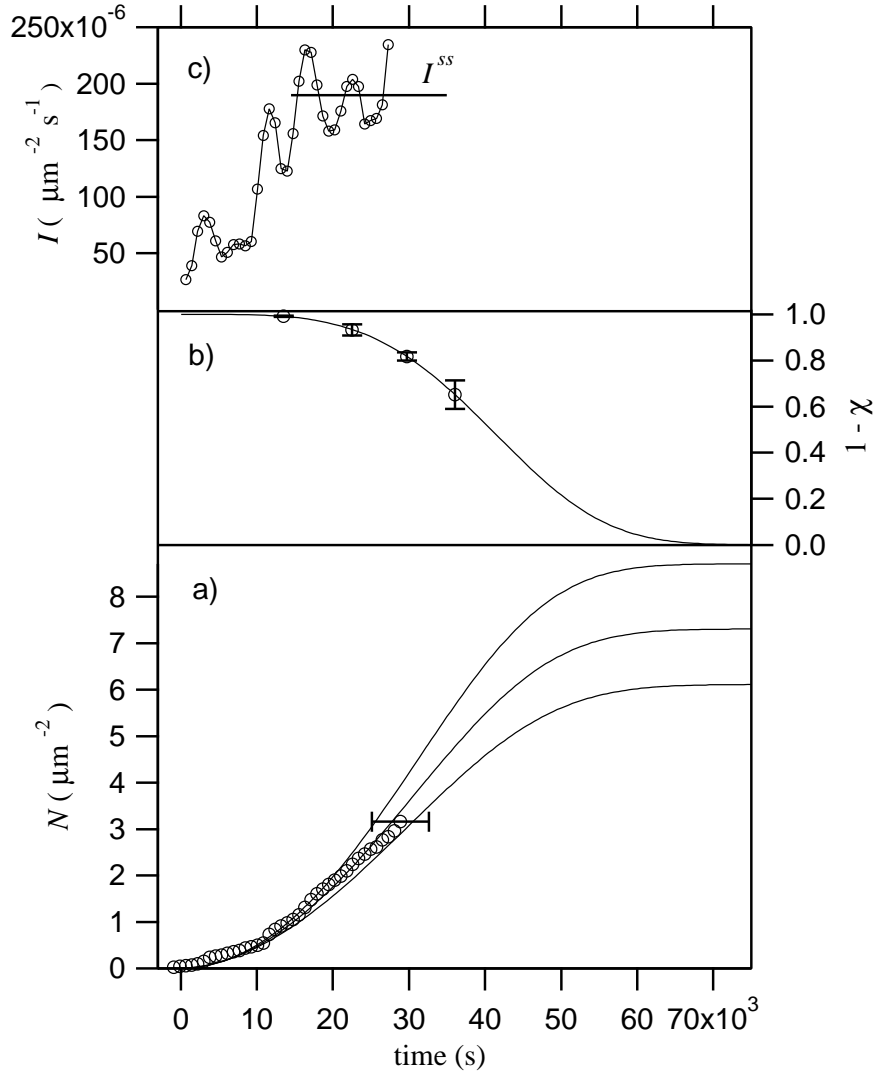


**Figure 7.11:** Crystallization of  $\text{Ge}_4\text{Sb}_1\text{Te}_5$  at  $140^\circ\text{C}$ . (a) Number of crystals  $N$  per unit area obtained from diameter back calculation (circles). The error bar on the last data point is the same for all other points and denotes the uncertainty in the time when a specific crystal nucleated. The first crystal nucleates close to  $t = 0$ , i.e., the time lag  $\tau$  is zero for this alloy within the resolution of the measurement (indicated by the horizontal error bar, cf. Sec. 7.3.1). The solid curves are calculations from Eq. (7.17) based on JMA parameters (the outer curves represent errors, i.e., worst case calculations). (b) Measured amorphous surface fraction  $1 - \chi$  after each anneal (circles), and JMA fit (solid curve), taken from Fig. 7.2 for  $140^\circ\text{C}$ . (c) Calculated nucleation rate  $I$  according to Eq. (7.20). Transient effects dominate up to 15000 s. For  $t > 15000$  s, the steady state appears to be reached. The steady state nucleation rate  $I^{ss}$  is obtained by averaging the values for  $t > 15000$  s (solid horizontal line). This value is plotted in Fig. 7.13.

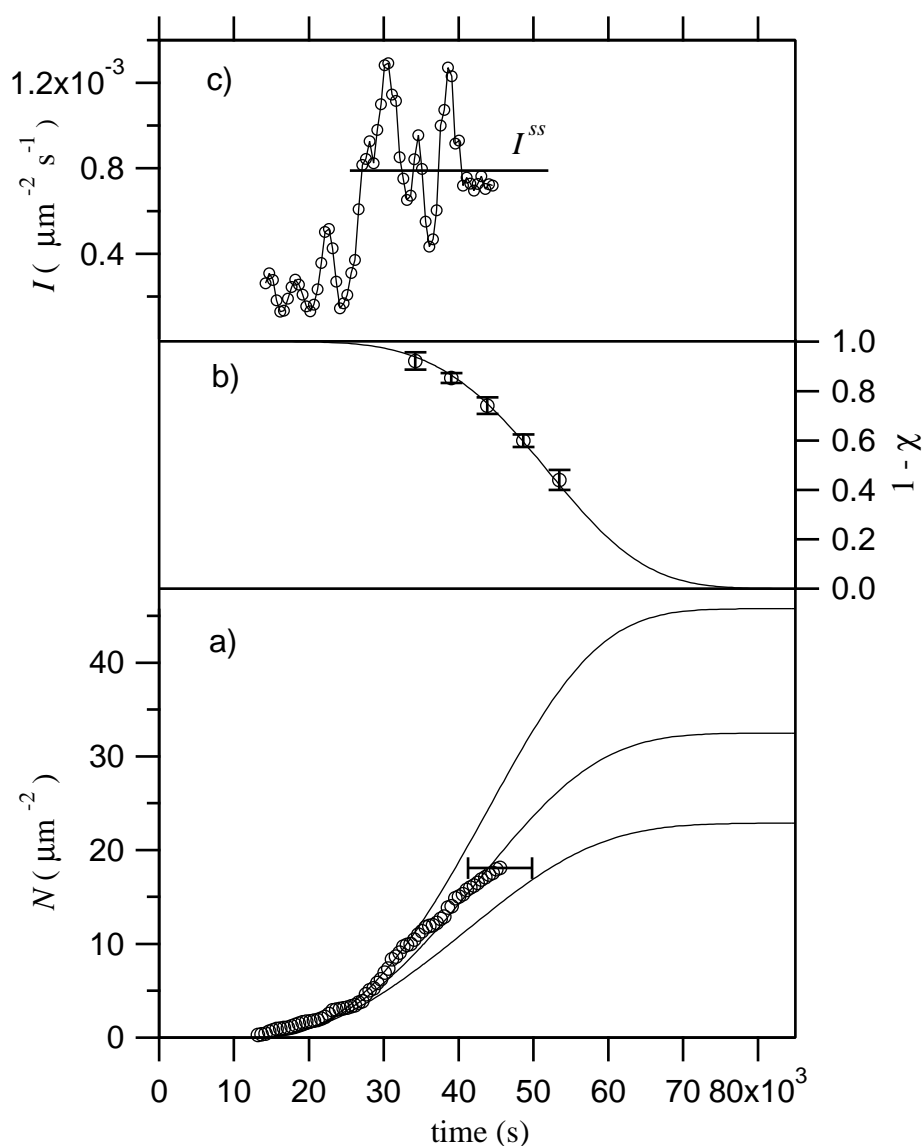


**Figure 7.12:** Crystallization of  $\text{Ge}_2\text{Sb}_2\text{Te}_5$  at  $115^\circ\text{C}$ . (a) Number of crystals  $N$  per unit area obtained from diameter back calculation (circles). The error bar on the last data point is the same for all other points and denotes the uncertainty in the time when a specific crystal nucleated. No crystals nucleate for  $t < 13000$  s (time lag  $\tau$ , cf. Fig. 7.1). The solid curves are calculations from Eq. (7.17) based on JMA parameters (the outer curves represent errors, i. e., worst case calculations). (b) Measured amorphous surface fraction  $1 - \chi$  after each anneal (circles), and JMA fit (solid curve), taken from Fig. 7.4 for  $115^\circ\text{C}$ . (c) Calculated nucleation rate  $I$  according to Eq. (7.20). Transient effects dominate up to 25000 s. For  $t > 25000$  s, the steady state appears to be reached. The steady state nucleation rate  $I^{ss}$  is obtained by averaging the values for  $t > 25000$  s (solid horizontal line). This value is plotted in Fig. 7.13.

**Table 7.4:** Fit parameters for the steady state nucleation rate  $I^{ss}$  [Arrhenius fit:  $\ln(I^{ss}) = \ln(I_0^{ss}) - E_{I^{ss}}/(k_B T)$ ] in Fig. 7.13. The critical work for heterogeneous cluster formation,  $\Delta G_c^{\text{het}}$  [Eq. (3.34)], is obtained from Eq. (7.21).

Alloy	$\ln(I_0^{ss})$ ( $I_0^{ss}$ in $\mu\text{m}^{-2}\text{s}^{-1}$ )	$E_{I^{ss}}$ (eV)	$\Delta G_c^{\text{het}}$ (eV)
$\text{Ge}_4\text{Sb}_1\text{Te}_5$	$105.96 \pm 5.53$	$4.09 \pm 0.20$	$1.35 \pm 0.23$
$\text{Ge}_2\text{Sb}_2\text{Te}_5$	$97.53 \pm 4.86$	$3.50 \pm 0.17$	$1.15 \pm 0.22$
$\text{Ge}_1\text{Sb}_2\text{Te}_4$	$78.75 \pm 5.69$	$2.82 \pm 0.18$	$0.93 \pm 0.23$

Eq. (7.8)].  $I(t_i)$  is plotted in Figs. 7.11(c) and 7.12(c). Although the differentiated data is noisy, it appears clearly that the nucleation rate is lower for  $t < 15000$  s than for  $t > 15000$  s for  $\text{Ge}_4\text{Sb}_1\text{Te}_5$  [Fig. 7.11(c)]. Similarly, for  $\text{Ge}_2\text{Sb}_2\text{Te}_5$ , the nucleation rate appears lower for  $t < 25000$  s than for  $t > 25000$  s [Fig. 7.12(c)]. Hence, transient nucleation (Sec. 3.1.3) appears predominant for  $t < 15000$  s ( $\text{Ge}_4\text{Sb}_1\text{Te}_5$ ) and  $t < 25000$  s ( $\text{Ge}_2\text{Sb}_2\text{Te}_5$ ), whereas the steady state is *assumed* to be reached for  $t > 15000$  s ( $\text{Ge}_4\text{Sb}_1\text{Te}_5$ ) and  $t > 25000$  s ( $\text{Ge}_2\text{Sb}_2\text{Te}_5$ ) because the nucleation rate appears time-independent within the noise of the data. The steady state nucleation rate<sup>6</sup>,  $I^{ss}$ , is determined as the average of the data for  $t > 15000$  s [ $\text{Ge}_4\text{Sb}_1\text{Te}_5$ , Fig. 7.11(c)] and  $t > 25000$  s [ $\text{Ge}_2\text{Sb}_2\text{Te}_5$ , Fig. 7.12(c)]. This procedure was repeated for all temperatures in the range mentioned at the beginning of this section.  $I^{ss}$  is plotted as a function of temperature in Fig. 7.13. Results for  $\text{Ge}_1\text{Sb}_2\text{Te}_4$ , which were obtained using the same analysis in a Diploma work that was advised within this PhD project [93], are included in this plot. The fit parameters for the Arrhenius fits in Fig. 7.13 are listed in Table 7.4.

According to the classical theory of steady state nucleation (Sec. 3.1), the critical work for heterogeneous cluster formation,  $\Delta G_c^{\text{het}}$  [Eq. (3.34)], can be found from

$$\Delta G_c^{\text{het}} = E_{I^{ss}} - E_u, \quad (7.21)$$

<sup>6</sup>The superscript ‘het’ that was used for the heterogeneous steady state nucleation rate,  $I^{ss,\text{het}}$ , in Sec. 3.1.2 [e. g., Eq. (3.36)] is dropped throughout Chap. 7 for simplicity. Confusion with *homogeneous* nucleation is not possible in this chapter as homogeneous nucleation is not involved in the thin film experiments.

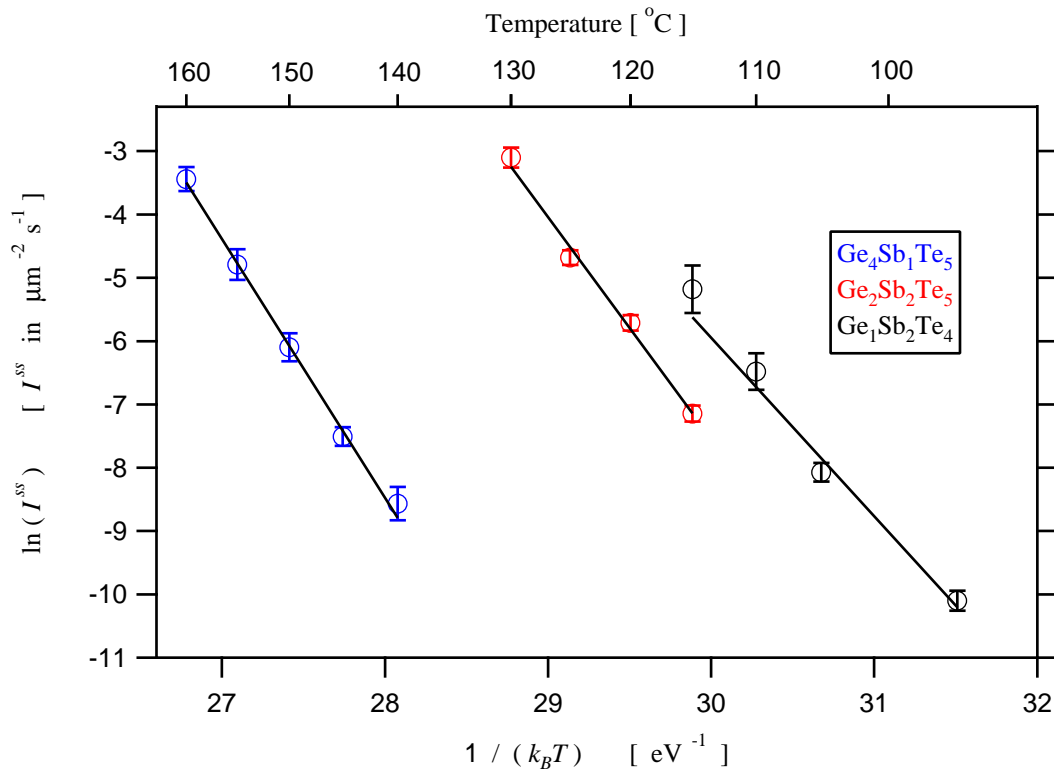


**Figure 7.13:** (Color). Steady state nucleation rate  $I^{ss}$  for  $\text{Ge}_4\text{Sb}_1\text{Te}_5$  (blue),  $\text{Ge}_2\text{Sb}_2\text{Te}_5$  (red), and  $\text{Ge}_1\text{Sb}_2\text{Te}_4$  (black) as a function of temperature. The data points were taken from an average of the nucleation rate  $I$  for large times [e. g., Figs. 7.11(c) and 7.12(c), horizontal solid line]. Fit parameters are listed in Table 7.4.

where  $E_u$  is the activation energy for the growth velocity (Table 5.3) and  $E_{Jss}$  the activation energy for the (heterogeneous) steady state nucleation rate (Table 7.4). Equation (7.21) can be verified by the use of Eqs. (3.35), (3.17), (5.12), and (5.15).

$\Delta G_c^{\text{het}}$  is given in Table 7.4 and provides a lower limit for the critical work for *homogeneous* nucleation  $\Delta G_c$  [Eq. (3.34)].

## 7.4 Discussion

### 7.4.1 Activation energy $E_k$ for the Avrami rate constant $k$

The activation energy  $E_k$  for the Avrami rate constant  $k$  (Table 7.2) differs slightly from the activation energy  $E_{kis}$  determined from electrical film resistance measurements by Kissinger analysis [133]:  $E_{kis} = (3.48 \pm 0.12)$  eV for  $\text{Ge}_4\text{Sb}_1\text{Te}_5$  [7] and  $E_{kis} = (2.24 \pm 0.11)$  eV for  $\text{Ge}_2\text{Sb}_2\text{Te}_5$  [8]. However,  $E_k$  and  $E_{kis}$  should usually coincide [134, 135]. The reason for this deviation is most likely the result of differences in surface and interface energies in the two experiments:  $E_k$  and  $E_{kis}$  usually encompass contributions of both nucleation and growth. As nucleation occurs at the film surface (Secs. 6.3.2 and 6.4.1), a different surface induces a different heterogeneous nucleation reduction factor  $f(\theta)$  [Eq. (3.26a)]. This affects the nucleation rate [Eq. (3.36)] and thereby the activation energy  $E_k$  or  $E_{kis}$ .

For instance, it was shown by Njoroge and co-workers [94, 124] that the activation energy  $E_{kis}$  differs between AgIn-Sb<sub>2</sub>Te films covered with a ZnS/SiO<sub>2</sub> capping layer versus a Si<sub>3</sub>N<sub>4</sub> capping layer, and versus films prepared without a capping layer (and therefore exposed to natural oxidation). Also, it was shown by Ohshima [136] that the crystallization temperature of Ge<sub>1</sub>Sb<sub>2</sub>Te<sub>4</sub> depends on the choice of the capping layer.

The values for  $E_{kis}$  reported above were obtained from measurements on uncapped films that were exposed to natural oxidation, like the films used in the present work. However, in the same way as for different capping layers (as explained above), a different stage of film oxidation can induce different nucleation characteristics and therefore influence the activation energy  $E_k$  or  $E_{kis}$ : It is known from electrical resistance measurements that the crystallization temperature for GeSbTe alloys differs for different stages of oxidation [94]. This might explain the discrepancy between  $E_k$  and  $E_{kis}$ : The samples used for the Kissinger analysis were measured shortly after deposition, i. e.,

oxidation was kept to a minimum. On the other hand, the samples used in the present work were measured after storing them for several weeks in vacuum. Hence, the latter should have oxidized more than the former.

The samples used for the Kissinger analysis were prepared in the same way as the samples in this work (direct current dynamic magnetron sputtering in the same sputter chamber using the same sputter parameters). Hence, it is unlikely that the deposition method can explain the discrepancy.

### 7.4.2 Avrami exponent $n$

The Avrami exponent  $n$  for  $\text{Ge}_2\text{Sb}_2\text{Te}_5$  has been measured frequently by various techniques but the data are not in agreement: Avrami exponents between about  $n = 2$  and  $n = 6$  have been obtained for this alloy (an overview of the numerous corresponding publications can be found in Sec. II. A of Ref. [137]). The discussion in Sec. 7.4.1 also applies to the Avrami exponent: the deviation among different data sets can be the result of differences in surface and interface energies in these experiments, e. g., due to differences in the stage of film surface oxidation or due to different capping layers. Differences in sample preparation (e. g., deposition method) can also account for this deviation.

Moreover, it should be noted that the magnitude of the JMA parameters  $n$  and  $k$  depend critically on the choice of the zero point in the time in the JMA equation [Eq. (3.66)]. In this work, the zero point in time was set equal to the time lag, which could unambiguously be determined by the back calculation of the nucleation time of the largest crystal. However, in most studies, some physical property change is correlated to the crystallized fraction  $\chi$ . This fraction is then fitted by Eq. (3.66), which yields  $n$  and  $k$ . For instance, in some studies, the running integral over the crystallization peak in a differential scanning calorimeter (DSC) during an isothermal measurement is chosen to be proportional to  $\chi(t)$ . In other experiments, the reflectivity/transmissivity change in thin films during an isothermal measurement is correlated to  $\chi(t)$ . In both cases, the choice of the zero point in time is not unambiguous, as the onset of a crystallization peak in a DSC or the onset of the reflectivity/transmissivity change is not clearly defined. In some studies, the zero point in time is chosen to be equal to the time when the isothermal temperature is reached. However, in particular

in a large furnace, also this point is not clearly defined as the isothermal temperature is either slowly approached from below or by oscillations around the setpoint [depending on the proportional integral derivative (PID) controller setting]. In the present study, the time constant of the DSC furnace is very small due to the small furnace size, so that this issue becomes negligible. The difficulty of the choice in the zero point in time in other studies inevitably results in discrepancy among data presented in different publications.

An additional problem of extracting JMA parameters from an experiment that does not allow *direct* observation of crystals but only correlates some physical property change to  $\chi$  (e. g., calorimetric or reflectivity/transmissivity measurements) is that those experiments often probe a signal that depends on the transformed *volume*: The running integral of the crystallization peak in the DSC is proportional to the transformed *volume* fraction  $\chi(t)$  of the sample, and the reflectivity/transmissivity of a film depends on the thickness of the crystallized layer. If nucleation however occurs heterogeneously at the film *surface*, the JMA analysis in such studies is meaningless: If the three-dimensional JMA analysis (Sec. 3.3.1) is used, nucleation centers are not randomly distributed in the volume, i. e., the main condition for the JMA analysis is violated. If the two-dimensional JMA analysis (Sec. 3.3.2) is applied, the measured signal cannot be correlated to the transformed *surface* fraction because it depends on the transformed *volume* fraction. Hence, the discrepancy of JMA parameters in different studies is often the result of an incorrect application of the JMA equation.

In this study, however, the analysis is entirely consistent due to the *direct* observation of crystals in combination with the high-precision DSC furnace:

- The AFM measures the crystallized *surface* fraction.
- The *two-dimensional* analysis (Sec. 3.3.2) is performed.
- Nucleation centers appear randomly distributed on the sample *surface* as seen in the AFM images (e. g., Figs. 5.5 – 5.12).
- The zero point in time is clearly defined by the time lag, which is obtained from direct crystal observation.

### 7.4.3 Activation energy for the steady state nucleation rate

#### $E_{I^{ss}}$ and critical work for nucleation $\Delta G_c$

Using the same analysis of Sec. 7.3.3, Privitera et al. [97] found an activation energy for the steady state nucleation rate of  $E_{I^{ss}} = (2.9 \pm 0.5)$  eV for  $\text{Ge}_2\text{Sb}_2\text{Te}_5$  by *in-situ* TEM, which is lower than the value determined in this work of  $E_{I^{ss}} = (3.50 \pm 0.17)$  eV (Table 7.4). As a result, they obtain a value for  $\Delta G_c^{\text{het}}$  of less than 1 eV, which is lower than the value in Table 7.4. The discussion in Sec. 7.4.1 also applies here: The deviation is most likely the result of differences in surface and interface energies in the two experiments due to differences in the sample preparation or differences in the stage of film surface oxidation.

### 7.4.4 Amorphous phase and undercooled liquid

With the exception of the time lag  $\tau$  (Table 7.1 and Fig. 7.1), all nucleation parameters presented in Chap. 7 were extracted from a stage of the measurement during which the crystal growth velocity was time-independent. Therefore, based on the assumption that the crystal growth velocity measurements apply to the undercooled liquid (and not to the amorphous phase, Sec. 5.4.3), it can be concluded that the nucleation parameters apply to the undercooled liquid as well.

For the time lag, however, this statement cannot be made because the first crystal nucleated before the first AFM scan was taken. However, growth velocity data is not available for the time before the first AFM scan. It remains unknown if the time lag applies to amorphous phase or undercooled liquid, or if it contains contributions of both amorphous phase and undercooled liquid. The latter case applies if equilibrium is reached by structural relaxation at some point during the first isothermal anneal.

The fact that structural relaxation may still be present before the first AFM scan would complicate the analysis of transient nucleation in Figs. 7.11(c) and 7.12(c): Structural relaxation would induce a decrease in the nucleation rate because the nucleation rate is proportional to the diffusivity  $D$  [Eq. (3.18)]. Transient nucleation, however, induces an increasing nucleation rate. Hence, only the steady state nucleation rate  $I^{ss}$  was extracted from Figs. 7.11(c) and 7.12(c), which is adopted for large times.

### 7.4.5 Time dependence of the nucleation rate

The nucleation rate  $I$  was analyzed by two methods: the JMA analysis (Sec. 7.3.2) and the back calculation analysis (Sec. 7.3.3). While the former method yields a nucleation rate that increases approximately linearly with time, the latter method yields transient nucleation for small times and a steady state (time-independent nucleation rate) for large times. Clearly, the results of both methods contradict each other.

The contradiction is a consequence of the fact that quantitative nucleation rate data is extremely difficult to obtain because the nucleation rate  $I$  is always related to the *time derivative* of the observable (which is the crystallized surface fraction  $\chi$  for the JMA analysis [Eq. (3.71)] and the counted number of crystals  $N$  for the back calculation method [Eq. (7.20)]). However, differentiation of data is always noisy. Therefore, the *time dependence* of  $I$  that can be obtained from both methods within the limited amount of data points available is not necessarily correct, in particular since large error bars have to be taken into account for the analysis. However, the *order of magnitude* of  $I$  certainly *is* correct and the same for both methods at any temperature and time. The nucleation rate  $I$  obtained in both methods should therefore be considered as some quantity that, once it is integrated over time, yields the correct time dependence of the observables  $\chi$  and  $N$  [Eqs. (3.71) and (7.20)]. This is because integration smooths any curve. In particular, Figs. 7.11(a) and 7.12(a) show that the number of crystals  $N$  as a function of time is the same for both JMA method and back calculation method within error, even though the nucleation rate differs.

Due to the difficulty of relating a time derivative to an observable, *assumptions* had to be made for a quantitative statement of the time dependence of  $I$ . For the back calculation analysis, it was assumed that the steady state was reached for large times [Figs. 7.11(c) and 7.12(c)]. This statement appears correct *within error and within the limited amount of data points available*. For the JMA analysis, it was assumed that  $n$  is time-independent, which appears correct within error and within the limited amount of data points available (Figs. 7.2–7.4). Therefore, the fit curves in Figs. 7.2–7.4 are assumed to be straight lines for all times. This assumption led to a nucleation rate that increases with time as  $t^{n-3}$  for all times. However,  $n$  does not necessarily have to be time-independent. In particular, it is questionable if the straight lines in Figs. 7.2–7.4 can be extrapolated to small times (where no data for  $\chi$  is available) because transient

nucleation usually makes the Avrami exponent  $n$  time-dependent [138]). Hence,  $I \propto t^{n-3}$  is particularly questionable for small times. The Avrami rate  $k$  constant (Fig. 7.7) should not be affected by the fact that  $n$  might be time-dependent: As discussed in Sec. 7.3.2,  $\ln(k)$  is insensitive to a change in the slope of the straight lines in Figs. 7.2–7.4 to a very good approximation because the intersection of the straight lines with the vertical axis is a *product* of  $n$  and  $\ln(k)$ . Therefore, the rate constant  $k$  should remain reliable.

Both JMA method and back calculation yield that the nucleation rate increases *somehow* with time. Therefore, it is apparent that transient nucleation plays a significant role during crystallization.

The advantage of the JMA method over the back calculation method is that it yields a good order of magnitude estimate for the nucleation rate without the need of counting crystals, which is a tedious and cumbersome process. Only the crystallized fraction  $\chi$  and the crystal growth velocity  $u$  have to be known, both as a function of time, in order to calculate the nucleation rate. On the other hand, the advantage of the back calculation method is that it is based on *direct* observation of crystals, which is physically more justified to give a correct time dependence of the nucleation rate than the JMA method. Direct observation of crystals is an achievement of the AFM measurements presented in this study and is not possible in many other studies found in the literature that report an observation of an *overall* crystallization rate (e. g., calorimetry, reflectivity, or electrical resistivity measurements). For this reason, the back calculation method, and not the JMA method, was chosen to be published elsewhere [115].

#### 7.4.6 Steady-state nucleation

The value  $\Delta G_c^{\text{het}}$  [Eq. (7.21), Table 7.4] was obtained under the assumption that Volmer's spherical cap model for classical nucleation theory (Sec. 3.1.2) is valid. In the following, it will be checked if the value  $\Delta G_c^{\text{het}}$  is self-consistent with the spherical cap model by substituting  $\Delta G_c^{\text{het}}$  in the lower line of Eq. (3.36) and comparing the result to the nucleation rate data in Fig. 7.13. Equation (3.36) states the heterogeneous nucleation rate per unit *volume*, whereas the nucleation rate data in Fig. 7.13 is given per unit *area*. Before substituting  $\Delta G_c^{\text{het}}$  in Eq. (3.36), this equation therefore

has to be converted to a nucleation rate per unit *area*: The quantity  $\epsilon$  is the fraction of atoms at the film surface (i. e., the equivalent amount of one atomic layer), which are all assumed to act as heterogeneous nucleation sites (Secs. 6.3.2 and 6.4.1). The unit length in Eq. (3.36) is the ‘meter’. An atomic distance is on the order of  $3 \text{ \AA} = 3 \cdot 10^{-10} \text{ m}$ . Therefore, if

$$\epsilon = \frac{3 \cdot 10^{-10} \text{ m}}{1 \text{ m}} = 3 \cdot 10^{-10} \quad (7.22)$$

is chosen, Eq. (3.36) is converted to a nucleation rate per unit *area*<sup>7</sup>:

$$I_A^{ss}(T) = 3 \cdot 10^{-10} \cdot \frac{10^{36}}{\hat{\eta}} \exp\left(-\frac{\Delta G_c^{\text{het}}}{k_B T}\right) \frac{1}{\text{m}^2 \text{s}}. \quad (7.23)$$

Alternatively, Eq. (7.23) can be derived from Eq. (3.36) by integration: The steady state nucleation probability  $P^{ss}$  per unit time (dimension:  $\frac{1}{\text{s}}$ ) in a volume  $V$  (dimension:  $\text{m}^3$ ) can be obtained from the steady state nucleation rate  $I_V^{ss}$  (dimension:  $\frac{1}{\text{m}^3 \text{s}}$ ) by the integration

$$P^{ss} = \int_V I_V^{ss}(x, y, z) \, dx \, dy \, dz, \quad (7.24)$$

where  $x$ ,  $y$ , and  $z$  are the spatial coordinates. Similarly, the steady state nucleation probability  $P_A^{ss}$  within a slice of thickness  $\Delta z = z_2 - z_1$  (Fig. 7.14) per unit time and per unit surface area of the slice (dimension of  $P_A^{ss}$ :  $\frac{1}{\text{m}^2 \text{s}}$ ) can be obtained by

$$P_A^{ss} = \int_{z_1}^{z_2} I_V^{ss}(x, y, z) \, dz. \quad (7.25)$$

If the nucleation rate is constant in space within the slice [ $I_V^{ss}(x, y, z) = I_V^{ss}$ ], this simplifies to

$$P_A^{ss} = \Delta z \cdot I_V^{ss}. \quad (7.26)$$

If the integration boundaries are chosen as  $z_1 = 0$  and  $z_2 = 3 \text{ \AA}$  (i. e., the thickness  $\Delta z$  of the slice is one atomic layer, within which the steady state nucleation rate is constant in space, and within which *all* atoms can act as a nucleation site), this yields

$$P_A^{ss} = 3 \cdot 10^{-10} \text{ m} \cdot I_V^{ss}, \quad (7.27)$$

which is equivalent to Eq. (7.23), where  $I_A^{ss} \equiv P_A^{ss}$ .

<sup>7</sup>Throughout Sec. 7.4.6 the *heterogeneous* steady state nucleation rate per unit *volume* [as given in Eq. (3.36), dimension:  $\frac{1}{\text{m}^3 \text{s}}$ ] is denoted as  $I_V^{ss}$ , whereas the *heterogeneous* steady state nucleation rate per unit *area* of film surface (dimension:  $\frac{1}{\text{m}^2 \text{s}}$ ) is denoted as  $I_A^{ss}$ . The additional indices  $A$  and  $V$  are used to avoid confusion.

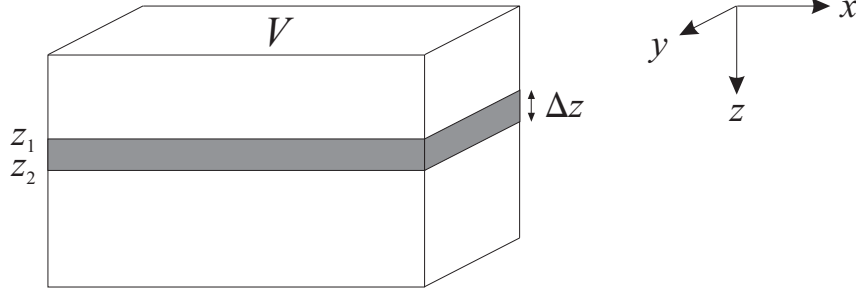


**Figure 7.14:** Schematic sketch of a volume  $V$  in which steady state nucleation at a rate of  $I_V^{ss}$  occurs. The nucleation probability  $I_A^{ss} \equiv P_A^{ss}$  within the dark slice of thickness  $\Delta z$  per unit time and per unit surface area of the slice is then given by Eq. (7.25).

In order to compare the data in Fig. 7.13 and Table 7.4 to Eq. (7.23), the viscosity  $\eta$  must be estimated.  $\eta$  is estimated to be on the order of  $10^{13}$  poise at a temperature  $T_{13}$ :  $T_{13} \sim 190^\circ\text{C}$  for  $\text{Ge}_4\text{Sb}_1\text{Te}_5$ ,  $T_{13} \sim 155^\circ\text{C}$  for  $\text{Ge}_2\text{Sb}_2\text{Te}_5$ , and  $T_{13} \sim 145^\circ\text{C}$  for  $\text{Ge}_1\text{Sb}_2\text{Te}_4$ .  $T_{13}$  is close to the calorimetric glass transition temperature  $T_g$  obtained by differential scanning calorimetry<sup>8</sup> (Chap. 8 below). Additionally, it is assumed that the fit curves to the data for the crystal growth velocity  $u$  (Fig. 5.14, Table 5.3) and the steady state crystal nucleation rate  $I_A^{ss}$  (Fig. 7.13, Table 7.4) can be extrapolated to  $T_{13}$ . Hence,  $\Delta G_c^{\text{het}}$  is also assumed to apply for temperatures around  $T_{13}$ . This gives

$$I_A^{ss}(T_{13}) = 3 \cdot 10^{-10} \cdot \frac{10^{36}}{10^{13}} \cdot \exp\left(-\frac{\Delta G_c^{\text{het}}}{k_B T}\right) \frac{1}{\text{m}^2\text{s}}. \quad (7.28)$$

Substituting  $\Delta G_c^{\text{het}}$  (Table 7.4) and the values for  $T_{13}$  mentioned above yields

$$\begin{aligned} I_A^{ss}(T_{13}) &= 3 \cdot 10^{-10} \cdot \frac{10^{36}}{10^{13}} \cdot \exp\left(-\frac{1.35 \cdot 1.602 \cdot 10^{-19} \text{J}}{1.381 \cdot 10^{-23} \frac{\text{J}}{\text{K}} \cdot (273.15 + 190)\text{K}}\right) \frac{1}{\text{m}^2\text{s}} \\ &= 6.2 \cdot 10^{-14} \frac{1}{\mu\text{m}^2\text{s}} \end{aligned} \quad (7.29a)$$

for  $\text{Ge}_4\text{Sb}_1\text{Te}_5$ . A similar calculation for the other two alloys yields

$$I_A^{ss}(T_{13}) = 8.8 \cdot 10^{-13} \frac{1}{\mu\text{m}^2\text{s}} \quad (\text{Ge}_2\text{Sb}_2\text{Te}_5), \quad (7.29b)$$

<sup>8</sup> $T_{13}$  was chosen slightly lower than the values for  $T_g$  obtained in Sec. 8.3 below because the heating rate in the scanning experiments in Sec. 8.3 was relatively large ( $40 \text{ K min}^{-1}$ ).  $T_g$  should increase with increasing heating rate (Sec. 2.2.1). However, it will be discussed below that the exact value that is assumed for  $T_{13}$  is unimportant.

and

$$I_A^{ss}(T_{13}) = 1.9 \cdot 10^{-10} \frac{1}{\mu\text{m}^2\text{s}} \quad (\text{Ge}_1\text{Sb}_2\text{Te}_4). \quad (7.29\text{c})$$

Extrapolation of the straight lines in Fig. 7.13 (using the fit parameters  $I_0^{ss}$  and  $E_{I^{ss}}$  in Table 7.4) to the temperature  $T_{13}$  mentioned above yields

$$\ln[I_A^{ss}(T_{13})] = 3.5 \Leftrightarrow I_A^{ss}(T_{13}) = 33.8 \frac{1}{\mu\text{m}^2\text{s}} \quad (\text{Ge}_4\text{Sb}_1\text{Te}_5), \quad (7.30\text{a})$$

$$\ln[I_A^{ss}(T_{13})] = 2.7 \Leftrightarrow I_A^{ss}(T_{13}) = 14.9 \frac{1}{\mu\text{m}^2\text{s}} \quad (\text{Ge}_2\text{Sb}_2\text{Te}_5), \quad (7.30\text{b})$$

$$\ln[I_A^{ss}(T_{13})] = 0.5 \Leftrightarrow I_A^{ss}(T_{13}) = 1.7 \frac{1}{\mu\text{m}^2\text{s}} \quad (\text{Ge}_1\text{Sb}_2\text{Te}_4). \quad (7.30\text{c})$$

Equations (7.29) and (7.30) disagree by 10–15 orders of magnitude depending on the alloy. This large deviation cannot be explained by the uncertainty in  $\Delta G_c^{\text{het}}$  given in Table 7.4 or by the uncertainty in the temperature  $T_{13}$  at which the viscosity adopts a value of  $10^{13}$  poise. Varying  $T_{13}$  by  $\pm 50$  K changes the discrepancy between Eqs. (7.29) and (7.30) only by around  $\pm 3$  orders of magnitude for all alloys.

A possibility to explain the discrepancy is to assume that the Stokes-Einstein-Equation [Eq. (2.3)], on which Eq. (3.36) is based, is violated for temperatures around  $T_{13}$  (cf. the discussion on the Stokes-Einstein equation in Sec. 3.1.1.4.1). Another possibility is that the steady state was not attained in Figs. 7.11(c) and 7.12(c), so that the data points Fig. 7.13 would not describe the steady state. Since Eq. (7.21) is only valid in the steady state, the values for  $\Delta G_c^{\text{het}}$  in Table 7.4 would be incorrect for this case.

However, it seems unlikely that these explanations can account for a discrepancy of up to 15 orders of magnitude between Eqs. (7.29) and (7.30). It appears more likely that Volmer's spherical cap model for heterogeneous nucleation (Sec. 3.1.2) breaks down in these experiments, possibly because the wetting angle  $\theta$  is too small [139, 140, 141, 142]: The number of atoms  $i_c^{\text{het}}$  in the critical cluster for heterogeneous nucleation is given by Eq. (3.33). If  $i_c^{\text{hom}} \sim 100$  is assumed for the number of atoms in the critical cluster for *homogeneous* nucleation, Eqs. (3.33) and (3.26a) yield  $i_c^{\text{het}} < 4$  for  $\theta < 40^\circ$  or  $i_c^{\text{het}} < 2$  for  $\theta < 35^\circ$  (cf. Fig. 3.4). Hence, a critical cluster is not well defined for low wetting angles due to the small value for  $i_c^{\text{het}}$ . In this case, the height of the nucleus falls below a monolayer thickness. Hence, the spherical cap model must clearly break down.

Kim and Cantor have proposed that nucleation can be interpreted as the onset of an adsorption of a solid-like layer on the heterogeneity for this case [143, 142].

Moreover, the spherical cap model assumes a *flat* heterogeneity. However, it is clear that heterogeneities are not necessarily atomically flat on the size scale of a critical cluster that only contains a few atoms for a low wetting angle. Heterogeneities usually contain atomic steps and other features that act as preferred nucleation sites [141]. For the GeSbTe alloys, nucleation was observed at the film surface (Sec. 6.3.2), which is not atomically flat but exhibits a finite roughness.

## 7.5 Conclusions

1. Analysis of the crystal size distribution (back calculation of crystal diameters) at temperatures between around 90 and 160 °C revealed a time lag for nucleation  $\tau$ . The time lag was thermally activated for AgIn-Sb<sub>2</sub>Te, Ge<sub>2</sub>Sb<sub>2</sub>Te<sub>5</sub>, and Ge<sub>1</sub>Sb<sub>2</sub>Te<sub>4</sub> (activation energies between 2 and 3 eV), while it was zero within the uncertainty of measurement for Ge<sub>4</sub>Sb<sub>1</sub>Te<sub>5</sub>. A higher time resolution may reveal the time lag for this alloy.
2. The analysis of the crystal size distribution revealed an early exhaustion of nucleation sites for AgIn-Sb<sub>2</sub>Te. Steady state nucleation is not reached for this alloy.
3. The Johnson-Mehl-Avrami (JMA) analysis revealed an Avrami exponent of  $n \sim 4$  for Ge<sub>4</sub>Sb<sub>1</sub>Te<sub>5</sub> and Ge<sub>2</sub>Sb<sub>2</sub>Te<sub>5</sub>. Therefore, the nucleation rate increases with time. The analysis of the crystal size distribution also revealed that the nucleation rate increases with time (during at least the first stage of the crystallization process). Therefore, transient nucleation plays a significant role during isothermal crystallization around 150 °C. A reliable quantitative expression for the time dependence of the nucleation rate  $I$  during transient nucleation is however difficult to obtain because  $I$  cannot be measured directly but can only be obtained indirectly from a time derivative of the observed crystallized fraction or crystal number.
4. The analysis of the crystal size distribution revealed that steady state nucleation is probably attained for the GeSbTe alloys during the isothermal crystallization

process between around 90 and 160°C. The steady state nucleation rate  $I^{ss}$  is thermally activated (activation energies between 2.6 and 4.3 eV).

5. The critical work for heterogeneous cluster formation,  $\Delta G_c^{\text{het}}$ , is around 1 eV for the GeSbTe alloys. This value, however, appears inconsistent with Volmer's spherical cap model for heterogeneous nucleation. It is possible that this model breaks down in these experiments due to a low wetting angle.
6. The number of crystals after complete surface crystallization (as extrapolated by the JMA analysis) increases with increasing temperature for the GeSbTe alloys but is independent of temperature for AgIn-Sb<sub>2</sub>Te. This behavior could be explained by a relation of the activation energies for nucleation and growth and the Avrami exponent  $n$ . It is consistent with the re-crystallization mechanisms observed upon laser annealing of amorphous marks.
7. The crystal nucleation parameters determined in this chapter are useful for modelling crystallization kinetics.

# Chapter 8

## The calorimetric glass transition temperature

### 8.1 Preface

It was mentioned in Sec. 1.1 that it is highly necessary to understand the crystallization kinetics of phase change materials in more detail. For diffusion-limited kinetics, those depend strongly on the temperature dependence of the shear viscosity  $\eta$  in the undercooled liquid state [Eqs. (3.22) and (3.49)]. Unfortunately, little is known about this temperature dependence for phase change materials because the undercooled liquid state is not easily available for experiments due to rapid crystallization. A crucial parameter is the glass transition temperature  $T_g$ , at which the viscosity of the undercooled liquid is on the order of  $10^{12}$  Pa s (Sec. 2.2.1). No unambiguous experimental evidence for the glass transition in phase change materials has been found so far. Speculations, however, are numerous. Mansuripur and co-workers assume a value of  $T_g = 400^\circ\text{C}$  to model crystallization and amorphization kinetics of  $\text{Ge}_2\text{Sb}_2\text{Te}_5$  [15]. Hudgens and Johnson assume  $T_g = 350^\circ\text{C}$  for the same alloy [4]. Lankhorst presents a model for estimating  $T_g$  for a variety of phase change materials based on the enthalpy of atomisation [144]. He obtains values for  $T_g$  that are in many cases much lower than the crystallization temperature [7, 9, 8, 94, 106, 145, 120, 103] upon heating at low and moderate rates ( $\dot{T} < 100$  K/min), e. g.,  $T_g = 190^\circ\text{C}$  ( $\text{Ge}_4\text{Sb}_1\text{Te}_5$ ),  $T_g = 77^\circ\text{C}$  ( $\text{Ge}_1\text{Sb}_2\text{Te}_4$ ),  $T_g = 111^\circ\text{C}$  ( $\text{Ge}_2\text{Sb}_2\text{Te}_5$ ), and  $T_g \sim 80^\circ\text{C}$  (AgIn-doped  $\text{Sb}_2\text{Te}$ ).

Morales-Sanchez and co-workers report experimental evidence for the glass transition of  $\text{Ge}_2\text{Sb}_2\text{Te}_5$  around  $100^\circ\text{C}$  by differential scanning calorimetry (DSC, Sec. 4.2) [146]. However, the data presented in Ref. [146] is limited and difficult to interpret. Finally, the author of this thesis has assumed the glass transition temperatures of  $\text{Ge}_4\text{Sb}_1\text{Te}_5$ ,  $\text{Ge}_2\text{Sb}_2\text{Te}_5$ , and  $\text{Ag}_{0.055}\text{In}_{0.065}\text{Sb}_{0.59}\text{Te}_{0.29}$  to be close to the crystallization temperature of the amorphous phase upon furnace heating, i. e. between around  $150^\circ\text{C}$  and  $200^\circ\text{C}$  depending on the alloy [106, 107].

This chapter presents unambiguous experimental evidence of the glass transition by DSC measurements for the phase change materials mentioned above. Excerpts of this chapter have been submitted for publication elsewhere [147].

## 8.2 Experimental methods

A solution of 3 vol. % polymethyl methacrylate (PMMA) dissolved in chlorobenzene was deposited by spin coating (4000 revolutions per minute) on glass microscope slides. Films of composition  $\text{Ge}_1\text{Sb}_2\text{Te}_4$ ,  $\text{Ge}_2\text{Sb}_2\text{Te}_5$ , and  $\text{Ag}_{0.055}\text{In}_{0.065}\text{Sb}_{0.59}\text{Te}_{0.29}$  (the same composition as in the previous chapters, hereafter:  $\text{AgIn-Sb}_2\text{Te}$ ) were deposited on those PMMA layers by dynamic direct current magnetron sputtering from a single target. Films of composition  $\text{Ge}_4\text{Sb}_1\text{Te}_5$  were deposited on thin plates of stainless steel by static direct current magnetron sputtering from a single target. The sputter chamber mentioned in Sec. 5.2.1 was used. For all depositions, the background pressure was approximately  $10^{-6}$  mbar and the working pressure during sputtering in Ar ambient  $7 \times 10^{-3}$  mbar. The sputtering power was 50 W ( $\text{Ge}_1\text{Sb}_2\text{Te}_4$ ), 25 W ( $\text{Ge}_2\text{Sb}_2\text{Te}_5$  and  $\text{AgIn-Sb}_2\text{Te}$ ), and 100 W ( $\text{Ge}_4\text{Sb}_1\text{Te}_5$ ). The deposition rate was approximately 0.25 nm/s ( $\text{Ge}_1\text{Sb}_2\text{Te}_4$ ,  $\text{Ge}_2\text{Sb}_2\text{Te}_5$ , and  $\text{AgIn-Sb}_2\text{Te}$ ), and 2 nm/s ( $\text{Ge}_4\text{Sb}_1\text{Te}_5$ ). The target diameter was 5 cm ( $\text{Ge}_2\text{Sb}_2\text{Te}_5$  and  $\text{AgIn-Sb}_2\text{Te}$ ) and 10 cm ( $\text{Ge}_1\text{Sb}_2\text{Te}_4$  and  $\text{Ge}_4\text{Sb}_1\text{Te}_5$ ). The target-substrate distance was 5 cm in all cases. The film thickness was 1500 nm ( $\text{Ge}_1\text{Sb}_2\text{Te}_4$ ,  $\text{Ge}_2\text{Sb}_2\text{Te}_5$ , and  $\text{AgIn-Sb}_2\text{Te}$ ), and 7000 nm ( $\text{Ge}_4\text{Sb}_1\text{Te}_5$ ). After deposition, the PMMA layer underneath the  $\text{Ge}_1\text{Sb}_2\text{Te}_4$ ,  $\text{Ge}_2\text{Sb}_2\text{Te}_5$ , and  $\text{AgIn-Sb}_2\text{Te}$  films was dissolved in acetone. For  $\text{Ge}_4\text{Sb}_1\text{Te}_5$ , the films were peeled off the substrate by bending it. Both methods gave sample fragments on the order of a few square millimeters. X-ray diffraction (XRD) showed that the structure of the as-deposited films

was amorphous. The samples were prepared without capping layers.

A power-compensated DSC (Perkin Elmer Diamond<sup>1</sup>), calibrated with the melting point and enthalpy (heat) of fusion of indium and zinc, was used to measure the heat flow,  $\dot{H} = dH/dt$  ( $H$ : enthalpy) into the sample. About 5-10 mg of film fragments were sealed in standard Al sample pans [item (3) in Fig. 4.2] and were scanned at constant heating and cooling rates. An empty Al pan was used as the reference ('Furnace 2' in Fig. 4.2). The atmosphere was high purity argon. In contrast to the author's previous study by DSC [107, 106], special attention was paid to the measurement of the baselines in order to observe and measure structural relaxation curves.

### 8.3 Results and discussion

Figure 8.1 displays the heat flow as a function of temperature for all as-prepared alloys. For the conversion of the heat flow in units of W/g (which is the *measured* quantity) to the heat flow in kW/mol (which is displayed on the vertical axes in Fig. 8.1), a molar mass was used that represents a weighted average of the molar masses of the elements. For  $\text{Ge}_4\text{Sb}_1\text{Te}_5$ , e. g., the molar mass  $M_{\text{Ge}_4\text{Sb}_1\text{Te}_5}$  is

$$M_{\text{Ge}_4\text{Sb}_1\text{Te}_5} = \frac{4 \cdot M_{\text{Ge}} + 1 \cdot M_{\text{Sb}} + 5 \cdot M_{\text{Te}}}{4 + 1 + 5}, \quad (8.1)$$

where  $M_{\text{Ge}}$ ,  $M_{\text{Sb}}$ , and  $M_{\text{Te}}$  are the molar masses of the elements Ge, Sb, and Te, respectively. From earlier x-ray diffraction measurements [9, 94, 7, 8, 145, 148, 120], the large exothermic peak upon heating of the initially amorphous sample (black curve) can be identified as crystallization. The coordinates of the peak position,  $T_{c,p}$  and  $\dot{H}_p$ , and the heat of crystallization,  $\Delta H_c$ , are given in Table 8.1. For  $\text{Ge}_4\text{Sb}_1\text{Te}_5$  and  $\text{AgInSb}_2\text{Te}$ , the values for  $\Delta H_c$  in Table 8.1 agree with the values reported in the author's earlier study [107, 106]. For  $\text{Ge}_2\text{Sb}_2\text{Te}_5$ ,  $\Delta H_c$  in Table 8.1 is higher than the earlier value [107, 106], which was only an estimate due to overlapping signals and baseline reproducibility problems. Yamada and co-workers [120] obtained a value of  $\Delta H_c = 26.7 \text{ J/g} = 3.1 \text{ kJ/mol}$  for  $\text{Ge}_1\text{Sb}_2\text{Te}_4$ , which coincides with the value obtained in this work (Table 8.1).

---

<sup>1</sup>The 'Perkin Elmer Diamond' DSC is the follow-up model of the 'Perkin Elmer Pyris 1' DSC used for the anneals in Sec. 5.2.3.1. Differences between the two models are marginal.

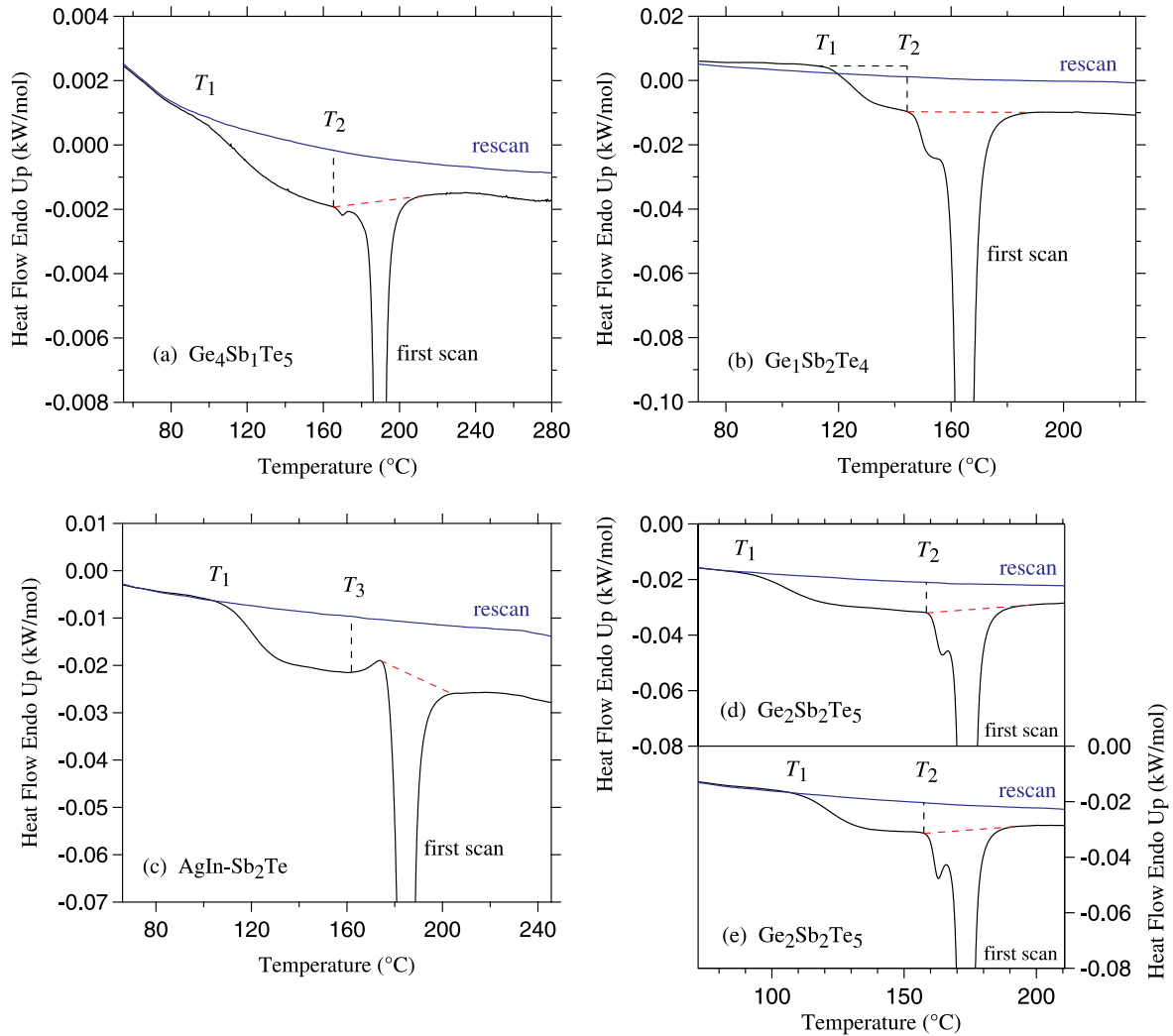


**Figure 8.1:** (Color). Heat flow as a function of temperature: (a)  $\text{Ge}_4\text{Sb}_1\text{Te}_5$ , sample age: 27 days. (b)  $\text{Ge}_1\text{Sb}_2\text{Te}_4$ , sample age: 106 days. (c)  $\text{AgIn-Sb}_2\text{Te}$ , sample age: 33 days. (d)  $\text{Ge}_2\text{Sb}_2\text{Te}_5$ , sample age: 3 days. (e)  $\text{Ge}_2\text{Sb}_2\text{Te}_5$ , sample age: 39 days. Black curve: first scan for the initially fully amorphous sample (heating). Due to its large extension, the main (exothermic) crystallization peak is not entirely shown for all alloys to make the baseline more visible. The quantities associated with the main crystallization peak are shown in Table 8.1. Blue curve: rescan of the crystallized sample (heating, reproduced in additional scans). The scan rate was  $\dot{T} = 40 \text{ K/min}$  for all alloys, except for  $\text{Ge}_4\text{Sb}_1\text{Te}_5$ , where it was  $\dot{T} = 5 \text{ K/min}$ . Comparison of the first scan and the rescan (the latter serves as a baseline) reveals the onset of observable structural relaxation at  $T_1$ , the onset of surface crystallization at  $T_2$ , and the onset of the endothermic signal characteristic of the glass transition at  $T_3$ . The expression ‘Endo Up’ at the vertical axis denotes that the endothermic direction is positive.

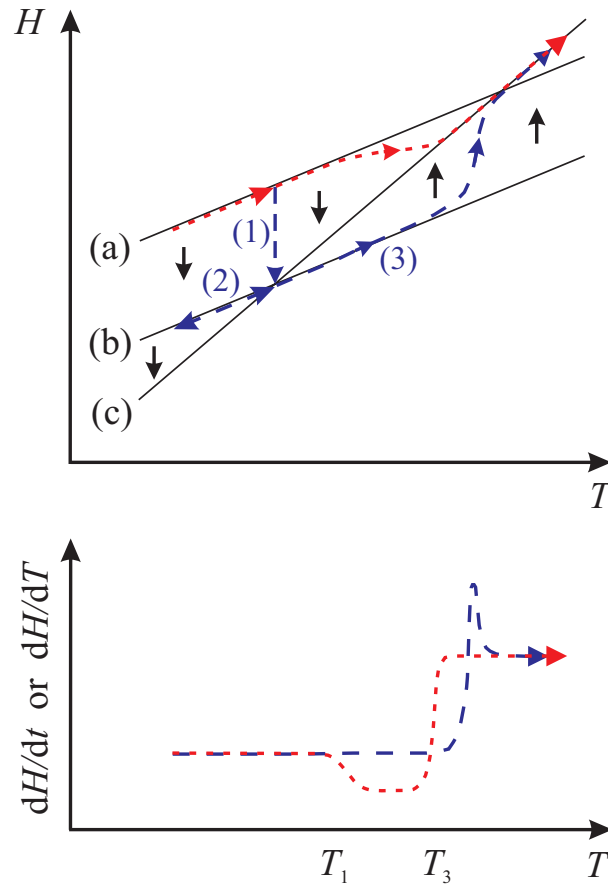
**Table 8.1:** Peak coordinates  $T_{c,p}$  and  $\dot{H}_p$  of the main crystallization peak (not entirely shown in Figs. 8.1 and 8.3 for better baseline visibility) during the first scan of the initially amorphous sample.  $T_{c,p}$  is the peak crystallization temperature and  $\dot{H}_p$  is the peak heat flow signal. The quantities  $\Delta H_{str,g}$  and  $\Delta H_{str,m}$  are the amount of heat that is released in the amorphous phase during structural relaxation, normalized per mass and per mole, respectively (integral of the thermal curve in Fig. 8.1 from  $T_1$  to  $T_2$  for the GeSbTe alloys and from  $T_1$  to  $T_3$  for AgIn-Sb<sub>2</sub>Te; i. e., the area to the left of the vertical black dotted line in Fig. 8.1). The quantities  $\Delta H_{c,g}$  and  $\Delta H_{c,m}$  are the heat of crystallization per mass and per mole, respectively (determined by the area underneath the red dotted line in Fig. 8.1). The heat of crystallization in Fig. 8.3 is the same as in Fig. 8.1 (for the same alloy) but is not listed here. The heating rate was  $\dot{T} = 40$  K/min for all scans, except for the scan shown in Fig. 8.1(a), where it was  $\dot{T} = 5$  K/min. For this reason, the peak height in Fig. 8.1(a) is lower.

Figure	Alloy	$T_{c,p}$ (°C)	$\dot{H}_p$ (kW/mol)	$\Delta H_{str,g}$ (J/g)	$\Delta H_{str,m}$ (kJ/mol) <sup>a</sup>	$\Delta H_{c,g}$ (J/g)	$\Delta H_{c,m}$ (kJ/mol) <sup>a</sup>
Fig. 8.1(a)	Ge <sub>4</sub> Sb <sub>1</sub> Te <sub>5</sub>	190.2	-0.126	9.4 ± 0.5	0.99 ± 0.05	37.1 ± 1.0	3.9 ± 0.1
Fig. 8.1(b)	Ge <sub>1</sub> Sb <sub>2</sub> Te <sub>4</sub>	164.6	-0.398	2.9 ± 0.5	0.34 ± 0.05	26.3 ± 1.0	3.1 ± 0.1
Fig. 8.1(c)	AgIn-Sb <sub>2</sub> Te	184.3	-0.987	5.9 ± 0.5	0.72 ± 0.05	35.2 ± 1.0	4.3 ± 0.1
Fig. 8.1(d)	Ge <sub>2</sub> Sb <sub>2</sub> Te <sub>5</sub>	173.4	-0.776	7.0 ± 0.5	0.80 ± 0.05	34.2 ± 1.0	3.9 ± 0.1
Fig. 8.1(e)	Ge <sub>2</sub> Sb <sub>2</sub> Te <sub>5</sub>	172.9	-0.900	5.1 ± 0.5	0.58 ± 0.05	34.2 ± 1.0	3.9 ± 0.1
Fig. 8.3(a)	Ge <sub>4</sub> Sb <sub>1</sub> Te <sub>5</sub>	215.9	-0.664	n/a	n/a	n/a	n/a
Fig. 8.3(b)	Ge <sub>1</sub> Sb <sub>2</sub> Te <sub>4</sub>	168.1	-0.478	n/a	n/a	n/a	n/a
Fig. 8.3(c)	AgIn-Sb <sub>2</sub> Te	184.3	-1.249	n/a	n/a	n/a	n/a
Fig. 8.3(d)	Ge <sub>2</sub> Sb <sub>2</sub> Te <sub>5</sub>	183.3	-1.002	n/a	n/a	n/a	n/a

<sup>a</sup>1 kJ/mol =  $\frac{1000}{eN_{Av}}$  eV/atom  $\approx 10.4$  meV/atom ( $e$ : elementary charge;  $N_{Av}$ : Avogadro's number).

The blue curve in Fig. 8.1 is the rescan of the crystallized sample. This rescan was reproduced in several additional heating cycles. Hence, it serves as a baseline for the first scan (black curve). A comparison of these two curves shows a heat release to the left side of the main crystallization peak, starting at a temperature  $T_1$ . This cannot be ascribed to crystallization because the isothermal time lag  $\tau$  for nucleation at the temperature  $T_1$  is too long to allow crystallization. Furthermore, the isothermal crystal growth velocity  $u$  is far too slow at  $T_1$  to observe crystallization. For example, the measurements of crystallization parameters by atomic force microscopy (AFM, Figs. 5.14 and 7.1) showed that  $\tau(140^\circ\text{C}) \sim 50$  min and  $u(140^\circ\text{C}) \sim 8 \text{ \AA}/\text{min}$  for  $\text{AgIn-Sb}_2\text{Te}$ ; and  $\tau(115^\circ\text{C}) \sim 4$  h and  $u(115^\circ\text{C}) \sim 4 \text{ \AA}/\text{min}$  for  $\text{Ge}_2\text{Sb}_2\text{Te}_5$ . The thermal history of the samples used for the measurement of the crystallization parameters by AFM and for the scanning experiments described in this chapter was almost the same: In the former experiments, a heating rate of 50 K/min was used to ramp up to the isothermal anneal temperature (Sec. 5.2.3.1), and in the latter a heating rate of 40 K/min (cf. the caption of Fig. 8.1). Hence, the comparison of the two experiments is appropriate. Therefore, the exothermic heat flow at  $T_1$  can be ascribed to structural relaxation of the amorphous phase, which is usually accompanied by heat release (cf. Fig. 2.7 and the red dotted curve in Fig. 8.2) [23, 149, 150, 151]. As shown in Figs. 8.1(d) and (e), the onset temperature  $T_1$  for observable structural relaxation depends on the sample age (the time the sample was stored at room temperature). The heat release during structural relaxation  $\Delta H_{str}$  was obtained from the area to the left of the vertical black dotted line in Fig. 8.1 (integral from  $T_1$  to  $T_2$  for the GeSbTe alloys and from  $T_1$  to  $T_3$  for  $\text{AgIn-Sb}_2\text{Te}$ ) and is given in Table 8.1. A broad, exothermic signal from structural relaxation has been observed in many other amorphous materials [149, 152, 153, 154] and is attributed to the presence of a spectrum of activation energies for the sites where relaxation occurs. Prolonged isothermal annealing, for example at room temperature, eliminates the sites with the lowest activation energies. As a result, upon heating a lower heat of relaxation  $\Delta H_{str}$  and a higher onset  $T_1$  are observed.

At the temperature  $T_2$ , an onset to a small exothermic peak occurs for the GeSbTe alloys (this peak is less pronounced for  $\text{Ge}_4\text{Sb}_1\text{Te}_5$ ). This can be ascribed to heterogeneous nucleation at the (naturally oxidized) sample surface. It is known from cross-sectional transmission electron microscopy (Sec. 6.3.2 and Ref. [119]) that the



**Figure 8.2:** (Color). Top graph: Schematic evolution of the enthalpy  $H$  as a function of temperature  $T$ . The curves (a) and (b) denote isoconfigurational states (amorphous phase, cf. Fig. 2.7). The undercooled liquid (equilibrium) is denoted by curve (c). Structural relaxation of the amorphous phase changes the enthalpy of the amorphous phase towards the enthalpy of the undercooled liquid (solid black arrows). Dotted curve (red): Enthalpy evolution during continuous heating without pre-annealing (corresponds to Fig. 8.1). Dashed curve (blue): Enthalpy evolution during pre-annealing (1), cooling (2), and subsequent continuous heating (3) at the *same* rate as for the dotted red curve (corresponds to Fig. 8.3). Bottom graph: Time or temperature derivative of the enthalpy  $H$  as measured in the DSC. Endothermic signals are positive. The onset of structural relaxation at  $T_1$  is accompanied by an exothermic signal.  $T_1$  depends on thermal history: the more relaxed the amorphous phase is, the higher is  $T_1$  [Figs. 8.1(d) and (e)]. If the pre-anneal is long enough (vertical dashed blue arrow in the top graph), the exothermic heat release at  $T_1$  is not observed during subsequent heating. The onset of the endothermic signal characteristic of the glass transition at  $T_3$  is more pronounced if the sample is pre-annealed (dashed blue curve in the bottom graph). It is instructive to compare this figure to Fig. 5.16.

sample surface of naturally oxidized GeSbTe alloys crystallizes prior to the rest of the film. Surface crystallization effects similar to those shown in Fig. 8.1 have also been observed in 4-point-probe electrical film resistance measurements [94] and stress measurements [155] upon heating naturally oxidized GeSbTe alloys of the same composition as those studied here.

Crystallization of  $\text{Ge}_1\text{Sb}_2\text{Te}_4$  [145, 120, 148, 156] and  $\text{Ge}_2\text{Sb}_2\text{Te}_5$  [120, 119, 157, 158, 106, 107] has been studied intensely by DSC over the past 20 years but all of those studies have focused on the determination of the peak crystallization temperature  $T_{c,p}$ . Even though in some studies of  $\text{Ge}_1\text{Sb}_2\text{Te}_4$  and  $\text{Ge}_2\text{Sb}_2\text{Te}_5$  a heat release is visible in the amorphous phase [148, 156, 158], this effect has neither been related to structural relaxation nor surface crystallization, mostly because no reference was made to a reproducible baseline. The author's earlier study [107, 106] revealed indication of such a heat release for  $\text{Ge}_2\text{Sb}_2\text{Te}_5$  at around 100°C as well, but baseline reproducibility problems hampered the precise interpretation of this effect.

The calorimetric signal of the glass transition is an endothermic step, since the heat capacity increases due to the availability of configurational degrees of freedom (cf. Fig. 2.6) [23, 150, 151]. In Fig. 8.1, an onset for such a step is only visible for AgIn-Sb<sub>2</sub>Te at a temperature  $T_3$ . For the other alloys, crystallization interferes, as is common in many other glasses. Since the glass transition is a kinetic phenomenon, it is sometimes possible to reveal  $T_g$  by pre-annealing the amorphous phase [150, 151]. This is schematically shown in Fig. 8.2: During the pre-anneal, equilibrium [curve (c)] is approached by structural relaxation (vertical blue dashed arrow). This increases the shear viscosity, i. e., the viscosity in the isoconfigurational state (b) is higher than in state (a) (Fig. 2.4) [20, 21]. During subsequent continuous heating (dashed blue curve in Fig. 8.2), structural relaxation is initially not observed due to the large viscosity (or equivalently, low mobility). This is in contrast to the sample that was not pre-annealed (red dotted curve), for which structural relaxation is observed at  $T_1$  for the same heating rate. During further heating of the pre-annealed sample (dashed blue line in Fig. 8.2), the mobility increases and structural relaxation becomes finally very pronounced, leading to a strong endothermic signal in the DSC associated with the glass transition (dashed blue curve, bottom of Fig. 8.2). Figure 8.3 shows the scans on the pre-annealed samples. Pre-anneal time and temperature were chosen in such a way

that the surface crystallization was completed during the pre-anneal. The isothermal surface crystallization parameters determined by atomic force microscopy (Chaps. 5 and 7) were used for the calculation of the appropriate pre-anneal time and temperature. Hence, no surface crystallization signal appears in Fig. 8.3 at a temperature  $T_2$ . This additionally facilitates the detection of the glass transition, the onset of which appears at a temperature  $T_3$ . However, the main crystallization peak interferes, so that the endothermic step associated with the glass transition (Fig. 8.2) cannot be resolved entirely. The peak crystallization temperature  $T_{c,p}$  of the pre-annealed samples increases by few Kelvin (Table 8.1) due to a higher viscosity in the amorphous phase prior to crystallization. For AgIn-Sb<sub>2</sub>Te,  $T_{c,p}$  was not affected by the pre-anneal.

The reduced glass transition temperature, defined as  $T_{rg} = T_g/T_l$ , can be estimated by taking  $T_g$  to be close to  $T_3$  or  $T_{c,p}$ , and by using the values for  $T_l$  determined below in Chap. 9 (Table 9.1). For Ge<sub>1</sub>Sb<sub>2</sub>Te<sub>4</sub> (which is not listed in Table 9.1), the ternary Ge–Sb–Te phase diagram gives a value of  $T_l \sim 620^\circ\text{C}$  [159, 160]. This yields a value of  $T_{rg}$  that is on the order of 0.5 for all four alloys studied in this chapter. Usually,  $T_{rg}$  ranges between around 0.45 and 0.85 for known glass formers. Examples are SiO<sub>2</sub> ( $T_{rg} = 0.835$ ), B<sub>2</sub>O<sub>3</sub> ( $T_{rg} = 0.76$ ), GeO<sub>2</sub> ( $T_{rg} = 0.65$ ), Se ( $T_{rg} = 0.61$ ), Pd<sub>82</sub>Si<sub>18</sub> ( $T_{rg} = 0.60$ ), Fe<sub>80</sub>B<sub>20</sub> ( $T_{rg} \sim 0.49$ ), and Au<sub>77</sub>Ge<sub>14</sub>Si<sub>9</sub> ( $T_{rg} = 0.475$ ) [41]. Turnbull showed by calculations based on Eqs. (3.22) and (2.9) that the maximum in the steady-state crystal nucleation rate as a function of temperature in the undercooled liquid decreases with increasing value of  $T_{rg}$  [70].<sup>2</sup> Hence, the ‘ease’ of glass formation by continuous cooling from the melt approximately increases with increasing value for  $T_{rg}$ : Materials that exhibit a large value for  $T_{rg}$  can usually be quenched into a glass at low or moderate cooling rates and are therefore called *easy glass formers*. In contrast, materials with a low value for  $T_{rg}$  can usually be quenched into a glass only at extremely high cooling rates and are therefore called *marginal glass formers*. This categorizes the Te alloys as marginal glass formers due to their relatively low value for  $T_{rg}$ . It is this property that makes these materials useful for fast phase change recording since it enables fast crystallization.

Figure 8.3 also reveals heat release in the crystalline phase during the first heat-

---

<sup>2</sup>These calculations assume that the other parameters on which the nucleation rate depends [ $\alpha$  and  $\beta$ , defined in Eq. (9.4) below] are held fixed. A more rigorous discussion of this issue is provided in Sec. 9.5.4.1 below.

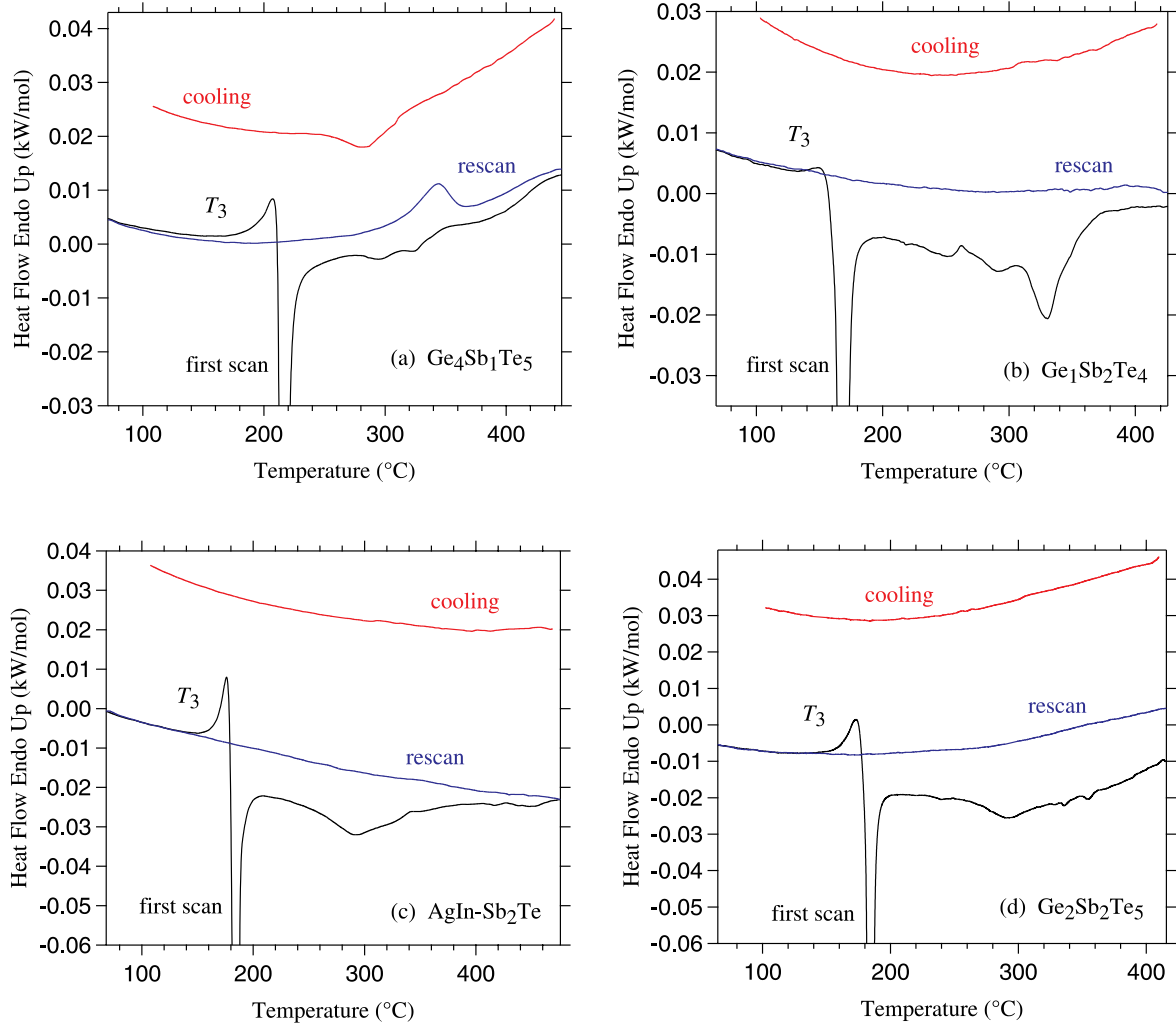


**Figure 8.3:** (Color). Heat flow as a function of temperature on pre-annealed samples. (a)  $\text{Ge}_4\text{Sb}_1\text{Te}_5$ , pre-anneal for 47 h at 136 °C. (b)  $\text{Ge}_1\text{Sb}_2\text{Te}_4$ , pre-anneal for 40 h at 100 °C. (c)  $\text{AgIn-Sb}_2\text{Te}$ , pre-anneal for 48 hours at 112 °C. (d)  $\text{Ge}_2\text{Sb}_2\text{Te}_5$ , pre-anneal for 37 h at 114 °C. Black curve: first scan for the initially fully amorphous sample (heating). Due to its large extension, the main (exothermic) crystallization peak is not entirely shown for all alloys to make the baseline more visible. The quantities associated with the main crystallization peak are shown in Table 8.1. Blue curve: rescan of the crystallized sample (heating, reproduced in additional scans). Red curve (top): cooling signal (reproduced in additional scans). The scan rate was  $\dot{T} = \pm 40$  K/min for all alloys. The onset of the endothermic signal characteristic of the glass transition occurs at a temperature  $T_3$ .

ing scan (black curve). Comparison of this curve with the rescan (blue) reveals that this heat release is irreversible. Possible explanations are crystal-to-crystal transformations, phase separation, and grain growth. Indeed, an irreversible crystal-to-crystal-transformation between a cubic and a hexagonal phase was reported by XRD for  $\text{Ge}_1\text{Sb}_2\text{Te}_4$  [145, 120, 148] and  $\text{Ge}_2\text{Sb}_2\text{Te}_5$  [120, 8, 94] around 200–300°C. On the other hand, a separation of an  $\text{AgSbTe}_2$  phase was reported upon annealing the alloy  $\text{Ag}_{0.08}\text{In}_{0.13}\text{Sb}_{0.49}\text{Te}_{0.30}$  (similar in composition to the  $\text{AgIn-Sb}_2\text{Te}$  alloy studied in this work) for 1 h at 350°C [161].

$\text{Ge}_4\text{Sb}_1\text{Te}_5$  exhibits a reversible transformation of  $2.6\pm 0.4$  J/g ( $= 0.27\pm 0.04$  kJ/mol) between 300 and 350°C (Fig. 8.3). However, this transformation is not visible in the first scan (black curve). Hence, it is likely that phase separation during the first heating scan creates a high-temperatures phase, which transforms reversibly upon subsequent cooling and heating. For the other alloys, the cooling curves do not show any transformations (red curves at the top of Fig. 8.3).

## 8.4 Conclusions

1. Structural relaxation upon continuous heating of amorphous phase change materials can be measured in the DSC.
2. The onset temperature  $T_1$  for structural relaxation depends on thermal history:  $T_1$  increases with increasing sample age or pre-annealing time. The heat released during structural relaxation is on the order of 0.5–1.0 kJ/mol and also depends on thermal history.
3. The heat of amorphous-to-crystal transformation (heat of crystallization) is between 3.0 and 4.5 kJ/mol for all alloys.
4. An irreversible heat release in the crystalline phase follows the amorphous-to-crystalline phase transformation for all alloys upon heating. This might be related to crystal-to-crystal transformations, phase separation, or grain growth.
5. For  $\text{Ge}_4\text{Sb}_1\text{Te}_5$ , an additional reversible transformation of around 0.2–0.3 kJ/mol is observed, probably as a result of a reversible crystal-to-crystal transformation.

6. Pre-annealing the amorphous phase reveals that the glass transition temperature  $T_g$  is within 10 K of the crystallization temperature upon continuous heating at 40 K/min for all alloys.
7. The ratio of the glass transition temperature to the liquidus temperature is around 0.5 for all alloys, which classifies them as marginal glass formers. This property allows fast crystallization and makes these alloys useful for phase change recording.
8. The knowledge of the glass transition temperature is useful to model kinetics of nucleation and growth, which depend crucially on the temperature dependence of the viscosity.

## Part III

Nucleation parameters in  
undercooled droplets measured  
close to the melting point of  
liquidus temperature



# Chapter 9

## The crystal nucleation rate

### 9.1 Preface

The experiments presented in Chaps. 5 and 7 of this work qualitatively showed that it is likely that the crystal nucleation rate determines the re-crystallization mechanism of amorphous marks observed upon laser heating (Fig. 1.2) more than the crystal growth velocity. *Quantitative* extrapolations of the crystallization parameters determined in Chaps. 5 and 7 to higher temperatures than around 150–200 °C, i. e., to the temperature range over which crystallization may occur during laser heating, have not been performed. Such extrapolations are difficult because the activation energies of the atomic transport coefficients in the undercooled liquid are strongly temperature dependent around  $T_g$  (e. g., Fig. 2.4, and Refs. [47, 20, 21]). Therefore, the experiments presented in Chaps. 5 and 7 can only *qualitatively* be compared to kinetics under operating conditions. On the other hand, they are useful to estimate the stability of the amorphous phase against spontaneous re-crystallization at temperatures around  $T_g$ .

This chapter presents estimates of the crystal-melt interfacial energy  $\sigma$  [Eq. (3.3)], which is the most important parameter for the calculation of the steady-state nucleation rate  $I^{ss}$  [Eq. (3.22b)]. Direct measurements of  $\sigma$  are difficult. Indirectly,  $\sigma$  can be determined from undercooling experiments if nucleation during continuous cooling is homogeneous [64, 77, 73, 72]. Hence, in the experiments presented in this chapter, liquid droplets of Sb- and Te-based alloys are undercooled below the liquidus temperature  $T_l$ , and crystallization during continuous cooling is observed in a differential

thermal analyzer (DTA, Sec. 4.3). Since the atomic transport coefficients are only weakly temperature dependent around  $T_l$  (e.g., Fig. 2.4, and Refs. [47, 20, 21]), the knowledge of  $\sigma$  allows quantitative extrapolations of the nucleation rate from  $T_l$  to the temperature regime between  $T_g$  and  $T_l$  over which crystallization may occur under operating conditions.

The undercooling of a droplet is usually limited by the presence of impurities, surface oxides, and container walls that act as heterogeneous crystal nucleants [64]. To approach the limit of homogeneous nucleation, which yields the largest undercooling<sup>1</sup>, heterogeneous nucleation sites must be removed or deactivated. Several such techniques have been found to significantly increase the undercooling. They are only briefly reviewed here; a major review can be found in Refs. [64, 26]:

**Emulsion technique:** The liquid is dispersed into a large number of small droplets (approximate size: 10–100  $\mu\text{m}$ ). This isolates heterogeneous nucleation sites in a few droplets. The remainder of the droplets that do not contain heterogeneous sites can be undercooled far, possibly to the homogeneous limit. The droplets may be coated to prevent interactions.

**Substrate technique:** Similar to the emulsion technique, small droplets are cooled on a glass substrate, which does not trigger nucleation because it is amorphous (cf. the discussion in Sec. 6.4.1). This is usually performed in vacuum or an inert atmosphere to reduce oxidation. Crystallization upon continuous cooling can be observed by optical microscopy. This is visible as surface roughening or for high melting point materials as a light flash due to recalescence<sup>2</sup>.

**Containerless solidification technique:** Nucleation frequently occurs at container walls. Levitating liquid droplets in electromagnetic or electrostatic fields has increased undercooling significantly. The temperature of the droplet can be measured with a pyrometer. Large undercoolings have also been obtained in zero gravity on the space shuttle and during free fall in a drop tower.

---

<sup>1</sup>Homogeneous nucleation sets the ultimate undercoolability of a melt since the critical work for homogeneous cluster formation  $\Delta G_c^{\text{hom}}$  is always larger than the critical work for heterogeneous cluster formation  $\Delta G_c^{\text{het}}$  [Eq. (3.34)].

<sup>2</sup>The re-heat of an undercooled liquid due to release of the heat of crystallization is called ‘recalescence’.

**Fluxing technique:** The liquid droplet is surrounded with a liquid flux, which isolates the droplet from the container walls and eliminates nucleants from the surface of the droplet by dissolution and inclusion [162, 123, 163, 122, 164, 165, 166, 73, 72, 167, 168]. This method was used for the undercooling experiments presented in this chapter because it significantly reduces evaporation of volatile droplets as a secondary effect<sup>3</sup>. This is in contrast to the containerless solidification and the substrate techniques, which cannot prevent evaporation. Moreover, in contrast to the emulsion technique, the fluxing technique can undercool *large* sample volumes. This can be useful to study volatile alloys because the overall chemical composition upon heating may be maintained for a longer time if the sample is large: If the volatility of the alloy components is different, a *small* sample volume may quickly change its overall composition due to a large surface-to-volume ratio.

Excerpts of this chapter have also been published elsewhere [170].

## 9.2 Experimental methods

B<sub>2</sub>O<sub>3</sub> flux was chosen for three reasons:

- B<sub>2</sub>O<sub>3</sub> is chemically more stable than all oxides that can form from elemental Ge, Sb, Te, Ag, and In (Fig. 9.1).
- Due to its low glass transition and melting temperature, 275 °C and 450 °C, respectively [47, 171, 172], the viscosity of B<sub>2</sub>O<sub>3</sub> is sufficiently low around the liquidus temperature  $T_l$  of the phase change alloys to serve as an effective flux<sup>4</sup>.
- B<sub>2</sub>O<sub>3</sub> is an easy glass former that does not crystallize at any temperature at ambient pressure [173, 174], and thereby provides a liquid or amorphous sample container at all temperatures.

As B<sub>2</sub>O<sub>3</sub> is hydrophilic, it had to be dehydrated by annealing in a Pt crucible for about 30 min at 1000 °C in air.

---

<sup>3</sup>The vapor pressure of the Sb and Te alloys used in this work was observed to be very high, probably a result of the large vapor pressure for elementary Sb and Te [169].

<sup>4</sup>The liquidus temperature  $T_l$  of all alloys is between 500 and 700 °C, as shown below in Table 9.1.

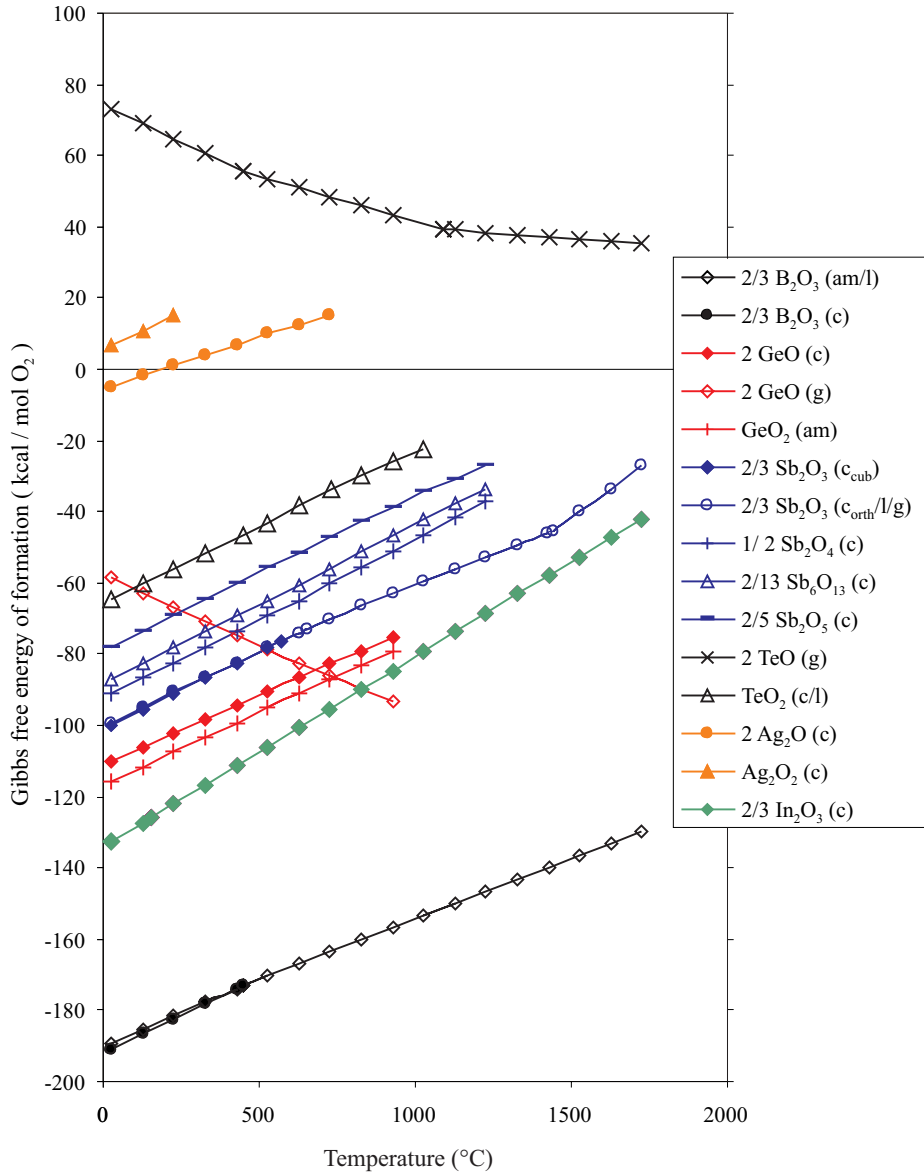


**Figure 9.1:** (Color). Gibbs free energy of formation (per mole of gaseous  $O_2$ ) for various oxides that can form from the elements that are contained in the Sb and Te alloys studied in this work. The general reaction for any element E is  $2\frac{x}{y} E(c,l,g) + O_2(g) \rightarrow \frac{2}{y} E_xO_y(c,l,g,am)$ . c: crystalline; l: liquid; g: gaseous; am: amorph;  $c_{cub}$ : cubic crystalline phase;  $c_{orth}$ : orthorhombic crystalline phase. Data taken from [105, 175].

A Perkin Elmer/Seiko Pyris Diamond thermogravimetric/differential thermal analyzer (TG/DTA, Sec. 4.3) was calibrated [84, 85, 86, 87] for both the heating and cooling mode using the melting point  $T_m$  and heat of fusion  $\Delta H_f$  of indium, tin, zinc, and aluminum as standards.

Crystalline bulk samples of the slightly off-eutectic [19] composition  $\text{Ge}_{12}\text{Sb}_{88}$  were prepared by alloying 5 N elemental Ge and Sb powder in an argon atmosphere (pre-evacuated to high vacuum) for 3 h at 1050°C. After cooling, optical microscopy revealed the eutectic microstructure of 5- $\mu\text{m}$ -fine lamellae. Crystalline bulk samples of compositions  $\text{Ag}_{0.055}\text{In}_{0.065}\text{Sb}_{0.59}\text{Te}_{0.29}$  (the same composition as used in Part II of this work, hereafter AgIn-Sb<sub>2</sub>Te),  $\text{Ge}_4\text{Sb}_1\text{Te}_5$  and  $\text{Ge}_2\text{Sb}_2\text{Te}_5$  were prepared by cutting chunks from a single sputter target with a razor blade. A typical sample of size between 0.03 and 1 mm<sup>3</sup>, determined from its mass and approximate density [7, 94, 9, 102], was placed into a cylindrical ceramic DTA sample pan (diameter and height: 5 mm) and surrounded with dehydrated amorphous  $\text{B}_2\text{O}_3$  chunks at room temperature, which provided a liquid sample container once the pan was heated.

The fluxed sample was repeatedly cycled in the DTA in Ar atmosphere at constant heating and cooling rates between 0.1 and 50 K min<sup>-1</sup>. Melting upon heating and crystallization upon cooling was observed by an endothermic and exothermic peak, respectively. The objective of this experiment was to undercool the sample as far as possible, and thereby to approach the limit of homogeneous nucleation, which yields the largest possible undercooling. The amount of undercooling as a function of fluxing time  $t_f$  and fluxing temperature  $T_f > T_l$  was investigated.

A power-compensated differential scanning calorimeter (DSC, Perkin Elmer, Pyris 1, Sec. 4.2), calibrated [84, 85, 86, 87] using the melting point and heat of fusion of indium, tin, and zinc, was used to measure the heat of fusion of  $\text{Ge}_{12}\text{Sb}_{88}$  and AgIn-Sb<sub>2</sub>Te from the area under the endothermic melting peak upon heating. Al sample pans were used [item (3) in Fig. 4.2]. The liquidus temperature  $T_l$  of  $\text{Ge}_{12}\text{Sb}_{88}$ , however, is slightly larger than 600°C (Table 9.1 below). In order to avoid reactions of the Al pan with the Pt holder (Sec. 4.2), a thin circular graphite disk was placed between Al pan and Pt holder for the measurement of  $\text{Ge}_{12}\text{Sb}_{88}$  (the DSC was calibrated for this condition). The heat of fusion of  $\text{Ge}_2\text{Sb}_2\text{Te}_5$  was taken from a previous DSC study [106, 107]. The heat of fusion of  $\text{Ge}_4\text{Sb}_1\text{Te}_5$  could not be measured in the DSC due to

the high liquidus temperature of more than 660°C (Table 9.1 below) and due to the high volatility. Therefore, it had to be estimated from the area of the endothermic DTA peak.

### 9.3 Results

The upper curves in Fig. 9.2 display the endothermic melting peak for all alloys measured in the DTA. The curves show that melting does not occur at a single melting point  $T_m$  but over a temperature range between the solidus temperature  $T_s$  and the liquidus temperature  $T_l$ . This is common for alloys (Sec. 2.1). Analysis of the melting peak for  $\text{Ge}_{12}\text{Sb}_{88}$  based on the binary phase diagram [19, 160] confirms that this composition is slightly off-eutectic (sharp peak from eutectic melting at 592°C, followed by a broader peak up to the liquidus temperature of the non-eutectic phase [18]). The eutectic composition is  $\text{Ge}_{15}\text{Sb}_{85}$  [19]. For  $\text{AgIn-Sb}_2\text{Te}$ , the measured value for  $T_l$  (Table 9.1) is close to the literature value [19, 159] of  $T_l = 545^\circ\text{C}$  for the alloy  $\text{Sb}_2\text{Te}$ , which is similar in composition to  $\text{AgIn-Sb}_2\text{Te}$ . The measured liquidus temperatures (Table 9.1) for  $\text{Ge}_4\text{Sb}_1\text{Te}_5$  and  $\text{Ge}_2\text{Sb}_2\text{Te}_5$  agree with other DSC and DTA studies [176, 159, 160, 106, 107]<sup>5</sup>.

Fluxing the sample slightly above the liquidus temperature gave almost no undercooling for all alloys (about 10 K), no matter how long the fluxing time  $t_f$  was. The undercooling is measured from the liquidus temperature, i. e.,  $\Delta T_n = T_l - T_n$ , where  $T_n$  is the onset of the exothermic crystallization peak upon cooling (Fig. 9.2). This is empirically justified by observations that the composition-dependence of  $T_n$  in undercooling experiments on binary alloy droplets roughly parallels the liquidus line [177, 178, 44, 179, 180]. Further justification comes from the observation that the reduced glass transition temperature  $T_{rg}$  defined by  $T_g/T_l$  shows a stronger correlation with critical cooling rate for glass formation than  $T_{rg}$  defined by  $T_g/T_s$  [25, 181]. Increasing the fluxing temperature  $T_f$  enhanced the undercooling, i. e.,  $\text{B}_2\text{O}_3$  acted as a more efficient flux at higher temperatures, probably due to its viscosity decrease or to the enhanced dissolution kinetics. Fluxing temperatures  $T_f$  above about 800°C did not further enhance the undercooling for any of the alloys. The fluxing time  $t_f$  did not

<sup>5</sup>The pseudobinary  $\text{GeTe-Sb}_2\text{Te}_3$  phase diagram in Ref. [176] is re-plotted in Fig. 1 of Ref. [120].

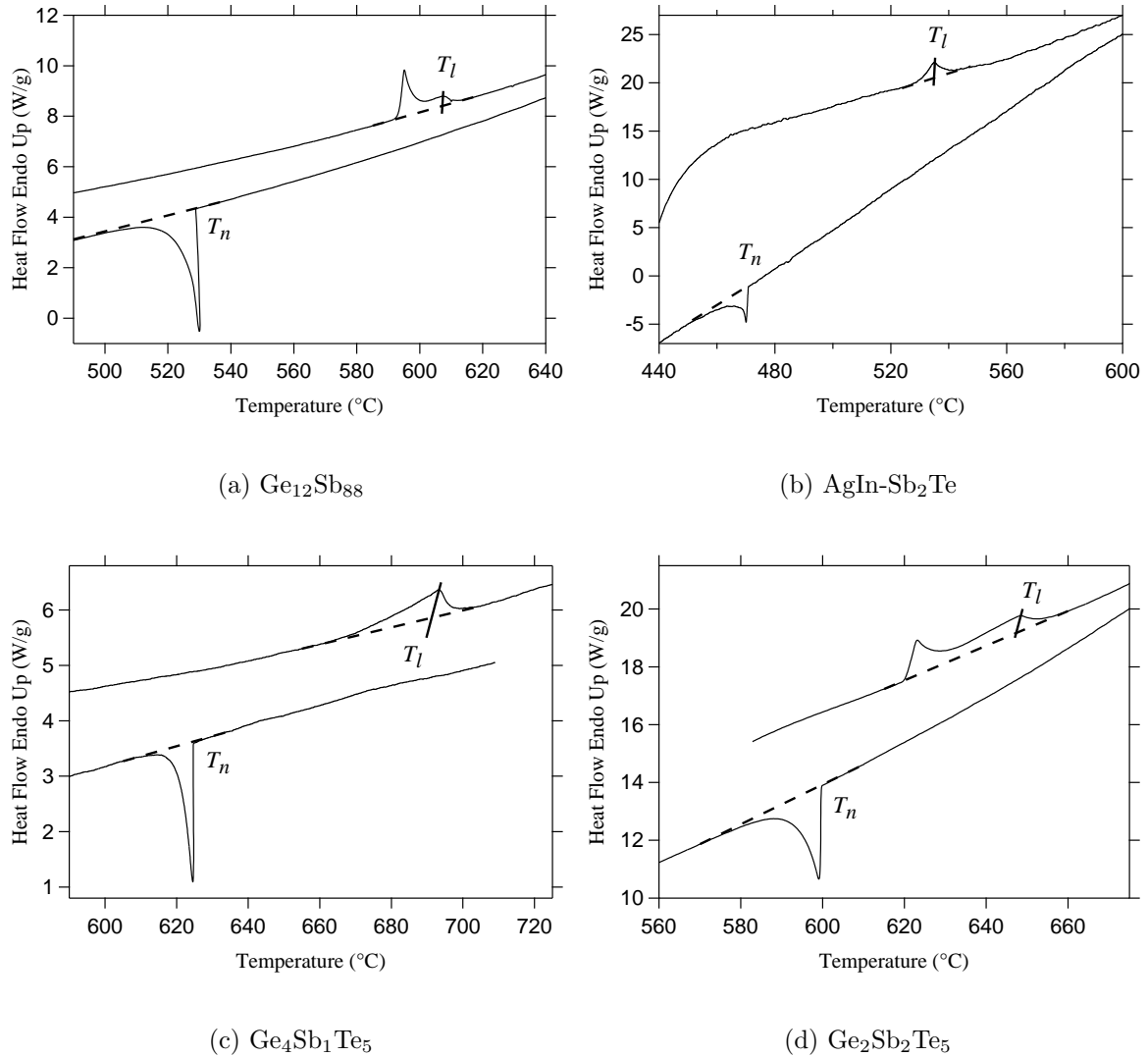


**Figure 9.2:** Heat flow as a function of temperature for  $\text{B}_2\text{O}_3$ -fluxed Sb and Te alloys measured by differential thermal analysis (DTA). Heating (upper curve): In order to assign the correct liquidus temperature  $T_l$  to the observed endothermic melting peak, an auxiliary line is drawn from the end of the signal to the interpolated baseline (dashed) at an angle obtained from a calibration experiment (cf. Fig. 2 in Ref. [84]). This angle in the four figures appears different due to different sample masses and due to the normalization of the vertical axis per mass. Cooling (lower curve): The nucleation temperature  $T_n$  is assigned to the onset of the exothermic crystallization peak. Above  $T_n$ , the sample remains entirely liquid. For each alloy, the cooling curve displays the *largest* undercooling  $\Delta T_n = T_l - T_n$  obtained (Table 9.1). The heating (cooling) rate was  $\dot{T} = \pm 10 \text{ K/min}$  for all alloys, except for  $\text{Ge}_4\text{Sb}_1\text{Te}_5$ , where it was  $\dot{T} = \pm 5 \text{ K/min}$ . The sample mass was (a) 3.881 mg; (b) 0.211 mg; (c) 3.087 mg; (d) 1.924 mg.

have a significant effect on the amount of undercooling: Fluxing times of a few minutes and of a few hours gave the same undercooling for the same fluxing temperature.

The lower curves in Fig. 9.2 display the exothermic crystallization peak of those cooling cycles that yielded the largest undercooling (cf. Table 9.1). The undercooling was independent of cooling rate and sample volume within the limits mentioned in Sec. 9.2. Crystallization occurs in the time interval during which the heat flow decreases upon cooling, i. e., crystallization is completed once the peak reaches its minimum. The subsequent increasing heat flow signal (exponential relaxation towards the baseline) is a result of the difference in temperature between sample and reference that was caused by the recalescence. The exothermic peaks therefore show that *complete* crystallization occurs within a very short time interval, implying that the crystal growth velocity is large at  $T_n$ .

During frequent cycling of the same sample, in particular at high fluxing temperatures  $T_f$  and for long fluxing times  $t_f$ , the liquidus temperature upon heating was observed to change. Since  $T_l$  is composition-dependent (e. g., Fig. 2.1), the composition must therefore have changed. This is probably a result of different vapor pressures or solution kinetics in the  $B_2O_3$  for the elements contained in the alloy. However, since the nucleation temperature  $T_n$  usually roughly parallels the liquidus temperature in the phase diagram, this should not affect the measured undercooling  $\Delta T_n = T_l - T_n$  if the change in  $T_l$  remains small (i. e., a few Kelvin). However, in this case, the undercooling has to be measured from the liquidus temperature in the *subsequent* heating cycle because the change in liquidus temperature occurs far quicker at higher temperatures due to enhanced kinetics. The upper curves shown in Fig. 9.2 all represent the heating cycle *subsequent* to the cooling cycle shown in the lower curve. Similarly, the values for  $T_l$  in Table 9.1 correspond to *this* heating cycle. The change in liquidus temperature for the heating cycles shown in Fig. 9.2 (with respect to the measured liquidus temperature in the *first* heating cycle on the *same* sample) are: +1.4 K ( $Ge_{12}Sb_{88}$ ); -3.7 K ( $AgIn-Sb_2Te$ ); -2.6 K ( $Ge_4Sb_1Te_5$ ); -4.8 K ( $Ge_2Sb_2Te_5$ ).

After cooling down to room temperature, the samples were exposed by boiling the sample pan in water and thereby dissolving the glassy  $B_2O_3$ . Optical microscopy revealed the eutectic microstructure of 5- $\mu$ m-fine lamellae for the  $Ge_{12}Sb_{88}$  alloy.

The heat of fusion  $\Delta H_f$  (area of the melting peak upon *heating*) determined from

**Table 9.1:** Liquidus temperature  $T_l$  upon heating, *lowest* nucleation temperature  $T_n$  observed upon cooling, *largest* undercooling  $\Delta T_n = T_l - T_n$ , and *largest* relative undercooling  $\Delta T_{n,r} = \Delta T_n/T_l$ , from differential thermal analysis measurements (Fig. 9.2). The uncertainty for the temperatures are  $\pm 1^\circ\text{C}$ . Heat of fusion per mass  $\Delta H_{f,g}$  and heat of fusion per mole  $\Delta H_{f,m}$  from differential scanning calorimetry (DSC) and differential thermal analysis (DTA) measurements (peak area upon *heating*). For  $\text{Ge}_4\text{Sb}_1\text{Te}_5$ , the error in  $\Delta H_f$  is larger than for the other alloys because the calorimetric data obtained from the DTA are less precise than those obtained from the DSC.

Alloy	$T_l$ ( $^\circ\text{C}$ )	$T_n$ ( $^\circ\text{C}$ )	$\Delta T_n$ ( $^\circ\text{C}$ )	$\Delta T_{n,r}$	$\Delta H_{f,g}$ (J/g)	$\Delta H_{f,m}$ (kJ/mol) <sup>a</sup>
$\text{Ge}_{12}\text{Sb}_{88}$	607.0	529.9	77.1	0.088	$185.8 \pm 2.8^b$	$21.5 \pm 0.3^b$
$\text{AgIn-Sb}_2\text{Te}$	534.1	471.9	62.2	0.077	$136.8 \pm 2.7^b$	$16.7 \pm 0.3^b$
$\text{Ge}_4\text{Sb}_1\text{Te}_5$	690.7	625.1	65.6	0.068	$114.9 \pm 13.8^c$	$12.1 \pm 1.4^c$
$\text{Ge}_2\text{Sb}_2\text{Te}_5$	643.2	600.7	42.5	0.046	$128.9 \pm 6.4^d$	$14.7 \pm 0.7^d$

<sup>a</sup>1 kJ/mol =  $\frac{1000}{eN_{\text{Av}}}$  eV/atom  $\approx 10.4$  meV/atom ( $e$ : elementary charge;  $N_{\text{Av}}$ : Avogadro's number).

<sup>b</sup>From DSC measurements.

<sup>c</sup>From DTA measurements.

<sup>d</sup>From previous DSC measurements [107, 106].

DSC and DTA measurements<sup>6</sup> are given in Table 9.1. The DSC curves are not shown but look very similar to the DTA curves (heating cycle) shown in Fig. 9.2. The heat of fusion for  $\text{AgIn-Sb}_2\text{Te}$  agrees approximately with a value published previously [106, 107].

<sup>6</sup>For the conversion of  $\Delta H_{f,g}$  (which is the *measured* quantity) to  $\Delta H_{f,m}$  in Table 9.1, a molar mass was used that represents a weighted average of the molar masses of the elements. For  $\text{Ge}_4\text{Sb}_1\text{Te}_5$ , e. g., the molar mass is given by Eq. (8.1).

## 9.4 Analysis

### 9.4.1 General method: Determination of the interfacial energy and the steady-state nucleation rate from observations during continuous cooling

Nucleation at a steady state rate  $I^{ss}$  of a new phase in an undercooled liquid of volume  $V$  cooled at a rate  $\dot{T} < 0$  leads to transformation if the probability of nucleation during cooling from the liquidus temperature  $T_l$  to the nucleation temperature  $T_n$  is unity [72, 73]:

$$\frac{V}{\dot{T}} \int_{T_l}^{T_n} I^{ss}(T) dT \sim 1. \quad (9.1)$$

The steady-state nucleation rate  $I^{ss}$  is given by Eq. (3.36) for the general case of *heterogeneous* nucleation. The free energy change  $\Delta G_{lc,V}$  in Eq. (3.36) can be estimated from the approximations by Turnbull (TB), Thompson and Spaepen (TS), and Hoffman (HM) if liquid heat capacity data is not available (Sec. 2.3.3). However, it should be noted that Eqs. (2.32)(a)–(c) apply to a single-component system (i. e., an element or a congruently melting compound), which exhibits a single melting temperature  $T_m$  (cf. the discussion at the beginning of Sec. 2.3). An exact calculation of  $\Delta G_{lc,V}$  for alloys is complicated and can only be performed if the free energy of all phases is known as a function of composition and temperature [43]. This is not the case for the Sb and Te alloys studied in this work. Therefore,  $\Delta G_{lc,V}$  is approximated in the following by substituting  $T_m$  with  $T_l$  in Eqs. (2.32)(a)–(c). This approximation is still expected to give satisfactory results [53]:

$$\begin{aligned} \Delta G_{lc,V}(T) &= \frac{\Delta H_{f,V} \Delta T}{T_l} && \text{(TB),} \\ \Delta G_{lc,V}(T) &= \frac{\Delta H_{f,V} \Delta T}{T_l} \cdot \left( \frac{2T}{T_l + T} \right) && \text{(TS),} \\ \Delta G_{lc,V}(T) &= \frac{\Delta H_{f,V} \Delta T}{T_l} \cdot \left( \frac{T}{T_l} \right) && \text{(HM).} \end{aligned} \quad (9.2)$$

$\Delta H_{f,V}$  is the heat of fusion per unit volume. The steady-state nucleation rate [Eq. (3.36)] is then given by:

$$\begin{aligned}
 I^{ss} &= \epsilon \frac{10^{36}}{\hat{\eta}} \exp\left(-\frac{16\pi}{3k_B T} \frac{\sigma^3 T_l^2}{(\Delta H_{f,V} \Delta T)^2} f(\theta)\right) \frac{1}{\text{m}^3 \text{s}} \quad (\text{TB}), \\
 I^{ss} &= \epsilon \frac{10^{36}}{\hat{\eta}} \exp\left(-\frac{16\pi}{3k_B T} \frac{\sigma^3 T_l^2}{(\Delta H_{f,V} \Delta T)^2} \left(\frac{T_l + T}{2T}\right)^2 f(\theta)\right) \frac{1}{\text{m}^3 \text{s}} \quad (\text{TS}), \\
 I^{ss} &= \epsilon \frac{10^{36}}{\hat{\eta}} \exp\left(-\frac{16\pi}{3k_B T} \frac{\sigma^3 T_l^2}{(\Delta H_{f,V} \Delta T)^2} \left(\frac{T_l}{T}\right)^2 f(\theta)\right) \frac{1}{\text{m}^3 \text{s}} \quad (\text{HM}). \quad (9.3)
 \end{aligned}$$

In order to facilitate the application of nucleation theory and to compare nucleation experiments on different materials quantitatively, Turnbull introduced a number of dimensionless parameters [70]. He argued that the crystal-vacuum interfacial energy is related to the heat of sublimation in molecular crystals described by van der Waals interactions and to the crystal lattice energy in ionic crystals [64]. He expected that the liquid-crystalline interfacial energy  $\sigma$  should scale with the molar heat of fusion  $\Delta H_{f,m}$ . Indeed, this was later observed experimentally on a large number of metals and semi-metals (e. g., Table 9.3 and Fig. 9.4 below). The dimensionless parameters are defined by [70]

$$\begin{aligned}
 \alpha &= \frac{\sigma \Omega^{2/3}}{\frac{\Delta H_{f,m}}{N_{\text{Av}}}} = \frac{(N_{\text{Av}} V_m^2)^{1/3} \sigma}{\Delta H_{f,m}}, & \beta &= \frac{\Delta H_{f,m}}{RT_l}, \\
 T_r &= \frac{T}{T_l}, & \Delta T_r &= \frac{T_l - T}{T_l}, \quad (9.4)
 \end{aligned}$$

where  $\alpha$  is the interfacial energy per atomic area in the interface, normalized by the heat of fusion per atom; it is a measure for the number of monolayers that can be melted with the interfacial energy.  $\beta$  is an entropy of fusion, normalized to the gas constant  $R$ .  $N_{\text{Av}}$ ,  $\Omega$ , and  $V_m$  are Avogadro's number, the atomic volume, and the molar volume, respectively. This yields the steady-state nucleation rate as a function

of dimensionless parameters<sup>7</sup>:

$$\begin{aligned}
 I^{ss} &= \epsilon \frac{10^{36}}{\hat{\eta}} \exp\left(-\frac{16\pi}{3} \frac{f(\theta)}{T_r(\Delta T_r)^2} \alpha^3 \beta\right) \frac{1}{\text{m}^3 \text{s}} && \text{(TB)}, \\
 I^{ss} &= \epsilon \frac{10^{36}}{\hat{\eta}} \exp\left(-\frac{4\pi}{3} \frac{(T_r^{-1} + 1)^2 f(\theta)}{T_r(\Delta T_r)^2} \alpha^3 \beta\right) \frac{1}{\text{m}^3 \text{s}} && \text{(TS)}, \\
 I^{ss} &= \epsilon \frac{10^{36}}{\hat{\eta}} \exp\left(-\frac{16\pi}{3} \frac{f(\theta)}{T_r^3(\Delta T_r)^2} \alpha^3 \beta\right) \frac{1}{\text{m}^3 \text{s}} && \text{(HM)}. \tag{9.5}
 \end{aligned}$$

It is instructive to set  $f(\theta) = 1$  and  $\epsilon = 1$  and thereby assume that nucleation in the undercooling experiments was homogeneous [123, 164, 72, 73]. Hence, substitution of Eq. (9.3) or Eq. (9.5) into Eq. (9.1) and numerical evaluation of the integral yields an estimate for the interfacial energy if the heat of fusion  $\Delta H_f$  and the viscosity  $\hat{\eta}$  are known. Alternatively, if liquid heat capacity data is available,  $\Delta G_{lc,V}$  can be calculated based on those data, and Eq. (3.36) can be substituted directly into Eq. (9.1) [using  $f(\theta) = 1$  and  $\epsilon = 1$ ]. Substituting the value for the interfacial energy obtained from the integration into Eq. (9.3) or Eq. (9.5) yields the temperature dependence of the steady-state nucleation rate. In case nucleation was heterogeneous, this analysis still yields a lower limit for the interfacial energy and an upper limit for the *homogeneous* steady-state nucleation rate.

### 9.4.2 Crystal-melt interfacial energy

The interfacial energy  $\sigma$  was calculated using the method described in Sec. 9.4.1, with  $f(\theta)$  and  $\epsilon$  set to unity. Hence, it is assumed that the largest observed undercooling  $\Delta T_n$  (Table 9.1) corresponds to homogeneous nucleation. Estimates of the free energy difference  $\Delta G_{lc}$  between undercooled liquid and crystal based on liquid heat capacity measurements are available only for AgIn-Sb<sub>2</sub>Te due to the higher liquidus temperature for the other alloys [106, 107]. Figure 9.3 compares the experimental curve of Refs. [106, 107] with the three approximations in Eq. (9.2) for this alloy. Only the TS and the HM approximations describe the measured curve satisfactorily, but not the TB approximation, which is usually used only for undercooling of metals, for which the

---

<sup>7</sup>In Ref. [170], the TS approximation used in Eq. (9.5) [Eq. (A5) in Ref. [170]] contained a misprint: An expression  $(T_r + 1)^2$  was erroneously printed in the exponential instead of  $(T_r^{-1} + 1)^2$ . However, the calculations in Ref. [170] were based on the correct equation, which is given in Eq. (9.5).

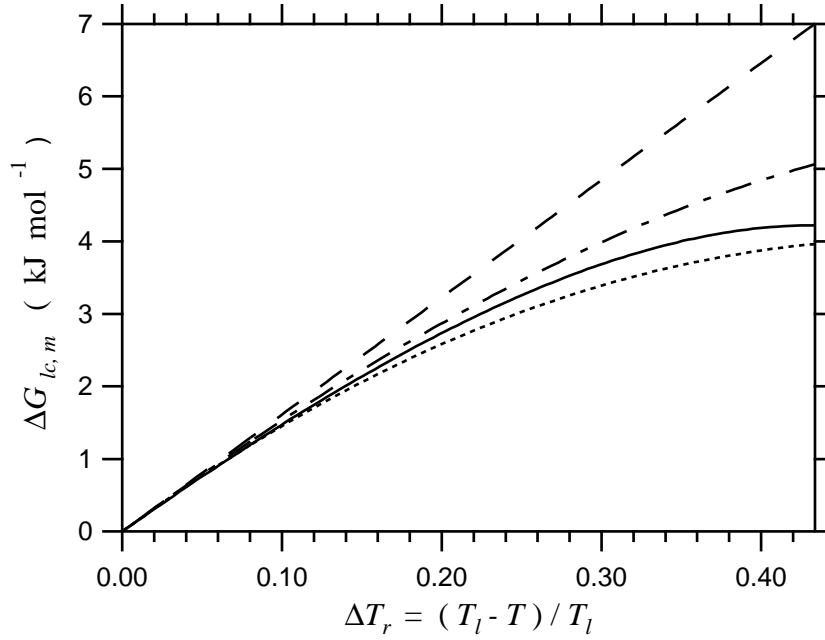


**Figure 9.3:** Difference in molar free energy  $\Delta G_{lc,m}$  between the undercooled liquid and the crystal as a function of relative undercooling  $\Delta T_r$  [Eq. (9.4)] for AgIn-Sb<sub>2</sub>Te. The solid curve is based on liquid heat capacity measurements from Refs. [106, 107]. The other curves are calculated from Eq. (9.2) using values for  $\Delta H_{f,m}$  and  $T_l$  given in Table 9.1: Turnbull approximation (TB, dashed), Thompson/Spaepen approximation (TS, dot-dashed), and Hoffman approximation (HM, dotted).

difference in specific heat between liquid and crystal near the melting point is close to zero. In the following it is therefore assumed that the TS and HM approximations also apply to the other alloys.

For small undercoolings  $\Delta T_{n,r}$  on the order of 0.1 as given in Table 9.1, the viscosity  $\eta$  can be assumed to be independent of temperature (Refs. [70, 64], cf. also Fig. 2.4). Viscosity data around the liquidus temperature are not available for any of the alloys studied here. The viscosity is therefore estimated to be  $\eta \sim 2 \times 10^{-2}$  poise, a typical value for many materials [70]. Using an oscillating crucible viscosimeter [182], such a value was also measured slightly above the liquidus temperature for Sb<sub>100-x</sub>Te<sub>x</sub>, where  $x$  ranged from 0 to 100 [183], as well as for Ge<sub>100-x</sub>Te<sub>x</sub>, where  $x$  ranged from 50 to 100 [184], and also for various other binary Te alloys [183, 185]. The exact knowledge of the viscosity is unimportant for the calculation of the interfacial

energy since  $\hat{\eta}$  is part of the pre-exponential factor in Eqs. (3.36) or (9.3) [cf. also the discussion in the paragraph below Eq. (3.22b)]. For the same reason, the application of a *temperature dependent* viscosity model based on Eq. (2.9) was found to give the same value for  $\sigma$  since the undercooling is not large.

Table 9.2 shows the calculated values for  $\sigma$  and  $\alpha$ . Both were assumed to be independent of temperature for the integration in Eq. (9.1). This is a reasonable assumption because the undercooling  $\Delta T_{n,r}$  is small (Table 9.1). For the calculation of  $\sigma$  (but not for the calculation of  $\alpha$ ), the mass density  $\rho$  of the material must be known. This can be seen in the equations above: the exponential part of Eq. (9.5) only depends on dimensionless parameters, but the exponential part of Eq. (9.3) depends on the heat of fusion per *volume*  $\Delta H_{f,V}$ , which can only be obtained from the *measured* heat of fusion per mass ( $\Delta H_{f,g}$ , Table 9.1) if the density  $\rho$  is known<sup>8</sup>. For the bulk crystal or the bulk liquid,  $\rho$  is unknown for any of the alloys studied here. Hence, it was estimated to be similar to values obtained for thin films by x-ray-reflectometry (XRR) [7, 94, 9, 102]:  $\rho = 6594 \text{ kg m}^{-3}$  ( $\text{Ge}_{12}\text{Sb}_{88}$ );  $\rho = 6590 \text{ kg m}^{-3}$  ( $\text{AgIn-Sb}_2\text{Te}$ );  $\rho = 6140 \text{ kg m}^{-3}$  ( $\text{Ge}_4\text{Sb}_1\text{Te}_5$ );  $\rho = 6400 \text{ kg m}^{-3}$  ( $\text{Ge}_2\text{Sb}_2\text{Te}_5$ ).

The uncertainty for the calculated interfacial energies  $\sigma$  and  $\alpha$  in Table 9.2 includes (a) the uncertainty in the heat of fusion  $\Delta H_f$  (Table 9.1), (b) the uncertainty on the choice of the TS or the HM approximation, and (c) the uncertainty in the pre-exponential factor  $10^{36}$  [Eq. (9.5)], which is two to four powers of ten [cf. also the discussion in the paragraph below Eq. (3.22b)]. Errors in the density  $\rho$  have not been considered for the calculation of the error in  $\sigma$  in Table 9.2 in order to demonstrate the contributions of the other errors more clearly<sup>9</sup>. The error in  $\alpha$  is independent of the error in  $\rho$  as explained above.

The normalized interfacial energy  $\alpha$  (Table 9.2) is slightly lower for  $\text{Ge}_2\text{Sb}_2\text{Te}_5$  than for the other three alloys. All values are smaller than values in Table 9.3, which

---

<sup>8</sup>For the calculation of the volume  $V$  [factor in front of the integral in Eq. (9.1)] from measured values of the sample mass, the density  $\rho$  also has to be known. However, the uncertainty of  $\rho$  in this calculation does not influence the uncertainties of  $\alpha$  or  $\sigma$  because the volume  $V$  in Eq. (9.1) is multiplied with the pre-exponential factor of Eq. (9.3) or (9.5) [cf. the discussion in the paragraph below Eq. (3.22b)].

<sup>9</sup>The uncertainty for  $\alpha$  for the alloy  $\text{Ge}_4\text{Sb}_1\text{Te}_5$  was erroneously given as 0.01 in Table I of Ref. [170]. Table 9.2 states the correct uncertainty of 0.02.

**Table 9.2:** Calculated lower limits for the crystal-melt interfacial energy  $\sigma$  [absolute value, Eq. (9.3)] and  $\alpha$  [normalized value, Eqs. (9.4) and (9.5)]. Normalized entropy of fusion  $\beta$  calculated from Eq. (9.4) using the values for  $\Delta H_{f,m}$  and  $T_l$  given in Table 9.1. Reduced glass transition temperature  $T_{rg} = T_g/T_l$ , where  $T_g$  was estimated from Fig. 8.3 and  $T_l$  taken from Table 9.1.

Alloy	$\sigma$ (mJ/m <sup>2</sup> )	$\alpha$	$\beta$	$T_{rg}$
Ge <sub>12</sub> Sb <sub>88</sub>	76 ± 5	0.20 ± 0.01	2.94 ± 0.04	~ 0.53
AgIn-Sb <sub>2</sub> Te	55 ± 4	0.19 ± 0.01	2.49 ± 0.05	~ 0.55
Ge <sub>4</sub> Sb <sub>1</sub> Te <sub>5</sub>	47 ± 6	0.22 ± 0.02	1.51 ± 0.18	~ 0.48
Ge <sub>2</sub> Sb <sub>2</sub> Te <sub>5</sub>	40 ± 3	0.16 ± 0.01	1.93 ± 0.10	~ 0.47

were obtained from undercooling experiments on pure metals and semi-metals, and far smaller than the values obtained by interface modeling for the closest-packed surfaces in pure metals ( $\alpha = 0.86$  for the face-centered-cubic and hexagonal-closed-packed crystal structures [186] and  $\alpha = 0.71$  for the body-centered-cubic crystal structure [187]). Undercooling data for non-metals are not available in the literature.

The values of the interfacial energies  $\sigma$  and  $\alpha$  in Table 9.2 are lower limits, since it was not established that nucleation was homogeneous in the experiments. If, as is likely, the observed nucleation was heterogeneous, larger undercoolings than those given in Table 9.1 should be possible. The corresponding values of  $\sigma$  and  $\alpha$  would be larger. For instance, for the (hypothetical) case of a relative undercooling that is 50% larger than observed in this study (Table 9.1 and Fig. 9.2), the analysis in Sec. 9.4.1 would yield values for  $\sigma$  and  $\alpha$  that are about 30% larger than those values given in Table 9.2.

The heat of fusion  $\Delta H_{f,m}$  determined from DSC and DTA measurements (Table 9.1) has been normalized to an entropy of fusion  $\beta$  according to Eq. (9.4) and is also given in Table 9.2.

**Table 9.3:** Maximum undercooling data for liquid metallic and semi-metallic elements. The data are a collection from various literature values and were taken from Ref. [64], except for the Si data, which were taken from Refs. [72, 73].  $\Delta T_{n,r}$ : largest relative undercooling;  $\sigma_n = \sigma \Omega^{2/3} N_{AV}$ : interfacial energy energy per atomic area in the interface multiplied by Avogadro's number  $N_{AV}$ ;  $\Omega$ : atomic volume;  $\Delta H_{f,m}$ : molar heat of fusion;  $\alpha = \sigma_n / \Delta H_{f,m}$ : normalized interfacial energy [Eq. (9.4)]. The parameters  $\alpha$  and  $\sigma_n$  are lower limits since nucleation in the corresponding experiments was not necessarily homogeneous. The data are plotted in Fig. 9.4.

Element	$\Delta T_{n,r}$	$\sigma_n$ (kJ/mol)	$\Delta H_{f,m}$ (kJ/mol)	$\alpha$
Ag	0.18	5.11	11.4	0.45
Al	0.19	4.25	10.5	0.40
Au	0.17	5.45	12.8	0.43
Bi	0.42	5.74	10.9	0.53
Cd	0.19	2.71	6.4	0.42
Co	0.19	7.14	15.5	0.46
Cu	0.17	5.58	13.0	0.43
Fe	0.23	8.65	15.2	0.57
Ga	0.57	3.35	5.6	0.60
Ge	0.34	14.40	32.2	0.45
Hg	0.38	1.48	2.3	0.64
Hf	0.18	10.60	24.1	0.44
In	0.26	1.86	3.3	0.57
Mn	0.20	6.90	14.7	0.47
Ni	0.28	10.40	17.7	0.59
Pb	0.40	3.51	5.0	0.70
Pd	0.18	7.49	16.7	0.45
Pt	0.19	8.80	19.7	0.45
Rh	0.20	10.40	22.6	0.46
Ru	0.13	7.58	19.7	0.38
Sb	0.23	7.58	19.9	0.38
Se	0.05	1.13	6.3	0.18
Si	0.21	17.07	50.2	0.34
Sn	0.38	4.10	7.1	0.58
Ta	0.20	12.50	24.7	0.51
Te	0.33	7.89	17.6	0.45
Ti	0.18	8.23	18.8	0.44
Zr	0.20	9.49	20.1	0.47

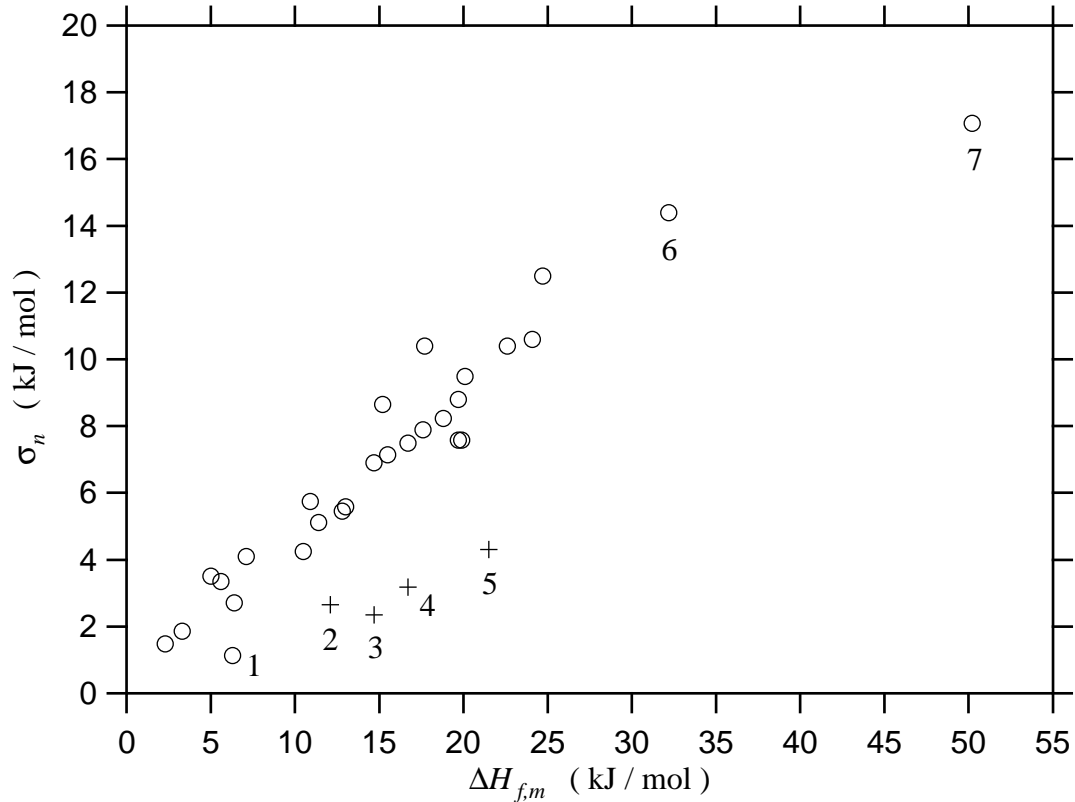


**Figure 9.4:** Crystal-melt interfacial energy  $\sigma_n = \sigma\Omega^{2/3}N_{Av}$  (per atomic area in the interface multiplied by Avogadro's number  $N_{Av}$ ) versus molar heat of fusion  $H_{f,m}$ . The circles represent metallic and semi-metallic elements (data taken from Table 9.3). The crosses represent the data obtained for the Sb and Te alloys studied in this work (Tables 9.1 and 9.2). The slope of the straight line that connects each data point with the origin of the graph is equal to the normalized interfacial energy  $\alpha = \sigma_n/\Delta H_{f,m}$  [Tables 9.2 and 9.3; Eq. (9.4)]. The  $\alpha$ -value for the Sb and Te alloys is found to be lower than for all metallic and semi-metallic elements (except Se) represented by the circles. 1: Se; 2:  $\text{Ge}_4\text{Sb}_1\text{Te}_5$ ; 3:  $\text{Ge}_2\text{Sb}_2\text{Te}_5$ ; 4:  $\text{AgIn-Sb}_2\text{Te}$ ; 5:  $\text{Ge}_{12}\text{Sb}_{88}$ ; 6: Ge; 7: Si. The other data points are not labeled for clarity but the corresponding elements can be identified using Table 9.3.

### 9.4.3 Critical work for cluster formation $\Delta G_c$ and critical radius $r_c$

The critical work  $\Delta G_c$  for homogeneous cluster formation [Eq. (3.5)] and the critical radius  $r_c$  [Eq. (3.4)] were calculated from the interfacial energy (Table 9.2), using the free energy approximations given in Eq. (9.2). The curves are shown Figs. 9.5 and 9.6. The curves based on the TB approximations are not displayed. The TB curve would be located below the TS curve for each alloy. The curve based on the heat capacity data for AgIn-Sb<sub>2</sub>Te is also displayed. For the calculation of  $r_c$  (but not for the calculation of  $\Delta G_c$ ), the mass density  $\rho$  is required, which was taken from the values stated in Sec. 9.4.2. Both  $\Delta G_c$  and  $r_c$  represent lower limits since it was not established that nucleation was homogeneous. For the (hypothetical) case of a relative undercooling that is 50% larger than observed in this study,  $r_c$  would be 30% larger than in Fig. 9.6 (for any undercooling), and  $\Delta G_c$  would be 2.2 times as high as in Fig. 9.5 (for any undercooling). This is a consequence of the fact that  $\sigma$  would increase by 30% as mentioned above, keeping in mind that  $r_c$  is proportional to  $\sigma$  [Eq. (3.4)] and that  $\Delta G_c$  is proportional to  $\sigma^3$  [Eq. (3.5)].

### 9.4.4 Nucleation rate

To extrapolate the steady-state nucleation rate  $I^{ss}(T)$  [Eqs. (9.3) or (9.5)] to larger undercoolings, the viscosity  $\eta$  has to be known over the entire temperature range.  $\eta$  is approximated by Eq. (2.9) under three constraints:

1.  $\eta(T_l) = 2 \times 10^{-2}$  poise as used above for small undercoolings.
2.  $\eta(T_g) = 10^{13}$  poise, which is commonly used to define the glass transition temperature  $T_g$  (Sec. 2.2.1).  $T_g$  was chosen to be close to the calorimetric glass transition temperature obtained by differential scanning calorimetry<sup>10</sup> (Chap. 8):  $T_g = 170^\circ\text{C}$  (AgIn-Sb<sub>2</sub>Te),  $T_g = 190^\circ\text{C}$  (Ge<sub>4</sub>Sb<sub>1</sub>Te<sub>5</sub>), and  $T_g = 155^\circ\text{C}$  (Ge<sub>2</sub>Sb<sub>2</sub>Te<sub>5</sub>).

---

<sup>10</sup> $T_g$  was chosen slightly lower than the values obtained in Sec. 8.3 because the heating rate in the scanning experiments of Sec. 8.3 was relatively large (40 K min<sup>-1</sup>), and because  $T_g$  should increase with increasing heating rate (Sec. 2.2.1). However, it will be discussed below that the exact value for  $T_g$  is unimportant for the extrapolations.

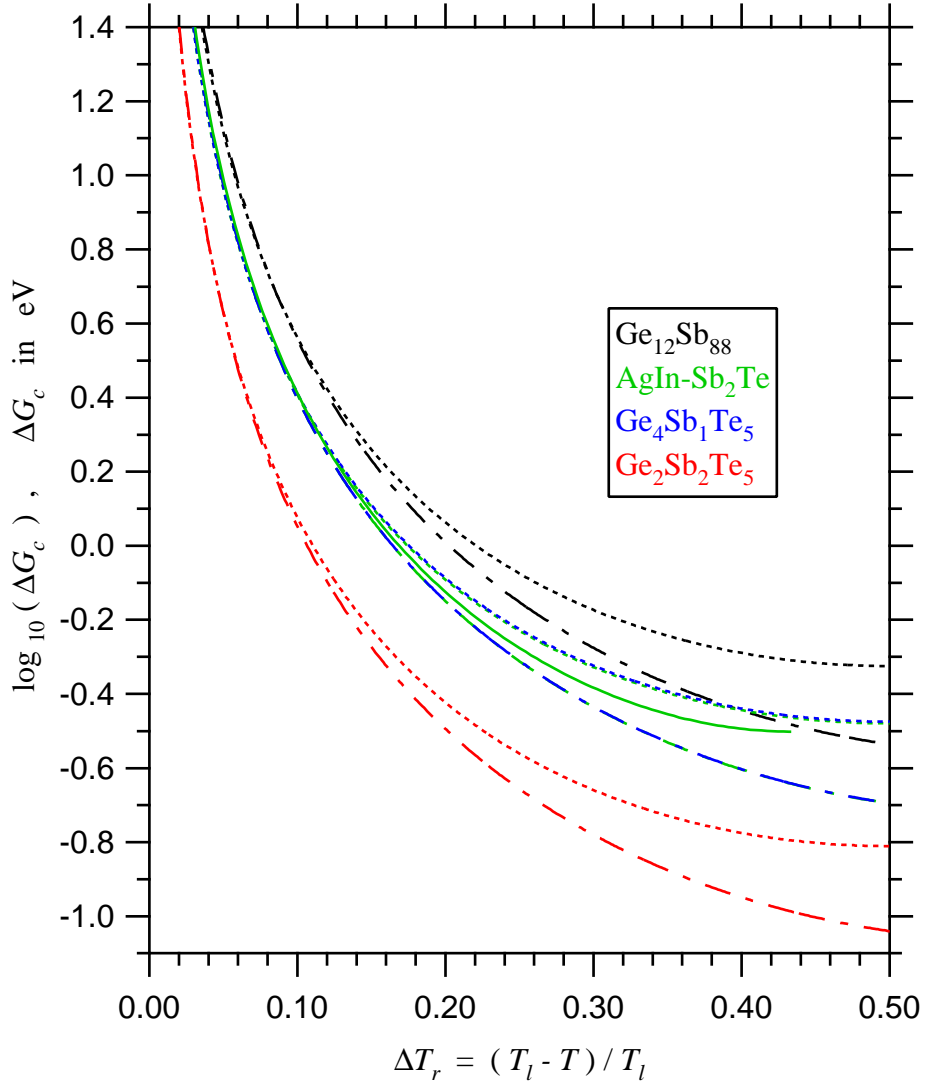


**Figure 9.5:** (Color). Lower limit for the critical work for homogeneous cluster formation  $\Delta G_c$  [Eq. (3.5)] as a function of relative undercooling  $\Delta T_r$  [Eq. (9.4)] for  $\text{Ge}_2\text{Sb}_2\text{Te}_5$  (red),  $\text{Ge}_4\text{Sb}_1\text{Te}_5$  (blue),  $\text{AgIn-Sb}_2\text{Te}$  (green), and  $\text{Ge}_{12}\text{Sb}_{88}$  (black). For each alloy, the upper curve (dotted) corresponds to the Hoffman (HM) approximation and the lower curve (dot-dashed) to the Thompson/Spaepen (TS) approximation of the free energy [Eq. (9.2)]. For  $\text{AgIn-Sb}_2\text{Te}$ , the intermediate curve (solid) corresponds to the free energy approximation from Refs. [107, 106]. The curves for  $\text{AgIn-Sb}_2\text{Te}$  and  $\text{Ge}_4\text{Sb}_1\text{Te}_5$  are difficult to distinguish because they are almost identical.

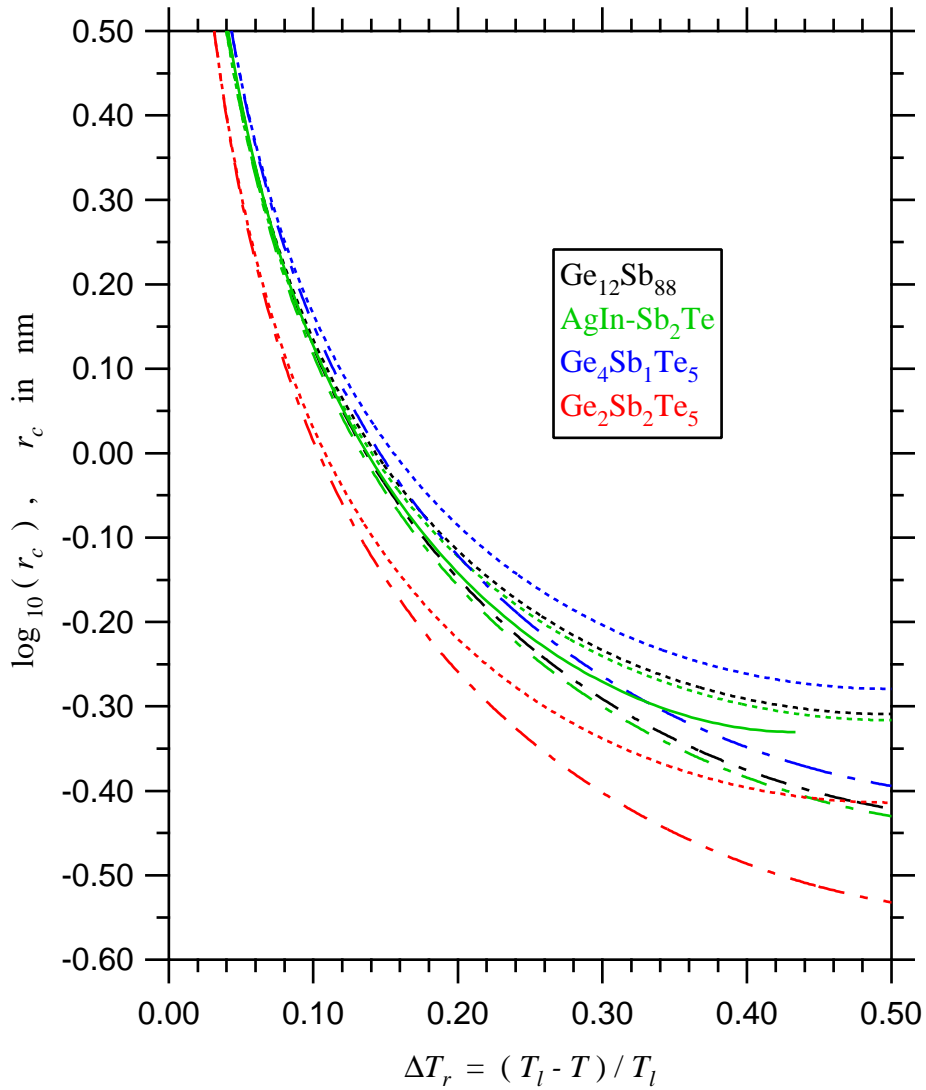


**Figure 9.6:** (Color). Lower limit for the critical radius  $r_c$  [Eq. (3.4)] as a function of relative undercooling  $\Delta T_r$  [Eq. (9.4)] for  $\text{Ge}_2\text{Sb}_2\text{Te}_5$  (red),  $\text{Ge}_4\text{Sb}_1\text{Te}_5$  (blue),  $\text{AgIn-Sb}_2\text{Te}$  (green), and  $\text{Ge}_{12}\text{Sb}_{88}$  (black). For each alloy, the upper curve (dotted) corresponds to the Hoffman (HM) approximation and the lower curve (dot-dashed) to the Thompson/Spaepen (TS) approximation of the free energy [Eq. (9.2)]. For  $\text{AgIn-Sb}_2\text{Te}$ , the intermediate curve (solid) corresponds to the free energy approximation from Refs. [107, 106].

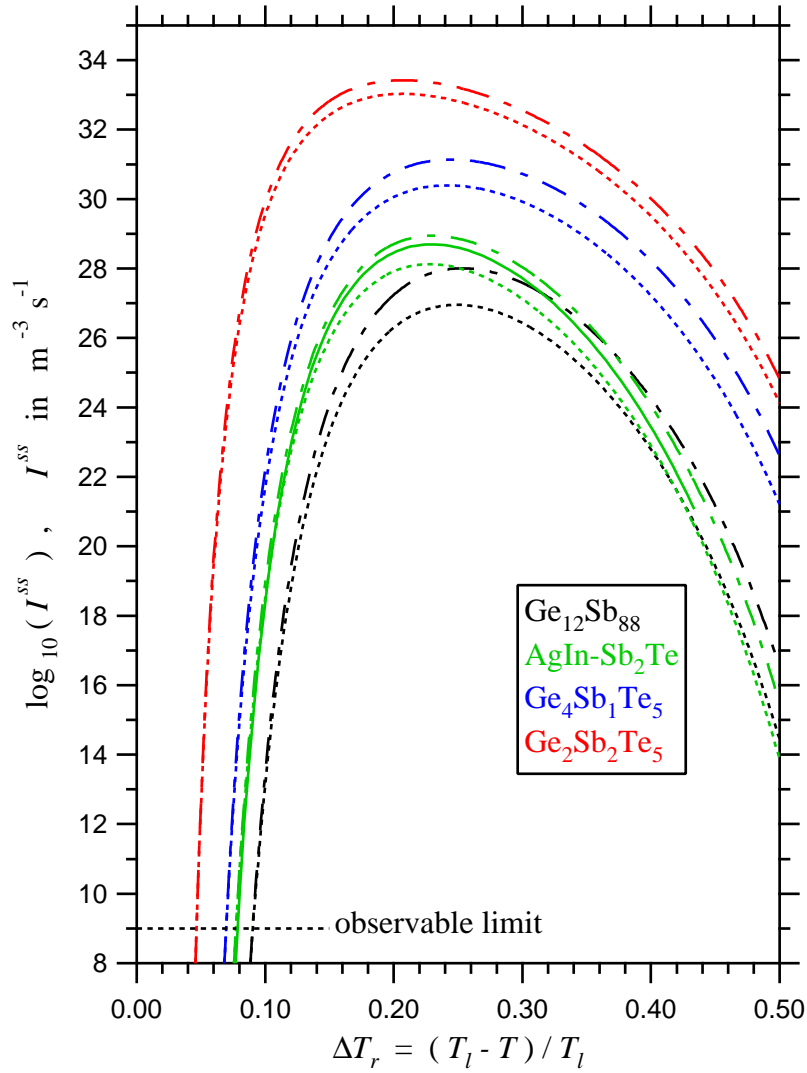


**Figure 9.7:** (Color). Upper limit for the homogeneous steady state crystal nucleation rate  $I^{ss}$  [Eqs. (9.3) or (9.5)] as a function of relative undercooling  $\Delta T_r$  [Eq. (9.4)] for  $\text{Ge}_2\text{Sb}_2\text{Te}_5$  (red),  $\text{Ge}_4\text{Sb}_1\text{Te}_5$  (blue),  $\text{AgIn-Sb}_2\text{Te}$  (green), and  $\text{Ge}_{12}\text{Sb}_{88}$  (black). For each alloy, the lower curve (dotted) corresponds to the Hoffman (HM) approximation and the upper curve (dot-dashed) to the Thompson/Spaepen (TS) approximation of the free energy [Eq. (9.2)]. For  $\text{AgIn-Sb}_2\text{Te}$ , the intermediate curve (solid) corresponds to the free energy approximation from Refs. [107, 106]. The extrapolations were performed under the three constraints mentioned in the beginning of Sec. 9.4.4 (here:  $m = 45$ ). For all alloys, nucleation is observed if  $I^{ss}$  exceeds about  $1 \text{ mm}^{-3}\text{s}^{-1}$  (observable limit); the corresponding undercoolings  $\Delta T_{n,r}$  are those of Table 9.1.

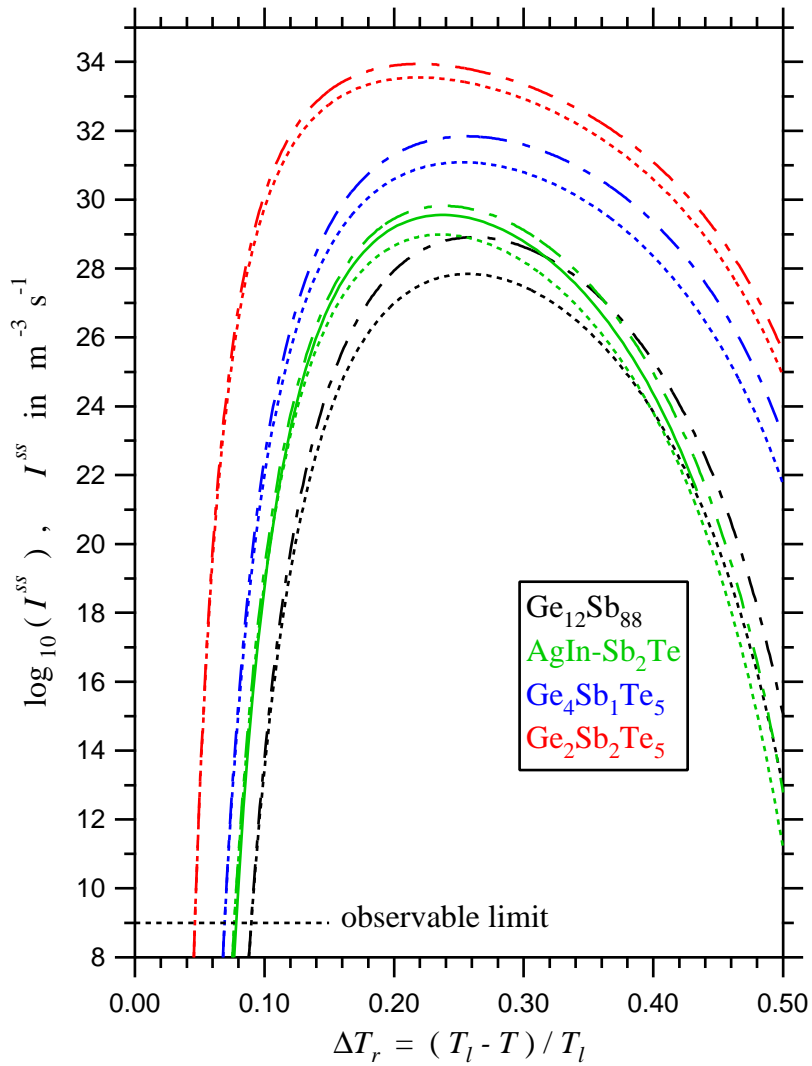


**Figure 9.8:** (Color). Upper limit for the homogeneous steady state crystal nucleation rate  $I^{ss}$  [Eqs. (9.3) or (9.5)] as a function of relative undercooling. The only difference to Fig. 9.7 is that a fragility parameter of  $m = 60$  was assumed in the constraints mentioned in the beginning of Sec. 9.4.4. For other details, see caption of Fig. 9.7.

For  $\text{Ge}_{12}\text{Sb}_{88}$ ,  $T_g$  was chosen to be close to the crystallization temperature in furnace heating experiments [13, 188, 189]:  $T_g = 195^\circ\text{C}$ .

3. The fragility index  $m$  [Eq. (2.8)] was matched to literature values [190, 191, 192] for various chalcogenides by setting  $m = 45$ .

Under these constraints, the (apparent) activation energy for the viscosity at  $T_g$ ,

$$E_\eta = \left. \frac{\partial \ln \eta(T)}{\partial \left(\frac{1}{k_B T}\right)} \right|_{T=T_g}, \quad (9.6)$$

adopted a value of about 4 eV for all alloys. This value can be calculated from the equation

$$E_\eta = \ln(10) \cdot k_B \cdot m \cdot T_g, \quad (9.7)$$

which is obtained upon the conversion of Eq. (9.6) to Eq. (2.8).

The steady-state nucleation rate  $I^{ss}(T)$  [Eqs. (9.3) or (9.5)] obtained this way is plotted in Fig. 9.7 for both the TS and the HM approximation. The curves based on the TB approximations are not displayed. The TB curve would be located above the TS curve for each alloy. The curve based on the heat capacity data for  $\text{AgInSb}_2\text{Te}$  is also indicated.  $I^{ss}$  increases rapidly for small undercoolings. This explains why the nucleation temperature  $T_n$  (Table 9.1) was observed to be independent of cooling rate and sample volume within the range given in Sec. 9.2: Nucleation can only occur once the observable limit on the order of  $1 \text{ mm}^{-3}\text{s}^{-1}$  is exceeded, i. e., one nucleation event in a typical sample volume of about  $1 \text{ mm}^3$  during the observable time window of one second. The height and the position of the maximum in  $I^{ss}$  (Fig. 9.7) depend only weakly on the choice of the glass transition temperature  $T_g$  and the fragility index  $m$  in the constraints above: If  $T_g$  is varied as  $\mp 40^\circ\text{C}$  or if  $m$  is varied as  $\pm 15$ , the height changes by about  $\pm 1$  order of magnitude, and the position on the horizontal axis by about  $\pm 0.01$ . This is demonstrated in Fig. 9.8 for the choice of  $m = 60$ , while the other constraints are the same as those mentioned above<sup>11</sup>. The more pronounced contribution to the uncertainty in the maximum height is that of the nucleation rate prefactor  $10^{36}$  [Eqs. (9.3) or (9.5)], i. e., about two to four orders of

<sup>11</sup>For  $m = 60$ , Eq. (9.7) yields  $E_\eta \sim 5.4 \text{ eV}$  for all alloys at  $T_g$ .

magnitude (Sec. 3.1.1.4). The part of the curve to the left of the maximum is essentially insensitive to those uncertainties.

Since it was not established that nucleation was homogeneous in the experiments, the nucleation rate  $I^{ss}$  as plotted in Figs. 9.7 or 9.8 is an upper limit for the homogeneous nucleation rate. For the (hypothetical) case of a relative undercooling that is 50% larger than observed in this study, the height of the maximum would decrease by about 4 orders of magnitude ( $\text{Ge}_{12}\text{Sb}_{88}$ ), 3.5 orders of magnitude ( $\text{AgIn-Sb}_2\text{Te}$ ), 3 orders of magnitude ( $\text{Ge}_4\text{Sb}_1\text{Te}_5$ ), and 2 orders of magnitude ( $\text{Ge}_2\text{Sb}_2\text{Te}_5$ ). The position of the maximum on the horizontal axis would shift by about 0.05 towards larger undercoolings for all alloys.

It should be noted that the Stokes-Einstein equation [Eq. (2.3)], which was used to express the pre-exponential factor in Eqs. (9.3) or (9.5) in terms of the viscosity  $\eta$ , may not hold for temperatures around  $T_g$ , which corresponds to an undercooling of about  $\Delta T_r = 0.5$  [Table 9.2, cf. the discussion in the paragraph below Eq. (3.19)]. Hence, care should be taken when Figs. 9.7 or 9.8 are interpreted for undercoolings larger than 0.4, which corresponds to about  $1.2T_g$ . In the same temperature range, the free energy approximations [Eq. (9.2)] should be less reliable.

Using the same analysis, Senkader and Wright [137] calculated the steady state nucleation rate for  $\text{Ge}_2\text{Sb}_2\text{Te}_5$  based on literature values for  $\Delta H_f$ ,  $T_l$ , and  $\eta$ . Even though they do not mention it explicitly, their calculation applies to *homogeneous* nucleation because the heterogeneous reduction factors  $f(\theta)$  and  $\epsilon$  do not appear in their treatment. As they do not have a value for the interfacial energy, they suggest that it could be taken as a ‘free’ parameter and assume  $\sigma = 100 \text{ mJ/m}^2$  (without experimental or theoretical justification). This value is 2.5 times as large as the value obtained in this work (Table 9.2). As a consequence, they obtain a nucleation rate, for which the maximum height is about  $10^{12} \frac{1}{\text{m}^3\text{s}}$  (Fig. 4 in Ref. [137]), i. e., more than 20 orders of magnitude lower than the maximum of the nucleation rate determined in this work (Figs. 9.7 or 9.8). This maximum value is so low that one crystal in a typical bit volume for optical data storage of  $V_b = 1 \mu\text{m} \times 1 \mu\text{m} \times 10 \text{ nm} = 10^{-20} \text{ m}^3$  would nucleate in the steady state within a time of

$$t_n = \frac{1}{I \cdot V_b} = \frac{1}{10^{12} \frac{1}{\text{m}^3\text{s}} \cdot 10^{-20} \text{m}^3} = 10^8 \text{ s} \sim 3 \text{ years.} \quad (9.8)$$

Their calculation of the steady state nucleation rate appears to be based on the correct equations, but it shows that their arbitrariness in the assumption for a value for  $\sigma$  can lead to results that do not appear useful for modeling the kinetics under operating conditions.

## 9.5 Discussion

### 9.5.1 Entropy of fusion

The values for the entropy of fusion  $\beta$  are remarkably large. This applies in particular to the Sb-rich alloys (Table 9.2). For simple metals,  $\beta$  is on the order of 1.2. Large entropies of fusion are also observed in Si and Ge ( $\beta = 3.6$ ), and are the result of a change in chemical bonding, from covalent to metallic, upon melting [193]. This suggests that the nature of the bonding in the crystalline and liquid phases of the phase change alloys may also be qualitatively different. The large difference in specific heat at the melting point for AgIn-Sb<sub>2</sub>Te [106, 107] points in the same direction. Interestingly, the entropy of fusion of pure Te ( $\beta = 2.9$ ) and pure Sb ( $\beta = 2.6$ ) is also large.

### 9.5.2 Crystal-melt interfacial energy

It is not entirely clear why the undercoolings  $\Delta T_{n,r}$  (Table 9.1) and the corresponding  $\alpha$ -values (Table 9.2) are significantly lower than the literature values for metallic elements (Table 9.3). It is possible that the fluxing method has not been as efficient and that significantly larger undercoolings are possible. However, it also appears possible that the  $\alpha$ -values for the Sb and Te alloys are lower than for metals for a clear physical reason: Metals can usually be undercooled far because the atomic structure of the liquid state exhibits polytetrahedral short-range order, which results in five-fold symmetry elements [194, 195]. The local structure of the liquid is therefore significantly different from the crystalline state, and hence, the corresponding interfacial energy and the undercooling are large. Polytetrahedral short-range order can be understood for metallic (i. e., isotropic) bonding because it *locally* yields a closer packing of the atoms and therefore a larger bonding energy than any other atomic arrangement [194, 195]. The five-fold coordination in the liquid state was first postulated by Frank in 1952

[196] in order to explain the large undercoolings obtained by Turnbull for pure metals [121, 57, 74], and was directly confirmed for the first time five decades later for liquid lead by Reichert and co-workers [197]. Further evidence for polytetrahedral short-range order in liquid metals comes from recent undercooling experiments on metallic alloys: Those alloys that nucleate a metastable icosahedral quasicrystalline phase<sup>12</sup> in the undercooled liquid can be undercooled far less than those alloys that nucleate an orthorhombic or cubic crystalline phase [77, 198]. As a consequence, the  $\alpha$ -value for the former case ( $\alpha < 0.3$ ) is significantly lower than for the latter ( $\alpha > 0.6$ ).

If the liquid phases for the Sb and Te alloys do not exhibit five-fold symmetry elements (which is possible if metallic bonding in the liquid is not involved), the local structure of liquid and crystal may be more similar than for metals. For this case, the smaller  $\alpha$ -values could be understood. An investigation of the local liquid structure may help to clarify this point. However, it would then remain an open question why the entropies of fusion  $\beta$  have been observed to be so large (Sec. 9.5.1). A possible explanation is that the crystalline phase that nucleates in the undercooling experiments is a *metastable* phase, different from the *stable* crystalline phase that was present prior to melting and that therefore determined the entropy of fusion (cf. Fig. 2.10). However, this appears unlikely because the undercoolings were not large: Under the assumption that  $T_n$  was higher than the (unknown) melting points for all metastable phases that can form from the liquid, only nucleation of the stable phase is thermodynamically possible at  $T_n$  (cf. Fig. 2.10).

### 9.5.3 Critical work for cluster formation $\Delta G_c$ and critical radius $r_c$

The extrapolations in Figs. 9.5 and 9.6 have been performed to deep undercoolings where no data for  $\sigma$  was taken. However, it was not established that  $\sigma$  is independent of temperature over such a large temperature range. Hence, care has to be taken when

---

<sup>12</sup>In mathematics, an icosahedron is a polyhedron having 20 faces. The faces of a *regular* icosahedron are equilateral triangles. If one atom is put on each of the 12 vertices, and another atom in the center, this results in the closest-packed possible structure for 13 atoms. It consists of 20 slightly distorted regular tetrahedra and exhibits five-fold symmetry; it is the building block for icosahedral quasicrystals [194, 195].

these curves are interpreted for deep undercoolings such as  $\Delta T_r = 0.5$ . Nevertheless, it appears that  $\Delta G_c$  is on the order of 0.1–0.4 eV for undercoolings of around  $\Delta T_r = 0.5$ , which corresponds to the region of the glass transition (Table 9.2). This is significantly lower than the value for  $\Delta G_c$  determined for the GeSbTe alloys in the thin film experiments (Table 7.4). This appears to be a paradox for the following reasons: According to the classical theory of *homogeneous* crystal nucleation,  $\Delta G_c$  is the *only* parameter that determines which phase nucleates from the undercooled liquid at a given temperature [cf. the discussion below Eq. (3.25b) until the end of Sec. 3.1.1]. Equation (3.22a) shows that the phase with the lowest value for  $\Delta G_c$  exhibits the largest nucleation rate and will therefore nucleate from the liquid at a given temperature. For Ge<sub>2</sub>Sb<sub>2</sub>Te<sub>5</sub>, the *metastable cubic* crystal phase nucleates in the thin film experiments (Sec. 6.3.1.5). Hence, the value for  $\Delta G_c$  in Table 7.4 applies to the liquid–cubic phase transition for this alloy. Ge<sub>2</sub>Sb<sub>2</sub>Te<sub>5</sub> also exhibits a *stable hexagonal* phase, which forms upon furnace heating the cubic phase above about 300 °C [120, 8, 94]. This phase probably nucleates in the fluxing experiments, and therefore, the extrapolation in Fig. 9.5 probably applies to the liquid–hexagonal phase transition. However, since it is the *cubic* phase and *not* the *hexagonal* phase that nucleates around  $T_g$ , the value for  $\Delta G_c$  would be expected to be lower for the cubic phase than for the hexagonal phase around  $T_g$ , which is not observed. Hence, this would imply that only the *heterogeneous* nucleation reduction factor  $f(\theta)$  in Eq. (3.36), which was ignored in the arguments above, can account for the discrepancy. However,  $f(\theta)$  must then be significantly lower for the fluxing experiments than for the thin film experiments. In other words, nucleation in the thin film experiments would have been closer to the homogeneous limit than in the fluxing experiments. This is unrealistic because the fluxing technique significantly increased the undercooling and thereby should have approached the limit of homogeneous nucleation more closely than in the thin film experiments. Hence, it appears that this paradox can only be solved if it is assumed that Volmer’s spherical cap model for heterogeneous nucleation breaks down in the thin film experiments. This statement is in agreement with the conclusions made in Sec. 7.4.6.

## 9.5.4 Nucleation rate

### 9.5.4.1 Crystallization

At fixed undercooling  $\Delta T_r$ , the steady-state nucleation rate  $I^{ss}$  [Eq. (9.5)] depends critically only on three parameters: the normalized interfacial energy  $\alpha$ , the entropy of fusion  $\beta$ , and the reduced glass transition temperature  $T_{rg} = T_g/T_l$  (Table 9.2). The latter determines the degree of undercooling  $\Delta T_r$  at which the viscosity  $\eta$  constrains the nucleation rate to decrease on the right side of the maximum [70]. At fixed undercooling  $\Delta T_r$ ,  $I^{ss}$  decreases with increasing parameters  $\alpha$ ,  $\beta$ , and  $T_{rg}$  [Eq. (9.5)]. The parameters  $\beta$  and  $T_{rg}$  are higher for the Sb-rich alloys than for GeSbTe alloys (Table 9.2), which causes a higher nucleation rate for the latter (Figs. 9.7 or 9.8). The nucleation rate is highest for  $\text{Ge}_2\text{Sb}_2\text{Te}_5$  due to its lower value of  $\alpha$  (Table 9.2), which affects the exponential part of the nucleation rate by a power of three [Eq. (9.5)].

Studies on the re-crystallization mechanism of amorphous marks upon laser irradiation revealed that  $\text{Ge}_4\text{Sb}_1\text{Te}_5$  and  $\text{Ge}_2\text{Sb}_2\text{Te}_5$  re-crystallize by nucleation and subsequent growth of crystals inside the amorphous mark. In contrast,  $\text{Ge}_{12}\text{Sb}_{88}$  and  $\text{AgIn-Sb}_2\text{Te}$  re-crystallize by the growth of the crystalline phase from the rim of the amorphous mark (Sec. 1.1, Fig. 1.2). This correlates with the findings of a lower nucleation rate for the Sb-rich alloys than for the GeSbTe alloys and is finally related to the relative difference in the parameters  $\alpha$ ,  $\beta$ , and  $T_{rg}$  among these alloys. In particular the entropy of fusion  $\beta$ , which is significantly larger for the Sb-rich alloys than for the GeSbTe alloys (Table 9.2), appears to be the decisive factor to determine whether growth-dominated or nucleation-dominated re-crystallization of amorphous marks occurs.

It should be noted, however, that the nucleation rates given in Figs. 9.7 or 9.8 and the crystal-melt interfacial energies  $\sigma$  and  $\alpha$  given in Table 9.2 strictly apply only to that crystal phase that actually nucleated in the undercooling experiments. For the  $\text{Ge}_2\text{Sb}_2\text{Te}_5$  alloy, this is probably not the metastable cubic phase, which is found following laser-induced crystallization [127], but the hexagonal phase, which is the stable phase, and which forms upon furnace heating the cubic phase above about 300 °C [120, 8, 94]. For an estimate of the crystal-melt interfacial energy for the cubic phase for  $\text{Ge}_2\text{Sb}_2\text{Te}_5$ , the undercooling should be measured from the (unknown)

liquidus temperature of the cubic phase, which should be lower than the (measured) liquidus temperature of the hexagonal phase (in Fig. 2.10, the  $\gamma$  phase may represent the hexagonal phase and the  $\delta$  phase may represent the cubic phase). Moreover, the (unknown) heat of fusion for the cubic phase would have to be used for the free energy approximations [Eq. (9.2)].

#### 9.5.4.2 Amorphization

The steady state nucleation rates given in Figs. 9.7 or 9.8 are too high to allow amorphization in both optical and electronic media under operating conditions. Nucleation interferes at the highest attainable cooling rates, which can be estimated by dimensional analysis of the heat conduction equation (Sec. 5.2.3.1) [104]: The minimum time for heat removal by conduction is on the order of

$$\tau = \frac{l^2 c_p^{(v)}}{\lambda}, \quad (9.9)$$

where  $l$  is the shortest dimension of an amorphous mark, which is at best on the order of 10 nm (film thickness for optical media and minimum programmable volume dimension for electronic media).  $\lambda$  and  $c_p^{(v)}$  are the thermal conductivity and the specific heat at constant pressure per unit volume, respectively, which are on the order of  $0.2 \text{ W m}^{-1} \text{ K}^{-1}$  and  $1.3 \times 10^6 \text{ J m}^{-3} \text{ K}^{-1}$ , respectively [4, 106, 107, 15, 199]. This yields  $\tau \sim 1 \text{ ns}$ , which implies that the highest attainable cooling rate is on the order of  $10^{10} \text{ K s}^{-1}$ . Consistently, such cooling rates were obtained by more accurate modeling of temperature profiles [15]. For optical data storage, the bit volume is on the order of  $V_b = 1 \mu\text{m} \times 1 \mu\text{m} \times 10 \text{ nm} = 10^{-20} \text{ m}^3$  [200] (limited by the wavelength of the laser light). For a cooling rate of  $10^{10} \text{ K s}^{-1}$ , the temperature decreases by 100 K over a time of  $t_c = 10 \text{ ns} = 10^{-8} \text{ s}$ . Therefore, nucleation would interfere if the nucleation rate were  $I^{ss} > V_b^{-1} t_c^{-1} = 10^{28} \text{ m}^{-3} \text{ s}^{-1}$  over a range of 100 K. This is certainly the case for the GeSbTe alloys (Figs. 9.7 or 9.8), but most likely also for the Sb-rich alloys, since the nucleation rates determined by the fluxing technique probably approached the limit of homogeneous nucleation far closer than the nucleation rates in phase change media, which are even enhanced by nucleation-promoting dielectric capping layers [136, 124, 94]. For electronic media, programmable volume sizes as small as  $V_b = 10^{-23} \text{ m}^3$  are reported [5, 201]. Hence, nucleation would interfere if  $I^{ss} > 10^{31} \text{ m}^{-3} \text{ s}^{-1}$  over a range

of 100 K, which is at least the case for  $\text{Ge}_2\text{Sb}_2\text{Te}_5$ , which is often reported as the material of choice for PC-RAM prototypes [4]. Therefore, it can be concluded that:

1. Melt quenching under operating conditions occurs during the incubation time, when the steady state distribution of critical nuclei is not yet formed (Sec. 3.1.3), so that the nucleation rate remains far smaller than its steady state value  $I^{ss}$ . As the incubation time is independent of the bit volume  $V_b$ , this statement applies equally to optical and electronic media for all alloys investigated. Consistently, it was reported by Kelton and Greer [202] that transient effects become increasingly important with increasing quench rate: While the steady state nucleation rate is readily maintained for cooling rates on the order of  $1 \text{ K s}^{-1}$  as used in the present experiments or in conventional metallurgical solidification, deviations from the steady state are already large at cooling rates in rapid solidification techniques, such as melt-spinning ( $\sim 10^6 \text{ K s}^{-1}$ ), and must be even larger for cooling rates under operating conditions of phase change media.
2. Amorphization would not be possible if the incubation time were absent. Hence, the existence of an incubation time makes phase change recording possible. This statement should apply for optical data storage to all alloys investigated and for electronic data storage at least to  $\text{Ge}_2\text{Sb}_2\text{Te}_5$ . Indeed, incubation times were reported upon crystallization on the timescale of minutes around  $T_g$  (Refs. [96, 97, 99]; and Chap. 7 of this work), as well as upon laser crystallization on the nanosecond timescale [14, 127, 126, 128, 129, 130].

## 9.6 Conclusions

1.  $\text{B}_2\text{O}_3$  is an effective flux to enhance the undercooling of liquid Sb and Te alloys.
2. The crystal-melt interfacial energy is lower than for most pure metals. This may indicate a similar local atomic configuration in the liquid and the crystal, which is not the case for pure metals.
3. On the other hand, the entropies of fusion are large, in particular for the Sb-rich alloys. This may indicate a qualitative change in the type of bonding between the

crystalline and the liquid phases. It remains unclear how conclusion (3.) can be brought in line with conclusion (2.). A possible explanation has been discussed in the end of Sec. 9.5.2.

4. A comparison of the nucleation data obtained from the fluxing experiments with those obtained from the thin film experiments (Chap. 7) suggests that Volmer's spherical cap model for heterogeneous nucleation breaks down in the thin film experiments. This conclusion has already been drawn in Chap. 7 and is confirmed by the observations from the fluxing experiments.
5. The molar entropy of fusion  $\beta$  and the reduced glass transition temperature  $T_{rg} = T_g/T_l$  were identified as crucial parameters that determine the steady state nucleation rate and thereby also the re-crystallization mechanism under operating conditions in both optical and electronic phase change media. Both parameters are higher for the Sb-rich alloys than for the GeSbTe alloys. This difference is in particular pronounced for the entropy of fusion. As a consequence, the steady state nucleation rate is higher for the GeSbTe alloys than for the Sb-rich alloys. The (normalized) interfacial energy  $\alpha$  was rather similar for all alloys, though slightly lower for  $\text{Ge}_2\text{Sb}_2\text{Te}_5$ . However, since  $\alpha$  is raised to the third power in the exponential of the nucleation rate, it caused an additional distinct increase in the nucleation rate for this alloy.
6. The presence of an incubation time makes phase change recording possible for both optical and electronic phase change media.
7. The crystal nucleation parameters determined in this chapter can be used to model crystallization kinetics.



# Acknowledgements (Danksagungen)

Zunächst möchte ich meinen beiden Betreuern Professor Matthias Wuttig (RWTH Aachen) und Professor Frans Spaepen (Harvard University) ganz herzlich danken, dass sie mir die Möglichkeit gegeben haben, ein anspruchsvolles und interessantes Forschungsprojekt an zwei verschiedenen Instituten und in zwei verschiedenen Ländern durchzuführen. Dies hat mich durch unzählige wertvolle Erfahrungen sowohl in wissenschaftlicher als auch privater Hinsicht sehr bereichert.

Matthias danke ich sehr dafür, mir viel Freiraum bei der Durchführung der Forschungsprojekte gewährt zu haben. Ich hatte während der gesamten Zeit immer die Möglichkeit, absolut eigenständig zu arbeiten, ohne an Vorgaben oder Richtungen gebunden zu sein. Ich weiß sehr genau von Doktoranden an anderen deutschen Instituten und Universitäten, dass dies durchaus nicht selbstverständlich ist. Dies hat mir enorm geholfen, wissenschaftliche Kreativität und Selbständigkeit zu entwickeln. Dadurch fühle ich jetzt gut vorbereitet auf die nächste Stufe einer wissenschaftlichen Laufbahn als Post-Doktorand. Matthias habe ich es weiterhin zu verdanken, dass er mich in einer sehr übersichtlichen Zeit hat promovieren lassen. Ferner konnte Matthias mich immer wieder dazu motivieren, mich für die Thematik der Phasenwechselmaterialien zu begeistern. Darüber hinaus hat er mich ständig dabei unterstützt, meine Arbeiten nach außen hin zu präsentieren.

Ich bin sehr glücklich und sehr dankbar darüber, dass ich die Möglichkeit hatte, über einen langen Zeitraum sehr intensiv mit Frans zusammenzuarbeiten. Von seinem außergewöhnlichen und weitumfassenden wissenschaftlichen Verständnis und seiner hohen experimentellen Erfahrung habe ich enorm profitiert. Frans hatte nicht nur ständig ein offenes Ohr für meine Fragen und ein großes Interesse an dieser Arbeit, sondern er hatte auch immer wieder die Fähigkeit, blitzschnell und auf den Punkt genau zu

erkennen, wo mein Problem liegt. Dadurch waren Gespräche mit ihm immer äußerst effizient und konstruktiv. Ohne seine Beiträge hätte diese Arbeit nicht in dieser Form vorliegen können. Es ist mir eine ganz große Ehre, ihn diese Arbeit unterzeichnen zu lassen.

Warren MoberlyChan (Center for Nanoscale Systems, Harvard University) bin ich sehr dankbar dafür, dass er mich in seine Vorlesung und sein Praktikum zur Transmissions-Elektronenmikroskopie (TEM) aufgenommen hat, obwohl ich kein eingeschriebener Harvard-Student war. Dieses Praktikum war die beste Universitäts-Veranstaltung, an der ich seit Beginn meines Studiums teilgenommen habe. Warrens ausgezeichneten Lehrfähigkeiten habe ich es zu verdanken, dass ich innerhalb von nur zehn Wochen ein gutes Verständnis der Grundlagen und eine selbständige Beherrschung aller wichtigen Messmodi des Mikroskops und der Probenpräparation erwarb.

Auch Cheng-Yen Wen (Harvard University, jetzt MIT) war mir eine sehr große Hilfe beim Erlernen der Transmissions-Elektronenmikroskopie. Ihm bin ich auch sehr dankbar für das Herstellen von TEM-Querschnittsproben und für das Durchführen von EDS-Messungen. Seinen Ruf als Experte in der TEM-Probenherstellung trägt er zu Recht.

Alle in dieser Arbeit untersuchten Filme sind durch Sputterdeposition von Henning Dieker (RWTH Aachen) hergestellt worden. Hierfür danke ich ihm sehr, denn ohne die Proben wären sämtliche Messungen nicht möglich gewesen.

Byron Gates und Jennah Kriebel (Whitesides Group, Harvard University) bin ich sehr dankbar für hilfreiche Diskussionen zu allgemeinen technischen Fragen in Bezug auf Rasterkraftmikroskopie-Messungen.

Allen Mitgliedern des Physikalischen Instituts 1A an der RWTH Aachen und der Materials Science Group an der Harvard University bin ich für ein sehr entspanntes Arbeitsklima und anregende Diskussionen dankbar. Viele interessante und hilfreiche Diskussionen zu dem Gebiet dieser Arbeit fanden insbesondere statt mit den Mitgliedern der Phasenwechselgruppe in Aachen, d. h. u. a. mit Kyungmin Chung, Ralf Detemple, Henning Dieker, Michael Klein, Dominic Lencer, Daniel Lüsebrink, Hajo Noerenberg, Martin Salinga, Christoph Steimer, Daniel Wamwangi, Ke Wang, Wojciech Welnic, Han-Willem Wöltgens, Stefan Ziegler und Matthias Wuttig.

Weiterhin möchte ich Bart Kooi (Rijksuniversiteit Groningen) sehr für hilfrei-

che Diskussionen zur Transmissions-Elektronenmikroskopie danken. Jan Tomforde (Universität zu Kiel) gab mir wertvolle Ratschläge zur Probenpräparation für DSC-Messungen. David T. Wu (Yale University) danke ich für sehr hilfreiche Diskussionen zur Nukleationstheorie und Jan Siegel (Consejo Superior de Investigaciones Científicas, Madrid) für Diskussionen über GeSb-Verbindungen.

Bernd Braunecker (Brown University) möchte ich ganz herzlich für das äußerst sorgfältige Lesen mehrerer Kapitel dieser Arbeit danken. Ich fand es sehr beeindruckend, in einer fachfremden Person so großes Interesse an der Arbeit zu wecken und außerdem hilfreiche Verbesserungsvorschläge zu bekommen.

Linn Eichler, Josefine Elbert, Günther Kluck-Ehlen und Barbara Sewall danke ich sehr für viele administrative, organisatorische und notwendige „Kleinigkeiten“. Stefan Hermes, Michael Huppertz, Oliver Lehmann und Frank Molea standen immer als technische Ansprechpartner zur Verfügung.

Ganz herzlich danken möchte ich den Professoren Thomas Hebbeker, Matthias Wutting, Frans Spaepen, Joachim Mayer und Walter Selke dafür, dass sie in der Promotionskommission mitgewirkt haben. Matthias und Frans standen als Berichterstatter zur Verfügung. Einen ganz besonders großen Dank möchte ich an Frans aussprechen, der extra für die mündliche Doktorprüfung aus Boston nach Aachen gekommen ist.

Die Studienstiftung des deutschen Volkes und der Deutsche Akademische Austauschdienst haben mich während der Promotion finanziell unterstützt und dadurch diese Arbeit erst ermöglicht. Insbesondere wurde hierdurch der Forschungsaufenthalt an der Harvard University möglich. Hierfür bin ich zutiefst dankbar.

Meinen Mitbewohnerinnen und Mitbewohnern in Boston danke ich sehr dafür gesorgt zu haben, dass ich einen Großteil der Abende und Wochenenden nicht hinter einem Mikroskop oder einem Computer verbracht habe. Aurora hat mit ihrem ständigen Einsatz für „social events“ immer wieder dafür gesorgt, dass unsere WG nicht nur ein „Zusammenwohnen von Individuen“ ist. Auch Sebastian, Ans und Bernd danke ich für die vielen entspannenden und unterhaltsamen Abende und Wochenenden zu Hause. Aurora und Bernd haben immer wieder auf meine „ausgewogene Ernährung“ geachtet, und zwar auch dann noch, wenn ich von einer „late night microscope session“ nach Hause kam. Ein ganz besonderer Dank gilt Ruth für ihre unermessliche Geduld während meiner anstrengenden Schreib- und Lernphasen.

Schließlich danke ich ganz herzlich meinen Eltern, Gisela und Wilhelm Kalb, die mich während des gesamten Studiums uneingeschränkt unterstützt haben.

Vielen Dank!

# Bibliography

- [1] N. Nobukuni, M. Takashima, T. Ohno, and M. Horie. Microstructural changes in GeSbTe film during repetitious overwriting in phase-change optical recording. *Journal of Applied Physics*, 78:6980, 1995.
- [2] N. Yamada. Erasable phase-change optical materials. *Materials Research Society Bulletin*, 21:48, 1996.
- [3] L. van Pieterse, M.H.R. Lankhorst, M. van Schijndel, A.E.T. Kuiper, and J.H.J. Roosen. Phase-change recording materials with a growth-dominated crystallization mechanism: A materials overview. *Journal of Applied Physics*, 97:083520, 2005.
- [4] S. Hudgens and B. Johnson. Overview of phase-change chalcogenide nonvolatile memory technology. *Materials Research Society Bulletin*, 29:829, 2004.
- [5] M.H.R. Lankhorst, B.W.S.M.M. Ketelaars, and R.A.M. Wolters. Low-cost and nanoscale non-volatile memory concept for future silicon chips. *Nature Materials*, 4:347, 2005.
- [6] A.L. Greer and N. Mathur. Changing face of the chameleon. *Nature*, 437:1246, 2005.
- [7] D. Wamwangi, W.K. Njoroge, and M. Wuttig. Crystallization kinetics of Ge<sub>4</sub>Sb<sub>1</sub>Te<sub>5</sub> films. *Thin Solid Films*, 408:310, 2002.
- [8] I. Friedrich, V. Weidenhof, W. Njoroge, P. Franz, and M. Wuttig. Structural transformations of Ge<sub>2</sub>Sb<sub>2</sub>Te<sub>5</sub> films studied by electrical resistance measurements. *Journal of Applied Physics*, 87:4130, 2000.

- [9] W.K. Njoroge and M. Wuttig. Crystallization kinetics of sputter-deposited amorphous AgInSbTe films. *Journal of Applied Physics*, 90:3816, 2001.
- [10] S. Privitera, E. Rimini, C. Bongiorno, R. Zonca, A. Pirovano, and R. Bez. Crystallization and phase separation in  $\text{Ge}_{2+x}\text{Sb}_2\text{Te}_5$  thin films. *Journal of Applied Physics*, 94:4409, 2003.
- [11] D.-H. Kim, F. Merget, M. Laurenzis, P. Haring Bolivar, and H. Kurz. Electrical percolation characteristics of  $\text{Ge}_2\text{Sb}_2\text{Te}_5$  and Sn doped  $\text{Ge}_2\text{Sb}_2\text{Te}_5$  thin films during the amorphous to crystalline phase transition. *Journal of Applied Physics*, 97:083538, 2005.
- [12] H.J. Borg, M. van Schijndel, J.C.N. Rijpers, H.H.R. Lankhorst, G. Zhou, M.J. Dekker, I.P.D. Ubbens, and M. Kuijper. Phase-change media for high-numerical-aperture and blue-wavelength recording. *Japanese Journal of Applied Physics*, 40, Part 1:1592, 2001.
- [13] L. van Pieteron, M. van Schijndel, J.C.N. Rijpers, and M. Kaiser. Te-free, Sb-based phase-change materials for high-speed rewritable optical recording. *Applied Physics Letters*, 83:1373, 2003.
- [14] J.H. Coombs, A.P.J.M. Jongenelis, W. van Es-Spiekman, and B.A.J. Jacobs. Laser-induced crystallization phenomena in GeTe-based alloys. II. composition dependence of nucleation and growth. *Journal of Applied Physics*, 78:4918, 1995.
- [15] C. Peng, L. Cheng, and M. Mansuripur. Experimental and theoretical investigations of laser-induced crystallization and amorphization in phase-change optical recording media. *Journal of Applied Physics*, 82:4183, 1997.
- [16] A.C. Sheila and T.E. Schlesinger. Modeling thermal cross talk and overwrite jitter in growth dominant phase change optical recording media at high data rates. *Journal of Applied Physics*, 91:2803, 2002.
- [17] E.R. Meinders, H.J. Borg, M.H.R. Lankhorst, J. Hellmig, and A.V. Mijiritskii. Numerical simulation of mark formation in dual-stack phase-change recording. *Journal of Applied Physics*, 91:9794, 2002.

- [18] J.F. Shackelford. *Introduction to Materials Science for Engineers*. Macmillan, New York, 2nd edition, 1988.
- [19] T. Massalski, editor. *Binary Alloy Phase Diagrams*. ASM International, Materials Park, OH, 2nd edition, 1990.
- [20] F. Spaepen. *Physics of Defects*. Les Houches XXXV. North-Holland, Amsterdam, 1981. Page 133.
- [21] F. Spaepen and D. Turnbull. Metallic glasses. *Annual Review of Physical Chemistry*, 35:241, 1984.
- [22] C. Kittel. *Einführung in die Festkörperphysik*. Oldenbourg, Munich, 9th edition, 1991.
- [23] S.R. Elliott. *Physics of amorphous materials*. Longman, London, 2nd edition, 1990.
- [24] F. Spaepen. An introduction to phase nucleation. In D.M. Herlach and D. Holland-Moritz, editors, *Proceedings Kurzschnule Phasenübergänge in Schmelzen*, page 45, Cologne, 2000. Deutsches Zentrum für Luft- und Raumfahrt (DLR). IB-333-01/1.
- [25] F. Spaepen. *Lectures on phase transformations*. Lecture notes for students, Leuven, Belgium, Fall 1984.
- [26] D.M. Herlach. Non-equilibrium solidification of undercooled metallic melts. *Materials Science and Engineering R*, 12:177, 1994.
- [27] D.R. Uhlmann and N.J. Kreidl, editors. *Glass: Science and Technology*, volume 3. Academic Press, 1986.
- [28] S.I. Tsao. *Structural Relaxation and Isoconfigurational Flow in Metallic Glasses*. PhD thesis, Harvard University, 1983.
- [29] S. Roorda, J.M. Poate, D.C. Jacobson, D.J. Eaglesham, B.S. Dennis, S. Dierker, W.C. Sinke, F. Spaepen, and P. Fuoss. Structural relaxation and defect annihilation in pure amorphous silicon. *Physical Review B*, 44:3702, 1991.

- [30] H.S. Chen, L.C. Kimerling, J.M. Poate, and W.L. Brown. Diffusion in a Pd-Cu-Si metallic glass. *Applied Physics Letters*, 32:461, 1978.
- [31] M.P. Rosenblum, F. Spaepen, and D. Turnbull. Diffusion and structural relaxation in compositionally modulated amorphous metal films. *Applied Physics Letters*, 37:184, 1980.
- [32] A.I. Taub and F. Spaepen. The kinetics of structural relaxation of a metallic glass. *Acta Metallurgica*, 28:1781, 1980.
- [33] M.H. Cohen and D. Turnbull. Molecular transport in liquids and glasses. *Journal of Chemical Physics*, 31:1164, 1959.
- [34] C.A. Angell, K.L. Ngai, G.B. McKenna, P.F. McMillan, and S.W. Martin. Relaxation in glassforming liquids and amorphous solids. *Journal of Applied Physics*, 88:3113, 2000.
- [35] P.G. Debenedetti and F.H. Stillinger. Supercooled liquids and the glass transition. *Nature*, 410:259, 2001.
- [36] C.A. Angell. Spectroscopy simulation and scattering, and the medium range order problem in glass. *Journal of Non-Crystalline Solids*, 73:1, 1985.
- [37] V.N. Novikov and A.P. Sokolov. Poisson's ratio and the fragility of glass-forming liquids. *Nature*, 431:961, 2004.
- [38] W. Götze. *Liquids, freezing and the glass transition*. Les Houches LI. North-Holland, Amsterdam, 1991. Page 287.
- [39] H. Vogel. Das Temperaturabhängigkeitsgesetz der Viskosität von Flüssigkeiten. *Physikalische Zeitschrift*, 22:645, 1921.
- [40] G.S. Fulcher. Analysis of recent measurements of the viscosity of glasses. *Journal of the American Ceramic Society*, 8:339, 1925.
- [41] F. Spaepen. The identification of the metallic glass state. In *Materials Research Society Symposia Proceedings*, volume 57, page 161, 1986.

- [42] H. Tanaka. Relation between thermodynamics and kinetics of glass-forming liquids. *Physical Review Letters*, 90:055701, 2003.
- [43] J.C. Baker and J.W. Cahn. *Solidification*. Papers presented at a Seminar of the American Society for Metals, October 11 and 12, 1969. American Society for Metals, Metals Park, OH, 1971. Page 23. Library of Congress Catalog Card Number 70-169608.
- [44] C.V. Thompson and F. Spaepen. Homogeneous crystal nucleation in binary metallic melts. *Acta Metallurgica*, 31:2021, 1983.
- [45] D. Turnbull. Kinetics of solidification of supercooled liquid mercury droplets. *Journal of Chemical Physics*, 20:411, 1952.
- [46] W. Kauzmann. The nature of the glassy state and the behavior of liquids at low temperatures. *Chemical Reviews*, 43:219, 1948.
- [47] R.H. Doremus. *Glass science*. John Wiley & Sons, New York, 2nd edition, 1994.
- [48] H.S. Chen and D. Turnbull. Thermal properties of gold-silicon binary alloy near eutectic composition. *Journal of Applied Physics*, 38:3646, 1967.
- [49] F. Spaepen. A structural model for the solid-liquid interface in monatomic systems. *Acta Metallurgica*, 23:729, 1975.
- [50] F. Spaepen. Homogeneous nucleation and the temperature dependence of the crystal-melt interfacial tension. *Solid State Physics*, 47:1, 1994.
- [51] J.H. Gibbs and E.A. DiMarzio. Nature of the glass transition and the glassy state. *Journal of Chemical Physics*, 28:373, 1958.
- [52] G. Adam and J.H. Gibbs. On temperature dependence of cooperative relaxation properties in glass-forming liquids. *Journal of Chemical Physics*, 43:139, 1965.
- [53] F. Spaepen, private communication.
- [54] L.-M. Martinez and C.A. Angell. A thermodynamic connection to the fragility of glass-forming liquids. *Nature*, 410:663, 2001.

- [55] R. Richert and C.A. Angell. Dynamics of glass-forming liquids. V. On the link between molecular dynamics and configurational entropy. *Journal of Chemical Physics*, 108:9016, 1998.
- [56] C.A. Angell. Ten questions on glassformers, and a real space ‘excitations’ model with some answers on fragility and phase transitions. *Journal of Physics – Condensed Matter*, 12:6463, 2000.
- [57] D. Turnbull. Formation of crystal nuclei in liquid metals. *Journal of Applied Physics*, 21:1022, 1950.
- [58] J.H. Perepezko and J.S. Paik. Thermodynamic properties of undercooled liquid metals. *Journal of Non-Crystalline Solids*, 61–62:113, 1984.
- [59] C.V. Thompson and F. Spaepen. On the approximation of the free energy change on crystallization. *Acta Metallurgica*, 27:1855, 1979.
- [60] J.D. Hoffman. Thermodynamic driving force in nucleation and growth processes. *Journal of Chemical Physics*, 29:1192, 1958.
- [61] T. Fließbach. *Statistische Physik*. Spektrum Verlag, Heidelberg, 3rd edition, 1999.
- [62] J.W. Gibbs. *The scientific papers of J. Willard Gibbs*. Dover Publications, New York, 1961.
- [63] J.W. Christian. *Transformation in metals and alloys*. Pergamon Press, Oxford, 2nd edition, 1975.
- [64] K.F. Kelton. Crystal nucleation in liquids and glasses. *Solid State Physics*, 45:75, 1991.
- [65] M. Volmer and A. Weber. Keimbildung in übersättigten Gebilden. *Zeitschrift für Physikalische Chemie*, 119:277, 1926.
- [66] R. Becker and W. Döring. Kinetische Behandlung der Keimbildung in übersättigten Dämpfen. *Annalen der Physik*, 24:719, 1935.

- [67] D. Turnbull and J.C. Fisher. Rate of nucleation in condensed systems. *Journal of Chemical Physics*, 17:71, 1949.
- [68] L.D. Landau and E.M. Lifshitz. *Statistical Physics*. Pergamon Press, Oxford, 1969.
- [69] J.A. Hodgdon and F.H. Stillinger. Stokes-Einstein violation in glass-forming liquids. *Physical Review E*, 48:207, 1993.
- [70] D. Turnbull. Under what conditions can a glass be formed? *Contemporary Physics*, 10:473, 1969.
- [71] C.V. Thompson, A. L. Greer, and F. Spaepen. Crystal nucleation in amorphous  $(\text{Au}_{100-y}\text{Cu}_y)_{77}\text{Si}_9\text{Ge}_{14}$  alloys. *Acta Metallurgica*, 31:1883, 1983.
- [72] Y. Shao and F. Spaepen. Undercooling of bulk liquid silicon in an oxide flux. *Journal of Applied Physics*, 79:2981, 1996.
- [73] Y. Shao. *Undercooling of Bulk Liquid Silicon and Glass Forming Ability of Nickel-Based Alloys*. PhD thesis, Harvard University, 1997.
- [74] D. Turnbull. Kinetics of solidification of supercooled liquid mercury droplets. *Journal of Chemical Physics*, 20:411, 1952.
- [75] M. Volmer. Über Keimbildung und Keimwirkung als Spezialfälle der heterogenen Katalyse. *Zeitschrift für Elektrochemie*, 35:555, 1929.
- [76] D.T. Wu. Nucleation theory. *Solid State Physics*, 50:37, 1997.
- [77] D. Holland-Moritz. Short-range order and solid-liquid interfaces in undercooled melts. *International Journal of Non-Equilibrium Processing*, 11:169, 1998.
- [78] M.J. Aziz. *Kinetics of condensed phase processes*. Lecture notes for students, Harvard University, Spring 2003.
- [79] J. Crank. *The mathematics of diffusion*. Clarendon Press, Oxford, 2nd edition, 1975.

- [80] W.A. Johnson and R.F. Mehl. Reaction kinetics in process of nucleation and growth. *Transactions of the American Institute of Mining, Metallurgical and Petroleum Engineers*, 135:416, 1939.
- [81] M. Avrami. Kinetics of phase change. I. General theory. *Journal of Chemical Physics*, 7:1103, 1939.
- [82] M. Avrami. Kinetics of phase change. II. Transformation-time relations for random distribution of nuclei. *Journal of Chemical Physics*, 8:212, 1940.
- [83] M. Avrami. Kinetics of phase change. III. Granulation, phase change, and microstructure. *Journal of Chemical Physics*, 9:177, 1941.
- [84] G.W.H. Höhne, H.K. Cammenga, W. Eysel, E. Gmelin, and W. Hemminger. The temperature calibration of scanning calorimeters. *Thermochimica Acta*, 160:1, 1990.
- [85] H.K. Cammenga, W. Eysel, E. Gmelin, W. Hemminger, G.W.H. Höhne, and S.M. Sarge. The temperature calibration of scanning calorimeters. Part 2. Calibration substances. *Thermochimica Acta*, 219:333, 1993.
- [86] S.M. Sarge, E. Gmelin, G.W.H. Höhne, H.K. Cammenga, W. Hemminger, and W. Eysel. The caloric calibration of scanning calorimeters. *Thermochimica Acta*, 247:129, 1994.
- [87] S.M. Sarge, G.W.H. Höhne, H.K. Cammenga, W. Eysel, and E. Gmelin. Temperature, heat and heat flow rate calibration of scanning calorimeters in the cooling mode. *Thermochimica Acta*, 361:1, 2000.
- [88] M. E. Brown, editor. *Introduction to Thermal Analysis - Techniques and Applications*. Kluwer Academic Publishers, Boston, 2001.
- [89] P.J. Haines, editor. *Principles of Thermal Analysis and Calorimetry*. Royal Society of Chemistry, Cambridge, Great Britain, 2002.
- [90] D.B. Williams and C.B. Carter. *Transmission Electron Microscopy – A Textbook for Materials Science*. Plenum Press, New York, 1996.

- [91] J. Kalb, F. Spaepen, and M. Wuttig. Kinetics of crystal nucleation and growth in thin films of amorphous Te alloys measured by atomic force microscopy. In *Materials Research Society Symposia Proceedings*, volume 803, page HH3.8, 2004.
- [92] J. Kalb, F. Spaepen, and M. Wuttig. Atomic force microscopy measurements of crystal nucleation and growth rates in thin films of amorphous Te alloys. *Applied Physics Letters*, 84:5240, 2004.
- [93] M. Klein. *Crystallization kinetics in thin films of amorphous tellurium alloys used for phase change recording*. Diploma thesis, RWTH Aachen, 2006.
- [94] W.K. Njoroge. *Phase Change Optical Recording—Preparation and X-ray Characterization of GeSbTe and AgInSbTe films*. PhD thesis, RWTH Aachen, 2001.
- [95] M. Libera and M. Chen. Time-resolved reflection and transmission studies of amorphous Ge–Te thin-film crystallization. *Journal of Applied Physics*, 73:2272, 1993.
- [96] G. Ruitenbergh, A.K. Petford-Long, and R.C. Doole. Determination of the isothermal nucleation and growth parameters for the crystallization of thin Ge<sub>2</sub>Sb<sub>2</sub>Te<sub>5</sub> films. *Journal of Applied Physics*, 92:3116, 2002.
- [97] S. Privitera, C. Bongiorno, E. Rimini, and R. Zonca. Crystal nucleation and growth processes in Ge<sub>2</sub>Sb<sub>2</sub>Te<sub>5</sub>. *Applied Physics Letters*, 84:4448, 2004.
- [98] M. Libera. Evolution of crystalline microstructure in GeTe thin films for optical storage applications. In *Materials Research Society Symposia Proceedings*, volume 343, page 89, 1994.
- [99] Q.M. Lu and M. Libera. Microstructural measurements of amorphous GeTe crystallization by hot-stage optical microscopy. *Journal of Applied Physics*, 77:517, 1995.
- [100] M. Libera. Local amorphous thin-film crystallization induced by focused electron-beam irradiation. *Applied Physics Letters*, 68:331, 1996.

- [101] B.J. Kooi, W.M.G. Groot, and J.Th.M. De Hosson. In situ transmission electron microscopy study of the crystallization of  $\text{Ge}_2\text{Sb}_2\text{Te}_5$ . *Journal of Applied Physics*, 95:924, 2004.
- [102] V. Weidenhof, I. Friedrich, S. Ziegler, and M. Wuttig. Atomic force microscopy study of laser induced phase transitions in  $\text{Ge}_2\text{Sb}_2\text{Te}_5$ . *Journal of Applied Physics*, 86:5879, 1999.
- [103] T.P. Leervad Pedersen, J. Kalb, W.K. Njoroge, D. Wamwangi, M. Wuttig, and F. Spaepen. Mechanical stresses upon crystallization in phase change materials. *Applied Physics Letters*, 79:3597, 2001.
- [104] H.S. Carslaw and J.C. Jaeger. *Conduction of heat in solids*. Clarendon Press, Oxford, 2nd edition, 1959.
- [105] R.C. Weast, editor. *CRC Handbook of Chemistry and Physics*. CRC Press, Boca Raton, FL, 60th edition, 1979.
- [106] J. Kalb, F. Spaepen, and M. Wuttig. Calorimetric measurements of phase transformations in thin films of amorphous Te alloys used for optical data storage. *Journal of Applied Physics*, 93:2389, 2003.
- [107] J.A. Kalb. *Stresses, viscous flow and crystallization kinetics in thin films of amorphous chalcogenides used for optical data storage*. Diploma thesis, RWTH Aachen, 2002.
- [108] S.S. Tsao and F. Spaepen. Structural relaxation of a metallic glass near equilibrium. *Acta Metallurgica*, 33:881, 1985.
- [109] C.A. Volkert. *Flow and Relaxation of Amorphous Metals*. PhD thesis, Harvard University, 1988.
- [110] A. Witvrouw, C.A. Volkert, and F. Spaepen. The viscosity of amorphous metallic thin films. *Materials Science and Engineering A*, 134:1274, 1991.
- [111] A. Witvrouw. *Viscosity and Elastic Constants of Amorphous Thin Films*. PhD thesis, Harvard University, 1992.

- [112] A. Witvrouw and F. Spaepen. Viscosity and elastic constants of amorphous Si and Ge. *Journal of Applied Physics*, 74:7154, 1993.
- [113] J.A. Mullin. *Viscous Flow and Structural Relaxation in Amorphous Silicon and Amorphous Selenium Thin Films*. PhD thesis, Harvard University, 2000.
- [114] J. Kalb, F. Spaepen, T.P. Leervad Pedersen, and M. Wuttig. Viscosity and elastic constants of thin films of amorphous Te alloys used for optical data storage. *Journal of Applied Physics*, 94:4908, 2003.
- [115] J.A. Kalb, C.Y. Wen, F. Spaepen, H. Dieker, and M. Wuttig. Crystal morphology and nucleation in thin films of amorphous Te alloys used for phase change recording. *Journal of Applied Physics*, 98:054902, 2005.
- [116] B.J. Kooi and J.Th.M. De Hosson. On the crystallization of thin films composed of  $\text{Sb}_{3.6}\text{Te}$  with Ge for rewritable data storage. *Journal of Applied Physics*, 95:4714, 2004.
- [117] W.J. MoberlyChan (Harvard University), private communication.
- [118] N. Yamada and T. Matsunaga. Structure of laser-crystallized  $\text{Ge}_2\text{Sb}_{2+x}\text{Te}_5$  sputtered thin films for use in optical memory. *Journal of Applied Physics*, 88:7020, 2000.
- [119] T.H. Jeong, M.R. Kim, H. Seo, S.J. Kim, and S.Y. Kim. Crystallization behavior of sputter-deposited amorphous  $\text{Ge}_2\text{Sb}_2\text{Te}_5$  thin films. *Journal of Applied Physics*, 86:774, 1999.
- [120] N. Yamada, E. Ohno, K. Nishiuchi, N. Akahira, and M. Takao. Rapid phase transitions of  $\text{GeTe-Sb}_2\text{Te}_3$  pseudobinary amorphous thin films for an optical disk memory. *Journal of Applied Physics*, 69:2849, 1991.
- [121] D. Turnbull and R.E. Cech. Microscopic observation of the solidification of small metal droplets. *Journal of Applied Physics*, 21:804, 1950.
- [122] G.M. Devaud. *Undercooling and Solidification Morphologies in Germanium and Silicon*. PhD thesis, Harvard University, 1986.

- [123] G. Devaud and D. Turnbull. Undercooling of molten silicon. *Applied Physics Letters*, 46:844, 1985.
- [124] W.K. Njoroge, H. Dieker, and M. Wuttig. Influence of dielectric capping layers on the crystallization kinetics of  $\text{Ag}_5\text{In}_6\text{Sb}_{59}\text{Te}_{30}$  films. *Journal of Applied Physics*, 96:2624, 2004.
- [125] U. Köster and H. Blanke. On nucleation of crystallization in  $\text{Co}_{70}\text{B}_{30}$  metallic glasses. *Scripta Metallurgica*, 17:495, 1983.
- [126] V. Weidenhof, I. Friedrich, S. Ziegler, and M. Wuttig. Laser induced crystallization of amorphous  $\text{Ge}_2\text{Sb}_2\text{Te}_5$  films. *Journal of Applied Physics*, 89:3168, 2001.
- [127] I. Friedrich, V. Weidenhof, S. Lenk, and M. Wuttig. Morphology and structure of laser-modified  $\text{Ge}_2\text{Sb}_2\text{Te}_5$  films studied by transmission electron microscopy. *Thin Solid Films*, 389:239, 2001.
- [128] H.-W. Wöltgens, R. Detemple, I. Friedrich, W.K. Njoroge, I. Thomas, V. Weidenhof, S. Ziegler, and M. Wuttig. Exploring the limits of fast phase change materials. In *Materials Research Society Symposia Proceedings*, volume 674, page V1.3, 2001.
- [129] S. Ziegler. *Rekristallisationskinetik von Phasenwechselmedien*. PhD thesis, RWTH Aachen, 2005.
- [130] H. Noerenberg. *Charakterisierung der Phasenumwandlungskinetik ternärer Chalkogenidlegierungen zur Datenspeicherung*. Diploma thesis, RWTH Aachen, 2005.
- [131] H.-J. Lee, H. Ni, D.T. Wu, and A.G. Ramirez. Experimental determination of kinetic parameters for crystallizing amorphous NiTi thin films. *Applied Physics Letters*, 87:114102, 2005.
- [132] H.-J. Lee, H. Ni, D.T. Wu, and A.G. Ramirez. Grain size estimations from the direct measurement of nucleation and growth. *Applied Physics Letters*, 87:124102, 2005.

- [133] H.E. Kissinger. Reaction kinetics in differential thermal analysis. *Analytical Chemistry*, 29:1702, 1957.
- [134] D.W. Henderson. Thermal analysis of non-isothermal crystallization kinetics in glass forming liquids. *Journal of Non-Crystalline Solids*, 30:301, 1979.
- [135] E. Woldt. The relationship between isothermal and non-isothermal description of Johnson-Mehl-Avrami-Kolmogorov kinetics. *Journal of Physics and Chemistry of Solids*, 53:521, 1992.
- [136] N. Ohshima. Crystallization of germanium–antimony–tellurium amorphous thin film sandwiched between various dielectric protective films. *Journal of Applied Physics*, 79:8357, 1996.
- [137] S. Senkader and C.D. Wright. Models for phase-change of  $\text{Ge}_2\text{Sb}_2\text{Te}_5$  in optical and electrical memory devices. *Journal of Applied Physics*, 95:504, 2004.
- [138] D.T. Wu (Yale University, author of Refs. [76], [131], and [132]), private communication.
- [139] W.T. Kim and B. Cantor. Solidification behavior of Pb droplets embedded in a Cu matrix. *Acta Metallurgica et Materialia*, 40:3339, 1992.
- [140] K.A.Q. O'Reilly and B. Cantor. Solidification behavior of Al particles embedded in a Zr aluminide matrix. *Acta Metallurgica et Materialia*, 43:405, 1995.
- [141] P.G. Höckel, H. Sieber, and J.H. Perepezko. *Solidification*. The Minerals, Metals & Materials Society, 1998. Page 289.
- [142] K.F. Kelton, A.L. Greer, D.M. Herlach, and D. Holland-Moritz. The influence of order on the nucleation barrier. *Materials Research Society Bulletin*, 29:940, 2004.
- [143] W.T. Kim and B. Cantor. An adsorption model of the heterogeneous nucleation of solidification. *Acta Metallurgica et Materialia*, 42:3115, 1994.
- [144] M.H.R. Lankhorst. Modelling glass transition temperatures of chalcogenide glasses. Applied to phase-change optical recording materials. *Journal of Non-Crystalline Solids*, 297:210, 2002.

- [145] N. Yamada, E. Ohno, N. Akahira, K. Nishiuchi, K. Nagata, and M. Takao. High speed overwritable phase change optical disk material. *Japanese Journal of Applied Physics*, 26, Supplement 26–4:61, 1987.
- [146] E. Morales-Sanchez, E.F. Prokhorov, A. Mendoza-Galvan, and J. Gonzalez-Hernandez. Determination of the glass transition and nucleation temperatures in  $\text{Ge}_2\text{Sb}_2\text{Te}_5$  sputtered films. *Journal of Applied Physics*, 91:697, 2002.
- [147] J.A. Kalb, M. Wuttig, and F. Spaepen. Calorimetric measurements of structural relaxation and glass transition temperatures in sputtered films of amorphous Te alloys used for phase change recording. *Submitted to the Journal of Applied Physics*.
- [148] F.X. Gan, S.S. Xue, and Z.X. Fan. Metastable phase formation and structural change characteristics of vapor deposited semiconductor films. *Annalen der Physik*, 1:391, 1992.
- [149] T.-W. Wu and F. Spaepen. The relation between embrittlement and structural relaxation in an amorphous metal. *Philosophical Magazine B*, 61:739, 1990.
- [150] C.T. Moynihan, P.B. Macedo, C.J. Montrose, P.K. Gupta, M.A. DeBolt, J.F. Dill, B.E. Dom, P.W. Drake, A.J. Easteal, P.B. Elterman, R.P. Moeller, H. Sasabe, and J.A. Wilder. Structural relaxation in vitreous materials. *Annals of the New York Academy of Sciences*, 279:15, 1976.
- [151] R.B. Stephens. The viscosity and structural relaxation rate of evaporated amorphous selenium. *Journal of Applied Physics*, 49:5855, 1978.
- [152] S. Roorda, S. Doorn, W.C. Sinke, P.M.L.O. Scholte, and E. van Loenen. Calorimetric evidence for structural relaxation in amorphous silicon. *Physical Review Letters*, 62:1880, 1989.
- [153] E.P. Donovan, F. Spaepen, D. Turnbull, J.M. Poate, and D.C. Jacobson. Calorimetric studies of crystallization and relaxation of amorphous Si and Ge prepared by ion implantation. *Journal of Applied Physics*, 57:1795, 1985.

- [154] E.P. Donovan, F. Spaepen, J.M. Poate, and D.C. Jacobson. Homogeneous and interfacial heat releases in amorphous silicon. *Applied Physics Letters*, 55:1516, 1989.
- [155] T.P. Leervad Pedersen. *Mechanical stresses upon phase transitions*. PhD thesis, RWTH Aachen, 2003.
- [156] D. Chiang, T.-R. Jeng, D.-R. Huang, Y.-Y. Chang, and C.-P. Liu. Kinetic crystallization behavior of phase-change medium. *Japanese Journal of Applied Physics*, 38:1649, 1999.
- [157] J. Park, M.R. Kim, W.S. Choi, H. Seo, and C. Yeon. Characterization of amorphous phases of  $\text{Ge}_2\text{Sb}_2\text{Te}_5$  phase-change optical recording material on their crystallization behavior. *Japanese Journal of Applied Physics*, 38:4775, 1999.
- [158] H. Seo, T.-H. Jeong, J.-W. Park, C. Yeon, S.-J. Kim, and S.-Y. Kim. Investigation of crystallization behavior of sputter-deposited nitrogen-doped amorphous  $\text{Ge}_2\text{Sb}_2\text{Te}_5$  thin films. *Japanese Journal of Applied Physics*, 39:745, 2000.
- [159] B. Legendre, C. Hancheng, S. Bordas, and M.T. Clavaguera-Mora. Phase diagram of the ternary system Ge-Sb-Te. I. The subternary GeTe-Sb<sub>2</sub>Te<sub>3</sub>-Te. *Thermochimica Acta*, 78:141, 1984.
- [160] S. Bordas, M.T. Clavaguera-Mora, B. Legendre, and C. Hancheng. Phase diagram of the ternary system Ge-Sb-Te. II. The subternary Ge-GeTe-Sb<sub>2</sub>Te<sub>3</sub>-Sb. *Thermochimica Acta*, 107:239, 1986.
- [161] H. Iwasaki, M. Harigaya, O. Nonoyama, Y. Kageyama, M. Takahashi, K. Yamada, H. Deguchi, and Y. Ide. Completely erasable phase change optical disc II: Application of Ag-In-Sb-Te mixed-phase system for rewritable compact disc compatible with CD-velocity and double CD-velocity. *Japanese Journal of Applied Physics*, 32, Part 1:5241, 1993.
- [162] H.W. Kui, A.L. Greer, and D. Turnbull. Formation of bulk metallic glass by fluxing. *Applied Physics Letters*, 45:615, 1984.

- [163] H.W. Kui. *Formation and properties of bulk metallic glass*. PhD thesis, Harvard University, 1986.
- [164] H.W. Kui and D. Turnbull. Melting of Ni<sub>40</sub>Pd<sub>40</sub>P<sub>20</sub> glass. *Applied Physics Letters*, 47:796, 1985.
- [165] C.F. Lau and H.W. Kui. Sound emission during crystallization of undercooled liquid germanium. *Journal of Applied Physics*, 67:3181, 1990.
- [166] C.F. Lau and H.W. Kui. Microstructures of undercooled germanium. *Acta Metallurgica et Materialia*, 39:323, 1991.
- [167] T. D. Shen and R. B. Schwarz. Bulk ferromagnetic glasses prepared by flux melting and water quenching. *Applied Physics Letters*, 75:49, 1999.
- [168] D.M. Herlach, D. Holland-Moritz, Th. Schenk, K. Schneider, G. Wilde, O. Boni, J. Fransaer, and F. Spaepen. Undercoolability of pure Co and Co-based alloys. *Journal of Non-Crystalline Solids*, 250–252:271, 1999.
- [169] E.A. Brandes and G.B. Brook, editors. *Smithells Metals Reference Book*. Butterworth-Heinemann, Oxford, 7th edition, 1992.
- [170] J.A. Kalb, F. Spaepen, and M. Wuttig. Kinetics of crystal nucleation in undercooled droplets of Sb- and Te-based alloys used for phase change recording. *Journal of Applied Physics*, 98:054910, 2005.
- [171] W.T. Laughlin and D.R. Uhlmann. Viscous flow in simple organic liquids. *Journal of Physical Chemistry*, 76:2317, 1972.
- [172] A.I. Priven. Calculation of the viscosity of glass-forming melts: V. Binary borate systems. *Glass Physics and Chemistry*, 26:541, 2000.
- [173] M.J. Aziz. *Kinetics of crystallization of B<sub>2</sub>O<sub>3</sub> under pressure and theory of motion of the crystal-melt interface at wide departures from equilibrium*. PhD thesis, Harvard University, 1983.
- [174] M.J. Aziz, E. Nygren, J.F. Hays, and D. Turnbull. Crystal growth kinetics of boron oxide under pressure. *Journal of Applied Physics*, 57:2233, 1985.

- [175] J.F. Elliott and M. Gleiser. *Thermochemistry for Steelmaking*. Addison-Wesley, London, 1960.
- [176] N.Kh. Abrikosov and G.T. Danilova-Dobryakova. An investigation of the structural diagram of  $\text{Sb}_2\text{Te}_3\text{-GeTe}$ . *Translated from Izvestiya Akademii Nauk SSSR, Neorganicheskie Materialy*, 1:204, 1965.
- [177] R.E. Cech and D. Turnbull. Microscopic observation of the solidification of Cu-Ni alloy droplets. *Journal of Metals*, 3:242, 1951.
- [178] J.H. Perepezko. In R. Mehrabian, B.H. Kear, and M. Cohen, editors, *Proceedings of the 2nd International Conference on Rapid Solidification Processing*, page 56, Baton Rouge, LA, 1980. Claitor's Press.
- [179] J.H. Perepezko. Nucleation in undercooled liquids. *Materials Science and Engineering*, 65:125, 1984.
- [180] D.H. Rasmussen, J.H. Perepezko, and C.R. Loper. Studies of the undercooling and nucleation of liquid metals and alloys utilizing the droplet technique. In N.J. Grant and B.C. Giessen, editors, *Proceedings of the 2nd International Conference on Rapidly Quenched Metals*, volume 1, page 51, Cambridge, MA, 1976. Massachusetts Institute of Technology Press.
- [181] Z.P. Lu, Y. Li, and S.C. Ng. Reduced glass transition temperature and glass forming ability of bulk glass forming alloys. *Journal of Non-Crystalline Solids*, 270:103, 2000.
- [182] F. Herwig and M. Wobst. Eine Schwingtiegelapparatur zur Bestimmung der Viskosität von Flüssigkeiten bei hohen Temperaturen. *Zeitschrift für Metallkunde*, 82:913, 1991.
- [183] F. Herwig and M. Wobst. Viskositätsuntersuchungen in den Systemen Antimon-Tellur und Zinn-Tellur. *Zeitschrift für Metallkunde*, 83:35, 1991.
- [184] F. Herwig and M. Wobst. Viskositätsuntersuchungen im System Germanium-Tellur. *Zeitschrift für Metallkunde*, 82:917, 1991.

- [185] H. Neumann, F. Herwig, and W. Hoyer. The short range order of liquid eutectic  $A_{III}$ -Te and  $A_{IV}$ -Te alloys. *Journal of Non-Crystalline Solids*, 205–207:438, 1996.
- [186] F. Spaepen and R.B. Meyer. The surface tension in a structural model for the solid-liquid interface. *Scripta Metallurgica*, 10:257, 1976.
- [187] C.V. Thompson II. *Crystal nucleation in easy glass-forming metallic alloys*. PhD thesis, Harvard University, 1981.
- [188] T. Okabe, S. Endo, and S. Saito. Simultaneous crystallization of both elements in amorphous Ge-Sb and Ge-Al eutectic alloys. *Journal of Non-Crystalline Solids*, 117–118:222, 1990.
- [189] A.K. Petford-Long, R.C. Doole, C.N. Afonso, and J. Solis. *In situ* studies of the crystallization kinetics in Sb-Ge films. *Journal of Applied Physics*, 77:607, 1995.
- [190] U. Senapati and A.K. Varshneya. Viscosity of chalcogenide glass-forming liquids: an anomaly in the ‘strong’ and ‘fragile’ classification. *Journal of Non-Crystalline Solids*, 197:210, 1996.
- [191] A.S. Tverjanovich. Calculation of viscosity of chalcogenide glasses near glass transition temperature from heat capacity or thermal expansion data. *Journal of Non-Crystalline Solids*, 298:226, 2002.
- [192] A.S. Tverjanovich. Temperature dependence of the viscosity of chalcogenide glass-forming melts. *Glass Physics and Chemistry*, 29:532, 2003.
- [193] T. E. Faber. *Introduction to the Theory of Liquid Metals*. Cambridge University Press, Cambridge, Great Britain, 1972.
- [194] F. Spaepen. Five-fold symmetry in liquids. *Nature*, 408:781, 2000.
- [195] D. Holland-Moritz, D.M. Herlach, and K.F. Kelton. Unterkühlt und dicht gepackt. *Physik Journal*, 4:37, 2005.
- [196] F.C. Frank. Supercooling of liquids. *Proceedings of the Royal Society of London A*, 215:43, 1952.

- [197] H. Reichert, O. Klein, H. Dosch, M. Denk, V. Honkimäki, T. Lippmann, and G. Reiter. Observation of five-fold local symmetry in liquid lead. *Nature*, 408:839, 2000.
- [198] D. Holland-Moritz. *Ordnungsphänomene, fest-flüssig Grenzfläche und Phasenselektionsverhalten in unterkühlten Metallschmelzen*. Habilitationsschrift, Ruhr-Universität Bochum, 2003.
- [199] E.-K. Kim, S.-I. Kwun, S.-M. Lee, H. Seo, and J.-G. Yoon. Thermal boundary resistance at  $\text{Ge}_2\text{Sb}_2\text{Te}_5/\text{ZnS}:\text{SiO}_2$  interface. *Applied Physics Letters*, 76:3864, 2000.
- [200] M. Kaiser, L. van Pieteron, and M.A. Verheijen. *In situ* transmission electron microscopy analysis of electron beam induced crystallization of amorphous marks in phase-change materials. *Journal of Applied Physics*, 96:3193, 2004.
- [201] P. Haring Bolivar, F. Merget, D.-H. Kim, B. Hadam, and H. Kurz, European Symposium on Phase Change and Ovonic Science (EPCOS), Balzers, Liechtenstein, 2004 (unpublished).
- [202] K.F. Kelton and A.L. Greer. Transient nucleation effects in glass formation. *Journal of Non-Crystalline Solids*, 79:295, 1986.



# Curriculum Vitae

## Angaben zur Person:

Name: Kalb  
Vornamen: Johannes Andreas  
Geburtsdatum: 21. Juni 1976  
Geburtsort: Neuss, Nordrhein-Westfalen  
Staatsangehörigkeit: deutsch  
Familienstand: ledig  
Kinder: keine

## Schulbildung:

08/1982 – 07/1986 Erich-Kästner-Grundschule Dormagen, Kreis Neuss  
08/1986 – 06/1995 Bettina-von-Arnim-Gymnasium Dormagen  
Abschluss: Abitur (Gesamtnote: 1,5)

## Zivildienst:

07/1995 – 08/1996 Universitätskliniken der Heinrich-Heine-Universität Düsseldorf  
(Pflegedienst in der Chirurgie auf einer Krankenstation) und  
Paracelsus-Klinik Neuss (Pflegedienst im Operationssaal)

## Studium:

10/1996 – 06/2002 Physik- und Mathematikstudium an der  
Rheinisch-Westfälischen Technischen Hochschule (RWTH) Aachen  
Abschlüsse: - Zwischenprüfung Lehramt  
Sekundarstufe II (Mathematik);  
Datum: 07/1998  
Gesamtnote: sehr gut

- Vordiplom (Physik);  
Datum: 08/1998  
Gesamtnote: sehr gut
- Diplom (Physik);  
Datum: 06/2002  
Gesamtnote: mit Auszeichnung (1,0)

Titel der Diplomarbeit: „Stresses, viscous flow and crystallization kinetics in thin films of amorphous chalcogenides used for optical data storage“, angefertigt am I. Physikalischen Institut der RWTH Aachen bei Prof. Dr. Matthias Wuttig;

Auszeichnung der Diplomarbeit mit dem Friedrich-Wilhelm-Preis der RWTH Aachen

#### **Promotion:**

02/2003 – 02/2006 Arbeit an der Promotion in Physik am I. Physikalischen Institut der RWTH Aachen bei Prof. Dr. Matthias Wuttig;  
Promotionsstipendiat des Deutschen Akademischen Austauschdienstes (DAAD) und der Studienstiftung des deutschen Volkes

#### **Studien- und Forschungsaufenthalte im Ausland:**

09/1998 – 06/1999 Vertiefung des Physikstudiums an der University of Edinburgh, Großbritannien

05/2001 – 09/2001 Forschungsaufenthalt im Rahmen der Diplomarbeit an der Division of Engineering and Applied Sciences, Harvard University, Boston/Cambridge, USA, bei Prof. Dr. Frans Spaepen

02/2003 – 08/2004 Forschungsaufenthalt im Rahmen der Promotion an der Division of Engineering and Applied Sciences, Harvard University, Boston/Cambridge, USA, bei Prof. Dr. Frans Spaepen

**Veröffentlichungen in rezensierten Fachzeitschriften:**

1. T.P. Leervad Pedersen, J. Kalb, W.K. Njoroge, D. Wamwangi, M. Wuttig und F. Spaepen.  
Mechanical stresses upon crystallization in phase change materials.  
*Applied Physics Letters*, 79:3597, 2001.
2. J. Kalb, F. Spaepen und M. Wuttig.  
Calorimetric measurements of phase transformations in thin films of amorphous Te alloys used for optical data storage.  
*Journal of Applied Physics*, 93:2389, 2003.
3. J. Kalb, F. Spaepen, T.P. Leervad Pedersen und M. Wuttig.  
Viscosity and elastic constants of thin films of amorphous Te alloys used for optical data storage.  
*Journal of Applied Physics*, 94:4908, 2003.
4. J. Kalb, F. Spaepen und M. Wuttig.  
Atomic force microscopy measurements of crystal nucleation and growth rates in thin films of amorphous Te alloys.  
*Applied Physics Letters*, 84:5240, 2004.
5. J.A. Kalb, C.Y. Wen, F. Spaepen, H. Dieker und M. Wuttig.  
Crystal morphology and nucleation in thin films of amorphous Te alloys used for phase change recording.  
*Journal of Applied Physics*, 98:054902, 2005.
6. J.A. Kalb, F. Spaepen und M. Wuttig.  
Kinetics of crystal nucleation in undercooled droplets of Sb and Te based alloys used for phase change recording.  
*Journal of Applied Physics*, 98:054910, 2005.
7. J.A. Kalb, M. Wuttig und F. Spaepen.  
Calorimetric measurements of structural relaxation and glass transition temperatures in sputtered films of amorphous Te alloys used for phase change recording.  
Eingereicht bei *Journal of Applied Physics*.

**Veröffentlichte Konferenzbeiträge:**

1. J. Kalb, F. Spaepen und M. Wuttig.  
Kinetics of crystal nucleation and growth in thin films of amorphous Te alloys measured by atomic force microscopy.  
Vortrag, Materials Research Society (MRS) Fall Meeting, Boston, USA, Dezember 2003.  
Rezensierter Beitrag veröffentlicht in:  
*Materials Research Society Symposia Proceedings*, 803:HH 3.8, 2004.

